

School of Molecular and Life Sciences

**Towards optical and potentiometric measurements of double layer
structures and dynamics**

Mattia Belotti
0000-0002-7382-337X

**This thesis is presented for the Degree of
Doctor of Philosophy in Chemistry
Curtin University**

May 2023

Declaration

To the best of my knowledge, I declare that this thesis is my own account of my research, and this thesis contains no material previously published by any other person except where due acknowledgement has been made.

This thesis contains as its main content work which has not previously been submitted for a degree or diploma at any university.

Mattia Belotti

Signature: 

Date: 11/05/2023

Abstract

This thesis focuses on exploring novel techniques to probe the electric double layer. In **Chapter 1**, techniques currently available to investigate the electric double layer are discussed, highlighting their scope and limitations. For example, some of them are probe techniques that will inevitably carry their double layer, making hard to separate from the one under investigation. Others require even more complex instrumentation.

Chapter 2 discusses how electrochemiluminescence and spectral tuning (colour changes) can be employed for the investigation of electrified electrode-electrolyte interfaces. Bioluminescence is a natural phenomenon, where light-emitting reactions often involve changes in oxidation states. Fireflies are probably one of the best-known bioluminescent species. Interestingly, firefly luciferin's emission can be triggered at an electrode and spectrally modulated by solvent, electrolyte, and voltage. The emission wavelength is modulated by modifying the solvent nature and/or cation size of the supporting electrolyte, suggesting an electrostatic mechanism behind the spectral tuning. However, due to the high cost of luciferin and the need for chemical derivatization procedures, luciferin is perhaps not the best candidate to develop a simple and accessible technique to probe the electric double layer.

Therefore, in **Chapter 3**, the possibility of spectrally tuning the electrochemiluminescence of luminol, a readily available and relatively inexpensive luminophore, is explored. Nevertheless, the spectral tuning of luminol resulted more complicated to achieve, as attempts to modify the reaction environment or use silicon working electrodes with different monolayer chemistries did not lead to similar results as those previously obtained for luciferin.

In **Chapter 4**, following the unsuccessful attempts with luminol spectral tuning, an intriguing class of chemicals is investigated as possible reaction media for the electrochemiluminescence of both luminol and firefly's luciferin: room temperature ionic liquids. Room temperature ionic liquids are liquid salts, and their numerous properties make them a promising avenue for studying the electric double layer. Additionally, the electrochemiluminescence in room temperature ionic liquids is underexplored, with many questions still unanswered. One of the unexpected results was that the light emission persisted for several seconds after the removal of an external bias. This discovery offers new insights into the nature of the electric double layer

in room temperature ionic liquids, particularly the stabilization of reactive oxygen species and the stability of cation-rich double layer structures.

Chapter 5 explores further the stability of cation-rich double layers in ionic liquids. Here it was shown that after applying an external negative voltage pulse to an electrode wetted by a room temperature ionic liquid, the electrode open circuit potential remained negative for hours or even days, confirming the theoretical hypothesis of crowding and overscreening long-lived double layers in room temperature ionic liquids.

Finally, **Chapter 6** explores the impact of such stable overscreening and crowding double layers on electrochemical reactions performed in room temperature ionic liquids. The formation of long-lived double layers is shown to have an impact on inner-sphere reactions, such as hydrogen evolution, particularly so in room temperature ionic liquids where these long-lived compact near-electrode ionic layers are more persistent. On the other hand, outer-sphere reactions seem relatively unaffected by crowding and screening structures.

The thesis concludes with **Chapter 7**, which provides conclusive remarks and an outlook based on the foreseen immediate and future implications of the results presented in this thesis.

Acknowledgments

Firstly, I acknowledge Curtin University and the School of Molecular and Life Sciences (MLS) which provided the facilities where I accomplished my PhD, as well as the Australian Research Council (ARC) for the financial support.

Secondly, I would like to acknowledge my main supervisor Associate Professor Simone Ciampi, for his guidance throughout my PhD, his unlimited support has been fundamental to improving as a scientist. Moreover, his knowledge, his enormous curiosity, and his passion for science have led me to carry out extremely interesting research, allowing publications in high-impact factor journals. I am proud, that I have had the opportunity to work with him. I would like to acknowledge my co-supervisor Dr. Nadim Darwish, who has also been an important mentor, proving his experience in electrochemical science. Ass. Prof. Simone Ciampi and Dr. Nadim Darwish have built an amazing group of researchers, a perfect environment to investigate the wonders of chemistry.

Additionally, a special thanks to Professor Michelle Coote (Flinders University) and her group for the computational works carried out for my publications. Other important collaborations I must acknowledge are Professor Ekaterina Pas (Monash University) and her group, as well as Professor Marco Garavelli and Dr. Mohsen M. T. El-Tahawy (University of Bologna) for developing theoretical models in supporting of my experimental results.

I would also like to acknowledge all the members of the Molecular Electronics group, Yan Vogel, Essam Dief, Chandramalika Peiris, Jinyang Zhang, Song Zhang, Stuart Ferrie, Xin Lyu, Carlos Torres Tiexin Li, Soraya Rahpeima and Harry Rodriguez.

I would like to thank my whole family, mainly, my dad, my mom, my brother, and my grandmother for their support despite of the great distance.

Finally, a huge thanks to my girlfriend Yasmin, for the great support and love she gives all the time. This adventure (my PhD) is just one of the one of many we are going to share together.

List of publications included in this thesis

Paper 1

Mattia Belotti, Mohsen M. T. El-Tahawy, Li-Juan Yu, Isabella C. Russell, Nadim Darwish, Michelle L. Coote, Marco Garavelli, and Simone Ciampi. Luciferase-free Luciferin Electrochemiluminescence. *Angew. Chem. Int. Ed.* **2022**, 61, 46 e202209670. (cover article)

Angewandte
Chemie
Für Zeitschrift der Gesellschaft Deutscher Chemiker
www.angewandte.de
2022-134/46



Treibbild
Mattia Belotti, Mohsen M. T. El-Tahawy, Nadim Darwish, Marco Garavelli, Simone Ciampi et al.
Luciferase-free Luciferin Electrochemiluminescence
www.angewandte.de

WILEY-VCH

Paper 2

Mattia Belotti, Mohsen M. T. El-Tahawy, Nadim Darwish, Marco Garavelli, and Simone Ciampi. Electrochemically Generated Luminescence of Luminol and Luciferin in Ionic Liquids, *ChemElectroChem* **2022**, 10, 1, e202201033.

Paper 3

Mattia Belotti, Xin Lyu, Longkun Xu, Peter Halat, Nadim Darwish, Debbie S. Silvester, Ching Goh, Ekaterina I. Izgorodina, Michelle L. Coote and Simone Ciampi. Experimental Evidence of Long-Lived Electric Fields of Ionic Liquid Bilayers. *J. Am. Chem. Soc.* **2021**, 143, 42, 17431–17440.

Paper 4

Mattia Belotti, Mohsen M. T. El-Tahawy, Nadim Darwish, Marco Garavelli, Michelle L. Coote and Simone Ciampi. Separating convective from diffusive mass transport mechanisms in ionic liquids by redox pro-fluorescence microscopy. *Anal. Chem.* **2023**, 95, 26, 9779–9786.

Conference presentation

Mattia Belotti, Mohsen M. T. El-Tahawy, Li-Juan Yu, Isabella C. Russell, Nadim Darwish, Michelle L. Cote, Marco Garavelli, and Simone Ciampi *Firefly's electrochemiluminescence*
Royal Australian Chemical Institute 2022 National Congress, Brisbane, 22nd Australasian
Electrochemistry Symposium, July 2022.

Dedication

I dedicate this thesis to my grandfathers Mario and Libero, and to my grandmother Caterina who recently passed away. A thought also to my grandmother Maria, which unfortunately I have never met.

Statement of contribution of others

Mattia Belotti is the main contributor to this study, including the execution of most of the experimental work. Other contributors have been involved in the work described in this thesis. Their contributions have been extremely important, and they are listed as co-authors on all the published works reported here. These are expanded on in Appendix 6.

Table of contents

Declaration.....	ii
Abstract.....	iii
Acknowledgments.....	v
List of publications included in this thesis	vi
Conference presentation.....	vii
Dedication.....	viii
Statement of contribution of others	ix
Table of contents	x
Chapter 1: Introduction	1
1.0 The electric double layer	1
1.1 Electrostatic catalysis, from single-molecule to bulk synthesis	6
1.2 Electric fields in semiconductors.....	8
1.3 Non-electrochemical detection of double layer structure	9
1.3.1 Surface forces to infer on EDL structure	9
1.3.2 X-ray photoelectron spectroscopy (XPS) to probe the EDL	12
1.3.3 Direct voltage profiling.....	13
1.3.4 Electrode kinetic measurement for EDL probing	16
1.3.5 Microdroplets fluorescence microscopy	17
1.4 A Thesis overview	18
Chapter 2: Luciferase-free Luciferin Electrochemiluminescence	25
2.0 Abstract	26
2.1 Introduction.....	26
2.2 Results and Discussion	28
2.3 Conclusion.....	40
Chapter 3: Luminol Electrochemiluminescence on Silicon.....	42
3.1 Introduction.....	43
3.2 Results and Discussion	44
3.3 Conclusions	49
3.4 Experimental Section.....	49
3.4.1 Materials.....	49
3.4.2 Silicon electrodes preparation	50
3.4.3 Electrochemical Methods	50
3.4.4. Plots Fitting.....	51

Chapter 4: Electrochemically Generated Luminescence of Luminol and Luciferin in Ionic Liquids	52
4.0 Abstract	52
4.1 Introduction.....	53
4.2 Results and Discussion	54
4.3 Conclusion.....	60
4.4 Experimental Section.....	60
Chapter 5: Experimental evidence of long-lived electric fields of ionic liquid bilayers	62
5.0 Abstract	63
5.1 Introduction.....	63
5.2 Results and Discussion	65
5.2.1 Interfacial Dynamics of [EMIM][EtSO ₄].	65
5.2.2 Comparison of Different RTILs	68
5.2.3 Effect of Electrode Material	69
5.2.4 Polarizable Molecular Dynamics Studies.	69
5.3 Conclusions	74
5.4 Experimental Section	75
5.4.1 Materials.....	75
5.4.2 Electrochemical Methods	75
5.4.3 Computational Methods.	78
Chapter 6: Separating convective from diffusive mass transport mechanisms in ionic liquids by redox pro-fluorescence microscopy	80
6.1 Abstract	81
6.2 Introduction.....	81
6.3 Experimental Section.....	83
6.3.1. Materials.....	83
6.3.2 Fluorescence and ECL imaging.	84
6.3.3 Photon counting.	86
6.3.4 Fluorescence and ECL spectroscopy.	86
6.3.5 Open circuit potentiometry.....	86
6.3.6 Cyclic voltammetry.	87
6.3.7 Digital simulations of voltammograms.	87
6.4 Results and Discussion	88
6.5 Conclusion.....	95

Chapter 7: Conclusion and outlook.....	97
Appendix 1: Supporting Information Paper 1	101
A1.1 Experimental Procedures	101
A1.1.1 Materials.	101
A1.1.2 Synthetic procedures.	101
A1.1.3 Spectroelectrochemical measurements.	102
A1.1.4 Photon Counting.	103
A1.1.5 Luminescence imaging.	103
A1.1.6 Fluorescence imaging.	104
A1.1.7 Theoretical calculations.....	105
A1.2 Supporting Figures.....	107
A1.3 Supporting Tables	129
Appendix 2: Supporting Information Paper 2	142
Appendix 3: Supporting Information Paper 3	149
A3.1 Supplementary Experimental and Computational Results	149
Appendix 4: Supporting Information Paper 4	178
Appendix 5: Copyright forms and declaration	199
Appendix 6: Statement of contributions of others	208
Statement of contribution of others for paper 1	208
Statement of contribution of others for paper 2	210
Statement of contribution of others for paper 3	211
Statement of contribution of others for paper 4	213
References	214

Chapter 1: Introduction

1.0 The electric double layer

The focus of this thesis is to describe new methodologies to probe the electrified interface. For this purpose, it is important to begin this first chapter with a review of the theoretical models used to describe the interface.

Firstly, electrochemistry is the study of chemical changes coupled to the flow of electricity. It is therefore obvious that electrochemical systems involve electrodes: an electrified solid in contact with an electrolyte.¹ While the bulk of the electrolyte remains electro-neutral regardless of the external voltage bias applied to the solid conductor, this electroneutrality is progressively lost as we approach the interface. Except for systems at their potential of zero charge (pzc),² the interface can be electrically described as two layers of charge of opposite sign, an electric double layer.^{1, 3-5} In other words, when the potential of an electrode is shifted away from its pzc, generally using a suitable reference electrode and an external potential source, the externally imposed charge needs to be balanced by the formation of excess counter-ions at the interface (Figure 1.1a), thus there is the formation of what is known as electric double layer (hereafter EDL).^{6, 7} This double layer is thicker when the electrolyte concentration is lower (Figure 1.1a), precisely for low concentration of supporting electrolyte (up to ~0.1 M), the Debye length is inversely proportional to the square root of the electrolyte concentration.⁸ The Debye length is the distance from a surface immersed in an electrolytic solution, where is possible to observe a tangible charge separation in the EDL and it is a fundamental detail in colloidal studies (Figure 1.1a).⁸ In fact, the classical electrolyte theories explain how counter-ion concentration drops exponentially with the distance from the interface.⁹ However, at high electrolyte concentration, it is predicted a Debye length similar to the molecular diameter of a solvated molecule.

The Debye length is how far away from the electrified interfaces, and into the solution, the electrode's potential has dropped by a magnitude of $1/e$ of its surface value.⁹ Consequently, any effect of the EDL on charge transfer reactions or non-redox reactions sensitive to voltage gradients, will be dependent on the distance from the electrified surface. For example, redox reactions have to satisfy a tunnelling distance (Figure 1.1b), and this has to be of a similar order to the EDL thickness.⁸ The effect of the EDL electric field can also be strong enough that can be exploited, for example, to assist in the electrostatic catalysis of non-redox reactions.¹⁰

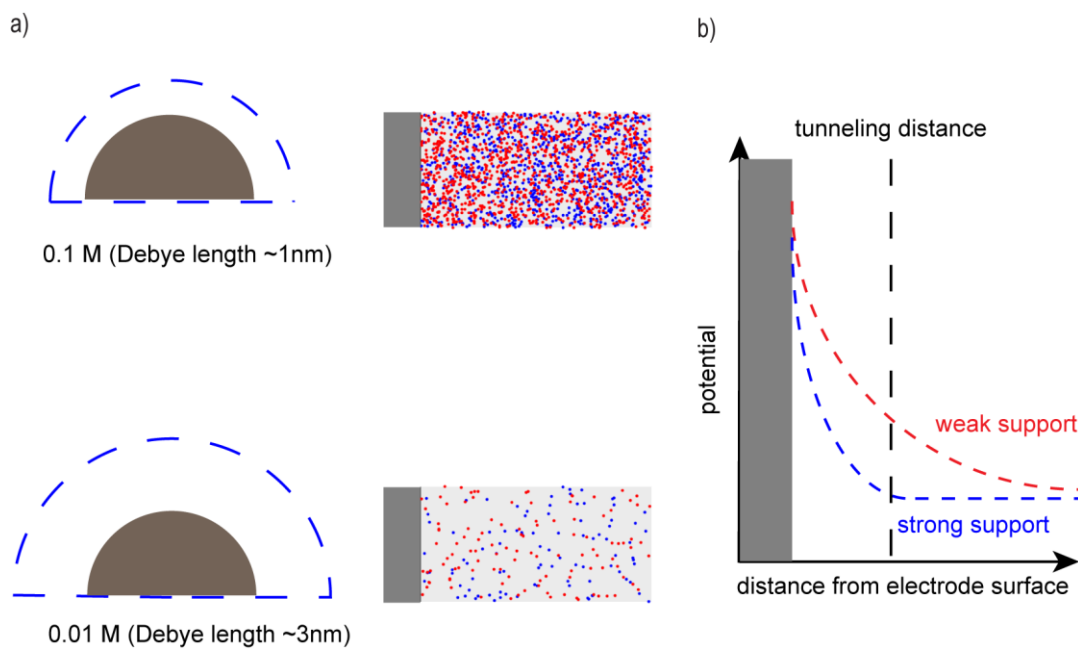


Figure 1.1: A charged surface (such as a particle or an electrode) immersed in a solution attracts ions of the opposite charge. The Debye layer is an ionic cloud that screens the surface's charge, and the Debye length, a characteristic distance at which significant charge separation can occur, is shorter for more highly supported electrolytes (a). The potential applied between the working and the reference electrode mainly drops in this unbalanced ionic cloud, and a more or less step near surface field affect the redox reactivity of molecules that approach the interface till they reach a tunnelling distance (b).⁸

However, the Debye length is complicated to estimate, which makes the predictions based on this theory unreliable at high electrolyte concentrations.⁹ The Debye length is a measure of the EDL thickness and it drops with the increasing of the ionic strength (Figure 1.1a), which means increasing the electrolyte concentration, however, the Debye length does not describe the structure of the EDL. While the potential profile refers to the molecules that can “feel” the full applied potential between the working and the reference electrode, the structure is the spatial distribution of ions at the interface, which depends on the nature of the liquid and from the features of the applied electric field. In order words, the structure of the EDL is how the ions are organized at the interface, generating different systems such as crowding.¹¹ The structure of the EDL was first described by the Helmholtz model.

In this model, when metal electrodes are considered at the equilibrium, being good conductors, they do not bear any electric field, consequently, any charge excess lies at the electrode surface, and this excess must be counterbalanced by the solution.¹² Consequently, the structure of the EDL is how the ions are placed at the interface to counterbalance the charge

excess, and for the Helmholtz, model this can happen in two ways, without or with ions adsorption on the surface. With the absence of any specific adsorption, only the water molecules are in direct contact with the surface, while the ions are located in the outer Helmholtz plane, a second layer where the whole charge excess is stored (Figure 1.2a).¹³ On the other hand, when there are adsorbed ions on the metal surface, the centres of these ions form the inner Helmholtz plane, whose charge is balanced by the electrode charged and by the ions in the inner Helmholtz plane (Figure 1.2b).¹³ The first weakness of this model is to explain the differential capacitance as a stable value, whilst measurements reveal on the other hand a capacitance that changes with potential and concentration.¹² Furthermore, the Helmholtz model allows to have an appropriate illustration when the electrolyte concentration is high, but it cannot give a proper description of the EDL at low concentrations, when the electrolyte concentration is significantly low, the thickness of the solution needed to counterbalance the surface charge may be relevant.¹²

At the beginning of the last century, the Gouy–Chapman model unfolded this issue describing the EDL even at low concentrations. The Gouy–Chapman model is based on a planar electrode, made by a metal that is an ideal conductor with the charge excess distributed uniformly on the whole surface, in contact with a solvent that is a dielectric continuum (Figure 1.2c). The great excess of charge is therefore limited to the electrode surface, where the electrostatic forces can balance the thermal processes, on the other hand at a greater distance the electrostatic forces drop as well as the electrolyte concentration. Hence, this model includes a diffuse layer, which thickness depends on electrolyte concentration and potential. To describe the change in concentration at EDL the corresponding equation is Poisson–Boltzmann, which can describe the model proposed by L. G. Gouy and D. L. Chapman,¹⁴ allowing to estimate the distribution of cations and anions, which are seen as point particles. This theory can describe quite well the EDL at low electrolyte concentrations and when the potential is close to the pzc,¹⁵ unfortunately at high concentrations the capacity is notably overestimated.

In the Gouy–Chapman theory, the anions, and the cations are seen as point charges, but this generates a problem when the polarization rises at very high values. In this situation the distance between the metal electrode and the charge part of the solution drops to zero, creating an unrealistic model of the EDL.¹² Therefore, Stern proposed a modification that considers the ions' size, consequently, when the electrolyte concentration is quite elevated, it is possible to image a minimum distance of approach for the ions. Hence, when the concentration is low

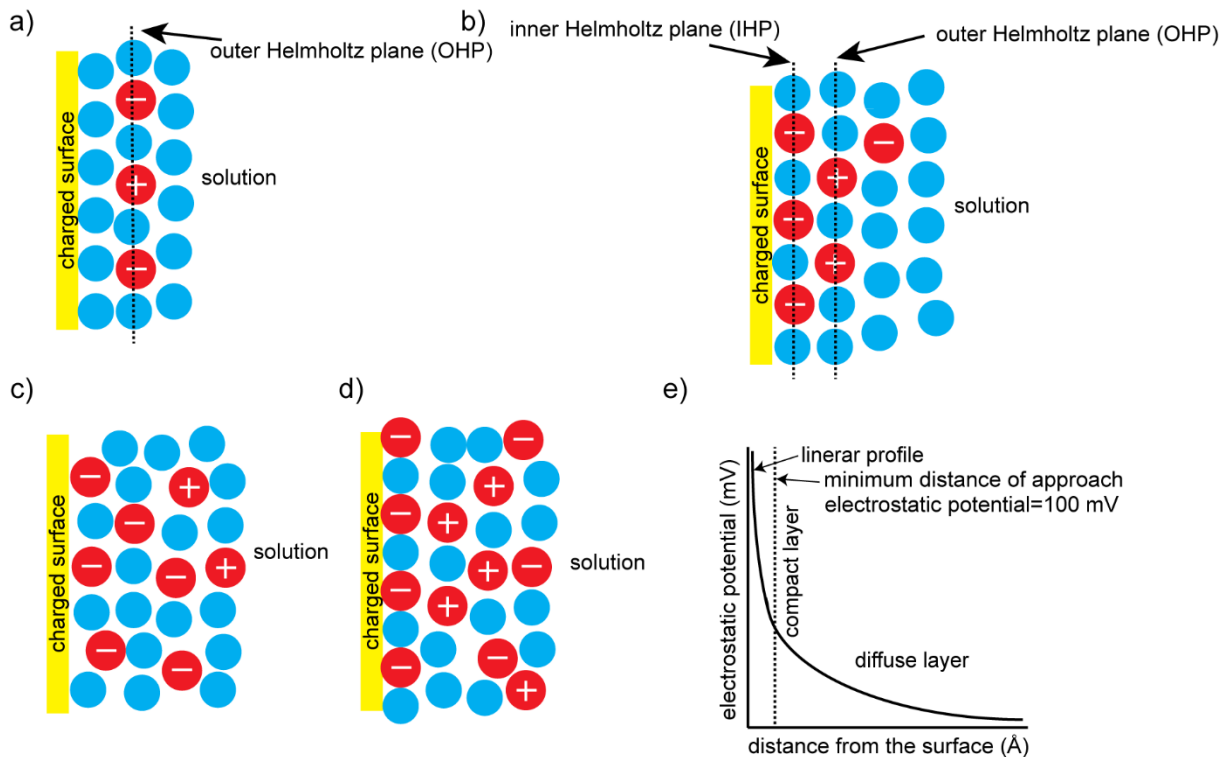


Figure 1.2: Schematic representations of the double layer in the absence of specific adsorption (a), and in the presence of specific adsorption (b). The model proposed by Gouy and Chapman (c) and the modification suggested by Stern (d). Potential profile according to the GCS theory in an aqueous solution 10^{-2} M electrolyte concentration (e).

enough the thickness of the diffuse layer is higher than this distance, allowing a good prediction on the capacitance, at least for potential values close to the pzc. On the other hand, at high concentrations the diffuse layer is compressed against this minimum distance, leading to a system like the one proposed by Helmholtz. Consequently, what has to be expected is the formation of several levels of different capacitance, and the distance becomes a fundamental notion allowing to discriminate between the inner Helmholtz plane (IHP) and the outer Helmholtz layer (OHP) (Figure 1.2d-e).^{12, 16}

This model, first proposed by Stern, is often named the Gouy–Chapman–Stern model (GCS), and allows making reasonable predictions for most of the real system, even though there is still some inconsistency, for example not considering ions pairing, and the nonspecific interactions of ions with the electrode surface.¹² Hence, in the Stern model, the EDL is formed to balance the surface's charge, moving away from the surface the potential drops, firstly linearly in the compact layer (or Stern layer, composed by the IHP and the OHP), indicated as 'linear profile' in Figure 1.2e.¹⁶ In this layer, the molecules are specifically adsorbed on the surface and then exponentially in the diffuse layer.^{12, 16} As previously said, all these models are following the Debye length measure, which predicts an exponential drop in electrolyte interaction increasing

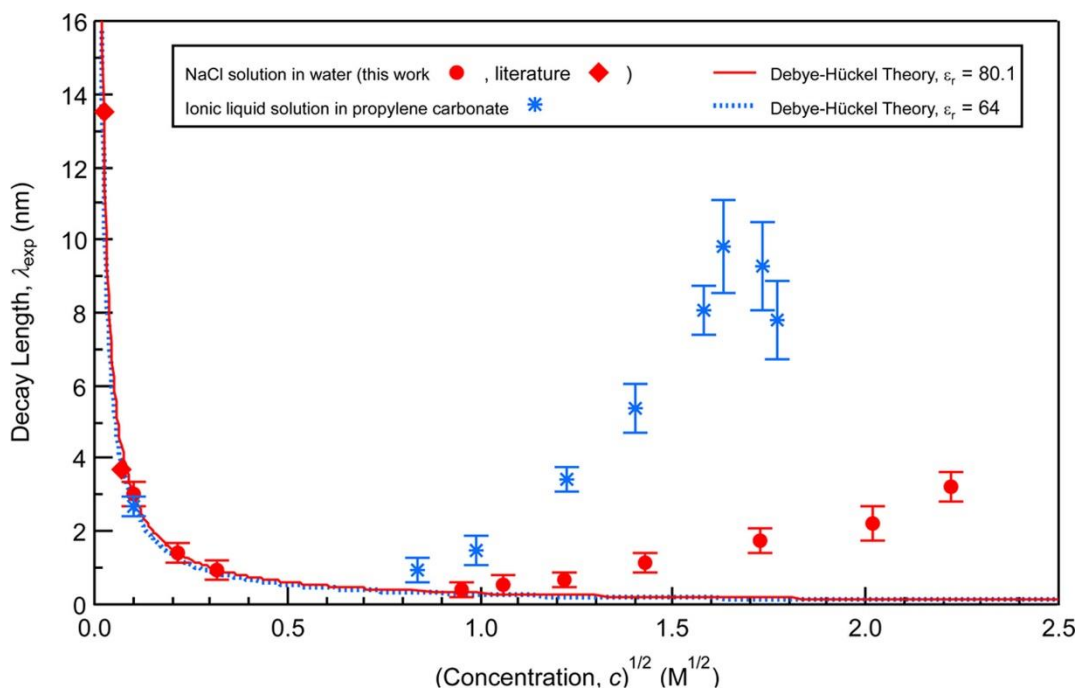


Figure 1.3: Theoretical and measured Debye length plotted against electrolyte concentration. The red curve is the theoretical Debye length for aqueous NaCl solution, but the measured value (red squares) shows how from ~ 1 M the real behavior is not correlated with the theoretical prediction. These results are even more “anomalous” when an ionic liquid-organic solvent mixture is considered (such as 1-butyl-1-methylpyrrolidinium bis [(trifluoromethane)]imide and propylene carbonate), the deviation from theoretical decay length (blue dashed line) is higher than for aqueous electrolyte solution. Reprinted with permission from *J. Phys. Chem. Lett.*, 2016, 7, 2157 (Ref. 10. Copyright 2016 American Chemical Society)

the distance from the surface, but more recent studies have suggested a non-monotonic decay, changing the paradigm.⁹

Indeed, further theoretical works have suggested an asymptotic drop in decay length with an increase in electrolyte concentration, and taking into account more features of the electrolyte, such as ion size or hardcore correlation, it is now clear that for concentrated solution the decay length exceeds the Debye one.^{9, 14, 17} Recently, some new studies have given a new insight for an aqueous salt solution and ionic liquids, for these systems, increasing the concentration a screening length is generated (Figure 1.3),⁹ particularly the EDL features in ionic liquids will be discussed in the thesis, in **Chapters 5** and **6**. This behaviour is completely unexpected by the Debye model, where the increase of ions concentration should lead to a decrease in the decay length.⁹ Particularly, ionic liquids are only made by ions, leading to a unique behaviour when they approach a charged surface, deeply different than the dilute solution.¹⁸

1.1 Electrostatic catalysis, from single-molecule to bulk synthesis

As briefly mentioned above, the loss of electro-neutrality near an electrode is the driving force of redox changes, redox reactions respond dramatically and predictably to changes in voltages, and for example, a voltage increase of 1 V can trigger an increase in redox current – that is, redox rates – as large as several millions in the current density value.¹ Since most chemists are trained to systematically separate reactions into redox and non-redox, the apparent role of an EDL is limited to the former class. Recent research is however beginning to demonstrate that the voltage/distance (electric field) drop of an EDL may play an important role in the electrostatic catalysis of non-redox reactions.¹ When the molecules are located for a long time in the EDL, its electrostatic environment can trigger non-redox chemical reactions, in other words, increasing our knowledge of the EDL can be fundamental to future development on electrostatic catalysis.⁸ The experiments of **Chapter 7** will attempt to broaden this understanding by looking at a specific example of a non-redox reaction that is expected to be kinetically affected by electric fields.^{19, 20}

In nature, enzymes are known to exploit electrostatic catalysis to perform biological reactions.²¹ Enzymes are fundamental proteins in all living organisms because they are responsible to catalyse all the chemical reactions occurring inside a cell.²¹ Nowadays, it is known how enzymes can catalyses reaction controlling selectivity, stereochemistry, and many other parameters that can affect a chemical reaction, making them the most powerful existing catalysts.²¹ Surprisingly, their catalytic power strongly depends on electric fields, indeed electrostatic interaction plays a central role in enzymatic activity so their catalysis can be defined as electrostatic catalysis.^{21, 22}

How an oriented external electric field can be a powerful tool to catalyse a wide number of non-redox reactions has been explained.²²⁻²⁵ Controlling the field direction alongside the reaction axis we can not only reduce the energy barrier but we can be able to control the selectivity,²⁴ or the kind of chemical reaction.²² Nevertheless, a complete mastery of it is far from being achieved, because experimental results are still penurious and still limited to complex and small-scale techniques.¹⁰ Indeed, while scanning–tunnelling microscopy (hereafter STM) experiments had demonstrated the feasibility of electrostatic catalysis,^{10, 25} where a single-molecule junction is carried out by controlling the electric field direction alongside the reaction axis (Figure 1.4).²⁵⁻²⁷

These chemical reactions can be performed in mild conditions, such as room temperature, atmospheric pressure, and pure liquid solvents.^{10, 25} Despite these experiments representing a great achievement in the comprehension of electrostatic catalysis, the development of this catalysis in bulk solution is far to be fulfilled.⁶ Therefore, the actual challenge is to develop electrostatic catalysis in diffuse systems, but previously, it is necessary to understand the nature of the electrode-liquid interface, that will allow measuring the electric field at the interface. Eventually, the last step will be to discriminate the electrostatic catalysis from the electrochemical catalysis in electrochemical systems. Nowadays, the main available technique to probe the electric field nature at the interface is the direct measurement of electrostatic forces,^{28, 29} X-ray photoelectron spectroscopy(XPS),³⁰ scanning electrochemical potential microscopy (SECPM), including STM-based option,^{31, 32} and electrode kinetic measurements.^{33, 34}

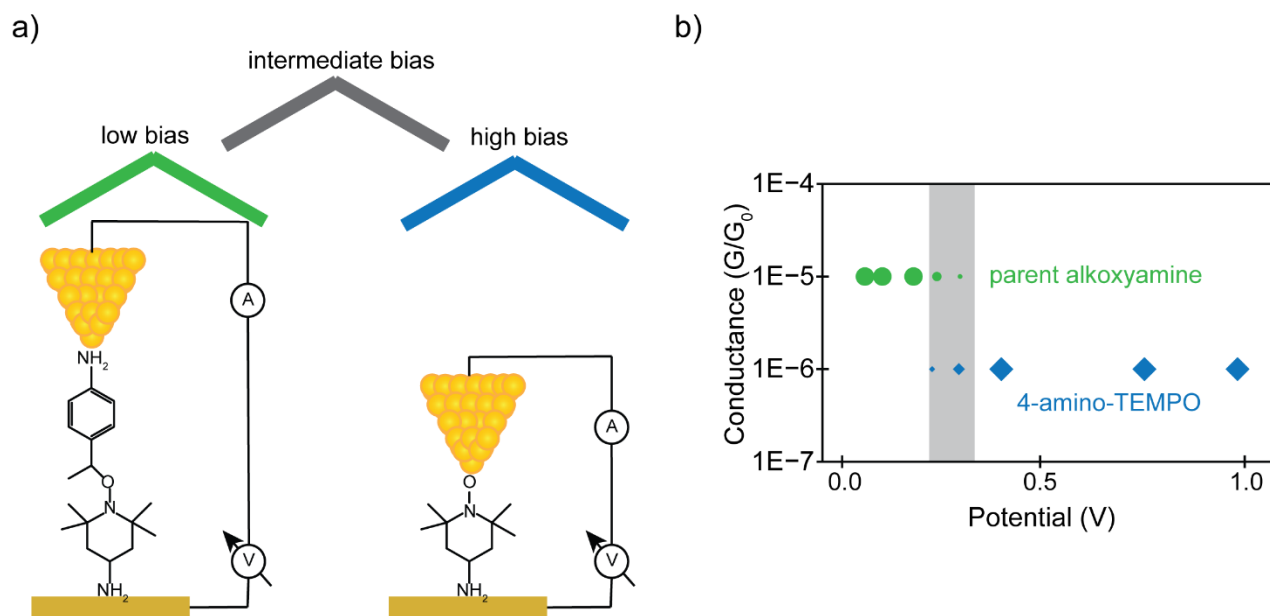


Figure 1.4: Cleavage of a C–O bond due to the effect of an external electric field. Schematic representation of scanning tunneling microscopy (STM) for a single molecule break-junction, where the effect of an external electric field on a C–O is investigated (a). Over 0.2 V the alkoxyamine fractionises generating nitroxide radicals. The two chemicals have an evident electric conductance, with the product that is less conducting by an order of magnitude. The potential between STM tip and substrate leads the redistribution, indeed up to 0.10 V an alkoxyamine-only population can be detected, at intermediate biases (between 0.15 V and 0.20 V) the population is a mixture of starting material and product and, finally, over 0.30 V only nitroxide is present (b).^{8, 25}

All these techniques are complex and highly demanding as well as they present some limitations that can affect the measurements. Hence, developing new and simpler ways to probe the electrode-liquid interface is a fundamental challenge on the road that will lead to electrostatic catalysis in diffuse systems. Recently, open circuit potentiometry has been proposed as the simplest way to probe the EDL structure and its stability in ionic liquid (**Chapter 5**), this technique may become a fundamental tool for probing EDL features.¹¹

1.2 Electric fields in semiconductors

As formerly explained, in conductors the excess charge is forced outside toward the surface, so the internal electric field is zero. However, this is not true for semiconductors, where the excess charge is also distributed inside the electrode, leading to different behaviour than normal metal electrodes. The semiconductors have a space charge region at the interface with the solution, in which the electric field has a gradient that allows an easy separation of ion pairs at the interface.³⁵

In 2016 Zhang and co-workers made the first attempt to measure the electrostatic effect on a redox molecule (ferrocene) confining them on a semiconductor surface.³⁶⁻³⁸ Electrochemical current is allowed to go through a semiconductor-electrolyte interface, where covalent organic monolayers build on the silicon hydrate orient molecules inside an electric field allowing both to probe and to take advantage of the near-surface electrostatic forces.^{6, 38} What has been observed is how the interaction between supporting electrolytes and organic monolayer can control the features of a redox couple, such as nitroxide/oxoammonium.³⁶ The main outcome of this work is the possibility to handle the oxidizing power of the studied redox couple, and it is emphasized how the electrostatic effect, due to the interaction with a supporting electrolyte, has a practical importance.³⁶ Finally, using lowly doped silicon instead of highly doped, led to an interesting “peak inversion” which consists in a reduction rate predominance at anodic bias, probably due to an electrostatic effect on the semiconductor space charge.³⁶

Subsequently, the same group has developed a new analytical technique and laboratory procedure to consider the impact of the electrostatic effect on redox kinetics, showing how this impact had been miscalculated.^{6, 37} In this publication Vogel and co-workers used first hydrosilylation to passivate silicon hydrate with an acetylene-terminated monolayer, thus they grafted ferrocene through click reaction, where azidomethylferrocene reacts with the acetylene end of the monolayer.^{37, 39} The analysis of these samples by cyclic voltammetry led to a full

width at half maximum (fwhm hereafter) higher than the ideal value, contrarily, damaging the surface and reducing the ferrocene coverage, the fwhm dropped below the ideal value, suggesting a predominance of repulsive forces when in the first case, while attractive forces dominate when coverage is lowered (Figure 1.5).³⁷

Subsequently, they have rejected all plausible explanations for these “non-idealities”, concluding that is mainly a “dynamic” space-charge effect of low-doped silicon interacting electrostatically with ferricenium molecules.³⁷ In a most recent study, Vogel and co-workers focused on electron transfer kinetic suggesting a common underestimation of its magnitude and reinforcing their previous discoveries.³⁸ They used the same ferrocene monolayer on lowly doped silicon to discriminate electron transfer kinetic from interactions between adsorbed species and diode effects.³⁸ This work can offer an important contribution to the study of non-redox electrostatic catalysis by helping in dividing between electrostatic and electrochemical effects.⁶ Electrostatic catalysis, on semiconductor electrodes, is explored in the last chapter of this thesis.

1.3 Non-electrochemical detection of double layer structure

1.3.1 Surface forces to infer on EDL structure

Amongst the different measurements somehow related to the EDL, the most complicated is the potential profiling. Consequently, some techniques have been developed through the years, including the estimation of surface electrostatic forces. It is known that, when two surfaces or colloid particles are placed in an aqueous solution at short distance, there are repulsions force deriving from the ordering of molecules at the interface, this repulsion force is generated by the contribution of two forces, van der Waals attraction force and repulsive electrostatic force due to double-layer.^{28, 29, 40-42} This theory, known as DLVO (from the initials of authors' surname, Derjaguin, Landau, Verwey, and Overbeek),^{43, 44} is proved to be reliable in describing colloid stability in aqueous solution, with experiments results supporting it.^{28, 45, 46} Nevertheless, DLVO fails when the electrolyte concentration is increased over certain values, as well as when short-range forces are involved because DLVO is unable to describe the addition repulsive forces present.^{45, 46}

Over the years, many experimental works have confirmed this theory, either for surface or colloid system.^{28, 29, 46} For surfaces, it has been demonstrated how the van der Waals

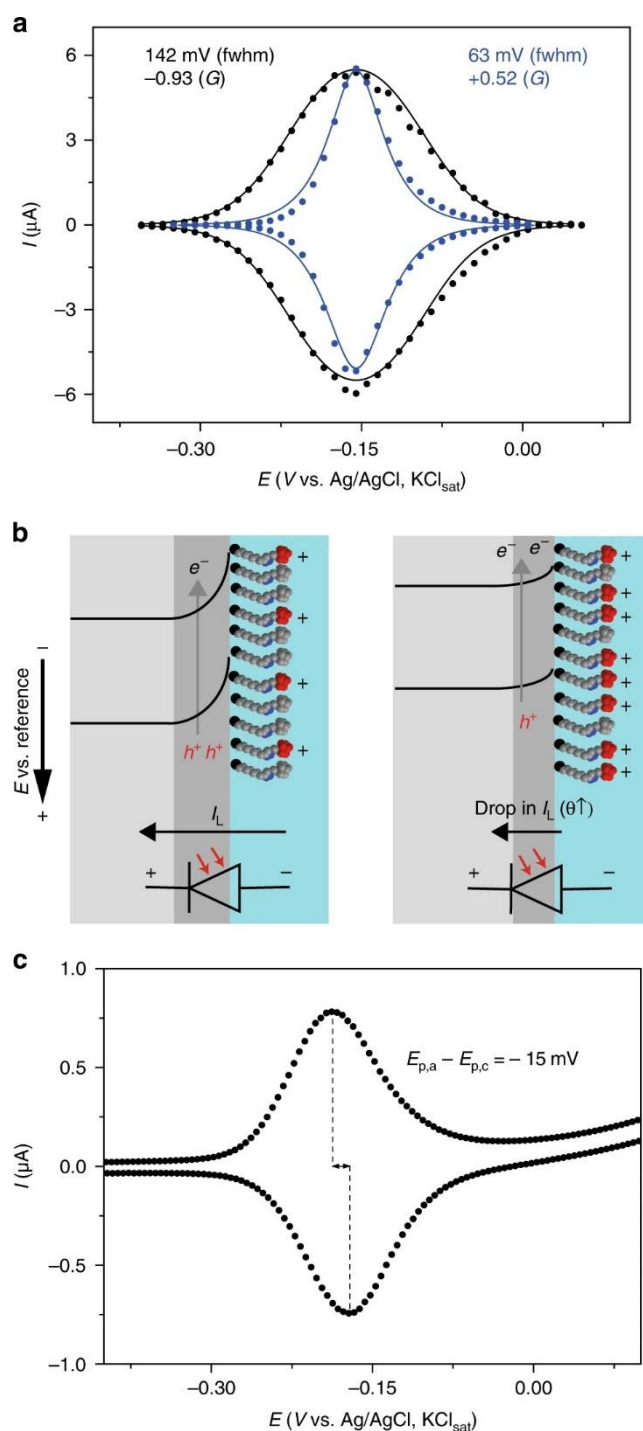


Figure 1.5: Experimental and simulated cyclic (lines) voltammery fwhm. When the electrode is purposely damaged, detaching part of the monolayer, leads to a dropping in the dielectric screening of molecules and space-charge (a). Deformation of semiconductor-side of the barrier as a consequence of an electrochemically prompted dipole layer of surface charges that causes “peak inversion” (b). Inverted voltammograms for ferrocene-ended monolayer on n-type silicon (25 mV s^{-1}). The cathodic peak position is 15 mV higher than anodic one (c). Reproduced from ref. 37 with permission from Springer Nature, Copyright 2017.

interactions depend on the distance between the surfaces and the electrolyte, the electrolyte influences also the double layer forces as well as the surface type, that modify the distance of the Outer Helmholtz Plane.²⁸ Considering colloidal particles, atom force microscopy has emerged as a powerful technique, allowing to measure the surface forces not only at macroscopic surfaces but also for particles and fibers.²⁹ It has been shown how deviations from the DLVO only occur when the bulk concentration is critical, moreover, these deviations are linked to the electrolyte nature and they seem to be correlated to hydration of cations, that at higher correlation are prevented to replace by H^+ in the EDL.⁴⁶

The first attempt to probe the EDL using electrostatic forces was carried out by Israelachvili and co-workers in the seventies, where the forces between two mica surfaces were measured in aqueous solution (Figure 1.6).²⁸ Their results showed van der Waals forces dominate at low distances, up to 5 nm, leading to adhesive contact between the surfaces and besides the under 15 nm van der Waals interactions seem independent from the electrolyte type and

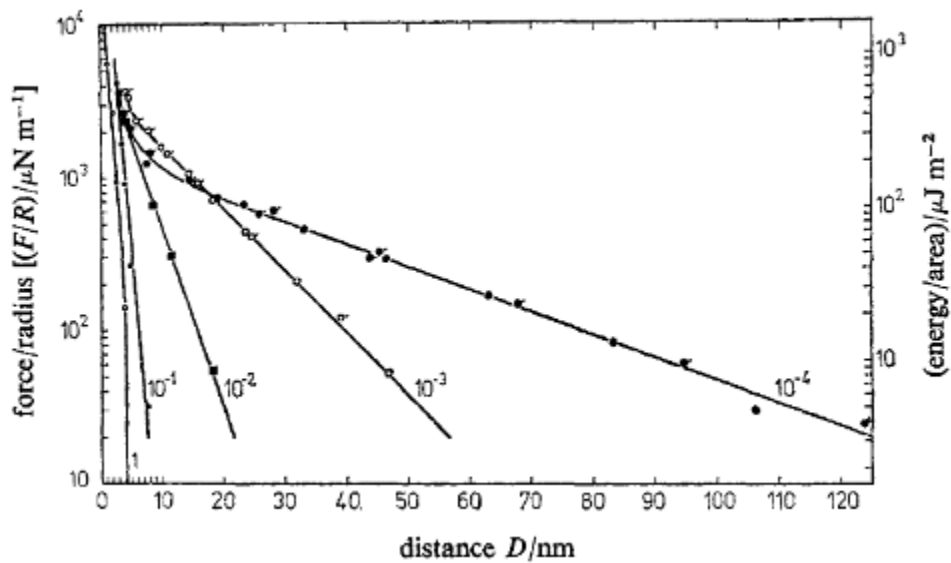


Figure 1.6: Repulsive forces between two mica surfaces (cylinders) measured as a function of their separation distance (D) in aqueous KNO_3 solution at pH 6. Relative concentrations are visible in the images in $mol L^{-1}$. The right axis shows the interaction energy between the two parallel surfaces per unit of area. Excluding the highest concentration ($1 mol L^{-1}$) the effective surface potential is constant and it is roughly 75 mV, suggesting a proportionality of the surface charge and \sqrt{C} . The theoretical Debye length is close to the experimental one just at low concentrations (10 % difference), while increasing the concentration, this discrepancy becomes massive, up to 250 % at $1 mol L^{-1}$. Reprinted with permission from J. Chem. Soc., Faraday Trans. 1 (ref 28) Copyright 1978, Royal Society of Chemistry.

concentration. Moreover, they saw additional repulsion forces, completely independent from electrolytes, and probably related to water. Interestingly, three ions electrolytes led to a reduction of EDL forces.²⁸

Further works explored the EDL between mica surfaces in different organic solvents,^{41, 45} showing how it is possible to rely on the DLVO theory when polar solvents are used, though the description becomes not accurate when non-polar solvents are studied.⁴⁵ Moreover, when solvents such as acetone, lead to a lower surface density, the van der Waals forces are dominant on the repulsion forces at the EDL, mainly when the electrolyte is absent, in this case, the great deviation from the theoretical prediction was observed.⁴⁵ Finally, hydrocarbon solvents have demonstrated a strong interaction with two mica surfaces placed at short distance, making a very stable layer.⁴¹

1.3.2 X-ray photoelectron spectroscopy (XPS) to probe the EDL

XPS is a powerful technique that allows measuring quantitatively the chemical compositions and bonding features by excitation of samples with X-ray.⁴⁷ XPS uses the kinetic energy of emitted photoelectrons to probe the samples and photoelectrons can probe to 10 nm depth,⁴⁷ the same range of the EDL, making XPS another exploitable technique to prove the EDL.^{7, 18, 48} Different groups tried to probe EDL using XPS,^{30, 48-50} using different samples, from dispersed titanium dioxide nanoparticles,⁴⁹ to the EDL between Iridium and aqueous solution⁵⁰ and between gold and aqueous solution with the addition of a neutral spectator.³⁰ Moreover, this technique can be used to probe the EDL also for a particular family of chemical, ionic liquids.⁴⁸

The first example of XPS analysis to probe the EDL was proposed by Favaro and co-workers (Figure 1.7).³⁰ In brief, the spectra recorded using XPS in water with a spectator neutral molecule (pyrazine) and different concentrations of a selected electrolyte (KOH), allowed to predict the voltage profile of the electric double layer, changing the applied potential and the electrolyte concentration. These kinds of experiments also allow estimating the pzc, making this technique a powerful tool to investigate the electric field at the electrode/solution interface.³⁰

To estimate the local potential at the interface the core-level binding energy is measured and how it changes with the applied potential, moreover the full-width at half-maximum is the main parameter to consider when the potential of the EDL needs to be measured.³⁰

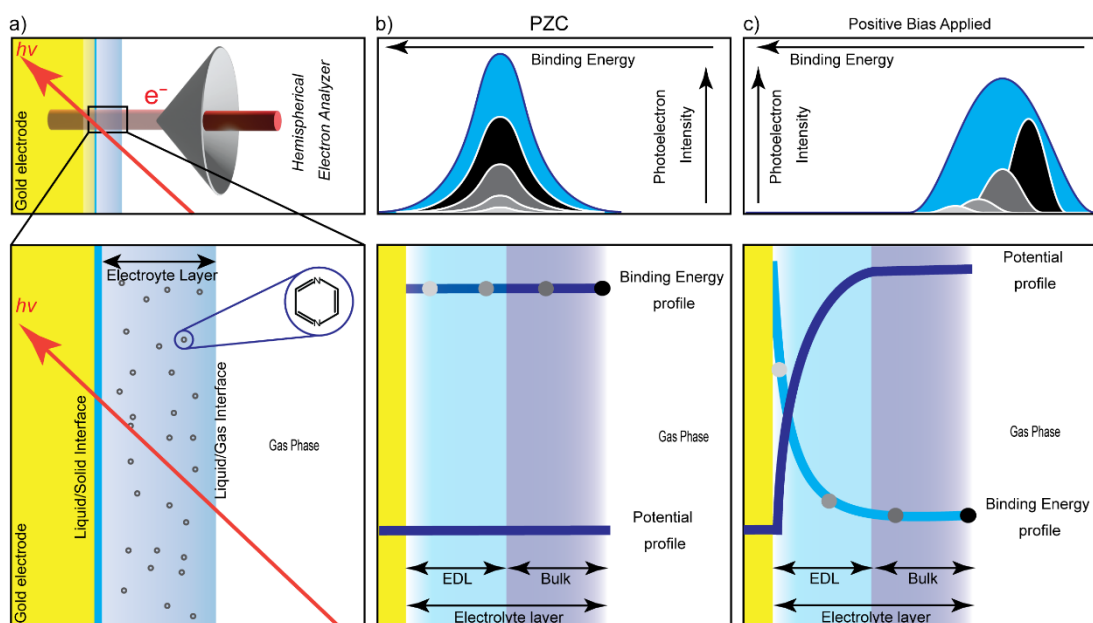


Figure 1.7: Representation of the probing of EDL using APXPS. Probing the EDL at a gold working electrode in a KOH (0.4 mM) water solution with 1.0 M pyrazine (a). Increasing FWHM for an EDL with a given thickness from the PZC, where no net charge density is present at the interface, the spectral broadening looks reduced (b) to a situation where a positive bias is applied, generating an EDL of 15.2 nm thickness (c). The different colours in (b) and (c) top panels indicate varying photoelectron intensities at different locations within the electrolyte layer. These locations are represented by the coloured circles in the (b) and (c) bottom panels.³⁰

Finally, the electric field of the EDL causes a broadening of water oxygen, and pyrazine nitrogen, unless at the pzc due to the absence of a net charge at the electrode surface.³⁰

Interestingly, when XPS is used to probe the EDL generated by ionic liquids in contact with charged electrodes, the Gouy-Chapman-Stern theory is not applicable. In this case, the structure becomes multilayered, giving further confirmation that the Gouy-Chapman model is not trustable when the ions concentration overcomes certain values.⁴⁸

1.3.3 Direct voltage profiling

Since the development of scanning tunneling microscopy (STM), its applicability in the study of surfaces and interfaces has been clear.⁵¹ AFM (atomic force microscopy) was initially used for EDL probing, even though, the many sources of error that characterise this technique have limited it as well as many others that allow surface forces measurements.⁵²⁻⁵⁶ Particularly, SECPM (scanning electrochemical potential microscopy) was proposed at the beginning of this century.⁵⁷ Subsequently, Liang et al. reviewed all the electrochemical scanning probe

microscopies developed so far, and explained how SECPM has leading importance in electrocatalysis studies.⁵⁸

The first attempt to probe the EDL using a similar approach to SECPM was reported by Kang and co-workers, they used a gold probe at the open circuit potential with the assumption that following some precautions the probe does not disturb the EDL.⁵⁹ Subsequently, Bard and co-workers developed SECPM as a new technique to probe a gap between a metal tip and different kinds of surfaces, from conductive metallic surfaces to insulating silicon oxide.⁵² SECPM gives advantages mainly for insulating surfaces because in the tunnelling mode, the tip crashed when the Si surface is anodized.⁵²

The main limitation of SECPM is the EDL carried by the probe itself, which leads to an interaction between it and the EDL of the surface being studied.^{32, 52, 60} This issue had been clear since the first publication of Bard and co-workers, later it has been confirmed by works of other groups. They suggested the possibility to extract the EDL potential from the deconvolution of the potential profile obtained by SECPM experiments, even though this deconvolution requires information about EDL at the surface and the tip, which are not easily estimated at the moment.³² Previously, other works have suggested an overlapping of the potential of the EDL surface with the probe EDL, underling how this is the real limitation of this technique.^{61, 62} Several theoretical works explain how using this technique the measured EDL is merely the results of the overlapping of the two EDL, the surface and the probed EDL.^{61, 62}

To overtake this issue, many attempts have been carried out; one of them is to measure the potential gradient using a probe perpendicular to the electrode surface, where the probe is free to oscillate avoiding any contact with the surface. Consequently, the measurement is performed as a function of the gap distance, leading to potential-distance plots such as those obtained by Yoon et al. (Figure 1.8).³² The use of probes associated with a potential, even small, bears some issues that this work has tried to overcome by using an insulator film around the metal tip.^{32, 52} Nevertheless, neither this trick has allowed removing all the issues when the probe is very close to the surface the profiles does not look like that of an unperturbed electrode surface, the sigmoidal curve with an inflection point is the clear sign of perturbation.³² In order words, even the insulator film is not enough to remove completely the EDL leads by the probe, so even though with this technique is possible to obtain an accurate potential profile, the absolute

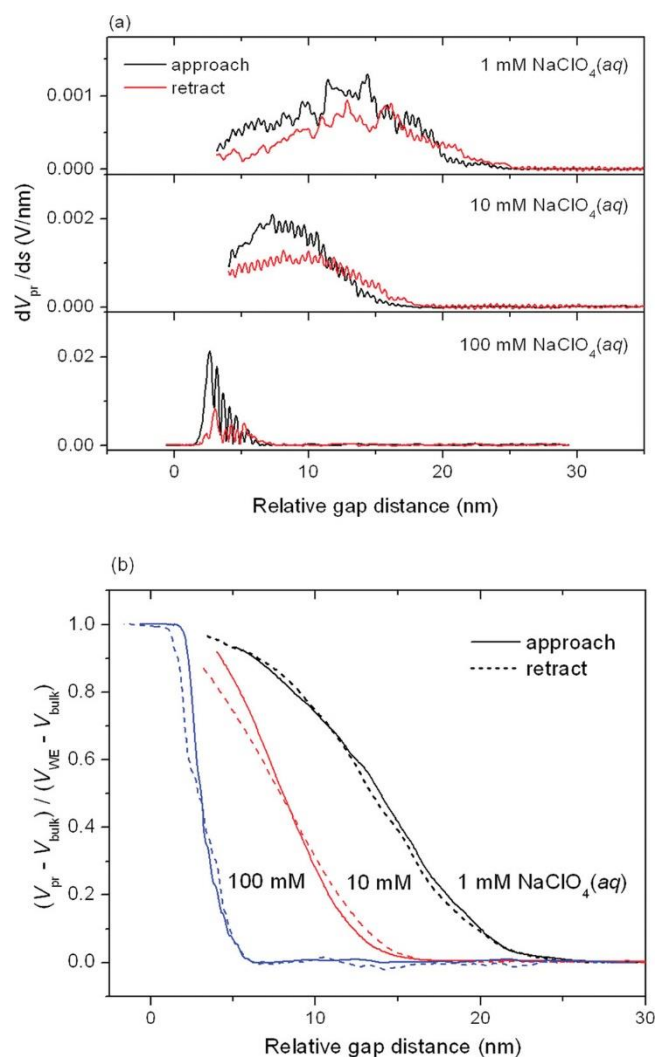


Figure 1.8: Direct measurement of the potential gradient plotted as function of probe distance (a). Different concentrations of NaClO_4 (0.001 M, 0.01 M, and 0.1 M) were compared. The probe was moved with a speed of 5 nm s^{-1} in a linear direction, oscillation frequency was set at 10 Hz. Potential profiles appear to be sharper when the electrolyte concentration is increased. Signals difference between the probe approaching and retracting look negligible, which is reducible to the similar value of linear translational speed as well as vibrational frequency owned by the probe (b). Reprinted with permission from *J. Phys. Chem. C* 2011, 115, 35, 17384 (Ref. 32). Copyright 2011 American Chemical Society.

potential at the surface is still indeterminable. Consequently, the results obtained by SECPM do not follow the prediction of Gouy-Chapman-Stern model, because a further theoretical investigation is needed to consider the interaction between the EDL and the tip used to probe the EDL itself.⁵²

1.3.4 Electrode kinetic measurement for EDL probing

In the EDL an electrical field exists, which obviously affects redox chemical reactions, which can be used to study the EDL itself. Eggers and co-workers have developed to build a monolayer of inert molecule on a plane surface.^{33, 63} Basically, they created a method to change the position of redox sites within the EDL, in fact, a norbornylogous monolayer allows to keep redox chemical species, such as ferrocene, in a desired position above the surface (Figure 1.9).³³ Using this technique they were able to measure the potential of the EDL at different distances from the electrode surface and their results respect the forecast made by theoretical calculation.³³ Basically, using an electrochemical technique such as cyclic voltammetry, Eggers and co-workers used the surface-bound ferrocene and the effect of the electric field on its apparent formal potential to estimate the potential drop, from the beginning of the EDL towards the bulks, by holding the redox species at different distance from the surface.³³ The mapping

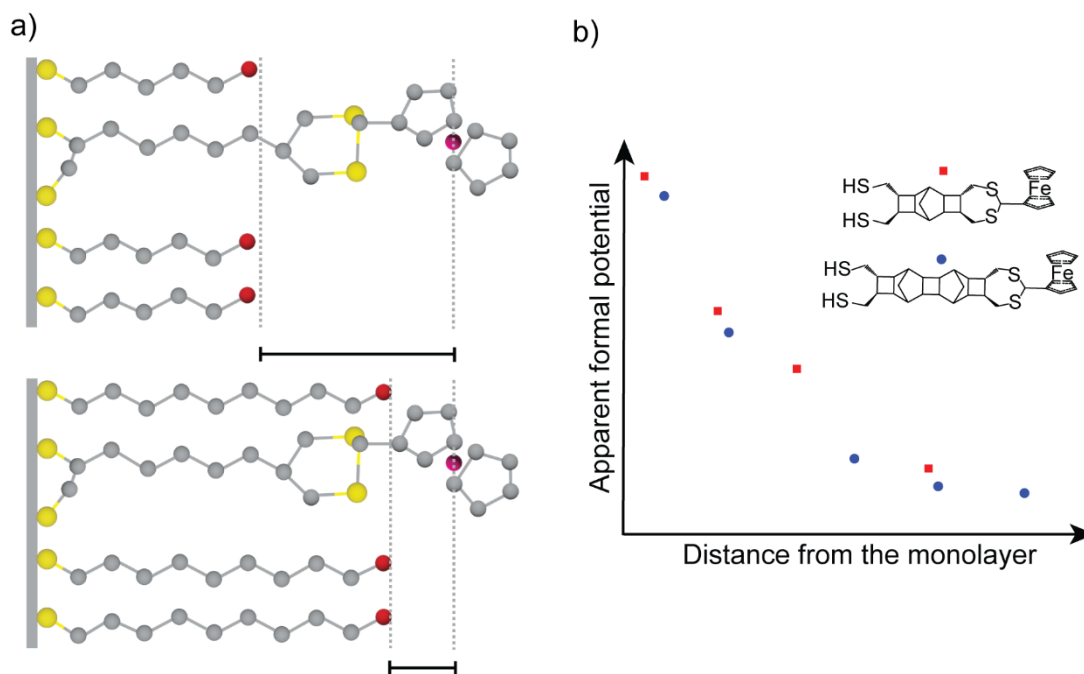


Figure 1.9: Norbornylogous bridges are used to hold in a desired position and redox-active chemical (ferrocene) (a). Ferrocene allows investigating the EDL through basic electrochemical experiments such as cyclic voltammetry. The formal potential of the redox couple can be used to estimate the potential drop in the EDL from its initiation to the bulk. The results gave a very similar potential profile to those foreseen by most common theories about EDL, for instance, a great drop in the Stern layer and a smaller potential drop in the following Gouy-Chapman layer.³³ A sharp potential drop is observed at the distal surface of the diluent molecule, thus a second small decrease in the potential is due to both the Stern layer and the diffuse layer (b).⁶³

of EDL obtained has confidence, with steps of 0.11 nm, allowing to have several points across the diameter of the counter ion, where the potential drop looks sharper.³³ Moreover, they found how the ion concentration may increase the electron transfer rate the latter decreases when the ferrocene moiety distance from the EDL is risen.³³ Generally, the apparent formal potential of the EDL drops increasing the distance from the surface, reaching a stable value after the Stern layer, when the redox species (ferrocene) is fixed in the diffuse layer.⁶³

This is due the strong correlation between ion pairing and the ferrocene redox reactions, therefore, approaching the bulk the anions concentration drops and this corresponds to a decrease in the electron transfer rate as the ferrocene redox occurs at positive bias.⁶³ More recent works have tried to use a different approach, moving the redox species in several different positions inside an alkyl-alkanethiolate monolayer, what has been observed, is a non-linearity in the potential drop close to the surface due to the ferrocene interactions with the electrode surface.⁶⁴ The same non-linearity has been observed even when the ferrocene is placed far from the electrode surface because both the short alkyl chain above the ferrocene cannot prevent the interaction with the electrolyte anions and the large energy packed underneath the ferrocene molecule.⁶⁴ These last results brought out the need for further investigation to develop a trustable and widely applicable electrode kinetic technique to probe the EDL.

1.3.5 Microdroplets fluorescence microscopy

In the last decade, many groups among which it is worth mentioning Zare group, have observed how a chemical reaction can be accelerated when performed inside microdroplets, from protein unfolding to addition-condensation and radical reaction.⁶⁵⁻⁷⁰ Nevertheless, how these reactions are triggered by microdroplets remains a mystery.⁷⁰ In the last years, Zare and co-workers have begun to investigate this phenomenon, with the aim to find a proper explanation about how microdroplets can accelerate chemical reaction.⁷⁰ Firstly, they exploit a fluorescence molecule, rhodamine, studying its behaviour in water-oil microdroplets. Interestingly, their observations unveiled an increase in rhodamine concentration on the microdroplets' surface, moreover, fluorescence polarization anisotropy resulted to be inversely proportional to the dye concentration, probably due to electrostatic interaction generated by the confinement of rhodamine in a limited surface.⁷⁰ Subsequently, in a following publication, Zare and co-workers

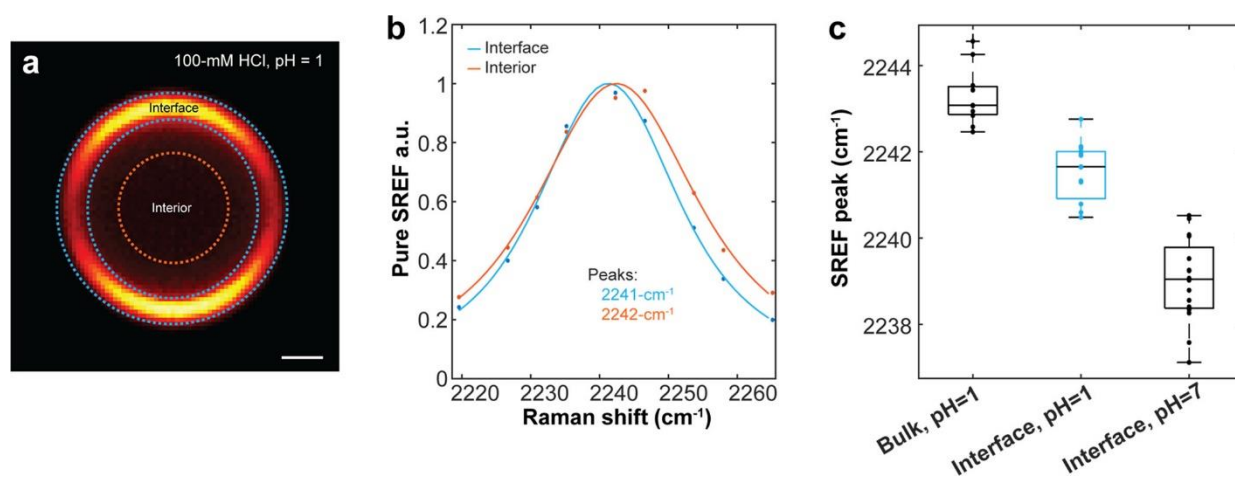


Figure 1.10: Stimulated Raman excited fluorescence microscopy of rhodamine at the water-oil interface of microdroplets with 0.1 M HCl. A frame of rhodamine fluorescence at water-oil microdroplets' interface, the images were obtained using SREFM with 20 μM of rhodamine in hexadecane (a). Background-subtracted SRFEM spectra of interface and microdroplet's interior (b). SERFM peaks are presented as a box plot, in the bulk at pH 1, at the microdroplet interface with half rhodamine concentration (10 μM) and pH 1, and at the interface at pH 7 (c). Reprinted with permission from *J. Phys. Chem. Lett.* 2020, 7423 (Ref. 71). Copyright 2020 American Chemical Society

developed a stimulated Raman excited fluorescence microscopy (SREFM) to measure, for the first time, the electric field at the water-oil microdroplets' interface.⁷¹ Using again rhodamine as a dye they measured an electric field with an order of magnitude of 10^7 V cm^{-1} , the generation of such an electric field is attributed to the charge separation that causes the adsorption of anions at the water-oil interface in microdroplets.⁷¹ To verify their theory they performed the same experiments adding HCl to neutralize anions, mainly OH^- , but observing no influence upon the Stark shift they could conclude that the origin of a strong electric field can be ascribed to negatively charged species adsorbed at the water-oil microdroplets' interface (Figure 1.10).⁷¹ Finally, it is possible to claim that the high strength of this electric field can be, at least in part, responsible for the fast kinetic of chemical reactions in microdroplets.⁷¹

1.4 A Thesis overview

The probing of the EDL and measurements of the electric field across the EDL are measurements fundamental to enhancing our knowledge of physical and chemical phenomena occurring at electrified solid-liquid interfaces. Accordingly, the improvement of current techniques must be achieved, as well as the development of newer and perhaps simpler techniques. Moreover, theoretical studies have suggested that the ordering of solvents and

ionic liquids can be exploited to scale up electrostatic catalysis,⁷² an emerging form of catalysis that so far has mainly been performed at the single-molecule level.¹⁰ In addition, EDL structure and dynamics are relevant to different fields, such as in the field of energy storage, where capacitors based on EDL have been emerging in the last decades.⁷³

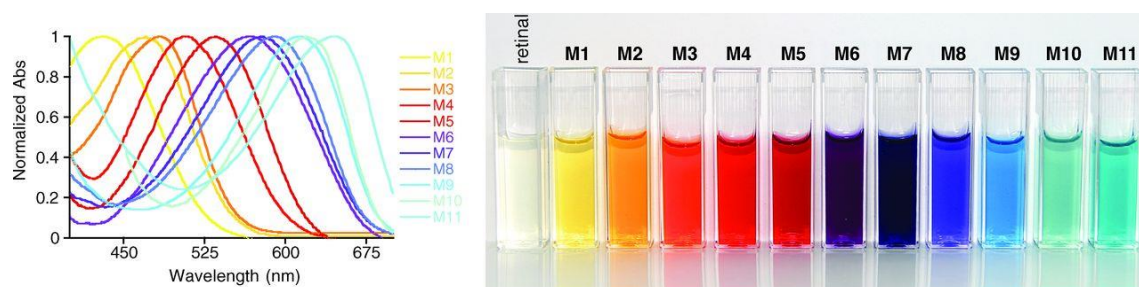
This thesis explores the viability and scope of new and simpler techniques to probe the EDL, trying to develop methods where electrochemical reactivity is exploited to investigate EDL structure, dynamic and voltage profile.

Firstly, attempts to exploit electrochemiluminescence to investigate spectral tuning were made. It is known how several chromophores can occur a shift in their wavelength emission when the electrostatic environment in which they are placed is changed. One example is retinal, a chromophore that plays a fundamental role in visual perception and whose absorption tuning is known to affect by electrostatic contribution (Figure 1.11).^{74, 75}

Nevertheless, retinal was not suitable for this research, because to investigate the EDL was necessary to study a bioluminescence reaction, developing an electrochemical method to perform such reaction and thus considering how variation in the EDL may affect and how the light emission. Fortunately, nature provides us with plenty of biochemical reactions that ended up with the emission of light, amongst them, luciferin has catalyzed the attention due to a large number of species that use this molecule to emit light at different wavelengths.⁷⁶

Chapter 2, in the form of paper 1, communicates the first firefly luciferin emission obtained through electrochemiluminescence. In Nature, the firefly luciferin is used by different species to emit at different wavelength, consequently, considering the electrostatic effect are suggested to be the main responsible of enzyme catalysis,²¹ the aim of this chapter is to see whether or not there is any correlation between the nature of the EDL and the emission of the firefly luciferin. Developing a mechanism to electrochemically tune the emission of the firefly luciferin by controlling the features of the liquid/solid interface, may allow to have an indirect methodology to investigate the EDL.

The mechanism behind firefly bioluminescence and spectral tuning has been studied for decades, during which many different explanations have been proposed (Figure 1.12).⁷⁷ Nowadays, an exhaustive and complete explanation is not still available, consequently,



Entry	Pigments	λ_{\max} nm	Protein shift nm (cm^{-1})	K_d , nM
1	<i>n</i> Bu-retinylidene PSB	440	---	---
2	hSWS	420	-20 (-1,082)	---
M1	Q108K:T51D:L117E	425	-15 (-802)	53±15
M2	Q108K:T51D	474	34 (1,630)	23±6
M3	Q108K:K40S	482	42 (1,980)	28±12
3	sensory rhodopsin II	487	47 (2,193)	---
4	rod-rhodopsin	500	60 (2,727)	---
M4	Q108K:K40L	508	68 (3,042)	29±5
5	hMWS	530	90 (3,859)	---
M5	Q108K:K40L:T51V	533	93 (3,966)	19±7
6	hLWS	560	120 (4,870)	---
7	bacteriorhodopsin	570	130 (5,183)	---
M6	Q108K:K40L:T51V:R58W	570	130 (5,183)	63±4
M7	Q108K:K40L:T51V:Y19W:R58W	577	137 (5,396)	86±6
8	sensory rhodopsin I	587	147 (5,691)	---
M8	Q108K:K40L:T51V:T53C:Y19W:R58W:T29L	591	151 (5,807)	55±5
M9	Q108K:K40L:T51V:T53C:Y19W:R58W:T29L:Q4W	613	173 (6,414)	65±8
M10	Q108K:K40L:T51V:T53C:Y19W:R58W:T29L:Q4R	622	182 (6,650)	70±6
M11	Q108K:K40L:T51V:T53C:Y19W:R58W:T29L:Q4R:A33W	644	204 (7,199)	42±6

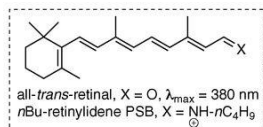


Figure 1.11: Selected UV-vis spectra of mutagen retinol protein (M1 to M11). In the table is possible to see how the absorption moves from 425 nm of M1 to 644 nm of M11, different rhodopsins are comprised to have a comparison. The electrostatic environment is changed by using mutant retinol-binding protein, revealing how a uniform distribution of neutral electrostatic potential in the binding pocket of the protein leads to a redshift. Reprinted with permission from *Science* 2012, 338, 1340 (Ref. 74). Copyright 2012 AMERICAN ASSOCIATION FOR THE ADVANCEMENT OF SCIENCE

approaching the problem in a novel way, such as electrochemistry, can provide new details and information to make a further step towards a complete understanding of this phenomenon. In paper 1, electrochemically generated chemiluminescence of firefly luciferin is carried out for the first time. This new way to activate a well-known biological reaction can provide a more complete description of a phenomenon such as bioluminescence and its spectral tuning, which may be exploited in the study of EDL features. Furthermore, paper 1 provides a wide study of electrochemiluminescence in different environments, where changing solvent nature, as well as the electrolyte is possible to control the emission wavelength, proving how features of the EDL are strictly correlated to generated light.

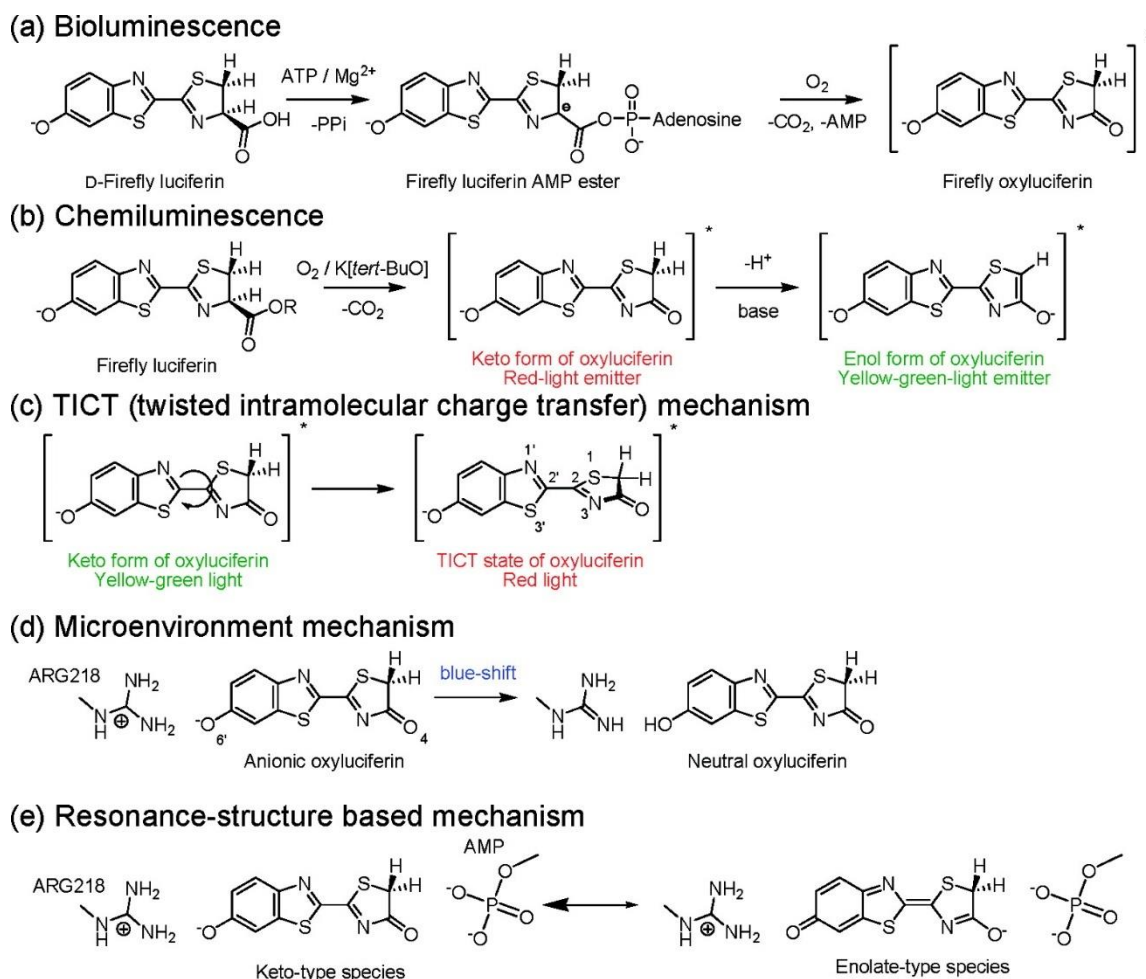


Figure 1.12: Schematic illustration of the suggested mechanism of bioluminescence (a) and chemiluminescence (b) of fireflies. The most dominant theories to explain luciferin spectral tuning, twisted-intramolecular charge-transfer (TICT) (c), microenvironment conditions (d), and keto-enol tautomerization process (e). Reprinted with permission from *J. Am. Chem. Soc.* 2007, 129, 28, 8756 (Ref. 77). Copyright 2007 American Chemical Society.

Chapter 3 reports an attempt to develop an electrochemical procedure to shift the emission of luminol. This chapter follows up the previous one by exploring further readouts of near-surface voltages, specifically looking at luminol, whose spectral tuning should be also voltage-dependent.

The application of luminol chemiluminescence is uncountable, from analytical chemistry,⁷⁸⁻⁸⁰ to medical and clinical utilization.⁸¹ The development of a luminol-based electrochemiluminescence technique would be an overwhelming achievement in the EDL investigation science due to the straightforward luminol chemiluminescence reaction and the

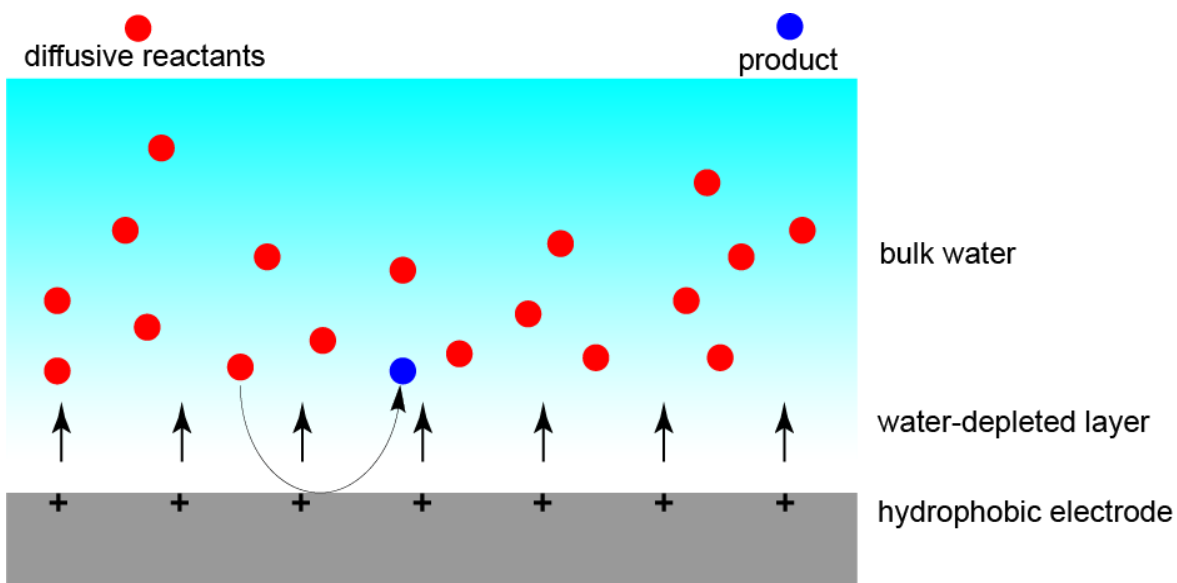


Figure 1.13: Schematic representation of a diffusive heterogeneous (solid electrode–liquid) system where surface charges deliver field lines across a “vacuum-like” gap (solvent-depleted region) present at the polar liquid–hydrophobic solid interface.⁸⁴

easy availability of luminol itself. Electrochemiluminescence of luminol is usually reported at anodic bias, using hydrogen peroxide as co-reactant in alkaline water.⁸²

Subsequently, differently than luciferin, in **Chapter 3** to modify the EDL the efforts are focused on the features of the electrode surfaces, rather than on the solvent/electrolyte nature.

Using a silicon wafer as working electrode, different monolayers attached to silicon surface allow to have more hydrophobic or more hydrophilic reaction site. Besides the probing of the EDL, this approach may provide some evidence of the highly debated existence of a “vacuum gap” (Figure 1.13).

Firstly predicted by Stillinger,⁸³ the “vacuum gap” is a solvent depletion layer, generated by the repulsion at a hydrophobic surface–water interface. There is still controversy over the existence of a molecularly thin region of decreased electron density at the solid–water interface. Contrasting views are caused by the evidence in support of a hydrophobic water gap having mainly originated from one type of measurement alone: neutron and x-ray reflectivity on crystalline substrates. Unambiguous reflectivity measurements in support of a few angstrom thin (1–7 Å) water-depleted layer, requires not only exceedingly flat substrates but also an exact knowledge of the interfacial chemistry.^{84–86} A general method capable of detecting the presence, or absence, of the hydrophobic water gap on rough samples, on chemically inhomogeneous

samples, on samples with surface impurities, or samples of unknown surface chemistry, does not exist yet.

Unfortunately, any attempt in tuning luminol emission varying electrode water-affinity failed. Finally, endeavours in aprotic solvents, to obtain the same spectral tuning seen for luciferin in the previous chapter, do not give the expected achievement, albeit the similarity of the reaction mechanisms, in which oxygen superoxide plays a cardinal part (Figure 1.14).⁸⁷

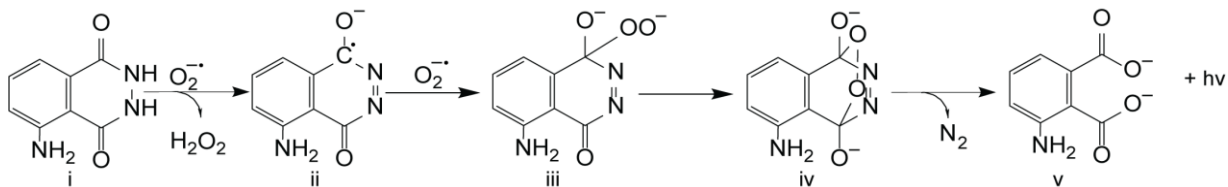


Figure 1.14: Luminol cathodic electrochemiluminescence reaction mechanism in aprotic solvents.⁸⁷ The reaction starts with the electrochemical generation of superoxide radicals, as in the electrochemiluminescence of firefly luciferin.

Chapter 4, in the form of paper 2, focuses its attention on a particular class of chemical, room temperature ionic liquids. After presenting the electrochemiluminescence of luciferin (**Chapter 2**) and of luminol (**Chapter 3**) in molecular solvents, this chapter presents the electrochemiluminescence of these two chemiluminescence molecules in room temperature ionic liquids. The number of publications related to room temperature ionic liquids has risen sharply with the new century, making them crucial in many fields of chemistry, from electrochemistry to organic synthesis.^{88, 89}

Room-temperature ionic liquids are those ionic liquids with a melting point below 25 °C, allowing to have a liquid only made by ions,⁸⁸ suggesting a unique behaviour when they are placed close to a charged surface. Many studies have been published about the EDL of ionic liquids, with some studies speculating on the formation of a compact layer of counterions at the electrode interface.^{90, 91}

Chapter 5, in the form of paper 3, proposes an extremely simple procedure to probe the residual field of a room temperature ionic liquid after an external pulse. The study of electrochemiluminescence in room temperature ionic liquid (**Chapter 4**) shows a persistent emission even after the removal of the external electric field. This chapter tries to explore which properties of the room temperature ionic liquids can be responsible for such phenomena. As

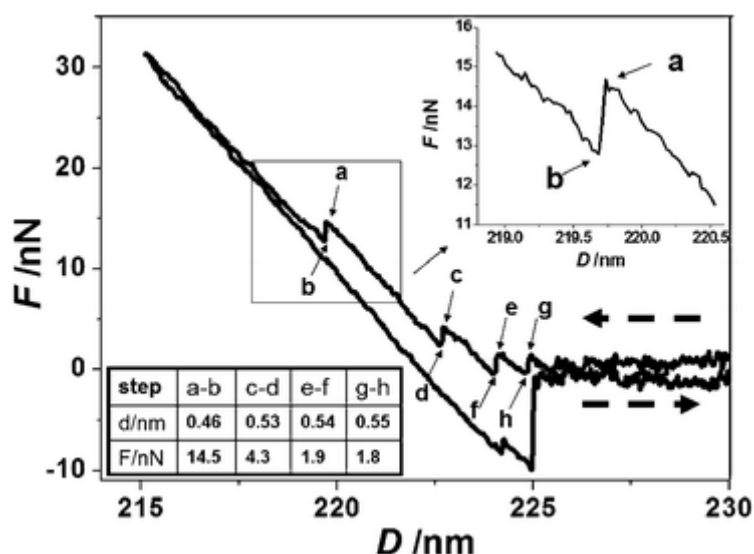


Figure 1.15: Presentation of AFM force curve with high quality measured at $-0.8V$. The letter a-h indicates saw-toothed transition forces, they are the consequence of the partial ease of the cantilever bending. The rupture force of any layer can be taken from the height of the force transition. Reprinted with permission from Royal Society of Chemistry 2012, 48, 582 (Ref. 94). Copyright 2012 Royal Society of Chemistry.

previously underlined, room temperature ionic liquid's EDL has distinctive attributes due to ionic composition. Experimental analysis of the EDL in ionic liquids has always involved a highly demanding technique (Figure 1.15).⁹²⁻⁹⁵

Chapter 5 proposes open circuit potentiometry (hereafter OCP) as an effortless way to probe modification in ionic liquid EDL. Measuring any fluctuation in the OCP value, before and after the application of an external electric field, might provide immediate insight into what happens at the ionic liquid-electrode interface.

Chapter 6, using an approach already seen in **Chapter 2**, presents an innovative way to estimate the diffusion coefficient in different ionic liquids. The feasibility of electrochemiluminescence in room temperature ionic liquids (**Chapter 4**) and the presence of a residual field at the interface between the electrode and the room temperature ionic liquid (**Chapter 5**), are combined in this chapter to investigate the influence of the EDL in room temperature ionic liquids on electrochemical reactions. This chapter aims to understand whether the generated compact layer at the liquid/electrode interface can be a limitation for inner-sphere chemical reactions, comparing them with outer-sphere reactions.

Chapter 7 is the conclusion and the outlook of the thesis.

Chapter 2: Luciferase-free Luciferin Electrochemiluminescence

In **Chapter 1**, various techniques to probe the electric double layer were presented along with an explanation of why they are highly demanding in terms of procedure and instrumentation, as well as their limitation. The outlook of **Chapter 1** explained how luminophores might be influenced by electrostatic interaction, potentially generating a shift in their emission wavelength. Consequently, it was interesting to exploit spectral tuning of known chemiluminescence molecules to investigate the EDL.

Chapter 2, in the form of paper 1 (Mattia Belotti, Mohsen M. T. El-Tahawy, Li-Juan Yu, Isabella C. Russell, Nadim Darwish, Michelle L. Coote, Marco Garavelli, and Simone Ciampi. Luciferase-free Luciferin Electrochemiluminescence. *Angew. Chem. Int. Ed.* **2022**, 61, 46 e202209670, DOI <https://doi.org/10.1002/anie.202209670>), proposes the first simple technique to detect the near-surface electric field by generating the excited state of a light emitter (firefly's luciferin) near the electrode. Light emission accompanying the oxidation of luciferin – one of nature's most widespread luminophores – covers most of the visible spectrum and is the basis of commercial assay kits for gene expression and metabolic ATP formation. The light path is an enzyme-assisted (luciferase) conversion of luciferin into oxyluciferin.^{77, 96-99} However, despite its fundamental and technological importance, key chemical details of this light-emitting reaction, as well as the mechanism of luciferin natural spectral tuning, remain poorly understood. Addressing this knowledge gap has been hindered by the lack of a laboratory model system capable of triggering luciferin luminescence in a simple reaction environment, ideally without the complexity of the enzyme pocket.

This chapter shows for the first time an electrochemical path to trigger firefly's luciferin luminescence without the natural catalyst, luciferase. Experimental and computational insights into the mechanism of enzyme-free luciferin electrochemiluminescence have been gained. They demonstrated the luciferin's spectral tuning from green to red by electrolyte engineering, proving that this shift does not require, as is still debated, a keto/enol isomerization of the light emitter, and report evidence of the electrostatic-assisted stabilization of the charge-transfer excited state by double layer electric

fields. This last finding can potentially lead to optical sensing of surface voltages and fields, removing much of the shortcomings of direct electrical measurements with nanoscopic conductive probes.

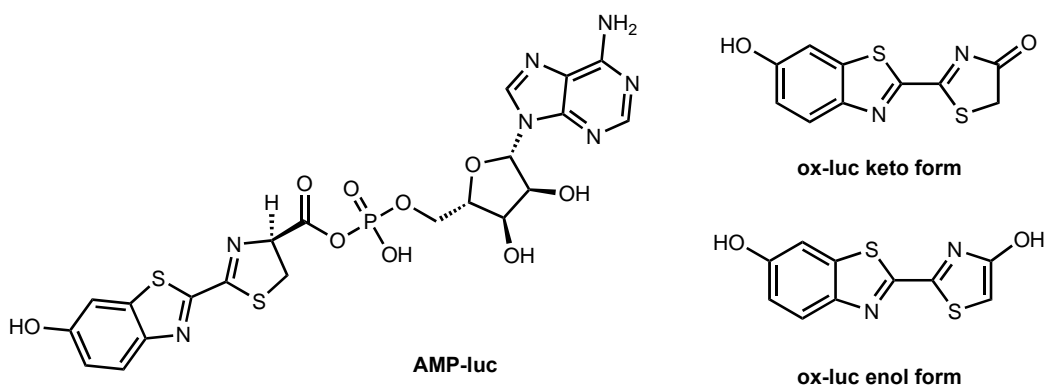
In addition, the electrochemical luciferin–oxyluciferin electrode reaction is used to demonstrate the proof-of-principle of optical measurement of diffusion coefficients. This optical mapping of electro-generated diffusion fronts can measure the diffusivity of small-size molecules (200–300 Da) in viscous solvents, in systems where mass transport by migration is likely to interfere with diffusion, as for electrodes evolving gaseous products, or can be applied to electrode geometries where hydrodynamic electrochemical measurements, such as rotating disk techniques, are not viable.

2.0 Abstract

Luciferin is one of Nature’s most widespread luminophores, and enzymes that catalyze luciferin luminescence are the basis of successful commercial “glow” assays for gene expression and metabolic ATP formation. Herein we report an electrochemical method to firefly’s luciferin luminescence in the absence of its natural biocatalyst – luciferase. We have gained experimental and computational insights on the mechanism of the enzyme-free luciferin electrochemiluminescence, demonstrated its spectral tuning from green to red by means of electrolyte engineering, proven that the colour change does not require, as still debated, a keto/enol isomerization of the light emitter, and gained evidence of the electrostatic-assisted stabilization of the charge-transfer excited state by double layer electric fields. Luciferin’s electrochemiluminescence, as well as the in-situ generation of fluorescent oxyluciferin, are applied towards an optical measurement of diffusion coefficients.

2.1 Introduction

Light-emitting chemical reactions have wide-ranging ramifications across Nature, and are broadly exploited in technology.¹⁰⁰⁻¹⁰² Light emission accompanying luciferin oxidation – a widespread natural luminophore – covers most of the visible spectrum,^{96, 97} and for example while American railroad worms emit red light, African fireflies’ bioluminescence is green.^{77, 98, 103, 104} From the technological standpoint, light emission upon the enzyme-assisted (luciferase) conversion of luciferin into oxyluciferin (**ox-luc** hereafter, Scheme 2.1) is the basis of methodologies for the optical detection of ATP formation,^{99, 105} bio-sensing of pollutants,^{96, 106} and gene expression bioassays.^{107, 108}



Scheme 2.1. Structures of **AMP-luc** and the keto and enol forms of **ox-luc**.

The first study on fireflies' bioluminescence was published in the late 1940s by McElroy,¹⁰⁹ who some years later also succeeded in isolating the light-emitting molecule.¹¹⁰ The reaction begins with the luciferase-catalyzed formation of the adenosine monophosphate ester of luciferin (**AMP-luc** hereafter, Scheme 2.1), followed by an oxidative decarboxylation that leads to the excited **ox-luc**, which in turn relaxes emitting light.¹¹¹⁻¹¹⁴ In 1971 White and co-workers, in a first attempt to explain the aforementioned broad spectral distribution, advanced the hypothesis of it being the result of a keto–enol tautomerization of the excited state, with its keto-form leading to red emission, while the enol decay being responsible for a yellow-green emission.¹¹¹ In the following decades several other mechanisms were proposed to account for the color range of natural luciferin luminescence, from changes in polarity of the light reaction micro-environment,¹¹⁵ to electrostatic interactions.¹¹⁶ Both the origin of luciferin spectral tuning and the chemical details of the adenylate firefly luciferin light-emitting path remain however poorly understood,¹¹⁷ largely because the lack of a laboratory model system capable of triggering this luminescent reaction in a simplified experimental environment, ideally without enzymes.^{118, 119} One of such laboratory systems could take the form of an electrical trigger of the luciferin light path, a method capable of the selective generation of the excited state light-emitter near an electrified surface. Demonstrating such an electrochemical path remains an unmet challenge. Besides removing the complexity of the protein environment, realizing an on/off switch of luciferin chemiluminescence is important as the environment sensed by the light-emitting excited state affects the energy of its radiative decay.¹²⁰ The development of luciferin electrochemiluminescence, therefore, offers the possibility of validating (or falsifying) the hypothesis of electric fields stabilizing/destabilizing the charge-transfer character of the emitting excited state, accounting for the natural luciferin spectral tuning.^{8, 116} Such new methodology,

alongside its validation via theoretical models, would also enable a systematic screen of the microenvironment (solvent and electrolyte) role on this widespread, yet actively debated,^{77, 121, 122} luminescent reaction.

2.2 Results and Discussion

As discussed above, luciferin light emission is catalyzed *in vivo* by an oxidoreductase, luciferase. The activity of this enzyme is known to be pH-dependent, and for luciferase immobilized on an electrode surface, the electrochemically induced depletion of protons has been previously shown to alter its activity.¹¹⁸ Our broad goal is, however, to remove altogether the need of an enzyme, and to simply rely on an external bias to trigger the luciferin light path at an electrified solid–liquid electrolyte interface. Several reports detail luciferin chemiluminescence in water,^{111, 123, 124} hence water was the first solvent choice to begin exploring an electrochemical path to luciferin's light emission.

However, despite our efforts, neither anodic nor cathodic voltage pulses applied to aqueous solutions (0.1 M KCl) of **AMP–luc** led to a light emission above the dark background (~500 cps) of a single-photon counter. There is a known correlation between oxygen concentration and luciferin's emission,^{121, 125} and once a dioxetane intermediate is formed, basic conditions can trigger the light path of **AMP–luc**.^{111, 121, 126} Hence, we decided to attempt triggering the luciferin light path by electrochemical generation of superoxide radical anion (superoxide hereafter), a basic oxidizing agent capable of also mediating radical chemistry that could lead to the dioxetane intermediate. This strategy has already been reported for the ECL of other luciferins.^{127, 128} DMSO was chosen as the solubility of **AMP–luc** is greater in DMSO than in water,^{111, 112, 129} and because – unlike in water – the one-electron reduction of oxygen leads in DMSO to superoxide.¹³⁰ Simultaneous photon counting and cyclic voltammetry data (Figure 2.1a) show a steep rise in the cathodic current at ~–0.8 V (blue trace), slightly preceding the appearance of a light output (black trace). The cathodic current rise corresponds to the onset of oxygen reduction, and control experiments with deoxygenated solutions showed no measurable luminescence (Figure S1, Appendix 1). The point where the photon counts peak, on average $(10 \pm 1.7) \times 10^4$ photon/s, is reached with a small delay relative to the cathodic flow peak of $(12 \pm 4.4) \times 10^{14}$ electron/s. We believe this delay is explained by the relatively high energy barrier of the first step of the light path (*vide infra*). Further, a significant portion of the experiments showed a shoulder on the cathodic wave at ~–0.7 V (Figure S2, Appendix 1). The

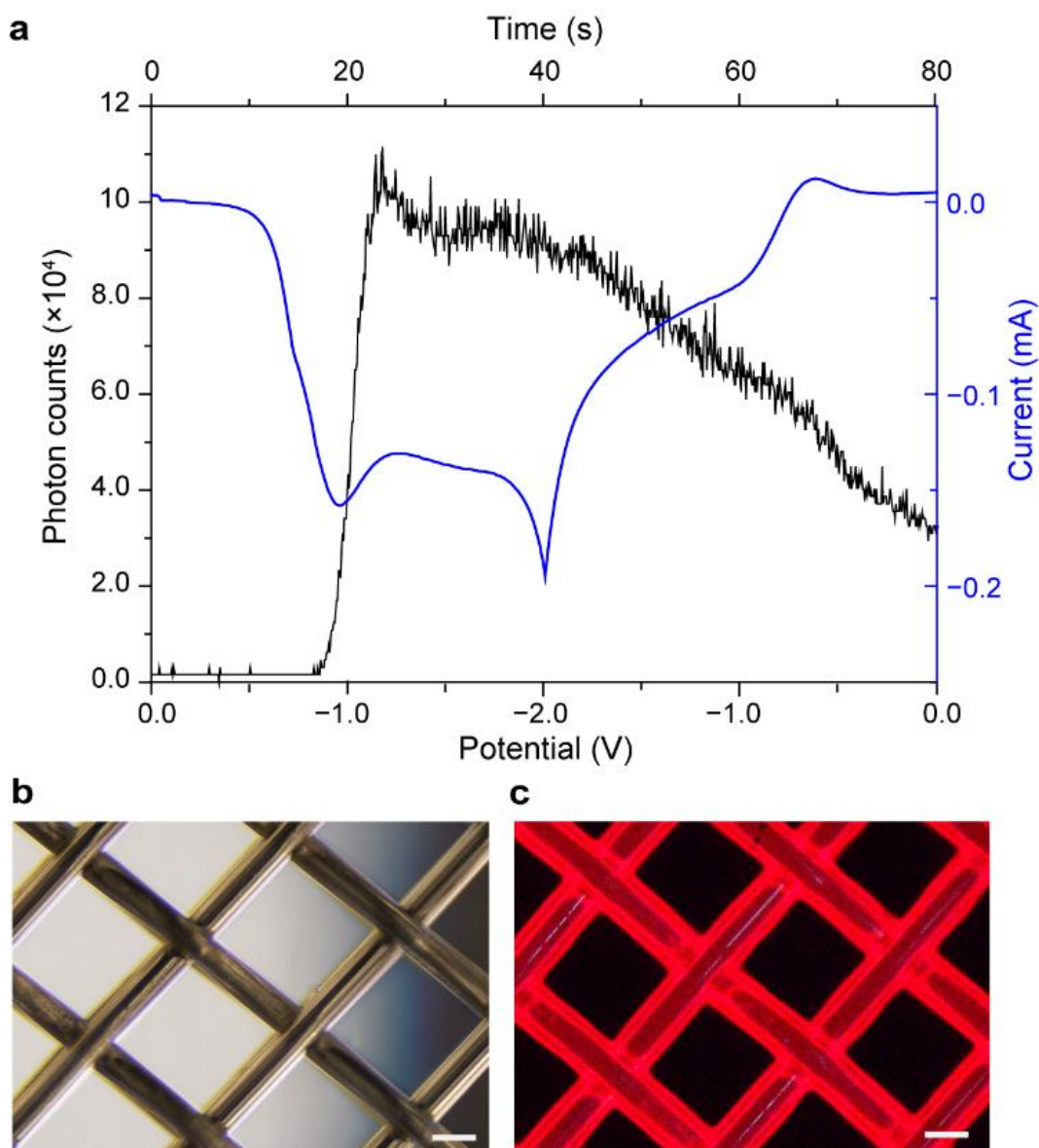
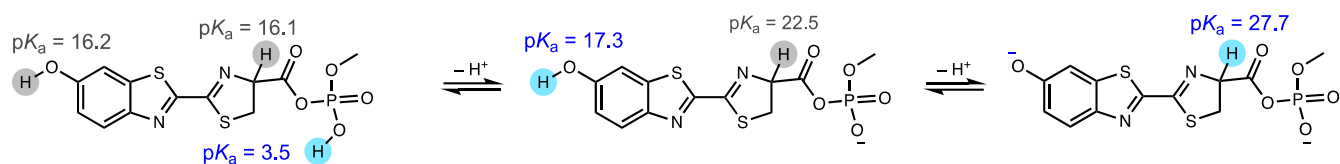


Figure 2.1. (a) Representative simultaneous photon counting and current recording for the electrochemically generated light emission of **AMP-luc** (0.43×10^{-3} M in oxygen-saturated 0.2 M $\text{Bu}_4\text{NClO}_4/\text{DMSO}$) at a platinum mesh electrode. The electrode potential was swept cyclically between 0.0 V and -2.0 V at a rate of 0.05 V/s (Figure S6, Appendix 1). The emission peak corresponds to $\sim 11.3 \times 10^4$ photon/s. (b) Bright field image (4 \times magnification) of the platinum electrode under ambient light, and (c) electrochemiluminescence image (4 \times magnification) captured in a dark room ~ 0.5 s after the onset of the cathodic voltage bias (-2.0 V). Scale bars in (b,c) are 100 μm .

origin of this parasitic signal is unclear, but its presence was generally associated with an even larger delay between current rise and light emission onset. This shoulder was absent in



Scheme 2.2. Predicted pK_a values for the 1st, 2nd and 3rd deprotonations of a model of **AMP-luc**. All pK_a values (298 K, DMSO) were computed via an isodesmotic method using 4-hydroxydinaphtho[2,1-d:1',2'-f][1,3,2]dioxaphosphepine 4-oxide (experimental $pK_a = 3.37$ ¹³¹) as a reference, and performed at the wB97XD/Def2-TZVP//M062X/6-31+G(d,p) level of theory using the SMD solvent model.

voltammograms performed without **AMP-luc** (Figure S3, Appendix 1). Further, photon counts traces as that of Figure 1a are qualitatively similar to data recorded with a conventional spectrometer monitoring emission at 626 nm (Figure S4, Appendix 1). The cyclic voltammetry of **AMP-luc** in $Bu_4NClO_4/DMSO$ results in a red glow easily visible by naked eye around the platinum-mesh electrode (Figure 2.1c). Similar experiments with an alkyl ester of luciferin (D-luciferin ethyl ester, Figure S5, Appendix 1) replacing the adenosine monophosphate ester (**AMP-luc**) resulted in a significantly lower emission, and consequently the latter was used to perform all experiments in this work. Considering the novelty of the above electrochemical trigger of luciferin luminescence, we carried out a computational study to investigate its reaction mechanism. We first established the proton state of a model of the starting material in DMSO by evaluating pK_a values for the first, second and third deprotonation steps (Scheme 2.2).

Under the reaction conditions, we expect the phosphate to be deprotonated ($pK_{a1} = 3.5$) but not the phenol ($pK_{a2} = 17.3$) or CH ($pK_{a3} = 27.7$). Using the singly deprotonated species, we next considered its reaction with superoxide (Scheme 2.3). Superoxide initially abstracts a hydrogen atom of the alpha carbon of the AMP ester, yielding the radical species **1** which is then kinetically trapped by a barrierless radical combination with a second superoxide. The resulting

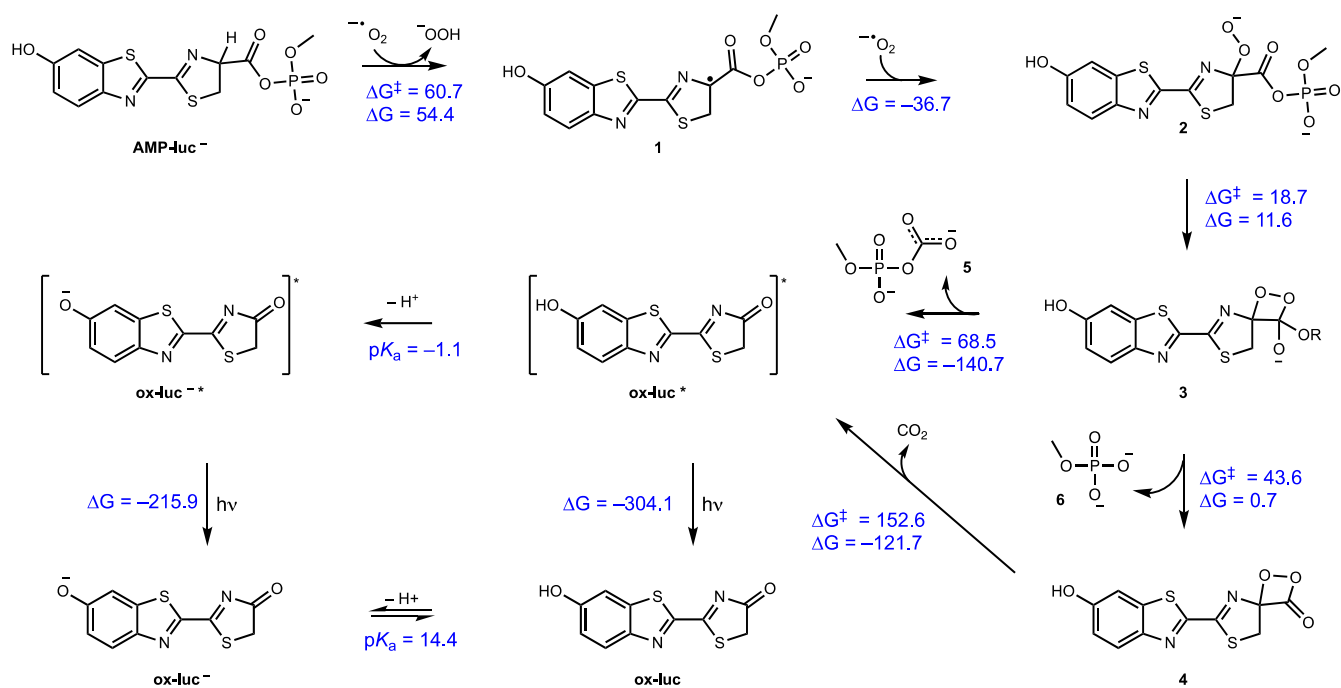
intermediate (**2**) undergoes a mildly endergonic rearrangement to form an unstable dioxetanone (**3**). This intermediate is kinetically trapped by a rapid exergonic decarboxylation to the excited state of **ox-luc** (**ox-luc***), which then releases light upon relaxation. The pathway in which the phosphate (**6**) and CO_2 are lost sequentially was found to be less kinetically favourable than the concerted loss of **5** (Scheme 2.3). Interestingly, the computed pK_a of **ox-luc*** in the S_1 excited state is -1.1 , whereas in the ground state it is 14.4 . Thus, if deprotonation kinetically

competes with **ox-luc*** radiative decay, the emitting species would be the phenoxide (**ox-luc⁻***), though once in the ground state the neutral form would be reformed and dominate.

We believe this is the case since **ox-luc*** deprotonation should be faster than its radiative decay lifetime that typically falls in the nanosecond timescale. This is also supported by the computational study presented afterwards (see Table 2.1 and the corresponding discussion). In order to experimentally validate the role played by the superoxide anion we have performed control experiments where the **AMP-luc** solution was added to a cuvette containing a small amount (0.02 g) of KO₂, but with no electrodes present. The results of these experiments (Figure S7, Appendix 1) indicate that there is sizable chemiluminescence even in an oxygen-free environment (argon atmosphere), provided superoxide radical anions are present, validating the light path discussed above and presented in Scheme 2.3.

Next, we tested experimentally whether this enzyme-free and electrode-triggered path to luciferin emission could be used to tune the luminescence color, either by changing the electrolyte and/or the magnitude of the external voltage bias. The design of these experiments is based on theoretical models that suggest a link between the electrostatic forces sensed by the light-emitting excited state and the energy (color) of the emitted light.¹³² Large electric fields exist at an electrode–electrolyte interface,^{8, 34} where the electro-neutrality of an electrolytic solution is lost. The voltage–distance profile – electric field – of the interface depends on the nature of the electrolyte,^{133, 134} and stronger near-surface double-layer fields are obtained by increasing the electrolytic support.^{8, 135}

In DMSO all attempts to tune the **AMP-luc** electrochemically generated emission from red to yellow-green by means of changes to the electrolyte and its concentration were at a first inspection unsuccessful (Figures S8–S10, Appendix 1). However, while the position of the main band centered at 626 nm did not shift appreciably, the low-energy shoulder present in all the spectra showed a ~10 nm blueshift in response to an external bias increase: from 674 nm at -1.0 V to 664 nm at -1.5 V (Figure 2.2a–b). A further cathodic increase of the applied potential didn't lead to a further shift in the shoulder's position (Figure 2.2c). To explain this shift, the nature of the light emitter, and the origin of the solvent dependent (vide infra) luminescence shift, we developed a theoretical model of the system.



Scheme 2.3. Proposed mechanism of the **AMP-luc** electrochemically generated light path, supported by first principles calculated Gibbs free reaction energies and barriers (298 K, kJ mol⁻¹) as obtained with wB97XD/Def2-TZVP//M062X/6-31+G(d,p) using SMD to model the DMSO solvent environment. Electrochemically generated superoxide abstracts a hydrogen atom to generate a radical intermediate (**1**) that is kinetically trapped by a barrierless radical combination with a second superoxide molecule. This undergoes a mildly endergonic rearrangement to yield an endoperoxide intermediate (**3**), which is kinetically trapped by a highly exergonic oxidative decarboxylation to yield the excited state of **ox-luc** (**ox-luc***), which in turn emits light upon relaxation to the product **ox-luc**. Sequential loss of the phosphate to yield **4** followed by decarboxylation to yield the excited state of **ox-luc*** was also considered but is less kinetically feasible. The excited state has a pK_a of -1.1 and thus in principle could deprotonate if the reaction is kinetically competitive with relaxation to the ground state. In the ground state the pK_a is 14.4 and the neutral form is preferred.

Several theories had been proposed to explain the different colors of the luciferin emission.¹²¹ Color changes may be caused by the light path proceeding through chemically different light emitters, and/or by changes to the nature of the reaction environment.

We theoretically studied in vacuum, in THF and in DMSO (that were both treated explicitly employing a hybrid quantum mechanics/molecular mechanics (QM/MM) approach)¹³⁶ with and without exogenous electric fields, the emission spectra of the two most plausible luciferin light-emitters^{111, 137}: the keto and enol form of deprotonated **ox-luc*** (**ox-luc****) (see Scheme 2.3 and Figure S11, Appendix 1). The other possible chemical forms of oxyluciferin are excluded as possible light emitters since they either emit out the visible range or they display very low

oscillator strengths.¹³⁸ Electric fields were aligned along the main molecular axes (z-direction, Figure S11, Appendix 1). Calculated emission maxima are collected in Table 1 and Table S4 and show that the enol-form emission is systematically blue-shifted compared to the keto form by approximately 49 nm (vacuum), 55 nm (THF), and 59 nm (DMSO). A previous study in which the DMSO solvent was treated implicitly, reached an opposite conclusion, suggesting the enol-form to be more stable.¹³⁹ Hence the importance of modelling explicit solvent molecules that accounts for local, directional, and anisotropic interactions. A similar blueshift is also found for both tautomers by changing the environment from gas to a polar solvent, with enol being more influenced than the keto form. At low concentrations of the counter ion, the negatively charged light emitting molecule is expected to be fully solvated by the high polar solvent, hence reducing the probability of ion-pair formation.

Remarkably, the calculated emission wavelength of the keto-form (**ox-luc***) in pure DMSO matches closely the experimental value recorded at low electrolytic support (633 nm versus 626 nm), in agreement with it being the thermodynamically stable species in the excited state. The enol-form would have an emission maximum at 574 nm, which rules out the possibility of this species being the prevalent light emitter in the experiments. On the other hand, direct light excitation of ground state **ox-luc** results into green fluorescence (peaking at ~560 nm) in DMSO¹⁴⁰. Interestingly, both experimental^{140, 141} and theoretical¹³⁷ studies confirm that it is the neutral and deprotonated enol form of **ox-luc** to dominate the ground state in solvents such as DMSO. It is thus apparent that it is this form responsible for the photoluminescence spectrum and green emission observed for oxyluciferin as it is the species that absorbs light. Due to the change in the pK_a of the phenol group upon excitation (see Scheme 2.3), the neutral enol form gets quickly deprotonated in the excited state, eventually leading to green emission as observed experimentally and in match with our predictions (574 nm, see Table 2.1), while excitation of the already deprotonated (anionic) ground state enol form directly leads to the green emitting species.

The emission in luciferin is attributed to the $S_1 \rightarrow S_0$ (first singlet excited state \rightarrow singlet ground state) radiative transition, which is accompanied with an internal negative charge transfer (CT hereafter) from the thiazolone to the benzothiazole system (see Table 2.1). Stabilization of the CT state in DMSO upon the formation of contact ion-pairs (with Li^+ binding the negative oxygen

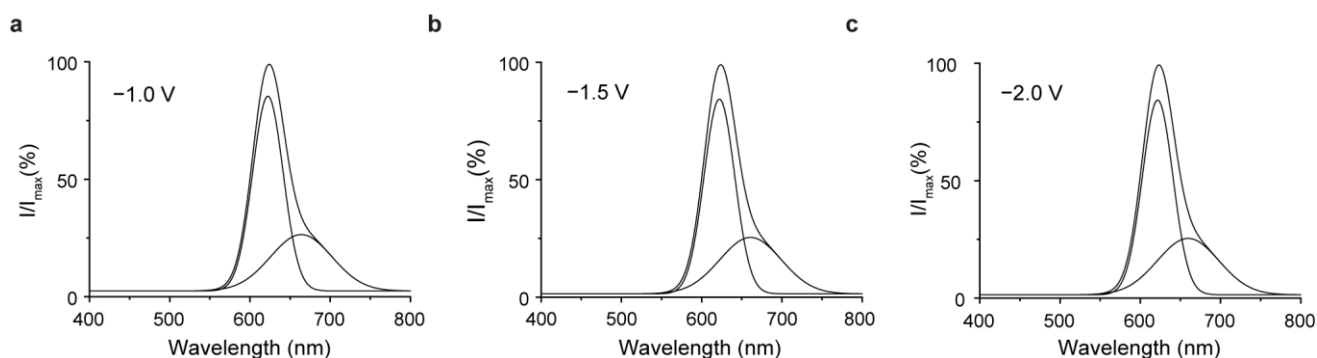


Figure 2.2. Deconvoluted emission spectra of **AMP-luc** (0.43×10^{-3} M) electrochemiluminescence in $\text{Bu}_4\text{NClO}_4/\text{DMSO}$ (2.0×10^{-1} M) on platinum mesh electrodes under negative voltage pulses of different magnitude [-1.0 V, (a); -1.5 V, (b); -2.0 V, (c)]. At a more negative voltage bias, the low energy shoulder shifts progressively towards shorter wavelengths (10 nm blueshift from -1.0 V to -1.5 V, while from -1.5 V to -2.0 V there is not any additional spectral shift). All potential biases are versus Ag/AgCl. The emission spectra recording takes 2 s and was started simultaneously with the cathodic pulse.

of the benzothiazole moiety) is expected to blueshift the emission of both keto-form and enol-form.

Very notably, such shift is indeed predicted by the calculated emission energies in DMSO in the presence of contact ion-pairs with Li^+ and K^+ (see Table S4, Appendix 1) and it is indeed experimentally observed (10–15 nm) at higher concentrations of Li^+ (Figure S8, Appendix 1) where contact ion-pairs are expected.

Finally, it is worth noting that the higher CT character for the enol-form compared to the keto-form is reflected in a larger energy difference between the S_0 and S_1 states, and therefore in a blueshift. By reducing the solvent polarity, moving for example from DMSO to THF-based electrolytes, contact ion-pairs are more likely to occur (Table S4, Appendix 1), which explains the mismatch between the predicted emission energy from the keto-form computed in neat THF (639 nm) and the experimental blue-shifted value measured in $\text{LiClO}_4/\text{THF}$ (575 nm, Table S4, Appendix 1). Accordingly, the emission maximum is tuned by the nature of the cation, with ion-pairs with Li^+ causing a more pronounced blueshift than for K^+ due to an enhanced stabilization of the S_0 CT state (Table 2.1), as already pointed out above. An electrolyte is necessary to couple electronic conduction in the solid electrode with ionic conduction in the electrolyte, which is required to trigger a redox change at the electrode, and it has therefore not been possible to test experimentally **AMP-luc** electrochemiluminescence in non-supported (electrolyte-free) THF. When trying to reach a conclusion on the prevalent form of the light emitter in THF we

note that the S_1 keto-form is more stable than the enol S_1 state by 55.5–67.4 kJ/mol, both in vacuum as well as in solution (see Table 2.1). Moreover, the reaction pathway forming the S_1 excited state ends with the keto-form. Consequently, the enol-form could only originate by tautomerization of the keto isomer. Such tautomerization is unlikely to occur as it is both kinetically and thermodynamically disfavoured (see Scheme 2.3).¹³⁸

Finally, it is worth noting that a good agreement between theory and experiments is eventually found for the emission in THF when considering keto-form/ Li^+ contact ion-pairs (578 nm vs 573 nm for the computational and experimental results, respectively: see Figure S12, Appendix 1), a scenario which is likely to occur in the less polar THF solvent (as mentioned above and also proposed by Hirano et al.¹³⁹), thus calling for the S_1 keto-form as the light emitter in THF and, in conclusion, in whatever environment.

We have validated experimentally such environmental shifts (Figure 2.3) by demonstrating that for the smallest cation, lithium, and in low dielectric solvents, the emission undergoes a significant blueshift (from 626 nm in 0.2 M $Bu_4NClO_4/DMSO$ to 605 nm in 0.2 M $LiClO_4/THF$). Furthermore, the lithium concentration has a clear energetic impact on the radiative decay of the light emitter, with lower concentrations showing a green instead of the red luminescence (573 nm in THF with 5.0×10^{-3} M $LiClO_4$). This suggests that, at high concentrations, Li^+ binds both oxygens at the two opposite sides of the luminophore, thus balancing (and quenching) the blueshifting effect due to the single oxygen complexation at the benzothiazole side found at lower lithium concentrations. Interestingly there may be a parallel between the blueshift in THF and similar shifts observed in vivo which are ascribed to the luciferase's active site hydrophobicity.^{137, 142-144} Moreover, even though different perchlorate-based salts were tried in THF (Bu_4NClO_4 and $NaClO_4$), spectral tuning of the **AMP-luc** towards the blue remains larger with $LiClO_4$ (Figure S13–S14, Appendix 1). It needs also to be highlighted that achieving a blueshift was always at the expenses of the emission intensity. Photon-counting experiments indicate ~900 photon/s for the electrolysis of **AMP-luc** in 5.0×10^{-3} M $LiClO_4/THF$, and ~3200 photon/s in 0.2 M $LiClO_4/THF$, both being considerably less than the $\sim 8.5 \times 10^4$ photon/s obtained for 0.2 M $Bu_4NClO_4/DMSO$. This drop is partly caused by a lower current density as

Table 2.1. Calculated QM (XMS-PT2)/MM emission energies for the excited state light emitter (**ox-luc***) at full and partial solvation.

Environment	Electric field (V/nm)	Emission maximum (oscillator strength)		Charge-transfer (CT) ^a		Relative energy (kJ/mol)	
		Enol	Keto	Enol	Keto	Enol	Keto
Vacuum	-1	572 (0.65)	622 (0.73)	-0.28	-0.23	48.5	-11.3
	0	611 (0.69)	660 (0.76)	-0.27	-0.18	67.4	0.0
	+1	652 (0.73)	695 (0.76)	-0.25	-0.11	84.9	10.9
DMSO (complete solvation)	-1	537 (0.62)	596 (0.75)	-0.26	-0.24	31.0	-12.1
	0	574 (0.66)	633 (0.77)	-0.26	-0.20	56.5	0.0
	+1	614 (0.70)	671 (0.78)	-0.25	-0.14	77.8	13.0
DMSO (half-solvated)	-1	570 (0.67)	627 (0.78)	0.27	-0.20	58.2	-4.2
	0	610 (0.70)	660 (0.79)	-0.26	-0.16	74.5	0.0
	+1	649 (0.74)	696 (0.79)	-0.23	-0.07	86.2	10.5
THF (complete solvation)	-1	546(0.61)	602 (0.71)	-0.26	-0.24	37.7	-10.5
	0	584 (0.65)	639 (0.74)	-0.27	-0.21	60.7	0.0
	+1	623 (0.69)	677 (0.76)	-0.26	-0.15	76.6	12.6
THF (half-solvated)	-1	566 (0.61)	630 (0.68)	-0.27	-0.23	39.7	-7.9
	0	606 (0.65)	661 (0.73)	-0.27	-0.19	52.3	0.0
	+1	643 (0.69)	698 (0.74)	-0.25	-0.13	67.4	20.5

^a The CT index is calculated as the difference between the electron densities on the benzothiazole side of the final (S_0) and starting (S_1) states.

the electrolyte resistance increases, and partly by the quenching effect of small cations on superoxide.¹⁴⁵ Furthermore, changes to the nature of anion did not have any measurable effect on the energy of the **AMP-luc** emission, not even with a completely non-coordinating anion such as BARF (Figure S15, Appendix 1). In DMSO, nor varying the type or concentration of the electrolyte had any effect on the emission wavelength, and only LiClO₄ at concentrations close to saturation (2.0 M) caused a very small blueshift (Figure S8, Appendix 1). Solvents with a dielectric constant similar to DMSO, such as DMF, resulted in a similar (hard to tune) red light emission (Figure S16, Appendix 1).

We now focus on finding a theoretical explanation for the asymmetric shape of the emission spectra of Figure 2.2 and Figure 2.3. The low-energy shoulder that, as discussed above, shifts with changes to the magnitude of the exogenous electric field, is probably the radiative decay of half-solvated **ox-luc**^{*} molecules. Molecules of **AMP-luc** adsorbed on the electrode's surface, a not unlikely scenario, can be roughly considered as half-solvated and half facing a vacuum-like environment (the electrode's surface). The observed redshift (relative to the main band, Figure 2.2) agrees with our theoretical predictions for the emission of a half-solvated molecule (Table 2.1). An oriented exogenous electric field will stabilize or destabilize **ox-luc**^{*} depending on the relative dipole-field orientation. The energies of both the keto and enol isomers have a high sensitivity to changes in the electric field magnitude and direction. Table 1 reports the calculated emission spectral tuning in response to an electric field (± 1 V/nm, Table 1) aligned along the z-direction, which is the direction of the S₁ → S₀ dipole moment change (Figure S11, Appendix 1), and therefore giving maximum field sensitivity. The field-dependent shifts for the half-solvated molecule are as high as 35–40 nm, and are due to changes in CT character, with a high CT resulting in a blueshift, while a CT reduction causing a redshift.

The experimental blueshift of the emission shoulder possibly indicates that the exogenous field is stabilizing S₀ more than S₁, owing to the CT character of the ground state that is also increasing upon the effect of the electric field: more electrons are pushed from the thiazolone towards the benzothiazole ring of **ox-luc**^{*} (see Table 2.1). As summarized in Table 2.1, such emission shift is predicted both for vacuum and solvated molecules, as well as for half-solvated systems. The main emission band did not shift in the experiments, possibly because in our freely diffusive solution system the majority of the emission occurs at some distance from the

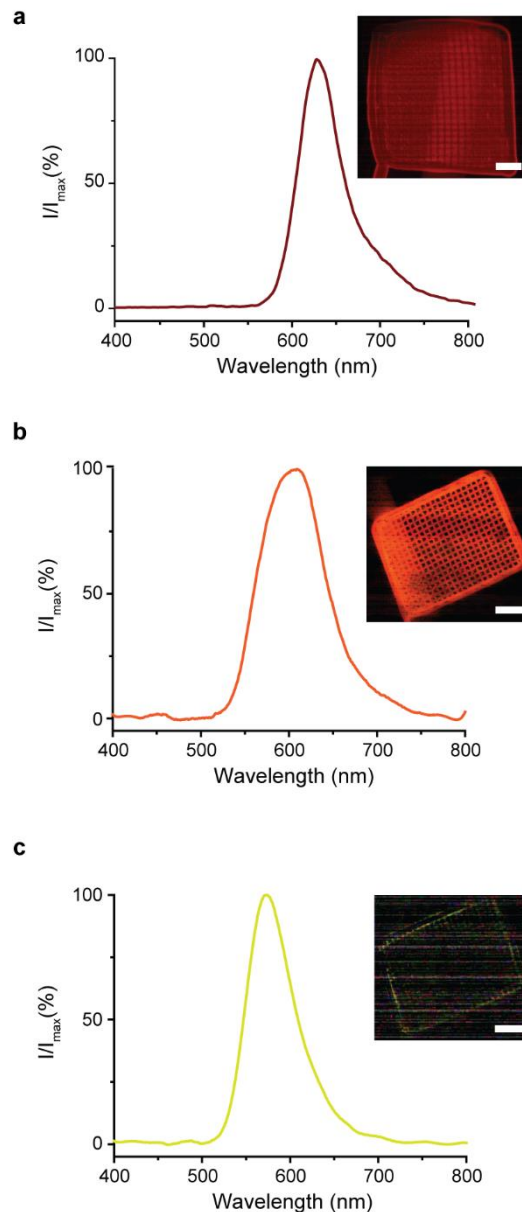


Figure 2.3. Spectral tuning of the electrochemically induced **AMP-luc** luminescence. Normalized emission spectra acquired by applying a constant negative bias (-2.0 V vs Ag/AgCl) to a platinum mesh working electrode (pictured in figure) in contact with a 0.43×10^{-3} M solution of **AMP-Luc**. The electrolyte was (a) 2.0×10^{-1} M Bu_4NClO_4 in DMSO, (b) 2.0×10^{-1} M LiClO_4 in THF, and (c) 5.0×10^{-3} M LiClO_4 in THF. The peaks maximums are progressively blue-shifted [626 nm (a) 605 nm (b), and 573 nm (c)]. Scale bars in the optical image insets are 1.0 mm.

electrode. As discussed above, voltage-dependent shifts towards higher energy were however observed for the emission shoulder, which is therefore tentatively attributed to adsorbed (half-solvated) molecules. The experimental shifts (~ 10 nm, Figure 2.2) are significantly lower than those theoretically expected for a 1 V/nm field. Such lower than predicted shifts are probably

an indirect indication of only a fraction of the external voltage bias dropping across the light emitter, or in other words, indicating that the Debye length is for instance 3–4 times greater than the molecular dimension. It can be envisioned that analogous optical “spectral tuning” measurements may become a viable alternative to a direct probing of the double potential profile, as such direct electrical measurements have serious intrinsic limitations, most notably that any electrified probe will carry its own double layer of charges which will add up to the one under investigation.^{7, 29, 33, 48, 52, 59} Beyond the value and scope of an electrochemical trigger of luciferin luminescence (and of other CT light emitters, such as luminol) to probe near surface electric fields, time-resolved microscopy of the **AMP–luc** electrochemiluminescence can enable a simple and direct optical measurement of diffusion coefficients.

Analogous “imaging” of electrochemiluminescent reactions and of electrochemically modulated fluorescence, to study electrode heterogeneity and mass transport, have been reported for luminol, rubrene and tris(2,2'-bipyridyl)ruthenium(II).¹⁴⁶⁻¹⁵⁰ Selected time-stamped micrographs in Figure 2.4a–c track the diffusion of the red glowing front away from the platinum surface after the electrolysis of **AMP–luc**. Due to the complexity of the light path, which involves several steps, chemical and electrochemical, it is hard to separate from a single optical readout individual diffusivity (D) values, but since D scale roughly with the inverse of size, the species more likely to govern the movement of the electrochemiluminescent front is superoxide. Analysis of the distance (r) travelled over time by the front, away from the electrode surface and along the A–B line marked in Figure 2.4, and by modelling diffusivity as an Einstein’s random walk ($r^2 = 2Dt$), we were able to estimate D for superoxide in DMSO to $(2.45 \pm 0.18) \times 10^{-6} \text{ cm}^2 \text{ s}^{-1}$. This “optical” D value is marginally lower, but of the same order of magnitude, as that obtained for superoxide in DMSO through more established electrochemical methods.¹⁵¹ We also remark that **AMP–luc** is profluorescent, as its electrolysis yields fluorescent **ox–luc**. Optical mapping of the diffusion of electrogenerated **ox–luc** is shown Figure S17, Appendix 1. We believe that this method will complement diffusivity measurements based on electrochemical techniques, such as hydrodynamic methods with rotating disk electrodes. Especially in viscous solvents, such as ionic liquids,¹⁵² adventitious evolution of gas bubbles often leads to mass transport complications, such as convection upon the detachment of surface pinned bubbles.¹⁵³⁻¹⁵⁷ Convection issues are hard to detect and account for in electrochemistry. Through an optical method as the one shown in Figure 2.4 and Figure S17, Appendix 1, it is possible to gauge the severity of convection events, or even to bypass them

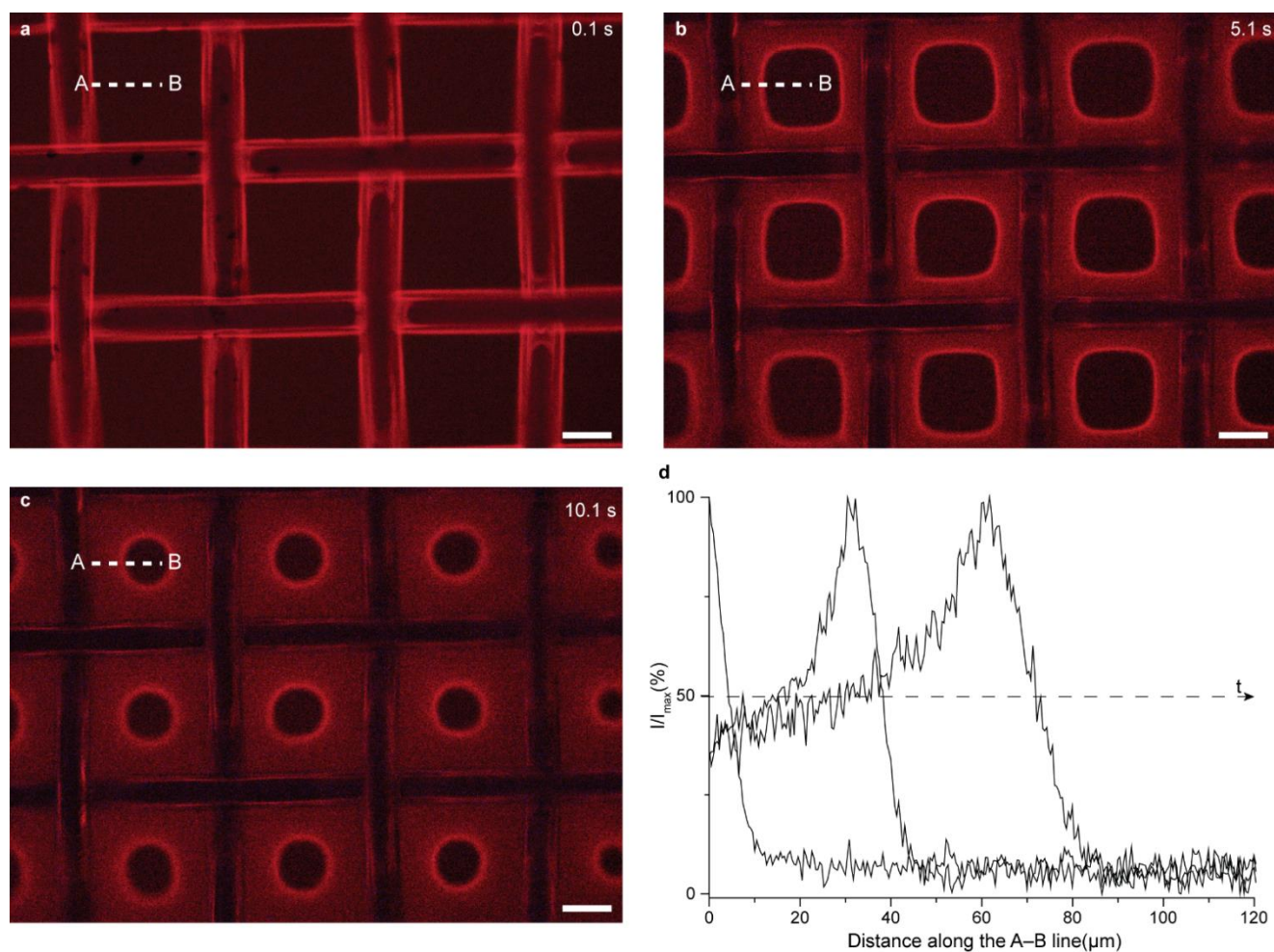


Figure 2.4. (a–c) Selected time-stamped micrographs (10× magnification) mapping the in-situ generated **AMP–luc** electrochemiluminescence upon the cathodic electrolysis of an oxygen-saturated **AMP–luc** solution (0.43×10^{-3} M in 2.0×10^{-1} M $\text{Bu}_4\text{NClO}_4/\text{DMSO}$, V) on a platinum mesh electrode. The images were captured in a dark room at 0.1 s (a), 5.1 s (b) and 10.1 s (c) after the onset of the cathodic bias voltage (-2.0 V). Scale bars in (a–c) are $100 \mu\text{m}$. (d) Electrochemiluminescence profiles sampled along the A–B line marked in (a–c), capturing the expansion of the diffusion front, away from the electrode’s surface, at electrolysis times (t) of 0.1, 5.1 and 10.1 s. Point A is placed approximately on the edge (top view) of the platinum surface.

by mapping local diffusivities instead of relying, as is typically done, on an average measurement of the entire electrode area.

2.3 Conclusion

We have reported for the first time the enzyme-free, electrochemically triggered luciferin light emission. Such laboratory model allows to trigger this luminescent reaction in a controlled environment, removing ambiguity introduced by the complexity of the protein environment of luciferase. The excited state of the light-emitter was generated near an electrified surface,

allowing to control simultaneously exogenous electric fields, solvation and ion pairs. Using quantum chemistry, we have shown that the light path is initiated by radical chemistry mediated by electrogenerated superoxide, we have clarified the nature of the light emitter and explained the debated spectral tuning of luciferin as field effects and ion pairing, rejecting the keto-enol tautomerization hypothesis. We believe that this or similar CT electrochemiluminescent systems will find use in clarifying debated topics in surface science, such as the existence of a density-depleted solvent region near hydrophobic surfaces.^{84-86, 158} Spectral tuning of the partially solvated luciferin light emitter by the electrode generated exogenous electric field, as was observed in this study, could be adapted to verify or falsify the existence of such depletion layer even on rough surfaces, on samples with surface impurities, or in samples with unknown chemical features, where X-ray or neutron-based methods would not be applicable.^{86, 159}

Finally, we have demonstrated that the electrochemiluminescence of **AMP-luc** can be used to map optically the diffusivity of superoxide away from its generation site (the electrode) towards the bulk of the electrolyte. This optical mapping of electro-generated diffusion fronts can measure diffusivity in viscous solvents, in systems where mass transport by convection is likely to interfere with diffusion, as for electrodes evolving gaseous products,¹⁵³ or can be applied to electrode geometries where hydrodynamic electrochemical measurements, such as rotating disk techniques, are not viable.

Chapter 3: Luminol Electrochemiluminescence on Silicon

Chapter 2 presented an innovative spectroelectrochemistry method for fireflies' luciferin. The chapter explained how electrochemistry makes possible to tune the emission wavelength, mimicking what happens in nature, where different species can emit different light (from green to red), although the light emitter is the same. Moreover, it was suggested the use of spectral tuning to probe the interface and the EDL.

Chapter 3 introduces an attempt to achieve spectral tuning of a common chemiluminescent molecule, luminol. Typically, luminol spectroelectrochemistry is performed in water,⁸² which is an obvious starting solvent for any experiment. However, using water as a solvent does not allow to change the reaction environment by varying solvent nature. This limitation can be overcome by working on the working electrode features instead of the solvent. Hence, this chapter presents attempts to achieve luminol spectral tuning using silicon as working electrode. Silicon allows building monolayer of different molecules on its surface, giving an opportunity to control the nature (especially the wettability) of the electrode. Furthermore, ECL in water using a silicon electrode as working electrode is a well-studied technique,^{82, 160} that should be easily exploited to shift luminol emission.

The luminol's spectral tuning can also be a powerful tool for investigating the vacuum gap, a volume at the interface between water and a hydrophobic surface where the water molecules are depleted.^{83, 85, 161-163} Data on the hydrophobic gap in non-water systems are however not available. ECL offers a rapid optical test of the gap, for detecting the present or the absence of the gap itself, sacrificing information on gap thickness. The emission of light from excited molecules, such as in electroluminescent paths, depends on the environment sensed by the light emitter (solvatochromism). A solvent, or its complete absence, will undoubtedly change spectral features.¹⁶⁴

Hence, spectral tuning may be a way to screen for the presence or absence of this gap, and even to gauge the field magnitude inside the gap. This last remark arises because many light-emitting excited state molecules undergo further spectral tuning in response to changes to electric fields.⁷⁷ Furthermore, theoretical modelling can predict the emission wavelength of several chemiluminescent reactions in vacuum,^{75, 165, 166} making this chemiluminescence

reaction a promising candidate for interfacial vacuum gap investigation. Recent theoretical studies predict large redshifts for the luminol emission maxima moving from bulk water to vacuum.⁸⁷ Thus, luminol ECL has been studied as a potential way to study the vacuum gap.

The luminescence reaction of luminol is one of the most investigated light-emitting reactions, and light path mechanisms are generally well understood. These paths are different in protic and non-protic solvents. In aprotic solvents such as dimethyl sulfoxide, and under cathodic conditions, oxygen is reduced to generate superoxide ($O_2^{\cdot-}$), and luminol (i) is oxidised to a radical anion (ii), it then reacts with a superoxide radical in a nucleophilic addition forming an intermediate (iii) that evolves into a bicyclic endoperoxide (iv). This collapse into an excited state intermediate, 3-aminophtalate*, which decays radioactively to 3-APA.⁸⁷ Free oxygen radicals are usually generated from either the reduction of oxygen in organic solvent or from the reduction or oxidation of hydrogen peroxide in water. Nevertheless, some studies have reported that the mechanism does not necessarily proceed via the bicyclic endoperoxide intermediate.^{167, 168}

To obtain the desired shift in the emission, it is important to confine this chemiluminescence reaction to the region near the liquid– hydrophobic-solid interface, so that a short-lived light-emitter can yield some information (via a spectral shift) on the presence or absence of a solvent-depleted region and on its eventual electrification.

3.1 Introduction

Hydrophobicity is a distinctive force that is based on repulsion instead of attraction, and it can be widely observed, from protein folding to cells membranes formation, from charge transfer to self-assembly, and from ultra-hydrophobicity to fluid flow control in microdevices.^{34, 169-173} One system where hydrophobic forces can generate an interesting structure is an interface between water an hydrophobic surface, which may lead to the formation of a depletion layer.^{84, 85} However, the thickness and even the existence of this depletion layer suffer from the lack of direct measurement, due to the absence of any applicable technique. Although, some authors have put forward data indicating water depletion thicknesses in the range of 1–7 Å,⁸⁴⁻⁸⁶ the existence of this “vacuum gap” is questioned by other authors.¹⁷⁴ These studies have exploited neutron and x-ray reflectivity to probe the water density at the interface,⁸⁴⁻⁸⁶ but despite the ability of these techniques to have a sub-angstrom vertical resolution on momentum transfer,¹⁷⁵

obtaining data about the electro density needs extremely flat surfaces and perfect knowledge of interface chemistry.¹⁷⁶ Consequently, the impossibility of keeping the roughness of the hydrophobic surface below 2 Å results in resolution-limited data, even without considering other complications such as sample preparation,^{174, 177} data analysis,¹⁷⁶ and the probability of radiation damage.⁸⁵

Similarly, surface plasmon resonance (SPR) is another technique that can detect variation in the refractive index at the liquid-solid interface, but it is limited by background subtraction issues and can be just exploited with SPR-active materials.¹⁷⁸ The only evidence of a low-density water layer close to the surface has been obtained using an extremely flat gold electrode with a rigid and composite monolayer,³⁴ while there are no data about the “vacuum-gap” on rough samples with an unknown and/or a no-homogeneous chemical composition of the surface.

Some techniques such as atomic force microscopy, can help overcome these issues, by directly probing the gap, but at the same time, they perturb it, making the interpretation of the results challenging.

In this chapter, an attempt is made to investigate the water depletion layer by exploiting an indirect measurement like ECL. Indeed, the spectra tuning of the emitted light is strictly connected with the environment where the excited state is place.¹⁷⁹ In the case of the molecule chosen for these experiments, luminol, the wavelength of the emission in water is around 430 nm,¹⁶⁴ while when the excited state is in the vacuum occurs a redshift to 536 nm.¹⁸⁰ Consequently, the idea is to place the emitting specie, oxidized 3-aminophthalhydrazide in the depletion layer. The thickness of this layer, as previously underlined, is in the order of some Angstrom.⁸⁵ To increase the hydrophobic effect as much as possible, aliphatic monolayers are built onto silicon electrodes, then used to perform ECL of luminol. Moreover, attempts to observe a depletion layer in other solvents are made, trying to cover the utter lack of data in non-water systems.

3.2 Results and Discussion

By applying an anodic bias to the silicon working electrode is possible to initiate the ECL reaction by the generation of superoxide through electrochemical splitting of hydrogen peroxide. As the applied bias is increased, the amount of generated superoxide increases resulting in higher emission intensity. In Figure 3.1 is possible to the normalized spectrum at

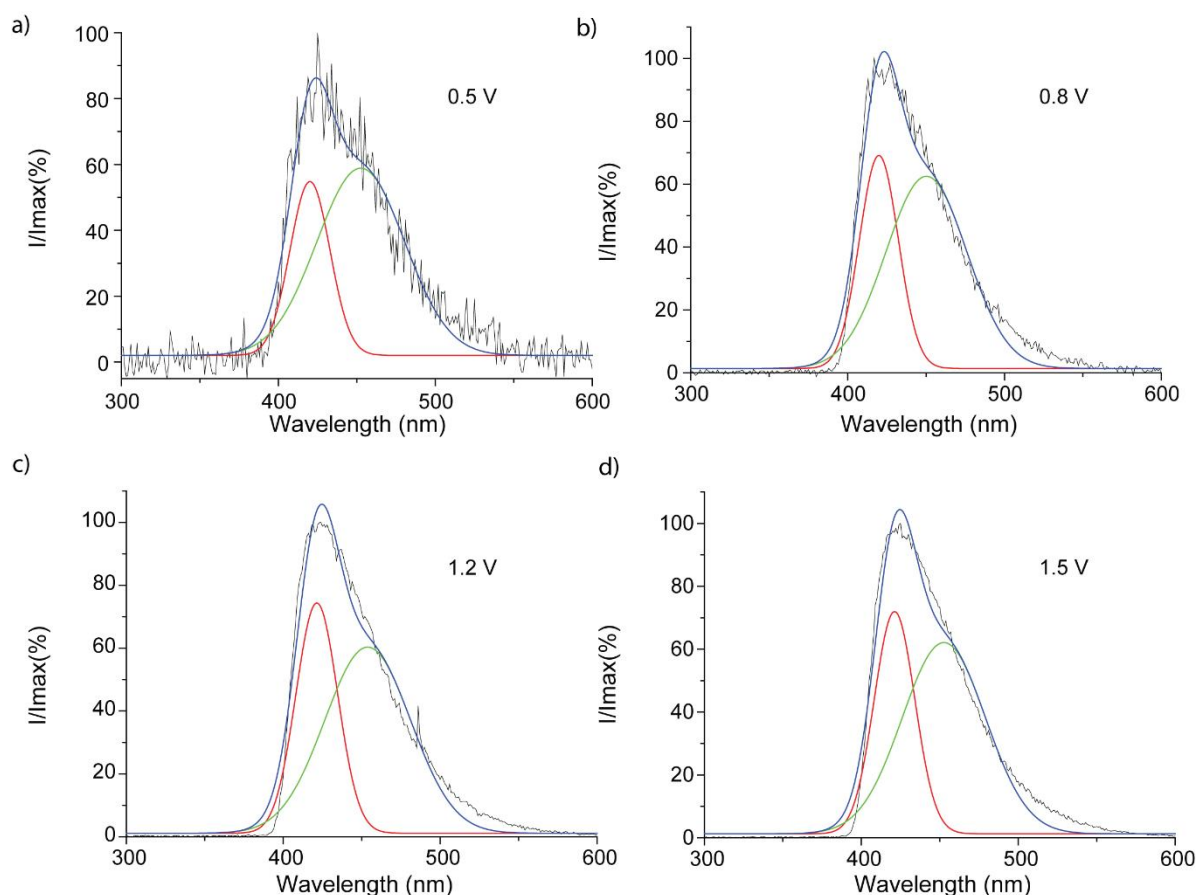


Figure 3.1: Deconvoluted emission spectra of luminol in KOH/H₂O (0.1 M) with 1% of H₂O₂. ECL was performed on a platinum mesh at different positive bias [0.5 V, (a); 0.8 V, (b); 1.2 V, (c); 1.5 V, (d)]. The main peak is always ~418 nm, while the second peak can shift between 450 nm and 455 nm. However, it was not possible to identify any correlation between this shift and the applied bias. The deconvolution was made by fixing the width value of the two peaks.

different bias, interestingly it is immediately noticeable a non-Gaussian shape of the emissions peaks due to a shoulder present at higher wavelength. The silicon working electrode was coated with a 1-nonyne layer, giving a hydrophobic nature to the surface. Considering that theoretical calculation pointed out a redshift of luminol emission in a vacuum-like environment,⁸⁷ and this explains the non-Gaussian shape of emission peaks can be related to luminol molecules reacting in the “vacuum-gap”.

When a molecule lies in the vacuum, the electric field (EF hereafter) is not shielded by the solvent molecules and consequently the EF magnitude on the reacting molecule is higher. The shoulder in the emission peak can be exploited to probe the features of the EDL, by considering the magnitude of the external electric field (EEF hereafter) and its effect on the shoulder position. The emission spectra are deconvoluted to separate the main peak to the red-shifted

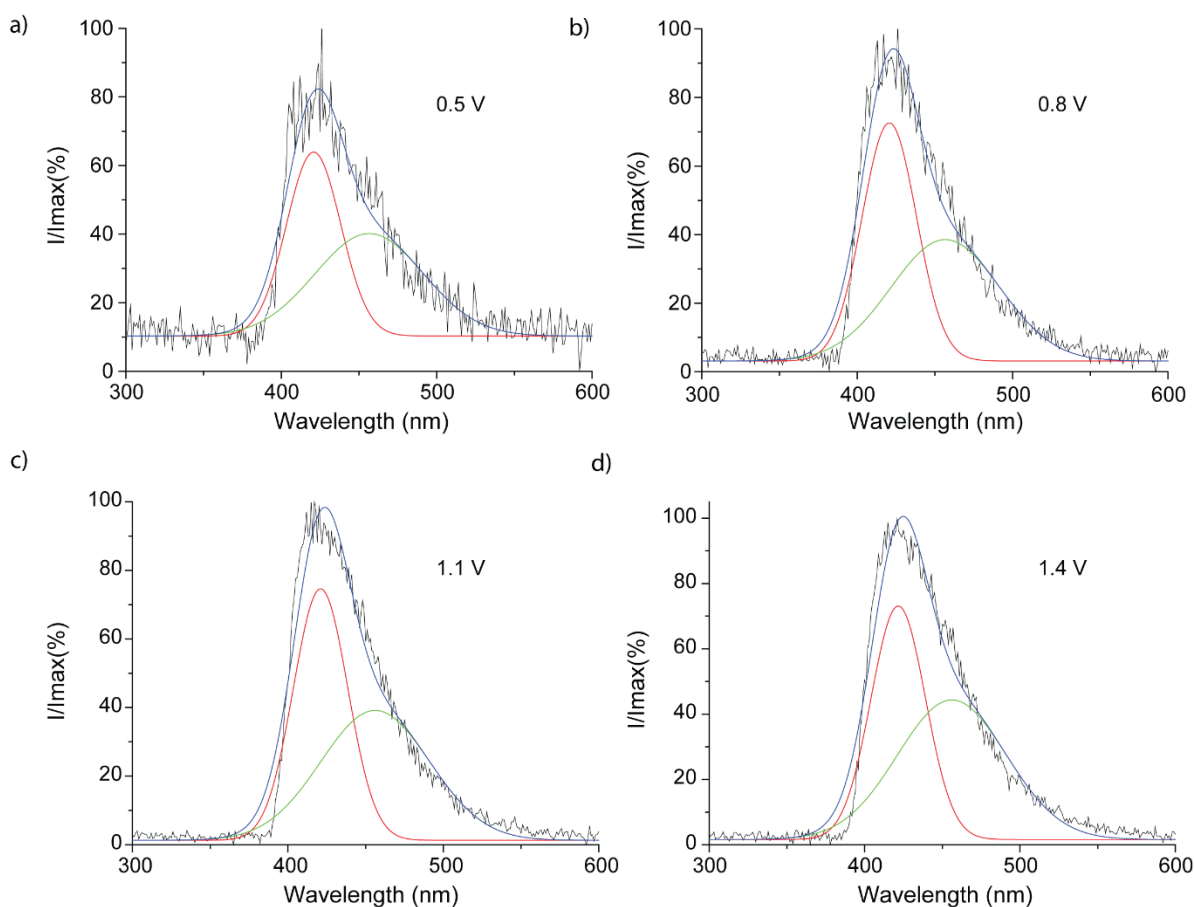


Figure 3.2: Deconvoluted emission spectra of luminol in KOH/H₂O (0.1 M) with 1% of H₂O₂. ECL was performed on a platinum mesh at different positive bias [0.5 V, (a); 0.8 V, (b); 1.1 V, (c); 1.4 V, (d)]. The main peak is always ~420 nm, while the second peak is fixed at 456 nm. However, it was not possible to identify any correlation between this shift and the applied bias. The deconvolution was made by fixing the width value of the two peaks.

shoulder, with the aiming of identifying a correlation between the applied bias and the position of the deconvoluted peaks. Unfortunately, as shown in Figure 3.1, there is no correlation between the EEF and the red-shift shoulder, despite this shoulder is always present, independently from the applied bias. Interestingly, in Figure 3.1, while the peak position is fixed at ~418 nm, the shoulder shifts up to 5 nm, although this shift appears to be a statistical variation rather than an effect of the EF. Repeating the experiments (Figure 3.2) starting from 0.5 V and increasing repeatedly the applied bias by 0.3 V, it is not observed a shift in either the main peak (~420 nm), and the shoulder peak at ~456 nm. This provides further evidence of the absence of any correlation between the applied bias and the shoulder position, except for statistical variations.

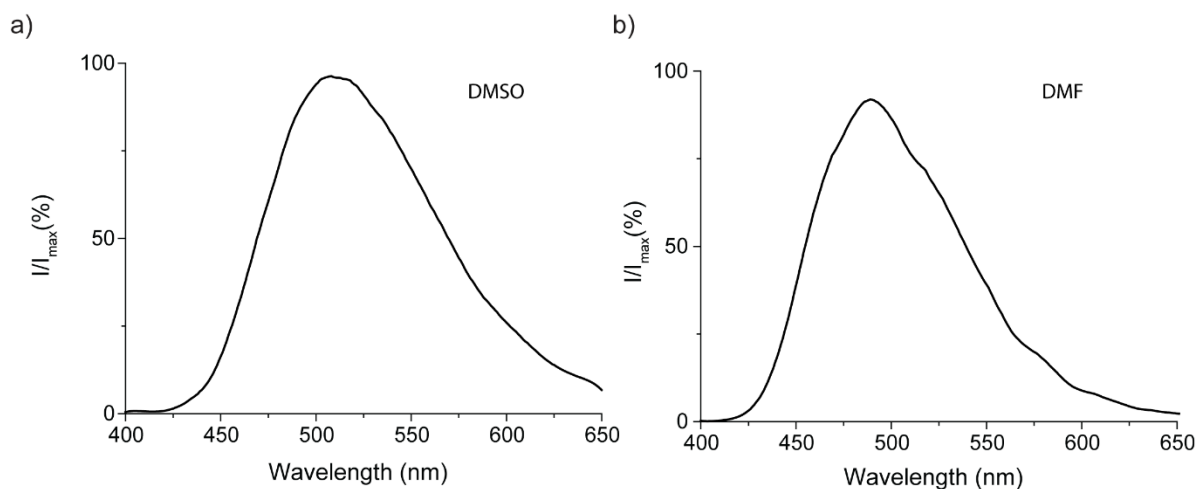


Figure 3.3: ECL of luminol. Normalized emission spectra acquired by applying a constant cathodic bias (-3.0 V vs Ag/AgCl) to a platinum mesh working electrode in contact with 25×10^{-3} M solution of luminol. The electrolyte was 0.1 M TBAClO₄ in DMSO (a) and in DMF (b). The peak position is 508 nm in DMSO and 488 nm in DMF.

After the attempts with luminol ECL in water, the same experiments were performed in organic solvents to determine whether the non-Gaussian shape of the emission peaks persisted. Initially, the feasibility of luminol ECL in organic solvents was tested using a platinum mesh as working electrode applying a cathodic pulse, in the absence of hydrogen peroxide, to generate oxygen superoxide which triggers the reaction.¹⁸¹ Figure 3.3 demonstrates the possibility to carry out luminol ECL in organic solvent, particularly 0.1 M TBAClO₄/DMSO and 0.1 M TBAClO₄/DMF, interestingly the peak position shifts from 508 nm in DMSO to 488 nm in DMF, probably due to the lower dielectric constant of DMF, indeed as shown in Chapter 2 lowering the dielectric constant leads to a blue shift in the ECL emission. Therefore, while the initial aim was to tune the emission by modifying the working electrode nature, it was found a further confirmation that the environment plays a central role in ECL, indeed changing the solvent nature (such as hydrophilicity and dielectric constant) is possible to tune the emission. The remarkable emission shift from water (~ 420 nm) to organic solvents (508 nm in DMSO and 488 nm in DMF) can be attributed to two different states of the excited molecule. In water, the excited state is fully protonated and/or has several hydrogen bonds with the water molecules, while is having less interaction with aprotic solvents.¹⁸²

However, it is important to keep in mind the original objective of this chapter, or rather to obtain a spectrum tuning by modifying the electrode nature. Hence, considering that, DMSO has shown a better reproducibility of the ECL emission spectra, consequently moving on silicon

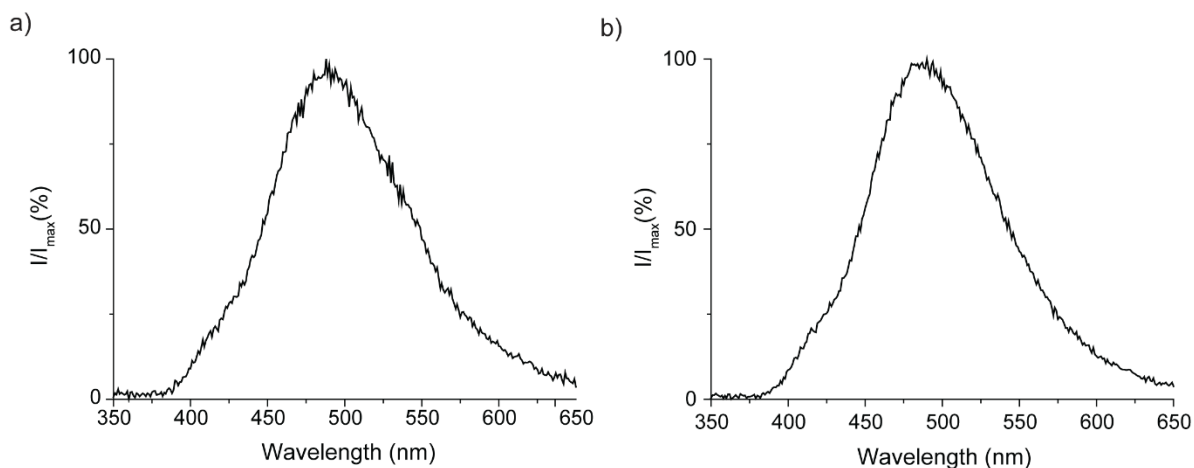


Figure 3.4: ECL of luminol. Normalized emission spectra acquired by applying a constant cathodic bias (-2.0 V vs Ag/AgCl) to a silicon working electrode (3×7 cm) in contact with 25×10^{-3} M solution of luminol. The electrolyte was 0.1 M TBAClO₄ in DMSO. The main peak position is between 480 nm and 485 nm, while the deconvoluted peak of the shoulder lies between 505 nm and 520 nm.

electrodes, DMSO was chosen as the principal solvent in investigating the ECL of luminol on modified silicon electrodes to make them more hydrophobic. The silicon electrodes were coated with 1-nonyne monolayer, as previously done for luminol ECL in water. However, attempts to perform luminol ECL in the same cell used for water (even though at cathodic bias) failed. Probably, the low surface area of the silicon working electrode does not allow to generate an EF strong enough to trigger the oxygen reduction reaction, necessary to generate the superoxide radical which begins the luminol ECL at cathodic bias. Subsequently, a further attempt was tried, increasing the working electrode surface remarkably. This strategy has allowed obtaining some emission spectra, even though a very low reproducibility made these experiments inconclusive. Indeed, an average of two out of 10 experiments lead to record emission spectra worthy to be further analysed. The best two recorded spectra are shown in Figure 3.4, interestingly the red-shifted shoulder is visible here as it was for the anodic experiments in water (Figures 3.1 and 3.2) and for DMSO and DMF with a platinum mesh as working electrode (Figure 3.3), but as for these previous experiments it was not possible to identify any correlation with the shoulder positions and the intensity of the EEF. Additionally, the main peak position in this system is between 480 nm and 485 nm, showing a blueshift when compared with the peak position of the spectra obtained on a platinum mesh working electrode (Figure 3.3).

3.3 Conclusions

Unless a red-shifted shoulder is clearly present in every plot, it is not possible to identify any correlation with the magnitude of the external electric field. In other words, the shoulder in the emission peak does not seem to feel the electric field in the different way than the main peak. Consequently, this shoulder cannot be attributed to the molecules that reacted in the depletion layer.

In conclusion, any attempt to tune the luminol emission wavelength by means of silicon-modified electrodes failed. The reasons behind this failure should be sought in the nature of the SAM on the silicon electrode, perhaps a more hydrophobic electrode is necessary to appreciate an emission shift. However, more hydrophobic SAM, based on fluorinated alkene, showed a lower reactivity towards silicon hydrate, making complicated the achievement of a high electrode coverage. Perhaps, a rigorous method for the preparation of fluorinated SAM must be implemented.

Moreover, the preparation of highly hydrophilic silicon electrodes to be used in hydrophobic electrolytic solution (like THF, as seen in Chapter 2), might be an alternative solution to tune the luminol emission by controlling the electrode nature.

3.4 Experimental Section

3.4.1 Materials

Unless noted otherwise, all reagents were of analytical grade and utilized without further purification. Milli-Q™ water (>18.2 MΩ cm) was used for cleaning procedures and to prepare electrolytic solutions. Hydrogen peroxide (H₂O₂, 30%, Sigma), sulfuric acid (H₂SO₄, 95-97%, Honeywell), 1-nonyne (98%, Sigma), luminol (97%, Sigma), ammonium fluoride (NH₄F, 40%, Honeywell), 2-propanol (99.5%, Ajax Finichem), potassium hydroxide (KOH, 95%, Ajax Finichem), dichloromethane (DCM, distilled before use), propan-2-ol (≥99,9 %, Univar), dimethyl sulfoxide (DMSO, ≥99.0%, Sigma) and tetrabutylammonium perchlorate (Bu₄NClO₄, 98.0%, Sigma). Prime-grade, single-side-polished silicon wafers (111-oriented (±0.5°) of p-type, boron-doped, 0.007–0.013 Ω cm, 500 mm thick, Siltronix, S.A.S. Archamps, France).

3.4.2 Silicon electrodes preparation

Silicon electrodes were obtained by cutting 1 × 1 cm samples from the silicon wafers. Thus, the silicon samples were washed with DCM, propan-2-ol and water, afterwards, the samples were immersed in Piranha solution (100°C, 1:3 H₂O₂:H₂SO₄) for 30 min. Silicon samples were rinsed with Milli-Q™ water, and etched in deoxygenated NH₄F solution (40% wt) for 14 min. The obtained hydrogen-terminated silicon samples were washed with water and DCM and dried under an argon stream. The dry silicon samples were covered with a small amount of 1-nonyne (~50 µL) and then a quartz slide was placed above the wet sample to prevent the 1-nonyne evaporation. Finally, the hydrosilylation reaction (2 h) was carried out inside a box maintained under nitrogen flux and with UV source (Vilber, model VL-215.M, 312 nm, and nominal power output of 30 W). After 2 h, the silicon electrodes were washed thoroughly with DCM prior to experiments. For some experiments, the cut sample was bigger (3×7 cm).

3.4.3 Electrochemical Methods

All ECL measurements were carried out with 25×10⁻³ M of luminol, dissolved in the water with KOH (0.1 M) or DMSO with Bu₄NClO₄ (0.2 M). When the solvent was water, besides the electrolyte 1% v/v of H₂O₂ solution was added, as it is necessary to the anodic ECL performed in water,⁸² while in DMSO, was bubble oxygen gas (≥99.95%, Coregas) for at least 20 min before experiments. An Emstat3 Blue potentiostat (PalmSens BV, Houten, Netherlands) potentiostat with a single-compartment, three-electrode setup was used to carry out all the experiments. A platinum mesh was used as the working electrode (EF-1265 SEC-C Gauze, 80 mesh, BASi, Lafayette, Indiana), a platinum wire as counter electrode (EF-1361 SEC-C counter electrode 0.5 mm diameter wire, BASi) and a leakless Ag|AgCl as the reference electrode in DMSO (ET072-1, eDAQ, Colorado Springs, Colorado, 3.4 M aqueous potassium chloride as filling solution), while in water a Ag/AgCl/KCl(sat.) was used the reference electrode.

The emission was recorded using a Cary Eclipse fluorescence spectrophotometer operated in Bio/Che-luminescence mode, a quartz cuvette of 0.5 mm optical length (EF-1364 SEC-C, BASi), fitted with a perforated PTFE cap was holding up the electrodes (EF-1359 SEC-C) was chosen as electrochemical cell. The cleaning of the platinum electrodes was carried out by cyclic voltammetry between -0.2 and 1.0 V (0.5 M HNO₃, 0.01 V s⁻¹).

3.4.4. Plots Fitting

The plots were analysed using OriginPro 9.0 (OriginLab Corporation). The data fitting was obtained using the multiple peaks fitting tool of OriginPro 9.0, using a Gaussian function. All the parameters were fitted until converged, while the width of the peaks was always fixed to 35 for the main peak and 70 for the shoulder peak.

Chapter 4: Electrochemically Generated Luminescence of Luminol and Luciferin in Ionic Liquids

In **Chapter 2**, the electrochemiluminescence (ECL) of luciferin and its spectral tuning was presented. In **Chapter 3** an attempt was reported towards tuning the emission of luminol by means of self-assembled monolayers on silicon electrodes.

In **Chapter 4**, in the form of paper 2 (Mattia Belotti, Mohsen M. T. El-Tahawy, Nadim Darwish, Marco Garavelli, and Simone Ciampi. Electrochemically Generated Luminescence of Luminol and Luciferin in Ionic Liquids, *ChemElectroChem* **2022**, 10, 1, e202201033, DOI <https://doi.org/10.1002/celc.202201033>), these two luminescence reactions are explored in a particular and extremely interesting class of chemicals: room temperature ionic liquids. In other words, this chapter explores the electrochemical path to trigger luminol and firefly's luciferin luminescence in room temperature ionic liquids. Chemiluminescent reactions are broadly exploited in science and technology. Over purely chemical counterparts, electrochemically triggered luminescence – ECL – has distinct advantages such as greater spatiotemporal reaction control and greater reaction selectivity. ECL reactions are generally carried out in solvent-based electrolytes, with only a handful of examples demonstrating ECL viability and performances in solvent-free electrolytes, namely room temperature ionic liquids.¹⁸³⁻¹⁸⁶ This is surprising, as owing to their large potential window of stability, low volatility, and good recyclability, ionic liquids are actively explored across most fields of electrochemistry, from energy storage to sensing and electrocatalysis. ECL in room temperature ionic liquids is underexplored and here we begin to address this by studying a prototypical ECL dye, luminol, as well as an emerging one, luciferin, using a common imidazolium-based ionic liquid.

4.0 Abstract

Electrochemiluminescence (ECL) is the generation of light triggered by an electrochemical reaction. ECL has been extensively studied in solvent-based electrolytes, but there is a lack of data on using electrode reactions to populate an excited-state light emitter in room temperature ionic liquids (RTILs). This work explores the current response, light intensity (photon counting), and spectral signatures of the cathodic ECL of luminol and firefly's luciferin in imidazolium-based RTILs. We have demonstrated that the cathodic (superoxide-triggered) ECL of both

luminol and adenylate-ester of firefly's luciferin is viable in RTILs, explored the effect of water contaminations, and importantly, shown that the ECL signal persists for up to ~700 s after the removal of the external cathodic pulse, which is probably due to the stabilization of superoxide by double-layer cation-rich structures. Remarkably long-lived RTIL double-layer structures, and their endogenous fields, are detected as stable and discrete open-circuit plateaus.

4.1 Introduction

The generation of light associated to electrochemical reactions has been actively researched since the 1920s, when it was first observed during the electrolysis of luminol in the presence of Grignard reagents.¹⁸⁷⁻¹⁸⁹ The systematic study of this branch of electrochemistry did however not start till the 1960s, with work done on radical ion annihilation electrochemiluminescence (ECL).¹⁹⁰⁻¹⁹² ECL is currently exploited across science and technology, with applications ranging from food and water-quality testing, to immunoassays and biosensors for biological warfare.^{98, 100, 193} In comparison with chemiluminescence, ECL requires an electrical trigger, meaning that it has distinct advantages over its purely chemical counterpart, such as allowing for a fine control of the time and location of the reaction.^{100, 155, 194-196} Furthermore, ECL can claim greater selectivity over chemiluminescence, as well as stability and simplicity.^{160, 197, 198}

Even though the number of ECL publications has been continuously rising since the 1990s,¹⁰⁰ the dominant reaction medium remains that of a molecular solvent added with an electrolyte. ECL requires coupling electronic conduction in a solid electrode with ionic conduction in the electrolyte connecting at least two electrodes: the ECL emitter needs to be dissolved in an ionic conductor. ECL in a molecular, solvent-free ionic conductor, such as a room temperature ionic liquid (RTIL) is viable but under-explored, with only a limited number of studies having been published in the last two decades, along with their possible applications.^{183-185, 199} The advantages of using an RTIL over a solvent-based electrolyte are several. Firstly, RTILs generally have very high boiling points, so that their use can mitigate undesirable solvent evaporation, hence solvent waste.¹⁸⁶ Secondly, RTILs have a good electrochemical and thermal stability, large ionic conductivity, and are therefore an ideal medium for electrochemical applications.^{88, 200} Thirdly, changes to the molecular nature of the solvent and electrolyte is a means of tuning the ECL emission wavelength,²⁰¹ hence given the variety of RTILs now available (covering a broad range of viscosities, acidities, hydrophobicities, and

polarizabilities²⁰⁰), it may be possible to harvest the large pool of RTILs to expand the spectral tuning of common ECL molecules.^{202, 203}

Herein we explore the ECL of luminol and luciferin using widespread, commercially available and inexpensive imidazolium-based RTILs.¹⁵² Luminol is arguably one of the most popular ECL dyes, it has a wide number of applications ranging from immunoassays, biosensing, to non-clinical applications such as the forensic detection of blood traces.^{100, 204} Luciferin is one of Nature's wonders, and is extremely fascinating due to its specie-specific breadth of colors, which covers almost all of the visible spectrum,^{96, 97} its debated luminescence mechanism,⁷⁷ and its several technological applications.^{99, 105, 107, 108} Furthermore, luminol's anodic ECL in the presence of hydrogen peroxide has been used as proof-of-principle to demonstrate ECL spatiotemporal control,⁸² while fundamental studies on luciferin ECL, without its natural biocatalyst (luciferase-free luciferin ECL), have only recently begun.²⁰¹

4.2 Results and Discussion

Luminol ECL is usually obtained under anodic biasing, and in the great majority of cases, it relies on aqueous electrolytes and hydrogen peroxide as co-reactant.^{100, 205} However, luminol ECL may also be triggered under cathodic regimes,^{100, 181} where it relies on the formation of superoxide radical anion (superoxide hereafter) through the one-electron reduction of dissolved oxygen (Figure 4.1a).²⁰⁶ This reaction has been previously reported in RTILs,^{183, 199} but no spectral data are available. As shown in Figure 4.1b the application of a cathodic voltage to an oxygen-saturated solution of luminol in 1-ethyl-3-methylimidazolium ethyl sulfate ([EMIM][EtSO₄]) leads to a blue emission which is already detectable at -1.0 V (*vide infra* for a discussion on the ECL intensity-to-bias relationship). Similar results were obtained in other RTILs (Figures S1–S2, Appendix 2). The emission of luminol in [EMIM][EtSO₄] peaks at 490 nm, which is analogous to the position observed in polar molecular solvents such as DMSO,¹⁸¹ and expected based on the polarity nature of [EMIM][EtSO₄].²⁰⁷ In [EMIM][EtSO₄] the luminol ECL persists well beyond the duration (30 s) of the cathodic -2.5 V pulse. As shown in Figure 4.1c, once the external potential is removed, light emission continues for over 700 s, while in a solvent-based electrolyte (Bu₄NClO₄/DMSO) it would fade off in ~ 35 s (Figure S3, Appendix 2). Figure 4.1d is an overlay plot of the simultaneous photon counting and current logging from the cyclic voltammetry experiment used to trigger the ECL. The plot shows that a small negative bias (-0.8 V) can trigger the ECL, but the photon count begins to rise sharply only around -2.0

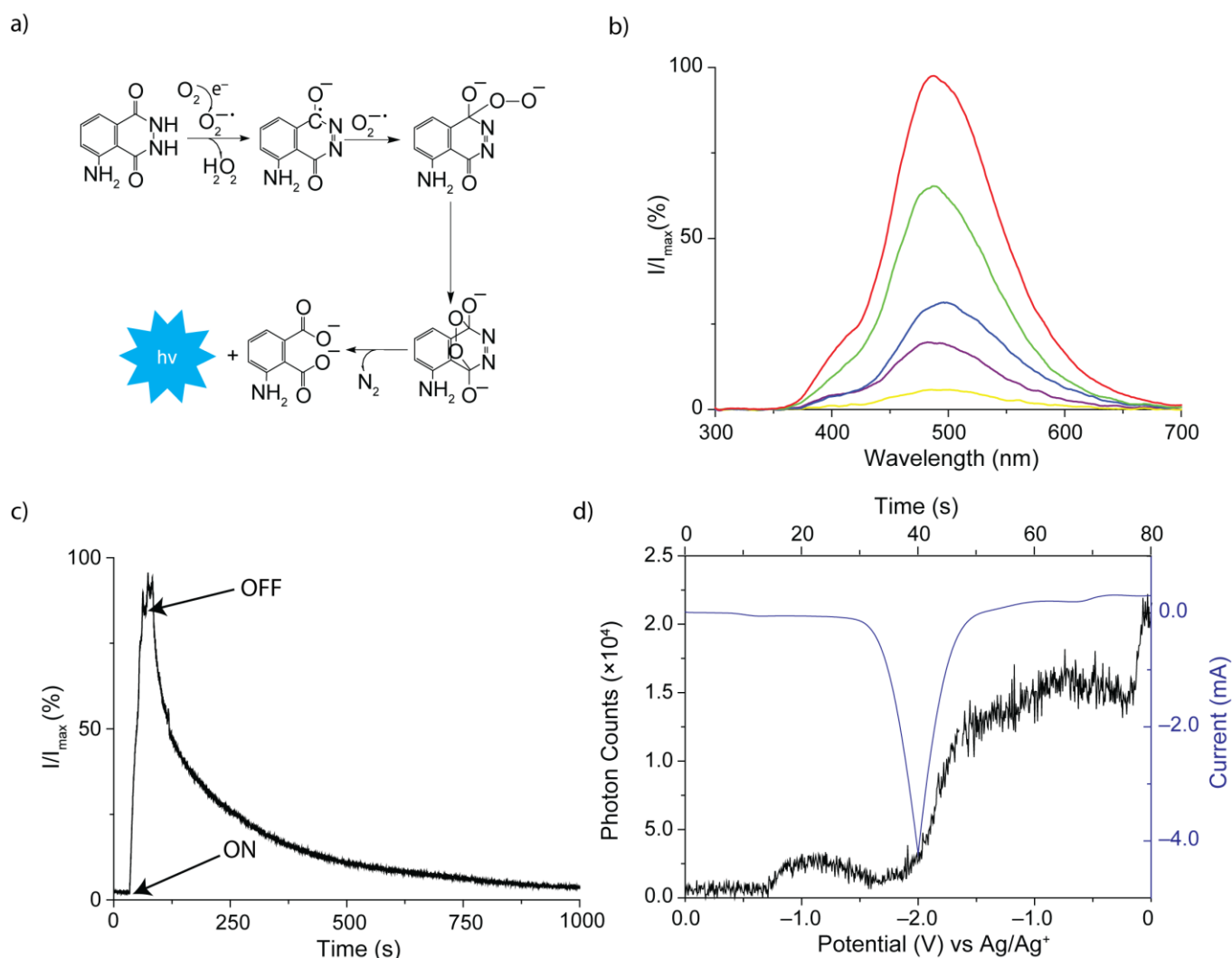


Figure 4.1. (a) Proposed mechanism for luminol cathodic ECL^{82, 155} (b) ECL of luminol (1.0×10^{-3} M) in [EMIM][EtSO $_4$], recorded at a platinum mesh electrode biased at either -1.0 V (violet line), -1.5 V (yellow line), -2.0 V (blue line), -2.5 V (green line) and -3.0 V (red line). Spectra are normalized to the maximum intensity of the -3.0 V data set. (c) Time-resolved emission spectra (490 nm). The ON label indicates when the working electrode voltage bias is switched from open-circuit to -2.5 V. The OFF label indicates the end of the 30 s voltage pulse. (d) Photon counting experiments of luminol ECL during a cyclic voltammogram (the voltage was swept from 0.0 V towards -2.0 V, and back, at a scan rate of 0.05 V/s). Overlay plot of simultaneously acquired photon counts and current trace.

V. At the photon counts peak, the luminol system emits $\sim 2.0 \times 10^4$ photon/s, which is one order of magnitude less than what was found for the same system in Bu $_4$ NCIO $_4$ /DMSO ($\sim 3.5 \times 10^5$ photon/s, Figure S4, Appendix 2).

As shown in Figure 4.1a, the luminol cathodic ECL mechanism in a RTIL, similarly than in an aprotic molecular solvent such as DMSO,¹⁸¹ begins with the electrochemical formation of

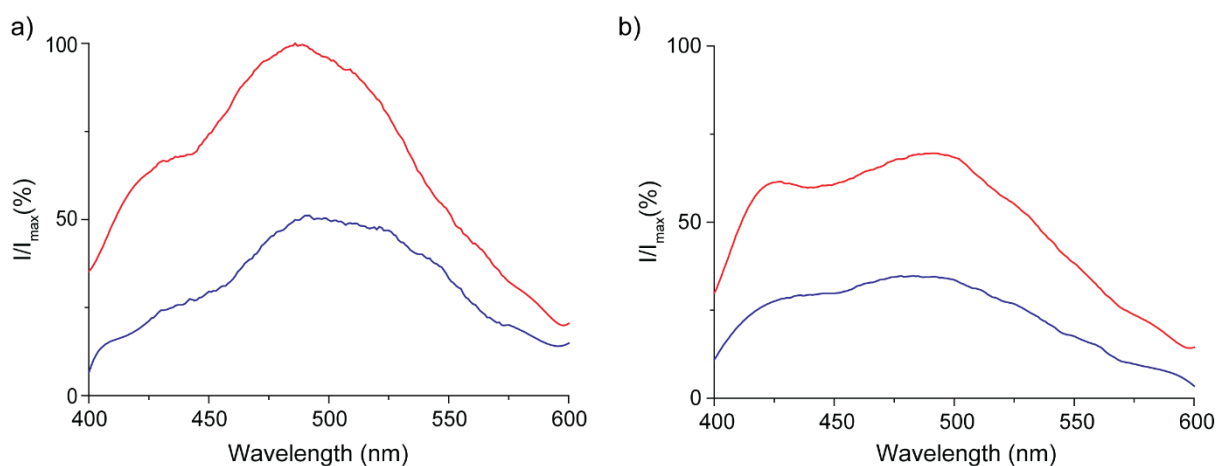


Figure 4.2. Electrogenenerated chemiluminescence of luminol (1.0×10^{-3} M) in [EMIM][EtSO₄], obtained using a platinum mesh biased at either -2.5 V (blue line) or at -3.0 V (red line). The RTIL is deliberately spiked with water [5% v/v (a); 10% v/v (b)]. A further increase of water concentration to 15% v/v quenches completely the emission. Spectra are normalized to the maximum intensity of the -3.0 V, 5% v/v water data set.

superoxide from oxygen, which in turn converts luminol to a diazasemiquinone radical. This radical intermediate then reacts in a cycloaddition reaction with a second superoxide, leading to the excited state of 3-aminophthalate*, which relaxes emitting light (Figure 4.1a).^{82, 181} Superoxide formation is quenched by the presence of water, which leads to H₂O₂ via oxygen reduction. H₂O₂ at low concentrations causes an increase in ECL intensity,¹⁸¹ but as found experimentally, further addition of water to the RTIL causes a progressive drop in emission (Figure 4.2).

The viability of generating electrochemically superoxide in RTILs has been already demonstrated,^{206, 208} and despite the stability of superoxide in RTILs remaining unclear, it strongly depends on the nature of the cation.²⁰⁹ Ion-pairing of superoxide with the RTIL cations may enhance its stability without reducing its reactivity.²¹⁰

Notably, our data suggest more than one mechanism being involved, and luminol reacting with different species electrogenerated at different potentials.

For example, the emission intensity at -1.0 V (Figure 4.1b) does not track the general trend in ECL rise with potential, probably because at this potential the emission is triggered by superoxide generated from oxygen, together with a contribution from a light path initiated by H₂O₂ and OH⁻. The latter requires water traces (see Karl-Fisher data in the experimental

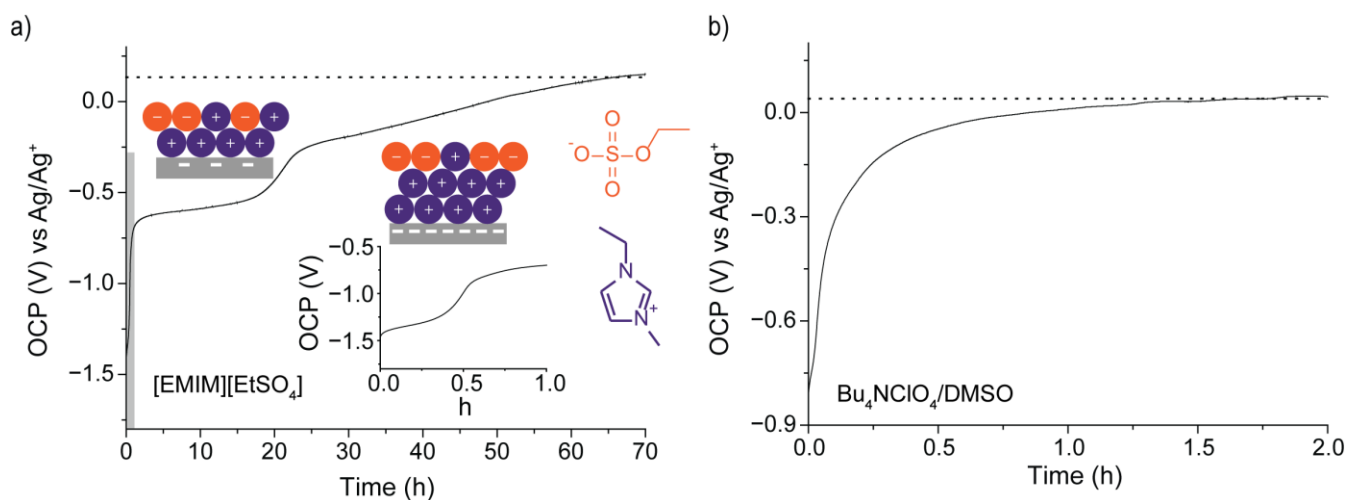


Figure 4.3. Open circuit potential (OCP)–time measurements recorded at a platinum mesh electrode immersed in neat [EMIM][EtSO₄] (a), and in 1.0×10^{-1} M Bu₄NClO₄ in DMSO (b). A negative potential step (60 s) was applied to the working electrode, away (-2.0 V) from the initial OCP rest value (dotted line) and the OCP relaxation monitored over time. In the molecular solvent the OCP relaxes rapidly and asymptotically back to the initial OCP (b). During the OCP relaxation in [EMIM][EtSO₄], discrete and long-lived OCP plateaus emerge around -0.65 V and -0.75 V. The inset in (a) highlights the shorter and more negative plateau located between -1.4 V and -1.5 V. This two plateaus have been ascribed to electrostatic signatures of crowding (first, more negative plateau) and overscreening (second, longer-lived plateau) double-layer structures.¹⁵²

section). Consequently, the ECL intensity -1.0 V lies between those recorded at -1.5 V and at -2.0 V. A similar anomaly was also observed in other RTILs (Figures S1–S2, Appendix 2). We believe therefore that an explanation of such outlier is the existence of multiple mechanisms for the cathodic ECL of luminol.^{181, 211} It is possible that at -1.5 V (and at more negative biases), H₂O₂ is effectively reduced to OH⁻ instead of reacting directly with luminol, ($2 \text{ luminol} + \text{H}_2\text{O}_2 \rightarrow 2 \text{ luminol radical anion} + 2 \text{H}_2\text{O} + 2 \text{H}^+$) as it may happen at -1.0 V, and so the ECL intensity does track the increase in current. At -2.0 V (and beyond) the current is so large that the ECL progressively increases despite the consumption of H₂O₂ (Figure 4.1b). Finally, in the return scan (towards anodic biases) there is sudden increase in ECL photon counting (Figure 4.1d). Here, at lower negative potential during the return scan, the superoxide radical anion is regenerated by H₂O₂ electro-oxidation to hydroperoxyl radical and then to superoxide radical anion,^{181, 211, 212} resulting in a rise the ECL emission. The delay between this peak and the current peak at -0.4 V (Figure 4.1d) may be attributed to a slower kinetic in RTILs, mainly due to their large viscosities.⁸⁸

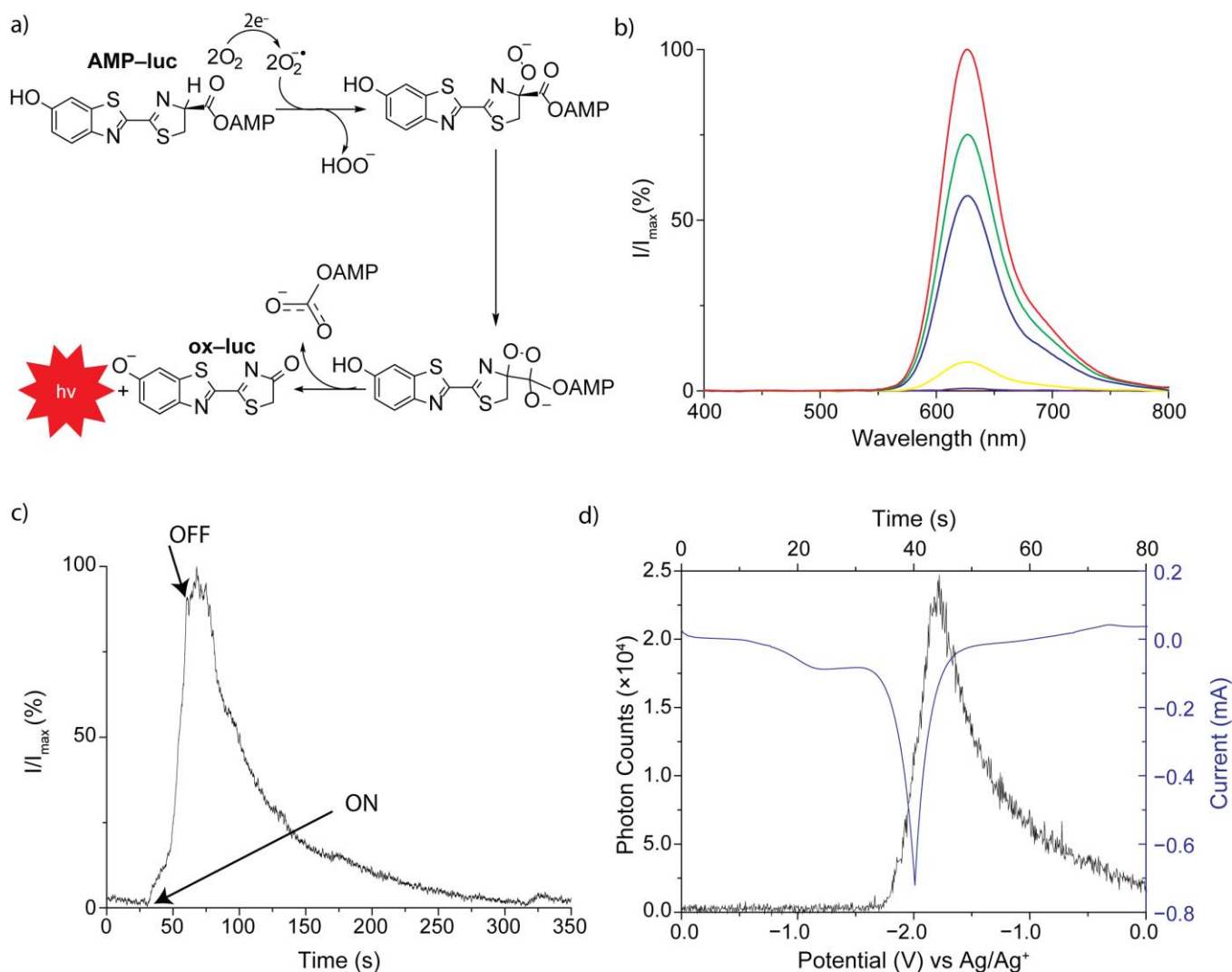


Figure 4.4. (a) Proposed mechanism for the firefly's luciferin ECL (extended mechanism in Figure S5, Appendix 2).²⁰¹ (b) ECL of **AMP-luc** (4.3×10^{-4} M) in [EMIM][EtSO $_4$] at a platinum mesh electrode biased at either -1.0 V (violet line), -1.5 V (yellow line), -2.0 V (blue line), -2.5 V (green line) and at -3.0 V (red line). Spectra are normalized to the maximum intensity of the -3.0 V data set. (c) Time-resolved emission spectra (626 nm). The ON label indicates the time at which the working electrode voltage bias is switched from open-circuit to -2.5 V. The OFF label indicates the end of the 30 s (-2.5 V) voltage pulse. (d) Photon counting experiments of **AMP-luc** ECL during a cyclic voltammogram (the voltage was swept from 0.0 V to -2.0 V, and back, at a scan rate of 0.05 V/s).

Since superoxide is complexed by large cations,²¹³ we hypothesized that a cation-rich RTILs structure at the electrified interface may increase superoxide stability, causing luminol emission not to drop suddenly after the removal of the external voltage. Such ordered bilayer structure at the interface between RTILs and charged electrodes is well documented.^{18, 90, 92, 152, 214-216} This is particularly true at negative potentials, where stable, cations-rich, near-surface RTILs

double-layer structures have been unambiguously demonstrated by atomic force microscopy (AFM).^{215, 216} However, AFM experiments with liquids are technically demanding and a simpler method to detect the presence of such cation-rich layer is by open circuit potentiometry (Figure 4.3a).¹⁵² Following a short (60 s) negative-potential pulse, the open-circuit potential (OCP) of a molecular solvent-based electrolyte/electrode system will rapidly and asymptotically return to its rest OCP value (Figure 4.3b). In sharp contrast to such rapid and asymptotic relaxation, in [EMIM][EtSO₄] we observed two stable OCP plateaus during the OCP relaxation measurements (Figure 4.3a). These two negative and consecutive OCP plateaus are interpreted as electrostatic signatures of the endogenous fields of overscreening and crowding structures (cation-rich near-surface structures formed after a negative pulse, see cartoons in Figure 4.3a).^{90, 152} The formation of a cation-rich crowding structure (the most negative OCP plateau) is proposed to be linked to the persistency of the ECL emission even after the removal of the external bias.

We then turned to a much less explored ECL luminophore: firefly's luciferin adenylate (**AMP-luc** hereafter).²⁰¹ **AMP-luc** ECL is here performed without its natural biocatalyst, luciferase, in contrast to most studies and applications of luciferin where luciferase is required to start the light path.¹¹⁸

The likely role of superoxide in the ECL reaction mechanism is shown in Figure 4.4a.²⁰¹ Two superoxide molecules are needed for the **AMP-luc** light path: the first to remove the hydrogen atom on the carbon in alpha-position of the AMP ester, and a second to generate an endoperoxide which leads to the formation of the excited state (oxyluciferin, **ox-luc**) upon a decarboxylation.²⁰¹ The ECL of **AMP-luc** in [EMIM][EtSO₄] peaks at an energy comparable to that observed in DMSO-based electrolytes (626 nm, Figure 4.4b).²⁰¹ The ECL of **AMP-luc** was also studied in other RTILs (Figures S6–S7, Appendix 2). Interestingly a non-Gaussian shape is visible in the emission profile (Figure 4.4b), and it could be related to half-solvated molecules trapped at the interface.²⁰¹ Data in Figure 4.4c show that the ECL of **AMP-luc** in [EMIM][EtSO₄] persists after the removal of the external bias, and as for luminol such persistence is possibly linked to the stability of the cation-rich crowding double-layer structure of [EMIM][EtSO₄] at platinum electrodes. As for luminol, the ECL of **AMP-luc** in DMSO drops fast once the external bias is removed (Figure S8, Appendix 2). Figure 4.4d shows the simultaneous photon counting and voltammetric current recording, with the emission beginning to rise at -1.8 V. At the photon

counts peak, the **AMP-luc** solution emits 2.5×10^4 photon/s, which is roughly ~4.5 times less than in DMSO.²⁰¹

4.3 Conclusion

We have reported the ECL of luminol and luciferin (**AMP-luc**) in imidazolium-based RTILs. Luciferin ECL normally requires a biocatalyst, luciferase, but here we show that radical chemistry mediated by electrogenerated superoxide can trigger the light path in an enzyme-free environment. However, the emission intensity in RTILs is lower, probably due to the higher viscosity which limits mass transport. Demonstrating the feasibility of ECL in RTILs of a conventional dye (luminol) as well as of a relatively less explored luminophore (firefly's luciferin) we have shown how RTILs can be a good and a greener alternative to conventional molecular solvents. Moreover, photon counting experiments have shown that although ECL intensities are lower in RTILs than in molecular solvents, same photon count order of magnitudes are achieved.

Importantly, the ECL emission of both, luminol and luciferin, persists for several minutes after the removal of the cathodic pulse (~700 s for luminol, ~200 s for **AMP-luc**). We propose this long-lived emission to be linked to the stability of superoxide in the cation-rich (crowding) double-layer structure that persists for hours at the interface between platinum cathodes and several imidazolium-based RTILs.¹⁵² Such long-lived ECL emission is not observed in solvent-based electrolytes.

4.4 Experimental Section

Unless noted otherwise, all reagents were of analytical grade and utilized as received. 5-Amino-2,3-dihydrophthalazine-1,4-dione (luminol, ≥97%), 1-ethyl-3-methylimidazolium ethyl sulfate ([EMIM][EtSO₄], ≥95%), tetrabutylammonium perchlorate (Bu₄NClO₄, 98.0%), and anhydrous dimethyl sulfoxide (DMSO, ≥99.0%) were purchased from Sigma–Aldrich. 1-Butyl-3-methylimidazolium bis(trifluoromethylsulfonyl)imide ([BMIM][NTf₂], 99.5%) and 1-Butyl-3-methylimidazolium hexafluorophosphate ([BMIM][PF₆], 99.5%) were purchased from Iolitec. Unless specified otherwise the water content, measured by a Karl–Fischer titrations, was ~600 ppm for [EMIM][EtSO₄], 300 ppm for [BMIM][NTf₂], and ~450 ppm for [BMIM][PF₆]. Firefly luciferin adenylate (**AMP-luc**) was synthesized and characterized according to procedures reported elsewhere.²⁰¹ Electrolytic solutions used for the ECL experiments were 1.0×10^{-3} M

luminol, and 4.3×10^{-4} M **AMP-luc**. Solutions for ECL were oxygen-saturated by means of a 20 min oxygen-gas bubbling procedure (Coregas, $\geq 99.95\%$). Spectroelectrochemical experiments were carried out with a Cary Eclipse spectrophotometer (Varian, Palo Alto, California) operated in Bio/Chemi-luminescence mode at 25 °C. The photomultiplier voltage was set to 800 V, and the emission slit to 20 nm. Each emission spectra were recorded in ~5 s. The spectra were normalized to maximum intensity, but they were not corrected for the variation in instrumental sensitivity over wavelength range. The spectroelectrochemical cell used for all ECL measurements was a quartz cuvette of 10 mm optical-path length (1/SX/10, Starna scientific, UK) fitted with a perforated PTFE cap/electrodes holder. A negative voltage bias was applied to a platinum mesh used as working electrode (011498 SEC-C Gauze, 80 mesh, 7 × 6 mm overall size, BASi), a platinum coil was used as counter electrode. A leakless Ag|AgCl electrode (ET072-1, eDAQ, with 3.4 M aqueous KCl as filling solution) was used as the reference electrode. All potentials are reported against the reference electrode. The spectroelectrochemical experiments were carried out under ambient air at room temperature by using a PalmSens4 (PalmSens BV, Houten, Netherlands) as potentiostat. Photon counting experiments were performed with a single-photon counting module (SPCM-AQR-14, Excelitas Technologies) interfaced with an avalanche photo-diode (APD) controller (Nanonics Imaging Ltd.). The APD controller time constant was set to 1.0 ms. The photon count output was recorded with a data logger (DrDAQ, Pico Technology, Figure S9, Appendix 2). The photon count rate was corrected for the nominal wavelength-dependent efficiency of the APD module (Nanonics Imaging Ltd.), which is 70 % for red light and 42 % for blue light. The water content was estimated by Karl-Fisher titration (Mettler-Toledo C20S compact coulometer, Honeywell HYDRANAL Coulo-mat AG reagent, Merck Water Standard 0.1%, USA), and with three samples run for each RTILs.

Chapter 5: Experimental evidence of long-lived electric fields of ionic liquid bilayers

In **Chapter 4** showcases the persistent electrochemically generated emission in ionic liquids. This phenomenon is referred to as “persistent” because after removing the external field, the intensity emission does not drop instantaneously. The observed phenomenon is clearly related to the particular electrode/ionic liquid interface and it has opened a way to investigate the features of ionic liquids electric double layer.

Chapter 5, in the form of Paper 3 (Mattia Belotti, Xin Lyu, Longkun Xu, Peter Halat, Nadim Darwish, Debbie S. Silvester, Ching Goh, Ekaterina I. Izgorodina, Michelle L. Coote and Simone Ciampi. Experimental evidence of long-lived electric fields of ionic liquid bilayers, *J. Am. Chem. Soc.* **2021** 143, 42, Pages 17431–17440, DOI <https://doi.org/10.1021/jacs.1c06385>), demonstrates, unambiguously, that near-surface ordered ionic liquid structures generate endogenous electric fields that persist for days. A complete and, correct description of double-layers formed by ionic liquids in the proximity of charged surfaces is of great practical importance, as this phase boundary governs charge transport, energy storage, and lubricating properties of interfaces. It is generally agreed that the relaxation ionic liquids bylayers at interfaces is significantly slower than in bulk, but how slow has remained unclear. Until now, it has been thought that relaxation times vary between a few seconds to several minutes, which we show here to be a very large underestimate. These contrasting views have been caused by experimentalists, in a search for ordered structural features, naturally focused on surface probe microscopy (atomic force microscopy) and x-ray reflectivity. While this was an obvious choice, both reflectivity and AFM are not free of technical limitations, and details on ordered near-surface structures have remained elusive. Here it is shown that the search for stable ionic liquid interfacial structures is greatly simplified if detection targets their specific electrical signatures. A first general and simple method capable of detecting the presence, or absence, of ordered bylayers is demonstrated by open-circuit potentiometry. This new method applies to several ionic liquids and electrode materials.

The endogenous electric fields associated with these ordered structures can potentially be harnessed for catalysis, providing a means of scaling electrostatic catalysis beyond single-

molecule STM experiments¹⁰ or for the development of safe supercapacitors with high energy storage, as well as in the emerging field of redox-enhanced electrochemical capacitors. Capacitors can be charged instantaneously, in fact, energy is stored by separating charged ions, while batteries require to be recharged over time. Despite, the number of available ionic liquids being astonishing, it was hard to know which would be suitable to be utilized in capacitors, but this study has unveiled an undemanding way to predict which ionic liquid is likely to be the best choice in an ionic liquid based capacitor.

Over and above these results, also provided means to predict and maximize endogenous electric fields. Polarizable molecular dynamics shows that when corrected for the effect of viscosity, the sum of cation and anion dipole moment projections along an external electric field is strongly correlated with the observed open circuit plateaus. This represents an excellent design parameter to predict the likelihood of forming stable ionic liquid bilayers having strong endogenous electric fields.

5.0 Abstract

Herein we demonstrate that ionic liquids can form long-lived double layers, generating electric fields detectable by straightforward open circuit potential (OCP) measurements. In imidazolium-based ionic liquids an external negative voltage pulse leads to an exceedingly stable near-surface dipolar layer, whose field manifests as long-lived (~1–100 h) discrete plateaus in OCP versus time traces. These plateaus occur within an ionic liquid-specific and sharp potential window, defining a simple experimental method to probe the onset of interfacial ordering phenomena, such as overscreening and crowding. Molecular dynamics modelling reveals that the OCP arises from the alignment of the individual ion dipoles to the external electric field pulse, with the magnitude of the resulting OCP correlated with the product of the projected dipole moment of cation with the ratio of predicted diffusion coefficient of cation and its volume. Our findings also reveal that a stable overscreened structure is more likely to form if the interface is first forced through crowding, possibly accounting for the scattered literature data on relaxation kinetics of near-surface structures in ionic liquids.

5.1 Introduction

Room-temperature ionic liquids (RTILs) are liquids with melting points below 100 °C, composed

solely of anions and cations.^{88, 186} They have been known for over a century,²¹⁷ but entered mainstream electrochemical research only in the middle of the 1990s, with the discovery of RTILs with stable anions.²¹⁸ Several such RTILs are now commercially available, and unlike conventional solvent-based electrolytes they can have exceedingly large electrochemical windows.^{88, 218, 219} This makes them valuable in applications ranging from energy generation and storage, to electrocatalysis.²²⁰⁻²²³ RTILs are typically comprised of large unsymmetrical ions²²⁴ that form what can be approximated as a coordinated network of ions,^{225, 226} with intermolecular forces tunable through changes in the molecular structure of the ions.^{227, 228} The unique nature of RTILs has important implications for the structure and dynamics of their interface with solid electrodes. While large molecular sizes and conformational flexibility prevent the formation of an ordered solid in the bulk,²²⁹ RTILs at interfaces are inherently ordered.²³⁰ Specifically, RTIL double-layer structures^{95, 231, 232} formed in the proximity of charged electrodes are of great practical importance as this phase boundary governs charge transport, energy storage and lubricating properties of electrode–RTIL systems.^{18, 223, 233} As the electrode is charged away from its potential of zero charge (PZC hereafter) in response to an external bias, counterions are enriched in a first ionic layer, where their lateral diffusivity is lower than in bulk.²³⁴ This charged first layer induces a second ionic layer of opposite charges, and so on, causing the potential profile to decay with damped oscillations. Despite a general consensus on the presence of an alternating out-of-plane arrangement of cation- and anion-rich layers,^{94, 235} the exact short-range ordering of RTILs near electrodes remains unclear.^{90, 216, 230, 236, 237} To date, experimental insights on the interface between RTILs and electrodes have relied on technically demanding atomic force microscopy,^{92, 94} X-ray reflectometry (XRR) experiments and Raman spectroscopy.^{93, 231} The lack of routine and straightforward measurements, suitable to probe the electrode–ionic liquid interface, is part of the reason why details of the near-electrode structure are still unclear. In the present work we address this problem by introducing open circuit potentiometry as a rapid and technically simple method to probe the interface between RTILs and electrodes.

Firstly, quantitative data on RTIL double layer dynamics, as well as data on the magnitude of the potential required to trigger the formation of ordered layers, are scattered. While solvation dynamics of bulk RTILs have a time scale between picoseconds and nanoseconds,²³⁸ the relaxation of RTILs at interfaces is significantly slower.²³⁹⁻²⁴² But how slow is unclear, with available data indicating relaxation times varying between few seconds to several minutes.^{239,}

²⁴² Secondly, while some authors argue that at potentials close to the PZC counter-ions will already overscreen electrode charges,^{90, 243} others advocate for such features occurring only at larger biases and persisting over large potential windows.²⁴⁴⁻²⁴⁶ For instance Yamamoto and co-workers put forward data in favour of RTILs over-screening at biases around +1.5 V,²³² while Uysal and co-workers observed this already at -0.4 V.²⁴⁷ Moreover, there is also the hypothesis of electrode “crowding” at large anodic and cathodic excursions,^{90, 91} as well as a debate around whether the thickness of the first ionic layer drops with increasing electrode charges,²⁴⁸⁻²⁵⁰ or whether it remains essentially unchanged.²⁵¹ Addressing these issues is important because the phase boundary ultimately governs how energy is stored in the electric field of electrochemical devices, such as capacitors,^{223, 252, 253} and how accessible the electrode surface is towards charge-transfer reactions. The latter is emerging as a viable strategy for controlling the balance between inner- and outer-sphere competing electron transfer reactions, both for electrocatalysis and electrosynthesis.^{254, 255} Moreover, recent computational work has shown that ionic liquids that are ordered as a result of exposure to external electric fields can generate strong internal electric fields that electrostatically catalyze chemical reactions, even when the external field is removed.⁷² Experimental confirmation of these fields, and measurements of their lifetime, would be the first step toward harnessing these electrostatic effects in chemical synthesis.^{8, 256-258} By means of open-circuit potentiometry we demonstrate that at electrode surfaces RTILs assume stable ordered structures, and generate significant endogenous electric fields that persist for days after an external potential is removed.

5.2 Results and Discussion

5.2.1 Interfacial Dynamics of [EMIM][EtSO₄]. Prior to studying the response of RTILs to an applied potential, we conducted a search of the minimum of the electrode–RTIL capacitance as a function of the electrode potential. This minimum provides a baseline reading for the disordered RTILs against which the ordered RTILs could be compared, and it was obtained through electrochemical impedance spectroscopy (EIS). The potential where capacitance reaches a minimum generally coincides with the electrode PZC,²⁴⁹ and EIS measurements with platinum electrodes indicate that this is close to -0.6 V vs Fc/Fc⁺ (Figure 5.1a). The accumulation of counter-ions at the electrode surface is likely to occur in both bias directions,²¹⁶ implying that the positive and negative branches of the capacitance–potential curve around the PZC are delimiting bias regions where the liquid side of the interface is enriched of either anions

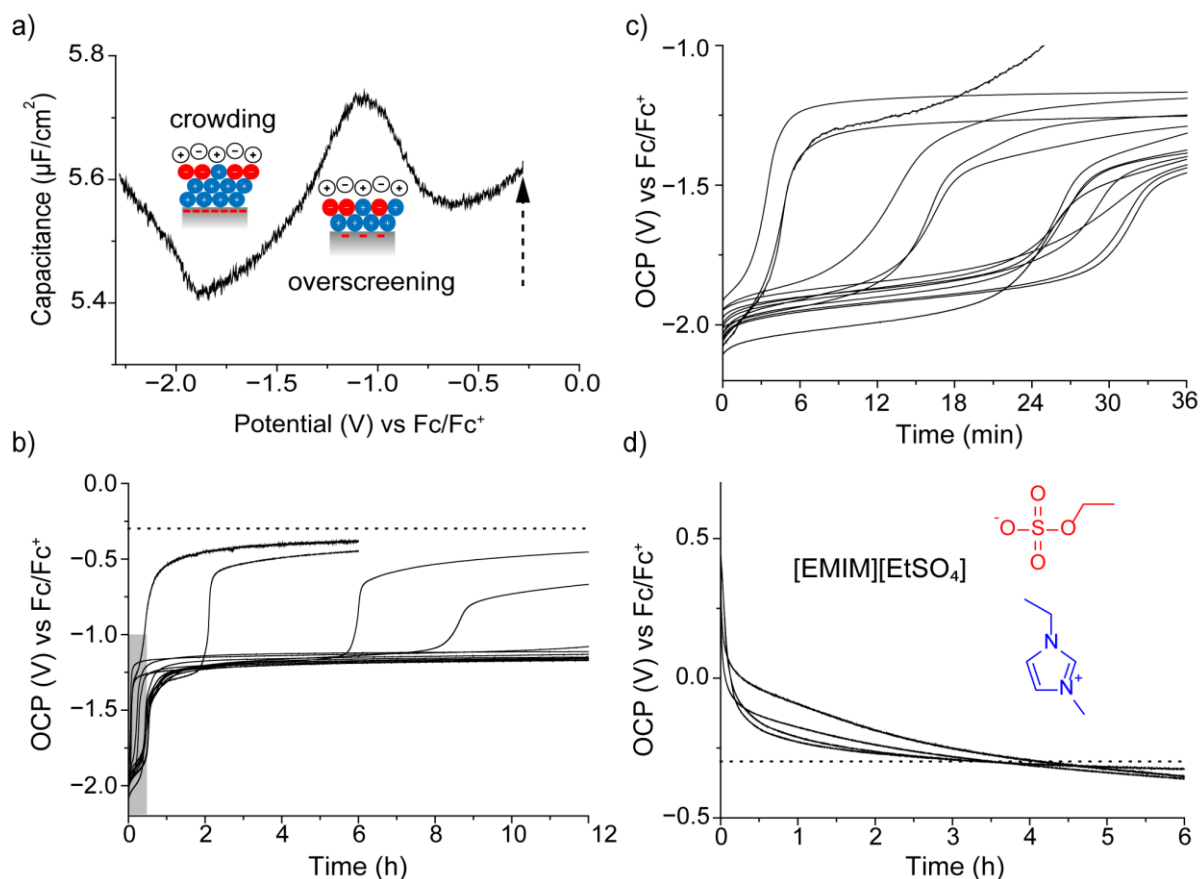


Figure 5.1. (a) Representative electrochemical impedance spectroscopy (EIS) capacitance–potential plot, with a schematic depiction of the onset of overscreening and crowding in correspondence of local capacitance maximum and minimum, respectively (platinum disk in [EMIM][EtSO₄]). The vertical arrow indicates the system initial OCP value, prior to any external biasing. Representative OCP–time measurements for platinum electrodes immersed in [EMIM][EtSO₄] recorded after the application of negative (b,c), and positive (d) potential steps (60 s, ± 2.0 V relative to the initial OCP). Dotted horizontal lines represent the average initial OCP. (b) Negative bias excursions lead to very stable OCP plateaus located between -1.1 V and -1.3 V vs Fc/Fc⁺. (c) A relatively short-lived and more negative OCP plateau, found between -1.9 V and -2.0 V, is evident upon close inspection of the first 30 minutes of the OCP relaxation data. The grey shaded area in (b) indicates the data region shown in (c).

or cations. Prior to exposure to an applied potential, the rest open circuit potential (OCP) was generally only slightly positive of the PZC. After a short (60 s) potential step, equal or smaller than ± 1.0 V away from this initial OCP (dashed arrow and dashed horizontal lines in Figure 5.1) we were only able to record a rapid, <30 minutes, equilibration of the electrode potential back to its initial rest value (Figure S1, Appendix 3). In this respect an electrode–RTIL interface, such as platinum immersed in [EMIM][EtSO₄], behaves qualitatively similar to the interface formed between electrodes and conventional molecular solvent-based electrolytes, such as Bu₄NClO₄

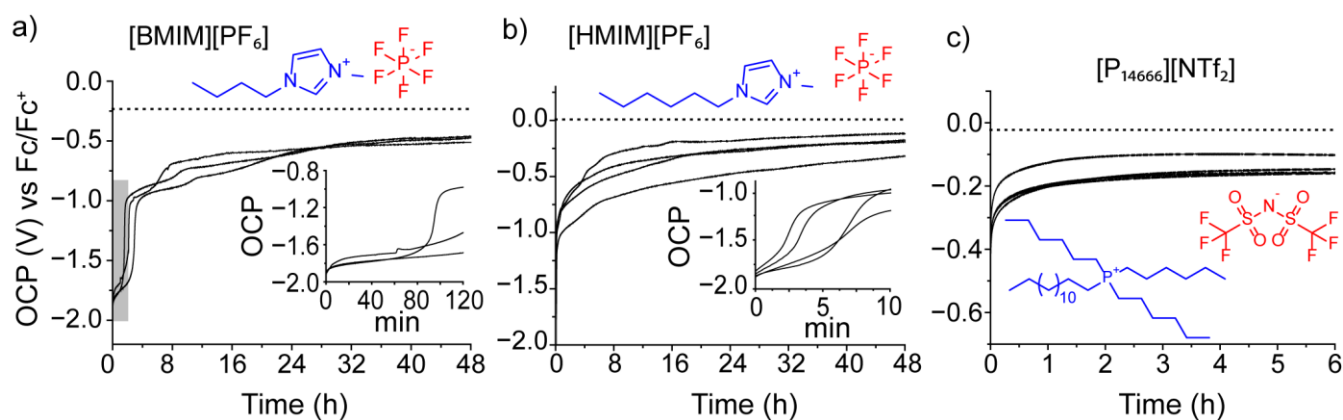


Figure 5.2. Representative OCP–time measurements acquired with platinum electrodes immersed in [BMIM][PF₆] (a), [HMIM][PF₆] (b), and in [P₁₄₆₆₆][NTf₂] (c) after a negative potential step (60 s). The potential step was of -2 V away from the electrode initial rest OCP (dotted horizontal lines). The grey shaded areas in (a,b) indicate the data plotted as figure insets. Data in (a) reveal the onset of crowding in [BMIM][PF₆] as an OCP vertical step located between -1.7 V and -1.8 V. The overscreening OCP signature is found between -0.9 V and -1.0 V. (b) OCP–time data for [HMIM][PF₆] with evidence of discernible OCP plateaus at ~ -1.7 V and poorly defined plateaus between -1.0 V and -0.75 V

in acetonitrile (Figure S2, Appendix 3). Surprisingly, the experimental OCP relaxation was rapid despite the magnitude of the cathodic step (-1.0 V) being more than sufficient for the interface to reach its capacitance maximum (~ -1.1 V vs Fc/Fc⁺, Figure 5.1a). It is therefore probable that the -1.0 V step triggered the formation of an ordered overscreened interface,^{91, 214} but this structure did not persist once the external bias was removed. As ordering will progressively increase with bias,²³² and since capacitance drops under fully occupied conditions,²³⁵ the presence of a minimum in the negative branch of the capacitance–potential curve at ~ -1.9 V vs Fc/Fc⁺ (Figure 5.1a) suggests the possibility of a thicker first layer of counter-ions forming at this more negative bias. We consequently measured the OCP relaxation that followed a cathodic step of -1.5 V from the initial rest potential. Once again, this bias is sufficient for the system to reach the capacitance minimum (crowding), but OCPs still relaxed asymptotically and very slowly (~ 3 h).

A remarkably different response was observed when the electrode potential was disturbed away from its rest potential by a potential step as large as -2.0 V. Applying such a large negative pulse was effective in locking the interface in a stable ‘cation-rich’ configuration. This cation-rich ordered configuration manifested as an OCP plateau between -1.1 V and -1.3 V vs Fc/Fc⁺, which persisted rarely less than 6 h (Figure 5.1b), and occasionally up to four days (Figures

S3–S6, Appendix 3). Importantly, the position of these long-lived OCP plateaus matches the onset of overscreening as assessed by EIS (Figure 5.1a). A closer inspection of the first part of the time-resolved OCP measurements revealed the consistent presence of a more negative plateau between -1.9 V and -2.0 V (Figure 5.1c). The position of this initial plateau closely matches the onset of crowding in the EIS data (Figure 5.1a). These initial cation-rich surface structures persist only for short times, from few seconds to ~ 30 minutes, which is of the same order of magnitude of relaxation times obtained for ionic liquid systems through much more complex techniques.^{239, 247} Chemisorption reactions, potentially triggered by the cathodic pulse, are an unlikely cause for the plateaus. For instance, while very gentle vibrations of the electrochemical cell did not disturb an overscreening OCP plateau, extracting and re-immersing the electrode in the liquid was enough to reset the initial OCP (Figure S6, Appendix 3). Molecules chemisorbed on surfaces are not so easily removed.²⁵⁹ Further evidence against chemisorption is the lack of a change in electrode active area following the pulse (Figure S7, Appendix 3). The existence of such negative plateaus is in accordance with the theory of Kornyshev and co-workers, where multiple layers of counter-ions balance surface charges (see schematics in Figure 5.1a).^{90, 260} Interestingly, only when the metal charge density has sufficiently decreased, the double layer can then adjust to an overscreening organization, where just a monolayer of counter-ions balances the surface charge (Figure 5.1a). In brief, implicit from our data is that a stable overscreened arrangement forms if the system is first forced into crowding. On the other hand, OCP relaxation responses following positive potential steps were featureless: no plateaus were detected and OCPs relaxed asymptotically (Figure 5.1d). A similar conclusion was previously reached by AFM data, where the force required for an AFM tip to push through the first ionic liquid layer was significantly larger for negative biases.^{216, 251} It was therefore not surprising that the occurrence of these negative OCP signatures was largely independent of the nature of the anion, with for instance [EMIM][EtSO₄] behaving very similarly to [EMIM][BF₄] (Figure S8, Appendix 3). We have not tested [EMIM][PF₆], because, in spite of its commercial availability, it is not liquid at room temperature.

5.2.2 Comparison of Different RTILs. To define the generality of OCP measurements in probing interfacial dynamics we then proceeded to test a range of RTILs with different cations. Imidazolium cations with longer alkyl side chains have higher permanent dipole moments, and this in turn increases the strength of their electrostatic interaction with the applied electric field.

To illustrate this trend experimentally, we measured OCP relaxations in RTILs containing butyl and hexyl substituents on the imidazolium ring. Data in Figure 5.2a,b show that after an anodic step the relaxation behavior of [BMIM][PF₆] and [HMIM][PF₆] is asymptotic and indistinguishable to that of the smaller [EMIM][EtSO₄] in Figure 5.1d. After a cathodic excursion, both [BMIM][PF₆] and [HMIM][PF₆] form negative plateaus, but especially in the case of [HMIM][PF₆], these OCP signatures are not as long-lived and well-defined as those observed with [EMIM][EtSO₄] (Figure 5.2a,b). OCP signatures for overscreening are still clearly visible for both [BMIM][PF₆] and [HMIM][PF₆], although shorter in the latter (insets in Figure 5.2). Crowding features, in the OCP–time plot, are clearly distinguishable only for [BMIM][PF₆]. Extending the duration of the cathodic step, from one to six minutes, did not alter the dynamics of the OCP relaxation (Figure S9, Appendix 3). The ability to form ordered dipolar structures disappears for larger cations, such as for example with [P₁₄₆₆₆][NTf₂] (Figure 5.2c), and despite previous reports suggesting that a more localized charge leads to stronger surface interactions,²¹⁵ pyrrolidinium-based RTILs did not generate clear OCP signatures ([BMPyrr][NTf₂], Figure S10, Appendix 3).

5.2.3 Effect of Electrode Material. There is also experimental evidence of a relationship between ordering on the liquid side of the interface and the mobility of surface atoms of the electronic conductor. Similarly to platinum, OCP plateaus were also observed on gold surfaces, but surprisingly they were not detected on covalent electrode materials of large self-diffusion activation energy,²⁶¹ such as silicon and carbon (Figures S11–S13, Appendix 3). Further, plateaus recorded with gold electrodes were located at less negative voltages than for platinum, between –0.6 V and –0.7 V, an observation for which we do not yet have a satisfactory explanation (Figure S14, Appendix 3). Differences in double-layer structures for a given RTIL between platinum and gold are not unprecedented,²⁶² but at present we can only speculate that a less negative OCP plateau for ordered dipolar structures on gold may relate to a difference in surface diffusivity between the two metals.²⁶³

5.2.4 Polarizable Molecular Dynamics Studies. To understand these results, we conducted polarizable molecular dynamics ²⁴⁶ simulations for [BMIM][PF₆], [EMIM][EtSO₄], and [HMIM][PF₆] in the presence and absence of an applied electric field of 0.2 V/Å along the z-axis. Imidazolium-based ionic liquids are known to exhibit strong hydrogen bonding between

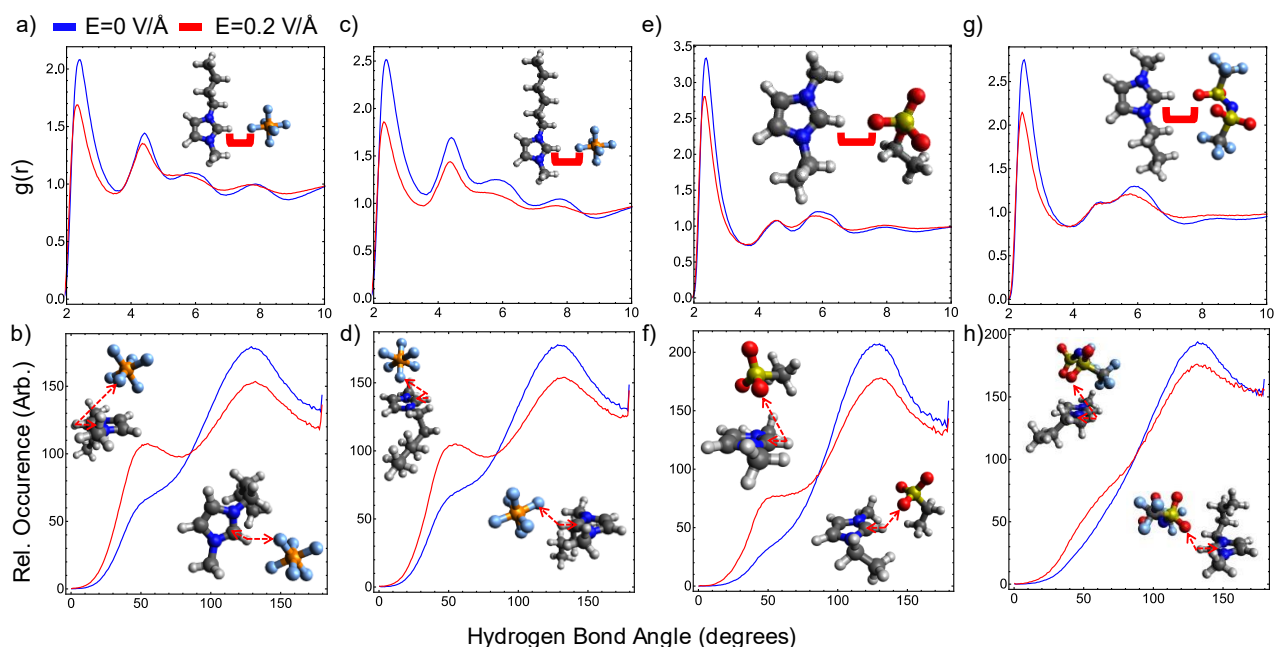


Figure 5.3. Normalized radial distribution functions of $(C_2)H-F$ distances in (a) [BMIM][PF₆] and (c) [BMIM][PF₆] and $(C_2)H-O$ distances in (e) [EMIM][EtSO₄] and (g) [BMIM][NTf₂]. Cone-corrected angular distribution functions of C_2-H-F angles in (b) [BMIM][PF₆] and (d) [HMIM][PF₆] and C_2-H-O distances in (f) [EMIM][EtSO₄] and (h) [BMIM][NTf₂]. In all panels, blue lines denote behavior without an external field, and red lines denote behavior in an external 0.2 V/Å field. Insets in (b), (d), (f) and (h) are motifs representative of the two main peaks at 55° and 130°.

the C_2-H bond on the imidazolium ring and electronegative atom on the anions.²⁶⁴ Radial distribution functions (RDFs, Figures 5.3a and 5.3c) of the $(C_2)H\cdots F$ interionic distances indicate the significant changes in the short and long-range order of both PF₆-based ionic liquids upon the application of the electric field. [EMIM][EtSO₄] and [BMIM][NTf₂] demonstrated smaller structural changes in the $(C_2)H\cdots O$ interionic distances (Figures 5.3e and 5.3g), suggesting that the constituent ions do not require a significant change in the bulk arrangement to align with the electric field. Angular distribution functions (ADFs) of the $C_2-H\cdots X$ bond (where X is either F (PF₆⁻) or O (EtSO₄⁻ and NTf₂⁻; Figures 5.3b, 5.3d, 5.3f and 5.3h) clearly identify that the hydrogen bond in all three ionic liquids undergoes a change from a more directional hydrogen-bond type (a peak at 130°) to a non-directional interaction above the imidazolium ring (a peak at 55°). The occurrence of the latter strongly suggests that ionic liquid ions re-align themselves in the electric field. Some anions become located right above the imidazolium ring, which corresponds to a typical interionic interaction mode in these ILs.

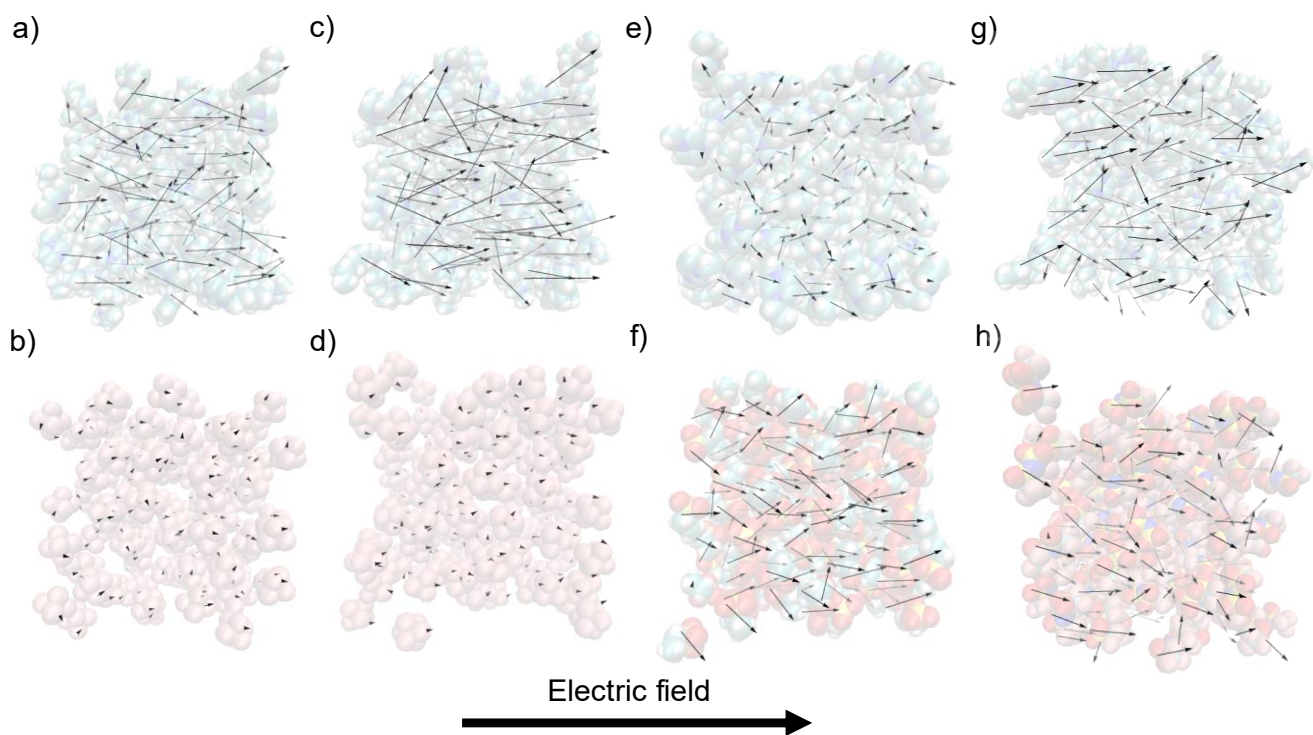


Figure 5.4. Visualizations of dipole moments of ions (a) BMIM⁺ and (b) PF₆⁻ in [BMIM][PF₆], (c) HMIM⁺ and (d) PF₆⁻ in [HMIM][PF₆], (e) EMIM⁺ and (f) EtSO₄⁻ in [EMIM][EtSO₄] and (g) BMIM⁺ and (h) NTf₂⁻ in [BMIM][NTf₂] under a 0.2 V/Å electric field in molecular dynamics simulations. Dipole vector lengths are calibrated to 1 Å/D.

The strong alignment of the ion dipole moments with the field is presented in Figure 5.4. Ion dipole moments were calculated with centre-of-mass reference points, with magnitudes equivalent to the ‘charge arm’ calculated with respect to center of charge.^{265, 266} The alignment is particularly stark for ions with non-zero dipole moments such as the imidazolium cations, EMIM⁺, BMIM⁺ and HMIM⁺, and the EtSO₄⁻ and NTf₂⁻ anions. The PF₆⁻ anion that does not have a nominal dipole moment, when calculated in isolation, becomes strongly polarized in the presence of other ions, with the dipole moment also becoming aligned in the field. The alignment of the individual ion dipole moments is not perfect due to strong intermolecular interactions between ionic liquid ions in the range of 320 to 420 kJ mol⁻¹ per single ion pair.²⁶⁷

The deviation from the field direction was estimated by calculating the average θ angle between the apparent dipole moment of each ion and the direction of the field (Figures 5.5a and 5.5b). It is not surprising and rather reassuring that, in the absence of the electric field, the average θ value was observed to be $\sim 90^\circ$ for all ions. This indicates a random distribution, with

cone-corrected angular distributions in the Supplementary Information (Figure S15, Appendix 3) serving as further proof. The situation changes dramatically as the field is introduced, with the average θ value falling between 35.6° for EtSO_4^- and 49.4° for EMIM^+ . Further analysis reveals that θ only weakly correlates with the dipole moment of the ions, smaller θ values loosely corresponding to larger dipole moments. In addition to the dipole orientation, each ion dipole moment was projected along the external field axis, μ_z , (Figures 5.5c and 5.5d). All ions besides PF_6^- exhibit a strong projection ranging from 2.24 D for EMIM^+ to 9.82 D for HMIM^+ . This is due to the strong permanent dipole moments present in the imidazolium cations, the EtSO_4^- and the NTf_2^- , whereas the PF_6^- anion does not have a permanent dipole moment due to symmetry. The projected induced dipole moment of PF_6^- anions is not negligible, averaging 0.53 D for both $[\text{BMIM}][\text{PF}_6]$ and $[\text{HMIM}][\text{PF}_6]$. The alignment of these ion dipoles to the applied electric field induces an opposing internal electric field that, we hypothesize, is responsible for the OCP observed when the external field is removed. The process of the ion re-alignment is also accompanied by cations moving to the anode and anions moving to the cathode. In our MD simulations diffusion coefficients of cations and anions increased by four orders of magnitude on average when the field was applied (see Tables S3 and S4, Appendix 3). BMIM^+ and HMIM^+ cations in the PF_6^- -based ionic liquids were found to diffuse slightly faster than cations in $[\text{EMIM}][\text{EtSO}_4]$ and $[\text{BMIM}][\text{NTf}_2]$, which can be explained by stronger hydrogen bonding preventing ions from moving freely in the latter. We also confirmed that the NTf_2^- anion maintained its *trans* configuration throughout the entire simulation in an external electric field (Figure S16, Appendix 3). The calculated diffusion coefficients, ranging from 3.7×10^{-7} to $2.5 \times 10^{-6} \text{ m}^2 \text{ s}^{-1}$, suggest that ions can easily move to electrodes, thus leading to crowding of cations at the anode as shown in Figure 5.1a. It was also noticed that the mobility of cations correlated with the projected dipole moment and the strength of intermolecular interactions within an ionic liquid. The ability of cations with a larger dipole moment and weak hydrogen bonding to anions to strongly re-align with an electric field is reflected in their increased diffusion coefficient. Since ions of opposite charge move in opposite directions in an electric field, it is not surprising that the projected dipole moment sum of the cation and anion did not correlate with the experimental OCP plateaus (Figure S17, Appendix 3). It is well known that cations will form a crowding layer next to the anode, thus creating a medium of different viscosity at the interface compared to that of the bulk of an ionic liquid.

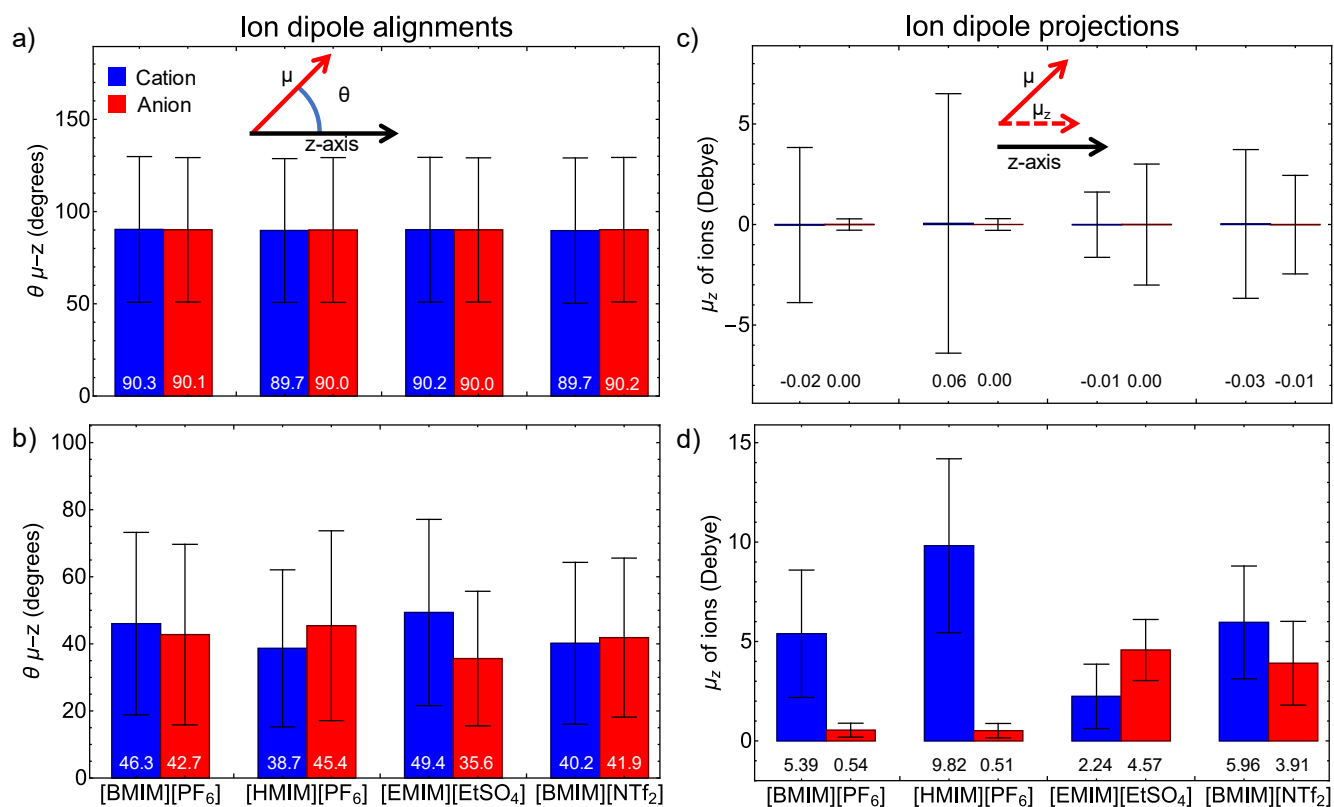


Figure 5.5. Average angles between ionic dipole moments and the z-axis (a) without an external electric field and (b) in an external field of 0.2 V/Å along the z-axis. Panel (c) displays mean ion dipole projections along the z-axis without an external electric field, and (d) in an external field of 0.2 V/Å oriented along the z-axis. Error bars in (a)–(d) represent standard deviations.

The density of coverage also depends on the cation size, with larger cations creating less dense coverage. Therefore, it was hypothesized that the average projected dipole moment of cation corrected for changed viscosity at the electrode interface and cation size should correlate with the OCP. Since viscosity is inversely proportional to diffusion coefficient, the product of the projected dipole moment of cation with the ratio of predicted diffusion coefficient of cation and its volume gives a strong correlation to the observed OCP plateaus (Figure 5.6) with an R^2 of 0.907. This correlation suggests that the mobility of cations in an electric field plays a key role in the formation of a stable crowding interface at the anode resulting in negative OCP plateaus. Lower mobility of EMIM⁺ and BMIM⁺ in an electric field in ionic liquids with strong hydrogen bonding, reflected in small structural changes, allows for cations to form a more stable crowding interface, thus exhibiting the lower OCP plateaus (Figures 5.1c and S18, Appendix 3). This conclusion is further reinforced by the absence of a clear plateau in [P₁₄₆₆₆][NTf₂] (Figure 5.2c),

in which the cation displays a negligible dipole moment and hence, very low mobility.^{265, 268} The presented MD simulations thus confirmed that ionic liquid ions are able to reorient their dipole moments along the external electric field without sacrificing their bulk structure to a great extent.

5.3 Conclusions

We have described a simple and straightforward method to detect order and electric fields of organized and long-lived ionic liquid double layers by open circuit potentiometry. We show that

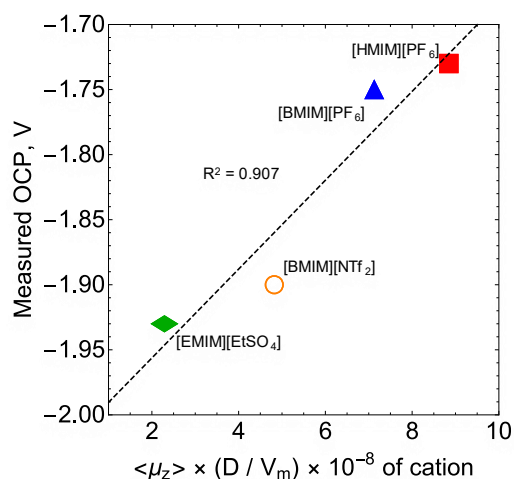


Figure 5.6. Correlation of measured OCP values (crowding) of ionic liquids against the product of average dipole moment projections and diffusion coefficients in the electric field, divided by cation molar volumes.

overscreened and crowded near-electrode structures are detectable as negative open-circuit signatures occurring within sharp potential windows, validating ionic liquids double layer models proposed by Kornyshev and co-workers.⁹⁰ Crowding manifests as negative OCP plateaus, which survive up to several tens of minutes. This structure rearranges into an overscreened double layer, lasting up to several days, where just a monolayer of counter-ions balances the surface charge. These fields can potentially be harnessed for the electrostatic catalysis of chemical reactions,^{10, 25, 72} for the development of safe supercapacitors, and can find applications in the emerging field of redox-enhanced electrochemical capacitors.^{269, 270} The presence of a stable blocking layer on the electrode may limit side reactions in electrosynthesis, such as reducing hydrogen evolution in the presence of trace water. Further, slow double layer dynamics in RTILs are known to manifest in voltammetry,²³⁹ and to introduce hysteresis in capacitance measurements²⁴¹; here we show that RTILs forming dense dielectric layers can be rapidly identified by OCP measurements. Polarisable molecular dynamics simulations demonstrated the loss of short- and long-range order in [BMIM][PF₆], [HMIM][PF₆] and to a lesser extent, [EMIM][EtSO₄] and [BMIM][NTf₂] under an external electric field. The ionic liquid ions were confirmed to align their dipole moments with the external field. The alignment of ions was found to depend on presence of strong hydrogen bonding in ionic

liquids. Cations with larger projected dipole moments were also found to have increased mobility in an electric field. The projected dipole moment of the cation, corrected for its volume and mobility in an electric field, correlate well with the observed crowding OCP plateaus, suggesting that increased dipole moment strength and mobility prevent cations from forming a more stable crowding interface. This represents an excellent design parameter to predict the likelihood of forming stable ionic liquid bilayers having strong endogenous electric fields.

5.4 Experimental Section

5.4.1 Materials. Unless noted otherwise, all reagents were of analytical grade and utilized without further purification. Milli-Q™ water (>18.2 MΩ cm) was used for cleaning procedures and to prepare electrolytic solutions. 1-Ethyl-3-methylimidazolium ethyl sulfate (≥95%, Sigma, [EMIM][EtSO₄]), 1-butyl-3-methylimidazolium hexafluorophosphate (≥97% Sigma, [BMIM][PF₆]), 1-hexyl-3-methylimidazolium hexafluorophosphate (≥97%, Sigma, [HMIM][PF₆]), trihexyltetradecylphosphonium bis(trifluoromethylsulfonyl)imide (>98%, Iolitec, Germany, [P₁₄₆₆₆][NTf₂]), 1-butyl-1-methylpyrrolidinium bis(trifluoromethylsulfonyl)imide (99.5%, Iolitec, Germany, [BMPyrr][NTf₂]), 1-ethyl-3-methylimidazolium tetrafluoroborate (>98%, Iolitec, Germany, [EMIM][BF₄]), 1-butyl-3-methylimidazolium bis(trifluoromethylsulfonyl)imide (99%, Iolitec, Germany, [BMIM][NTf₂]), acetonitrile (99.5%, VWR chemicals, USA, MeCN) and tetrabutylammonium perchlorate (≥98%, Sigma, Bu₄NClO₄) were used as received. The water content of all the ionic liquids used in this work was estimated by Karl Fisher titration (Mettler-Toledo C20S Compact Coulometer, Honeywell HYDRANAL™ Coulomat AG reagent, Merck Water Standard 0.1%, USA), and with at least three samples measured for each ionic liquid. The water content readings between samples of the same ionic liquid varied less than 50 ppm, and the average values were: [EMIM][EtSO₄], 930 ppm; [EMIM][BF₄], 500 ppm; [BMIM][PF₆], 490 ppm; [HMIM][PF₆], 745 ppm; [BMPyrr][NTf₂], 125 ppm; [P₁₄₆₆₆][NTf₂], 1215 ppm; [BMIM][NTf₂], 100 ppm.

5.4.2 Electrochemical Methods. All electrochemical measurements were carried out using a small (~4 mL) single-compartment three-electrode glass cell. Cyclic voltammetry (CV) and open circuit potentiometry (OCP) experiments were performed on an Emstat3 Blue potentiostat (PalmSens BV, Houten, Netherlands). Electrochemical impedance spectroscopy (EIS)

experiments were carried out using a CH 650D electrochemical analyser (CH Instruments, Austin, USA), imposing an AC potential amplitude of 15 mV (root mean square) over the DC offset (E_{dc}) of the working electrode. The AC frequency was varied between 0.1 Hz and 0.1 MHz. Reproducibility of the EIS data was highest at 1 kHz, as also observed by others,^{249, 271, 272} and therefore capacitance–voltage data in this work refer only to this frequency. The E_{dc} offset of the working electrode was ramped starting from the system's initial OCP and moved towards the cathodic limit of the sweep. The sweep rate was 40 mV/s. This sampling approach is common practice for EIS experiments in molten salts.²⁷³ The out-of-phase impedance (Z'') was used to estimate the electrode capacitance ($C = 1/(\omega Z'')^{-1}$). For all the electrochemical experiments the cell was loaded with a small sample (10 mL) of the ionic liquid, which was previously degassed by means of bubbling it with high-purity argon gas (99.997%, Coregas) for at least 20 min. Platinum wire was used as working and counter electrode for both CV and OCP experiments (0.5 mm diameter wire, 99.99+%, Goodfellow Cambridge Limited), while EIS data were recorded at platinum disk electrodes (eDAQ, ET052, 3 mm diameter). The size of the counter electrode was in excess of twenty times that of the working electrode. A plastic body silver/silver chloride “leakless” setup was used as the reference electrode (eDAQ, part ET072-1, 3.4 M aqueous potassium chloride as filling solution). The active area of the platinum wire working electrodes was either 0.28 cm² or 0.63 cm², as determined from the refinement of a E model (DigiElch-Professional v7, ElchSoft) against experimental voltammograms measured in 1.0×10^{-1} M MeCN/Bu₄NClO₄ and in the presence of 1.0×10^{-3} M of ferrocene (Fc in shorthand hereafter, Figures S19 and S20, Appendix 3). The active surface area of the platinum disk was 0.08 cm² (Figure S21, Appendix 3). The size of the working electrode had no measurable effect on the OCP versus time results. The reference electrode was calibrated before and after each experiment against the apparent formal potential of the ferrocene/ferricenium couple (Fc/Fc⁺) measured with the platinum disk using 1.0×10^{-3} M Fc in 2.0×10^{-1} M MeCN/Bu₄NClO₄, and unless specified otherwise potentials are reported against the Fc/Fc⁺ couple. Electrochemical experiments were performed at room temperature (23 ± 2 °C) inside a gas-tight acrylate box (Molecular Imaging, model GB306, USA) kept under nitrogen atmosphere. The nitrogen line was fitted with a Drierite™ gas drying unit (Sigma). Working and counter platinum electrodes were cleaned prior to the experiments by means of multiple cyclic voltammetry scans in aqueous 0.5 M sulfuric acid, ramping the potential between –0.2 and 1.0

V at a voltage sweep rate of 0.05 V s^{-1} . Control experiments with gold, carbon and silicon surfaces were done using, respectively, gold wire of 0.25 mm diameter (99.999+%, Goodfellow), glassy carbon plates of 12.7 mm diameter (TED PELLA, Inc.), and highly doped monolayer-coated oxide-free silicon wafers (prime grade, CZ, 111-oriented ($\pm 0.5^\circ$), 500 μm thick, single-side polished, boron-doped, 0.007–0.013 $\Omega \text{ cm}$, from Siltronix, S.A.S, Archamps, France). The gold wire was cleaned prior to the experiments by means of cyclic voltammetry in aqueous 50 mM sulphuric acid (sweeps in the -0.2 to 1.0 V range, at 0.05 V s^{-1}). Glassy carbon electrodes were polished to mirror-like finish with alumina slurry (0.05 μm , eDAQ, ET033) on a polishing cloth (Struers). After the polishing step, the electrodes were sonicated in water for one minute.

Hydrogen-terminated silicon electrodes were modified with an organic monolayer of 1,8-nonadiyne (98%, Sigma-Aldrich) in order to passivate the oxide-free surface against anodic decomposition. The procedure follows minor modification of literature procedures.^{36, 39, 274} In brief, silicon wafers ($1 \times 1 \text{ cm}$) were kept for 30 min in piranha solution (100°C , a 3:1 (v/v) mixture of concentrated sulfuric acid and 30 % hydrogen peroxide), then rinsed with water, and etched for 10 min in deoxygenated aqueous ammonium fluoride (40 wt. %). A small amount of ammonium sulfite was added to the etching solution as oxygen scavenger. Hydrogen-terminated silicon samples were then rinsed with water, dichloromethane, dried under a flow of nitrogen, and then covered with a deoxygenated sample of 1,8-nonadiyne. The silicon sample was then kept under nitrogen for 2 h at a distance of approximately 200 mm from a 312 nm UV source (Vilber, VL-215.M). The chemically passivated silicon electrodes were rinsed with dichloromethane, rested for 24 h in a sealed vial under dichloromethane at $+4^\circ\text{C}$, and then blown dry under a nitrogen stream before being analyzed. The silicon electrodes were mounted in a three-electrode and single-compartment polytetrafluoroethylene (PTFE) custom cell where a circular Viton gasket defined the geometric area of the working electrode to 0.28 cm^2 . Ohmic contact between the back of the silicon sample and a copper plate was achieved by gently scribing the back of the electrode with emery paper before applying on it a small amount of gallium–indium eutectic. The topography of both silicon and carbon samples was estimated before the electrochemical experiments by atomic force microscopy (AFM). AFM data were acquired on a Park NX10 (Park Systems Corporation, Suwon, Korea). The scanning was conducted in True Non-Contact™ mode. The silicon sample was fixed on a steel plate using

carbon tape, and then mounted on the AFM magnetic sample holder. Imaging was done in air, at room temperature, using n-type silicon AFM probes (OCML-AC160TS, Olympus Corporation, Tokyo, Japan) with a nominal resonance frequency of 300 kHz and a spring constant of 26 N/m. The image size was set to $5 \times 5 \mu\text{m}$, the resolution to 256 points/line, and the scan rate to 1 Hz (Figures S22 and S23, Appendix 3). Prior to the OCP-time measurements, electrodes were left to equilibrate in contact with the ionic liquid sample until the first derivative of the OCP versus time traces (dV/dt) dropped below $|0.0001|$. This was normally achieved within five minutes of immersing the electrodes in the liquid (Figures S24–S27, Appendix 3). After this initial stabilization phase, a potential step of variable magnitude and sign was applied to the working electrode. Unless specified otherwise the duration of this potential pulse was 60 s. OCP recording was resumed immediately after the pulse. The time that elapsed between the anodic, or cathodic, excursion and the resuming of the OCP measurement was less than 2 s.

5.4.3 Computational Methods. The CL&Pol²⁷⁵⁻²⁷⁷ force field optimized for ionic liquids was enforced on periodic simulation boxes containing 125 ion pairs of [BMIM][PF₆], [HMIM][PF₆] and [EMIM][EtSO₄]. Where necessary, k_{ij} parameters were calculated (See Table S1, Appendix 3). All systems had initial structures produced with PACKMOL,²⁷⁸ and were initially equilibrated for 5 ns in an NpT ensemble, proving to be ample time for each system's density to converge (Figure S28, Appendix 3). Average densities from the last nanosecond of equilibration were within 5% of experimental values (see Table S2, Appendix 3), with corresponding average volumes enforced for 10 ns NVT production runs. Separate NVT runs from identical restart files were performed, with the absence or presence of a 0.2 V/Å external field along the positive z-axis direction. Initially, all systems were allowed 0.1 ns to deform to the average box volume, and a further picosecond to align with the electric field where necessary before the production run. In all simulations, Nose-Hoover temperature grouped thermostats and barostats were used, with atoms thermalized to 353 K and drude particles thermalized to 1 K, and a 1 fs timestep was used in all simulations. The LAMMPS²⁷⁹ software package was used to run all simulations, utilizing the USER-DRUDE module. Trajectory analysis was performed using TRAVIS^{280, 281} software, with dipole moments calculated with force field charges, and each ion's centre of mass as a reference point. The magnitude of these calculated dipole moments are also known as the ion's 'charge arm.' Volume of cations was calculated based on the previously

published methodology.²⁶⁸ The volume for EMIM⁺ was taken from that work²⁶⁸ and the volumes of BMIM⁺ and HMIM⁺ cations are given in Table S5, Appendix 3. The diffusion coefficients were measured as the slope of the mean standard deviation (MSD) of each ion's centre of mass. All contributions of each ion across the production runs were considered, with maximum correlation times set to 30% of the trajectory. Correlation times of 1.5 to 3.0 ns were sampled, and produced linear fits of correlation coefficients of at least 0.99 in all cases. These analyses were performed with TRAVIS.

Chapter 6: Separating convective from diffusive mass transport mechanisms in ionic liquids by redox pro-fluorescence microscopy

Chapter 2 and **Chapter 4** presented the ECL of fireflies' luciferin. In **Chapter 2**, in electrolyte-supported molecular solvents (along with the spectral tuning of luciferin), and then, in **Chapter 4** in RTILs. Moreover, the fluorescence of the final product of the luciferin ECL has been briefly mentioned. Pro-fluorescence dyes are widely used in imaging, from chemistry to medicine and compared to ECL, fluorescence allows a higher emission intensity and better reproducibility. In **Chapter 5**, a new straightforward way to probe the EDL in RTILs was proposed. Combining the findings presented in the previous chapters, the idea was to study the EDL in RTILs using luciferin ECL. However due to the low yields of ECL in RTILs (as shown in **Chapter 4**) fluorescence microscopy was employed.

In **Chapter 6**, in the form of Paper 4 ([Mattia Belotti](https://doi.org/10.1021/acs.analchem.3c00168), Mohsen M. T. El-Tahawy, Marco Garavelli, Michelle L. Coote, K. Swaminathan Iyer, and Simone Ciampi. Separating Convective from Diffusive Mass Transport Mechanisms in Ionic Liquids by Redox Pro-fluorescence Microscopy *Anal. Chem.* **2023**, 95, 26, Pages 9779–9786, DOI <https://doi.org/10.1021/acs.analchem.3c00168>), the fluorescent of oxyluciferin is exploited to locally measure the diffusivity in RTILs during electrochemical process. The central feature of most electrochemical studies is a measurement of reactant and product diffusivity. Information on diffusion coefficients is generally obtained by modelling current transients and cyclic voltammetry data. Such indirect measurements however lack spatial resolution, can only provide an “average” diffusivity, and most importantly, are only accurate if mass transport by convection is negligible. Detecting and accounting for adventitious and localized convective disturbances in viscous and wet solvents, such as ionic liquids, remains an unmet technical challenge. Addressing this challenge requires developing experimental systems capable of visualizing and tracking the diffusion of electrode products with spatiotemporal resolution. In this chapter, an optical method to track the mass transport of electrode products in wet or dry, quiescent, or turbulent, ionic liquid–electrode interfaces. The electrochemical conversion of luciferin into oxyluciferin has been applied to demonstrate a proof-of-principle optical measurement of superoxide radical anions diffusion coefficients. The homogeneous reaction

of pro-fluorescent luciferin with electrochemically generated superoxide yields fluorescent oxyluciferin: a visual handle on mass transport. Herein, it is shown that in viscous solvents, where mass transport by convection is likely to interfere with diffusion for instance due to gas evolving side reactions, diffusion coefficients are likely to be overestimated by at least one order of magnitude. Such large errors are prevented through this new optical measurement of diffusivity. This method can also be applied to the study of reactive oxygen species lifetimes, near-electrode double layer order and structure, and simplifies the study of mass transport at electrodes of non-canonical geometry.

6.1 Abstract

The study of electrochemical reactivity requires analytical techniques capable of probing the diffusion of reactants and products to and from electrified interfaces. Information on diffusion coefficients are often obtained indirectly by modelling current transients and cyclic voltammetry data, but such measurements lack spatial resolution and are accurate only if mass transport by convection is negligible. Detecting and accounting for adventitious convection in viscous and wet solvents, such as ionic liquids, is technically challenging. We have developed a direct, spatiotemporally resolved optical tracking of diffusion fronts which can detect and resolve convective disturbances to linear diffusion. By tracking the movement of an electrode-generated fluorophore we demonstrate that parasitic gas evolving reactions lead to ten-fold overestimates of macroscopic diffusion coefficients. An hypothesis is put forward linking large barriers to inner-sphere redox reactions, such as hydrogen gas evolution, to the formation of cation-rich overscreening and crowding double layer structures in imidazolium-based ionic liquids.

6.2 Introduction

Room temperature ionic liquids (RTILs) are salts with melting point below 25 °C.²⁸² They are non-volatile ionic conductors, with emerging applications in technologies and processes ranging from batteries,²⁸³ to supercapacitors,²²⁰ electrocatalysis,²⁸⁴ and sensing.^{285, 286} For all RTIL-based electrochemical applications it is important to first obtain a correct and complete understanding of mass transport of reactants and products towards and away from the electrode.²⁸⁷⁻²⁸⁹ Equally important is to access quantitative information on structures and

dynamics of the electrode–RTIL interface.^{18, 90, 92, 152, 243} For instance, insights on double layer order obtained by atomic force microscopy (AFM),^{94, 290} Raman spectroscopy,⁹³ and more recently even through simple measurements of open circuit potential,¹⁵² have shown the existence of compact cation or anion-rich layers near polarized electrodes.¹⁵² It can be supposed that such highly ordered and compact RTIL arrangements, which can persist for several hours if formed in response to negative electrode biases,¹⁵² will introduce a kinetic limitation to heterogeneous charge-transfer reactions, especially for reactions highly dependent on the nature of the electrode interface, such as inner-sphere reduction of water, oxygen or protons.^{291, 292} Opposite to outer-sphere reactions, which proceed at appreciable rates even when there exist a solvent layer between electrode and reactant, inner-sphere reactions require a strong interaction between electrode’s surface and molecule being oxidized or reduced.^{16, 291, 293}

Hence a near-surface compact arrangement of large organic cations is likely introduce a barrier to a common unwanted inner-sphere reaction: evolution of hydrogen as bubbles.^{291, 294} Parasitic evolution of gas bubbles at electrodes is a common occurrence,^{153, 295-297} and partial masking of the electrode’s surface by a gas cavity can decrease its capacitance,²⁹⁸ or cause an increase in electrical conductivity during electrolysis.²⁹⁹⁻³⁰¹ Beside the loss of electroactive area, a convective contribution to mass transport will appear as the surface-pinned bubble grows and eventually departs the electrode.³⁰² Such bubble-induced “disturbance” to diffusion – a localized and transient stirring – is often neglected and/or hard to account for.³⁰³ In this work we seek to develop a simple tool to quantify, and to map across a macroscopic electrode, the impact of adventitious gas evolution reactions on the analysis of mass transport in RTILs. The study of reactant and product diffusivity is a central feature of most electrochemical investigations,^{155, 304} but in conventional “one-electrode, one-lead”¹⁹⁶ measurement, local information on convection disturbances to quiescent diffusion are inevitably lost.³⁰⁵⁻³⁰⁷ In the 1990s Engstrom and co-workers began developing fluorescence microscopy-based approaches to access two-dimensional information on concentration gradients across macroscopic electrodes.^{148, 149, 308} The same group also applied electrochemiluminescent (ECL) reactions to map current heterogeneity due to non-uniform diffusion at the edge of microelectrodes,^{146, 147, 309} demonstrating the electroanalytical value of optical techniques.^{82, 194, 310} Other groups have since then explored similar research lines, and have for example by developing

electrofluorochromic redox couples to monitor the evolution over time of electrode concentration profiles and pH gradients.^{150, 311-316}

In this paper we develop a strategy for the visualization of diffusion fronts by means of tracking the movement of electrochemically generated fluorophores. Such spatiotemporally resolved data on diffusion coefficients allowed us to detect and quantify bubble-induced convective disturbances of nominally quiescent electrode systems. We have applied this optical approach – redox profluorescence microscopy – to RTILs that have a different propensity of forming compact double layer cation-rich structures, hence a different intrinsic inhibition of adventitious inner-sphere gas-evolving redox reactions. The electrode-generated fluorophore is oxyluciferin (**ox-luc**, Figure 6.1a),³¹⁷ which is the final product of the cathodic electrochemiluminescent (ECL, Figure 6.1b) light-path of non-fluorescent firefly's luciferin adenylate ester (**AMP-luc**).²⁰¹

6.3 Experimental Section

6.3.1. Materials. Unless stated otherwise, all reagents were of analytical grade and used without further purification. Milli-Q™ water (> 18.2 MΩ cm) was used for cleaning procedures and, where specified, for adjusting the water content of the RTIL samples. D-luciferin sodium salt (≥95%, Cayman Chemical Company, Michigan) was used as starting material for the synthesis of firefly luciferyl adenylate (hereafter **AMP-luc**). **AMP-luc** was prepared and titrated as described previously.^{111, 201} Pyridine (≥99.5%) and acetonitrile (≥99.9%, MeCN) were purchased from Honeywell (North Carolina). 1-Butyl-1-methylpyrrolidinium bis-(trifluoromethylsulfonyl)imide (99.5%, [BMPyrr][NTf₂]), 1-ethyl-3-methylimidazolium tetrafluoroborate (>98%, [EMIM][BF₄]) were purchased from Iolitec (Germany). Adenosine 5'-monophosphate monohydrate (≥97%, AMP), *N,N'*-dicyclohexylcarbodiimide (99%), 1-ethyl-3-methylimidazolium ethyl sulfate (≥95%, [EMIM][EtSO₄]), tetrabutylammonium hexafluorophosphate (≥99.0%, Bu₄NPF₆), bis(cyclopentadienylcobalt(III) hexafluorophosphate (98%, Cc⁺), bis(pentamethylcyclopentadienyl)cobalt(III) hexafluorophosphate (98%, Me₁₀Cc⁺) and ferrocene (98%, Fc, sublimed before use) were purchased from Sigma. The water content in RTIL samples was estimated by Karl–Fisher (KF) titrations using a C20S compact KF coulometer (Mettler–Toledo, Ohio). Hydranal™ Coulomat AG reagent for the KF titration was purchased from Honeywell (North Carolina), and the 0.1% water standard was from Merck

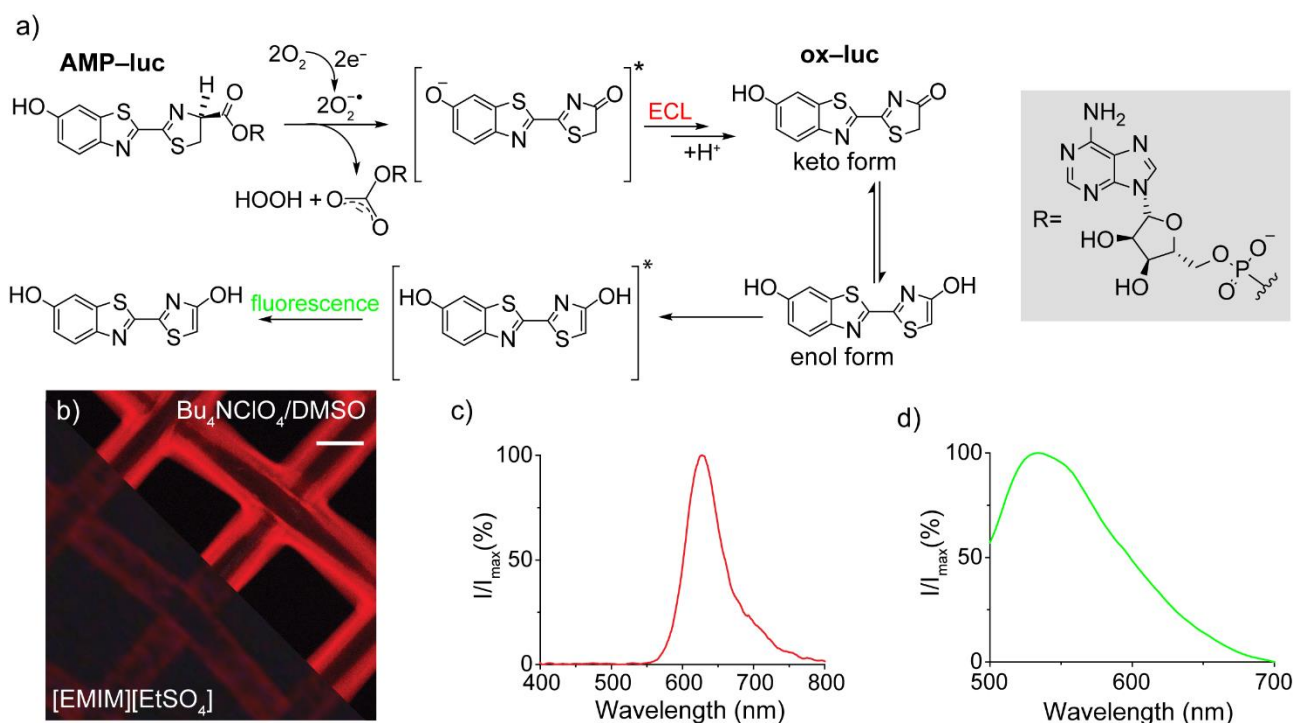


Figure 6.1. (a) Proposed mechanism for the cathodic electrochemiluminescence (ECL) of **AMP-luc**.²⁰¹ (b) The reaction of **AMP-luc** (0.4×10^{-3} M, oxygen-saturated, -2.0 V vs Ag/AgCl) with electrode-generated superoxide leads to the excited state of **ox-luc**, which relaxes emitting red light. The red ECL emission is intense for electrolyses in 2.0×10^{-1} M $\text{Bu}_4\text{NClO}_4/\text{DMSO}$ ($10\times$ magnification, CMOS sensor camera, unmodified micrograph) but very faint in $[\text{EMIM}][\text{EtSO}_4]$ (Laowa 25 mm F/2.8 2.5–5X, back-illuminated CMOS sensor, micrographs edited to maximise contrast). The scale bar is $100 \mu\text{m}$. (c) Cathodic **AMP-luc** ECL spectrum recorded in $[\text{EMIM}][\text{EtSO}_4]$. (d) Optical excitation of an electrolyzed **AMP-luc**/ $[\text{EMIM}][\text{EtSO}_4]$ triggers the green fluorescence of the **ox-luc** enol product.

(Germany). At least three KF titrations were performed for each RTIL. The reported values ($[\text{EMIM}][\text{EtSO}_4]$, 930 ppm; $[\text{BMPyrr}][\text{NTf}_2]$, 125 ppm; $[\text{EMIM}][\text{BF}_4]$, 2400 ppm) are the arithmetic average of the three titrations.

6.3.2 Fluorescence and ECL imaging. Unless specified otherwise, time-resolved fluorescence and ECL images were recorded on a Nikon ECLIPSE Ti2-U inverted microscope fitted with a custom-built optoelectrochemical single-compartment, three-electrode cell (Figure S1, Supporting Information, Appendix 4). Microscopy experiments were performed in a dark room, at room temperature (23 ± 2 °C) in air, and within 10 min of exposing the electrolytic **AMP-luc** solution to the atmosphere. For the fluorescence experiments the microscope was

fitted with a Plan Apo λ 10 \times /0.45 objective (part n. 88-379, Nikon, CFI Plan Fluor), a back-illuminated CMOS monochrome camera (DS-Qi2, Nikon), and a FITC filter/dichroic mirror cube (LED-FITC-A-NTF-ZERO, single band excitation filter 461.0–487.5 nm, single band emission filter 502.5–547.5 nm, and 495 nm dichroic beamsplitter, BrightLine®, Semrock, California). Fluorescence videos were recorded selecting a 20 ms exposure time, a capture rate of 5 frame/s, and a 1 \times gain. Microscopy experiments to map ECL in organic solvents (**AMP-luc** in Bu₄NClO₄/DMSO, e.g. video frame in Figure 1b, upper right section) were recorded using a colour camera (DS-Fi3, Nikon), setting the exposure to 1.0 s, and without filtering nor light excitation. ECL intensities for solutions of **AMP-luc** in RTILs were however too dim to be captured with the DS-Fi3 camera, so that ECL images (e.g. lower left section of Figure 1b, cathodic electrolysis of **AMP-luc** in [EMIM][EtSO₄]) were recorded with a more sensitive DSLR camera (Nikon D850) equipped with back-illuminated CMOS image sensor and using an ultra macro lens (Laowa 25 mm F/2.8 2.5–5X). The fluorescence of non-fluorescent **AMP-luc** solutions (4 \times 10⁻³ M, ~10 mL) was triggered electrochemically by applying a short (30 s) cathodic bias (-2.0 V vs reference electrode) to a platinum mesh working electrode (SEC-C Gauze, 80 mesh, 80 μ m wire diameter, 7 \times 6 mm outer size, purchased from BASi, Indiana). The reference electrode was a plastic body “leakless” Ag/AgCl electrode (eDAQ, part n. ET072-1, with 3.4 M aqueous potassium chloride as filling solution) and a platinum coil served as the counter electrode (0.5 mm diameter wire, 99.99+%, Goodfellow Cambridge Limited). The electrodes were connected to a portable potentiostat (Emstat3 blue, PalmSens BV, Netherlands). The **AMP-luc** solutions were bubbled with oxygen gas (\geq 99.95%, Coregas) for at least 20 min prior to the experiments. The platinum electrodes were cleaned daily through at least 50 consecutive cyclic voltammetry cycles (from -2.0 V to 1.0 V, potential scan rate of 0.01 V s⁻¹) in 5.0 \times 10⁻¹ M aqueous sulphuric acid. Local diffusivity values were calculated by analyzing the movement of the **ox-luc** fluorescent front away from the platinum surface. Time-stamped fluorescence intensity profiles were analysed with the open source image processing package Fiji,³¹⁸ in order to determine the distance (r) from the electrode surface at which the fluorescence intensity falls to half of its maximum value. This distance (r) was tracked as function of the time (t) after the cathodic pulse, and used to estimate diffusion coefficients (D) by assuming an Einstein’s random walk ($r^2 = 2Dt$).^{319, 320} This procedure was repeated for 10 different videos for each RTIL type, with at least 10 different locations analyzed in each video.

Fluorescence images were not background subtracted, and no attempts were made to improve contrast and sharpness. ECL images for RTIL samples were background-subtracted.

6.3.3 Photon counting. A single-photon counting module (SPCM-AQR-14, Excelitas Technologies), interfaced with an avalanche photodiode (APD) controller (Nanonics Imaging Ltd. time constant was set to 1.0 ms), was used to perform quantitative ECL measurements. A data logger (DrDAQ, Pico Technology) was used to record photon count rates. Electrolytic **AMP-luc** solutions and the three electrodes described for the fluorescence imaging experiments were placed inside a quart cuvette (10 mm optical path, Starna Pty Ltd., Australia). The cuvette was fitted with a custom PTFE cap/electrode holder to ensure reproducible electrodes positioning.

6.3.4 Fluorescence and ECL spectroscopy. ECL and fluorescence spectra were recorded on a Cary Eclipse (Varian, California) fluorescence spectrophotometer operated either in Bio/Chemi-luminescence mode (ECL, no excitation) or in Fluorescence mode (474 nm, excitation). The experiments were performed using the cuvette described in the Photon counting section, and the electrodes are described in the Fluorescence and ECL imaging section. The spectrometer's photomultiplier voltage was set to 800 V and the emission slit to 20 nm for both ECL and fluorescence measurements. The fluorescence excitation slit was set to 20 nm.

6.3.5 Open circuit potentiometry. Time-resolved open circuit potential (OCP) measurements were performed with an Emstat3 Blue potentiostat (PalmSens BV, Netherlands). A small RTIL sample (~5 mL) was loaded in a 10 mL beaker and degassed by means of bubbling argon gas (99.997%, Coregas) through it for at least 20 min. A platinum mesh (SEC-C Gauze, 80 mesh, BASi, Indiana) was used as working electrode, a platinum coil as counter electrode, and an Ag/AgCl "leakless" as the reference electrode (eDAQ, part ET072-1). The reference electrode potential was calibrated against the apparent formal potential of the ferrocene/ferricenium couple (Fc/Fc^+) as measured by cyclic voltammetry at a platinum disk electrode (eDAQ, ET052, 3 mm diameter) using the above specified reference and counter electrodes and a 1.0×10^{-3} M ferrocene solution in 1.0×10^{-1} M $\text{Bu}_4\text{NClO}_4/\text{MeCN}$. The working electrode was polished with alumina slurry (0.05 μm , eDAQ, ET033) and then cleaned electrochemically as described in

the Fluorescence Imaging section. The OCP measurements were started immediately after a 60 s cathodic pulse (-2.0 V relative to the initial, rest, OCP). To determine the working electrode's rest OCP, electrodes were let to equilibrate in the RTIL sample for at least 5 min after the end of the bubbling procedure. The length of the equilibration period was such to generally obtain a sufficiently stable OCP (dV/dt below $|0.0001|$). All OCP experiments were performed inside an acrylate glove box (Molecular Imaging, model GB306) kept under nitrogen gas that was dried with a Drierite™ gas-drying unit.

6.3.6 Cyclic voltammetry. Cyclic voltammetry experiments were carried out inside a custom-built acrylate glovebox kept under positive argon flow (4.0 L min^{-1} , $>99.999\%$, Coregas, Australia) using an Emstat3 Blue potentiostat (PalmSens BV, Netherlands) and a single-compartment, three-electrode glass cell. The cell was loaded with ~ 25 mL of either ferrocene (Fc), cobaltocenium hexafluorophosphate (Cc^+), or decamethylcobaltocenium hexafluorophosphate ($\text{Me}_{10}\text{Cc}^+$) solutions (1.0×10^{-3} M) in RTILs. Solutions were degassed prior to the measurements by means of a 20-min argon bubbling procedure. The working electrode was a platinum disk (eDAQ, ET052, 3 mm diameter), the counter electrode a platinum coil and the reference electrode a “leakless” Ag/AgCl electrode (eDAQ, part ET072-1). The working electrode was first polished with alumina slurry (0.05 μm , Dace Technology, Arizona) and then cleaned as described in the Fluorescence and ECL imaging section.

6.3.7 Digital simulations of voltammograms. Digital simulations of cyclic voltammograms were run on DigiElch8 (Gamry Instruments, Pennsylvania). Kinetic, thermodynamic and transport parameters were simulated by fitting data sets that covered a broad range of scan rates (from 1.0×10^{-2} to 5.0 V s^{-1}), and assuming an E mechanism. Charge transfer kinetic parameters were estimated using Butler–Volmer kinetics. Diffusion was modelled as semi-infinite 1D diffusion, and the symmetry factor, α , was set to 0.5. The cell iR drop was left uncompensated during the measurements and the actual value measured by electrochemical impedance spectroscopy prior to each experiment and then used for the simulations. Cells resistance values were approximately 400 Ω for [EMIM][EtSO₄], 570 Ω for [BMPyrr][NTf₂] and 150 Ω for Bu₄NPF₆/MeCN.

6.4 Results and Discussion

As shown in the top-right section of Figure 6.1b, the cathodic electrolysis of an oxygenated solution of **AMP-luc** in an organic solvent-based electrolyte (DMSO/Bu₄NClO₄) leads to a red glow visible to the naked eye (Figures S2–S3, Supporting Information, Appendix 4). The same electrolysis performed in RTILs, rather than in organic solvents, is however significantly less emissive (Figure 6.1b, and Figure S3, Supporting Information).³²¹ The ECL reaction is triggered by electrode-generated superoxide (Figure 6.1a and Figures S4, S5 and S6 Supporting Information).²⁰¹ As superoxide diffuses away from its generation site, the ECL's front also moves away from the platinum–RTIL interface. But while on one hand in DMSO/Bu₄NClO₄ it is possible to track the movement of this front (Figure S7, Supporting Information, Appendix 4), and therefore to estimate optically a diffusion coefficient for superoxide ($2.62 \times 10^{-6} \text{ cm}^2 \text{ s}^{-1}$ in agreement with previous reports),²⁰¹ on the other hand in RTILs the **AMP-luc** ECL reaction is too dim. Consequently, tracking optically the movement of the ECL front does not constitute a viable means of estimating diffusivities in RTILs. However, and very fortunately, the ECL product, **ox-luc** (Figure 6.1d), is fluorescent. Excitation with blue light of **AMP-luc** solutions undergoing electrolysis results in a bright green fluorescence which can be imaged with a CMOS camera and selecting exposure times as low as 20 ms (Figure 6.2a). Access to such fast capture rates, by focusing on redox pro-fluorescence rather than on ECL, means that the superoxide diffusion front can be visually mapped even in highly viscous RTILs (Figure 6.2a–c). Spatiotemporal D information become therefore available, data which are not accessible through conventional hydrodynamic measurements of diffusivity, such as rotating disk electrodes.³²² For example, from microscopy data as in Figure 6.2a–c the evolution of the fluorescence front can be rapidly sampled at several hundred different locations across the platinum electrode. The plot in Figure 6.2d shows the movement of the front at one of the ~200 locations analyzed (marked as A–B). The distance (r) travelled over time (t) by the front (taken arbitrarily as the point with an intensity half of the maximum value) along the A–B line away from the electrode, was used to compute diffusivity assuming an Einstein's random walk ($r^2 = 2Dt$). Data at electrolysis times beyond ~3 s were discarded since, as shown by Amatore and co-workers, natural convection becomes then dominant leading to underestimate the diffuse layer thickness.^{323–325} The histogram in Figure 6.2e shows the distribution across the macroscopic sample of the optically determined D . The mode of D is $4.80 \times 10^{-7} \text{ cm}^2 \text{ s}^{-1}$, but

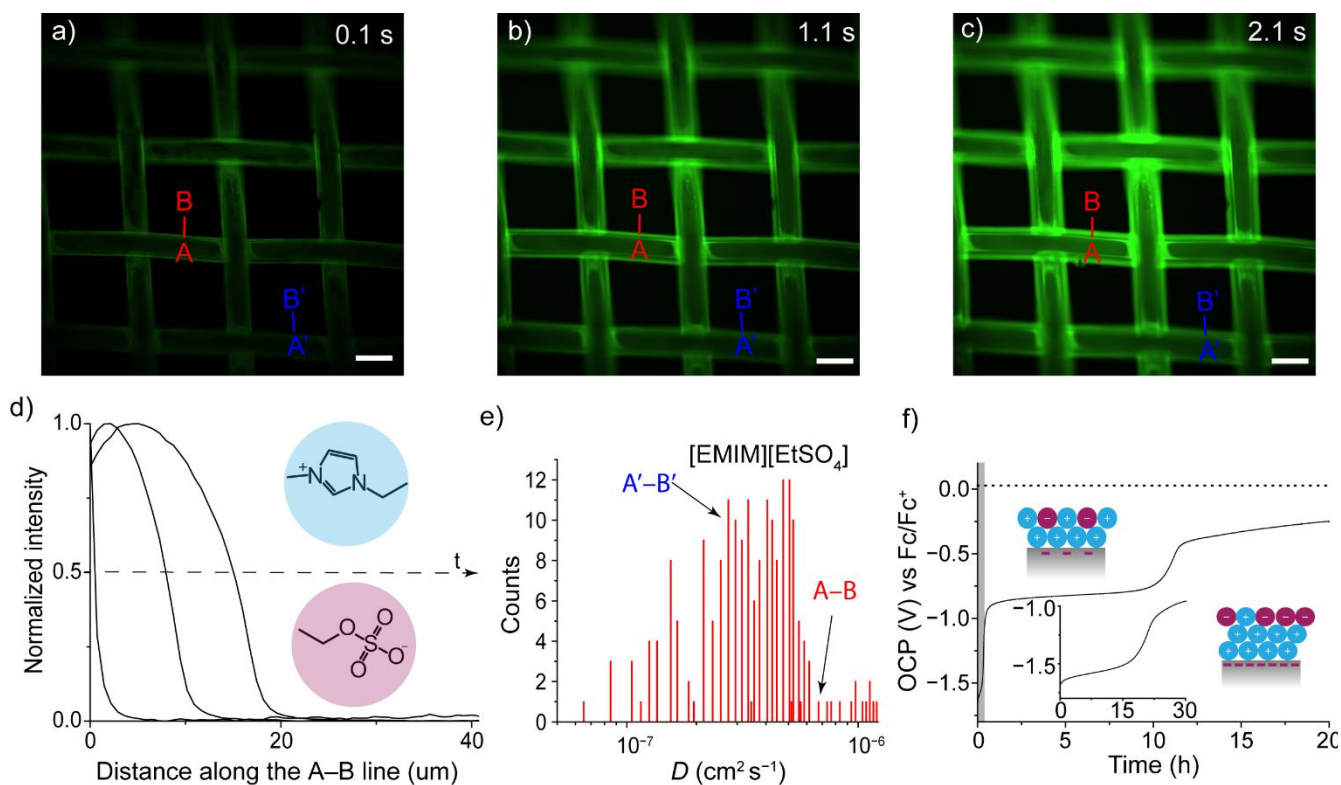


Figure 6.2. (a–c) Selected time-stamped fluorescence micrographs (10 \times magnification) recorded during the cathodic electrolysis (-2.0 V vs Ag/AgCl) of an oxygen-saturated **AMP-luc** solution (0.4×10^{-3} M in [EMIM][EtSO₄]) at a platinum mesh electrode. Scale bars in (a–c) are 100 μ m. (d) Representative fluorescence intensity plot profiles, sampled along the A–B line marked in (a–c), recorded 0.1, 1.1 and 2.1 s after the working electrode bias is stepped from open circuit to -2.0 V. The analysis of the movement over time of the superoxide diffusion front (triggering the **ox-luc** formation), as shown in (d) for a representative location, was repeated for at least 20 different working electrode locations per experiment, and at least 10 independent experiments were used to build the histogram plot shown in (e). The D values shown in (e) are calculated from the distance travelled by the fluorescence front between 0.1 s and 2.1 s, and as shown in (d), diffusivity is approximately uniform over this time interval. (f) Representative OCP–time measurement for a platinum mesh working electrode immersed in [EMIM][EtSO₄] (930 ppm of water). The electrode’s OCP was recorded continuously for 20 h, starting after the application of a 60 s negative pulse (-2.0 V vs the initial OCP). The horizontal dotted line represents the initial (rest) OCP value. The cartoons show the schematic depictions of overscreening and crowding near-electrode cation-rich structures RTILs.^{90, 152} The overscreening OCP signature remains stable for several hours, while the crowding plateau (inset) lasts for only ~ 15 min. The grey shaded area in (f) indicates the data expanded in the figure’s inset (crowding).

while for example the fluorescent front moves along the A–B line with a D of 5.25×10^{-7} cm² s⁻¹, the same measurement along A’–B’ indicates a slightly smaller D (3.35×10^{-7} cm² s⁻¹).

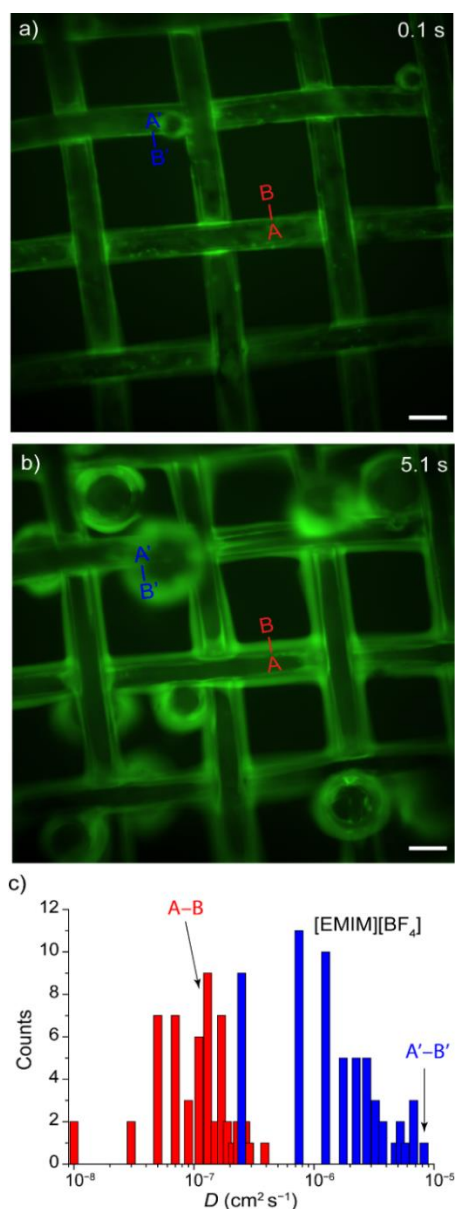


Figure 3. Time-stamped fluorescence micrographs (10× magnification) recorded (a) 0.1 s and (b) 5.1 s after the application of an external bias (−2.0 V vs Ag/AgCl) to an oxygen-saturated **AMP-luc** solution (0.4×10^{-3} M in [EMIM][BF₄], 2400 ppm of water). Scale bars are 100 μm. The movement of the fluorescent front was tracked at ~60 electrode locations (8–9 locations across 7 videos of 7 samples) close to sites where gas bubble are visible (e.g. along the A'–B' line), and at ~60 locations (8–9 locations across 7 videos) at least 100 μm away from bubbles (e.g. A–B line). (c) Histogram plot for the optically determined superoxide *D* values in [EMIM][BF₄]. Blue bars indicate measurements taken at electrode sites with clear convective (bubbles growing) disturbances, and red bars for measurements at quiescent sites. The *D* values in (c) are calculated from the distance travelled by the front after an electrolysis time of 5.1 s.

Such local differences in *D*, most likely due to natural convection,³²³⁻³²⁵ would however be lost

in a conventional electrochemical measurement and even advanced forms of redox microscopy would not be able to access these information.^{82, 194, 310} A small level of lateral asymmetry in the overall fluorescence intensity is visible in micrographs (e.g. Video S2) but was not due to the relative position of counter and working electrodes (Figure S8, Supporting Information), as observed before for ECL systems.³¹¹ In addition to natural convection, it is possible that a lateral heterogeneity in current density (across the Pt mesh) may lead to material transport via diffusioosmotic fluid flow,^{326, 327} which in turn may lead to the observed asymmetry. The average D obtained in [EMIM][EtSO₄] is one order of magnitude smaller than in DMSO,²⁰¹ as it expected based on the higher viscosity of the former (~100 cP vs. 2.0 cP).³²⁸

During the cathodic electrolysis of **AMP-luc** [EMIM][EtSO₄] the interface remains relatively quiescent and the distribution of D across the electrode surface is therefore relatively narrow (Figure 6.2e). This is surprising, as despite both the large negative potential used to trigger the pro-fluorescent reaction (-2.0 V vs Ag/AgC for 15 s) and the moderate level of water content in [EMIM][EtSO₄] (930 ppm), yet there was no evidence of hydrogen bubbles forming on the electrode. The formation and departure from the electrode of gas bubbles would have introduced convection hence caused highly dispersed D values. This leads to the question of what prevents in [EMIM][EtSO₄] gas evolution at such negative voltage biases. As introduced above, some RTILs form compact and long-lived cation-rich double layer structures on negatively biased electrodes. The compactness of such RTILs structures has been detected by Atkin and co-workers as a mechanical resistance to AFM tips approaching biased electrodes,^{290, 329} and manifest stable and discrete open circuit potential (OCP) plateaus.¹⁵² For example, OCP-time data in Figure 6.2f show that with [EMIM][EtSO₄], the imidazolium-rich layer formed at a platinum cathode persists for nearly 10 h once the cathodic bias has been removed. Only mechanical shaking of the electrochemical cell disrupts prematurely such ordered double-layer arrangement.¹⁵² More specifically, once the exogenous field (the negative electrode bias) is removed and the OCP logging started, both crowding and overscreening structures persist for ~15 min and ~10 h, respectively (Figure 6.2f).^{90, 152} Notably, in the fluorescence experiments described above the cathodic bias is not interrupted, hence cation-rich interfacial layers are likely to be present for the entire duration of the **AMP-luc** electrolysis. Although unlikely to interfere with the relatively anodic reduction of oxygen (Figure S9, Supporting Information, Appendix 4), we believe this compact layer, especially crowding, is

introducing a kinetic barrier to inner-sphere redox reactions, preventing, despite the presence of substantial levels of water, gas evolution even under very negative voltages. The formation of crowding and overscreening structures in [EMIM][EtSO₄] hinders the reduction of water traces to the point that this relatively hydrophilic RTIL (~1000 ppm of water) behaves alike an hydrophobic RTIL such as [BMPyrr][NTf₂] (~100 ppm of water, Figure S10, Supporting Information, Appendix 4). For both RTILs, the lack of bubble-induced convective disturbances accounts for a relatively narrow distribution of D values across the macroscopic electrode.

By mapping the **ox-luc** fluorescent front, a large dispersion in the diffusivity characteristics were however revealed for RTILs that do not form compact double-layers. For instance, in [EMIM][BF₄] (34 cP, ~2400 ppm of water) mapping diffusion fronts at random locations across the electrode unveiled superoxide D values spread over nearly four orders of magnitude (Figure 6.3). [EMIM][BF₄] does not have a significant barrier to water reduction (Figure S11, Supporting Information, Appendix 4) and hydrogen bubbles form on the electrode during the cathodic electrolysis of **AMP-luc**. Notably, when D is measured far away from a growing bubble, such as at the A–B line marked in Figure 6.3a–b, its value is, as expected, lower than for the less viscous [EMIM][EtSO₄] and experimental D values felt within a relatively narrow range (Figure 6.3c, red bars). Growing bubbles are clearly visible in the fluorescence micrographs (Figure 6.3b) and tracking the movement of **ox-luc** near the gas cavities – sites where quiescent diffusion is disturbed by convection – led to a significant local overestimate of D (Figure 6.3c, blue bars).

This spread in the superoxide diffusion coefficient in [EMIM][BF₄] is caused by the lack of a barrier towards inner-sphere reactions and not by the large hydrophilicity of this RTIL. For instance [EMIM][EtSO₄] does not show any evolution of bubbles even when deliberately spiked with 2% of water (Figure S12a, Supporting Information, Appendix 4). Even with such large level of water, the [EMIM][EtSO₄]-electrode interface retains its ability to form compact electrostatic structures detectable as long-lived negative OCP plateaus (Figure S12b, Appendix 4). [EMIM][BF₄] on the other hand cannot favourably align with the electrode electric field even at water levels as low as 500 ppm.¹⁵² The growth rate of the bubbles is not uniform, hence unlike for quiescent systems (Figure 6.2d), apparent D values measured on bubbles are not uniform over time (Figure S13, Supporting Information, Appendix 4). The formation of stable double

layers is strongly influenced by the nature of the RTIL, and for example cations with smaller alkyl chains can more easily pack at the a negative charged surface compared to larger cations.²¹⁶ However, [EMIM][EtSO₄] and [EMIM][BF₄] share the same cation, thus the strikingly different ability to form stable double layers is due to difference in the anion. Specifically, the reason lies in the [BF₄] anion lacking a dipole moment. The stronger dipole moment of [EtSO₄] facilitates its alignment with the external electric field, and consequently the generation of an internal electric field, which manifests as a long-lived OCP signature.¹⁵²

It is only when the water level becomes as high as 5.0% that the duration of overscreening plateaus in [EMIM][EtSO₄] is significantly reduced, while the evolution of gas bubbles becomes significant (Figure S12c,d, Supporting Information, Appendix 4). With [BMPyrr][NTf₂], another RTIL where cathodic biasing does not lead to discrete negative OCP signatures (Figure S10f, , Appendix 4), a water content of 2.0% is already sufficient to cause significant gas evolution under the negative bias of the pro-fluorescent experiments (Figure S12e,f, Supporting Information, Appendix 4). While, as shown above, an inner-sphere reaction such as hydrogen evolution is influenced by how accessible the electrode surface is, the presence or absence of ordered and compact RTIL structures is unlikely to have a significant effect on outer-sphere reactions.²⁹¹ To test this we turned to well-studied outer-sphere metallocenes.³³⁰ Crowding and overscreening are unlikely to impair the redox kinetics of molecules such as ferrocenes and cobaltocenes. The choice of Cc⁺ and Me₁₀Cc⁺ is because they both have, especially Me₁₀Cc⁺,^{331, 332} redox potentials sufficiently negative so to approach the cathodic bias used for the **AMP-luc** pro-fluorescent reaction and to closely match the position of the overscreening and crowding OCP signatures. By digital simulations of cyclic voltammetry experiments at different scan rates (from 1.0×10^{-2} to 5.0 V s^{-1}) we looked for evidence of a drop in the electron transfer rate constants (k_{et}) when the solvent was changed from MeCN to RTILs of similar viscosity (~100 cP) but that either form or do not form cation-rich structures that leads to discrete OCP signatures after a cathodic pulse ([EMIM][EtSO₄] and [BMPyrr][NTf₂] respectively).³³³ The fitting results are summarized in Figure 6.4. Firstly, in an organic solvent (MeCN/Bu₄NPF₆) the refined k_{et} is about one order of magnitude higher than in both RTILs. Secondly, a comparison between k_{et} obtained in [EMIM][EtSO₄] and in [BMPyrr][NTf₂] suggests for both Fc and Cc comparable, with the uncertainty, redox kinetics in both RTILs. Unfortunately data for Me₁₀Cc in [BMPyrr][NTf₂] were not reproducible, possibly due to the poor stabilization of Me₁₀Cc⁺ by

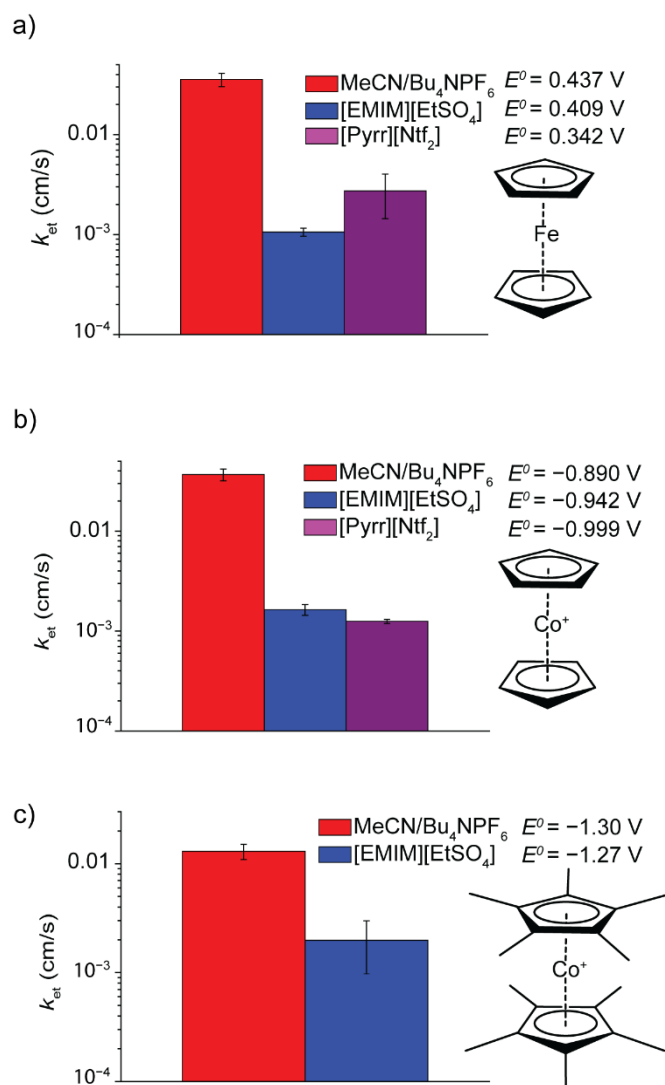


Figure 6.4. Comparison of the refined (digital simulations of experimental cyclic voltammograms, CVs) charge transfer rate constant (k_{et}) of three outer-sphere redox molecules (Fc (a), Cc^+ (b), and $Me_{10}Cc^+$ (c)). Voltammograms were obtained in 1.0×10^{-1} M MeCN/ Bu_4NPF_6 (red bars), [EMIM][EtSO₄] (blue bars), and [BMPyrr][NTf₂] (violet bars). Experiments were repeated at least five times for each system, and the CV voltage sweep rate was varied between 0.01 and 5.0 Vs⁻¹. (Supporting Information, Figure S14–S21, Appendix 4). The metallocene concentration was 1.0×10^{-3} M. No k_{et} value is reported for $Me_{10}Cc^+$ in [BMPyrr][NTf₂] as CVs of this system were poorly reproducible. Refined values of the apparent formal potential (E^0 vs Ag/AgCl) are indicated by labels in figure. The chemical structure of each metallocene is shown next to the relative graph.

the [NTf₂] anion.³³⁴ The drop in k_{et} moving from MeCN to [EMIM][EtSO₄] was comparable for Fc, Cc^+ and $Me_{10}Cc^+$. This is important, since in the case of a blocking effect by cathodic overscreening and crowding structures on the electron transfer of outer-sphere couples, a drop

in k_{et} would have been negligible for the relatively anodic Fc/Fc⁺ couple, but progressively larger for Cc⁺ and Me₁₀Cc⁺. The redox couple Cc/Cc⁺, has a redox potential 1.33-1.35 V more negative than that of the Fc/Fc⁺ couple (Figure 6.4a,b), and the Me₁₀Cc/Me₁₀Cc⁺ couple is about 1.67 V more negative than the Fc/Fc⁺ couple, and therefore close to the potential where ordered double layers form in [EMIM][EtSO₄] (Figure 6.2f) and yet the relative drop in k_{et} is comparable or even smaller for the latter.

6.5 Conclusion

We have developed a spatiotemporally resolved optical measurement of diffusion coefficients that can account for convective disturbances. This approach reduces the likelihood of overestimating diffusion coefficients in viscous systems where adventitious gas-evolving reactions cannot be ruled out. The cathodic generation of fluorescent oxyluciferin (**ox-luc**), by means of reacting firefly's luciferin adenylate ester (**AMP-luc**) with electrode-generated superoxide radical anion, was used to map superoxide diffusivity in RTILs. Literature diffusivity data for superoxide in RTILs are highly scattered, presumably because the presence of water impurities^{282, 335, 336} leads to unaccounted and poorly reproducible convective contribution to mass transport. Visual mapping of electro-generated **ox-luc** diffusion fronts addresses this issue and allows to measure accurately diffusion coefficients even in systems where convection cannot be removed. For example we demonstrate that in [EMIM][BF₄], D for superoxide increases from $6.40 \times 10^{-8} \text{ cm}^2 \text{ s}^{-1}$ in quiescent regions, to $2.30 \times 10^{-6} \text{ cm}^2 \text{ s}^{-1}$ in regions affected by convective disturbances (in proximity of evolving gas bubbles). A conventional macroscopic one-electrode, one-lead measurement would output an average and therefore overestimate diffusion coefficient. While evolution of gaseous products, and its interference with quiescent diffusion, cannot be removed, it can however be detected, accounted for, and even predicted. With regards to this last point – the likelihood of significant convective disturbances – we have been able to uncover a link between inner-sphere reduction of water and the stability of cation-rich double layer RTIL structures. Our results suggest that RTILs forming stable overscreening and crowding double layers can be biased to very negative voltages without detectable gas evolution from water splitting or proton reduction. Readily available time-resolved open-circuit potentiometry can be used to screen for RTILs likely to yield stable overscreening and crowding double layers under negative electrode biases. We also note that

while compact double layer RTIL structures pose a significant kinetic barrier to inner sphere reactions, such structure does not impair the electrode kinetics of outer-sphere redox reactions, such as for widespread metallocenes.

Chapter 7: Conclusion and outlook

In summary, this thesis has investigated approaches to probe electric double layer (EDL) structures and dynamics. Indirect probing of the EDL, such as through optical and potentiometric measurements, might complement more direct techniques such as SPM approaches. Understanding the nature of the EDL, and its features, can aid research in different fields, from capacitors and energy-storage devices,^{73, 337} to catalysis.⁶ This thesis has achieved results that may improve our ability to study the EDL. One important result was the detection of small spectral shifts for electrode-generated light emitters, presented in **Chapter 2**. Spectra tuning of the luciferin ECL reaction can be a response of local electric fields^{338, 339}, which means it can be potentially exploited as non-invasive technique to study the EDL, not just at solid–liquid interfaces, but perhaps also at liquid–liquid, and liquid–gas interfaces. Also highlighted was the importance that lithium ions play in controlling the emission wavelength during luciferin ECL. Further investigation might give additional insight into the exact role of this cation in this context³⁴⁰. Additionally, spectral tuning of partially solvated luciferin can be suitable for studies aiming to confirm or disprove the presence of a (debated) solvent depletion layer at the interface.^{86, 176}

In **Chapter 3**, the focus was on the nature of semiconductor electrodes, specifically modify silicon electrodes. It was found that all the attempts to tune the ECL emission were unsuccessful, indicating that the nature of the interfaces, and thus the EDL, is not the only parameter to consider while attempting to control the emission wavelength during ECL. However, spectral tuning of luminol chemiluminescence is possible.³⁴¹ This suggests that ECL spectral tuning might be achieved by exploring alternative surface chemistries. For instance, increasing hydrophobicity of the surface, using fluorinated monolayer,³⁴² or by studying different surface–solvent interactions, like hydrophobic surface and hydrophobic solvent, or more hydrophilic and hydrophobic solvents.

In **Chapter 4** the focus shifted to EDL structures in RTILs, here studied by looking at the ECL of both luminol and luciferin. However, despite no solvatochromic effect (and consequently spectral tuning) being observed, another phenomenon was worth noting. This was the long-lasting ECL emission (**Chapter 4**) of both luminol and luciferin in RTILs. Such long-lasting

emissions resulted in being correlated with the behaviour of the OPC that is shown in **Chapter 5**. The correlation between such long-lasting emission and the exogenous electric field observed in RTILs might be sought in the stabilization of the superoxide radical anion. The possibility to stability the superoxide radical anion has already been demonstrated, being associated with electro-donating solvents,³⁴³ and the anion's Lewis basicity nature.³⁴⁴ For all these reasons, a wide knowledge about how the RTILs are ordered at the interface may lead to some potential direct applications, such as harnessing electrostatic catalysis,⁷² and a new generation of batteries and supercapacitors.³⁴⁵

Finally, in **Chapter 6**, pro-fluorescence was employed to locally measure the diffusion coefficient in RTILs. Local measurements demonstrated how the diffusion coefficient can be strongly affected by interfacial phenomena. This strategy prevents overestimation of diffusivity in those systems with high viscosity and/or significant impurities. Additionally, pro-fluorescence microscopy is a powerful tool to optical investigate electrified interfaces, for example providing a further alternative for studying the EDL in RTILs.

Among the future implications of this research, it is possible to foresee that the study of EDL can allow progress in the electrostatic catalysis field. Hence, a natural follow-up of this thesis should be attempting to perform electrostatic catalysis in diffuse systems. For example, S_N2 reactions, like the Menshutkin reaction, have already been proposed as a possible candidate for electrostatic catalysis.^{19, 20}

However, the role played by the solvent, in enhancing or preventing electrostatic catalysis remains the main challenge.²⁰ An attempt to perform electrostatic catalysis has been made, having one reactant 'block' on the silicon surface as SAM (self-assembled monolayer), while the second reactant is in the bulk (Figure 7.1). In Figure 7.2, a brief visualization of the first results is displayed, the reaction has attached a ferrocene group to the SAMs, making the silicon surfaces electrochemically active.

Further studies are needed to fully understand the nature of this catalysis and to discriminate between electrostatic catalysis and other possible reaction pathways, like a radical-mediated process.

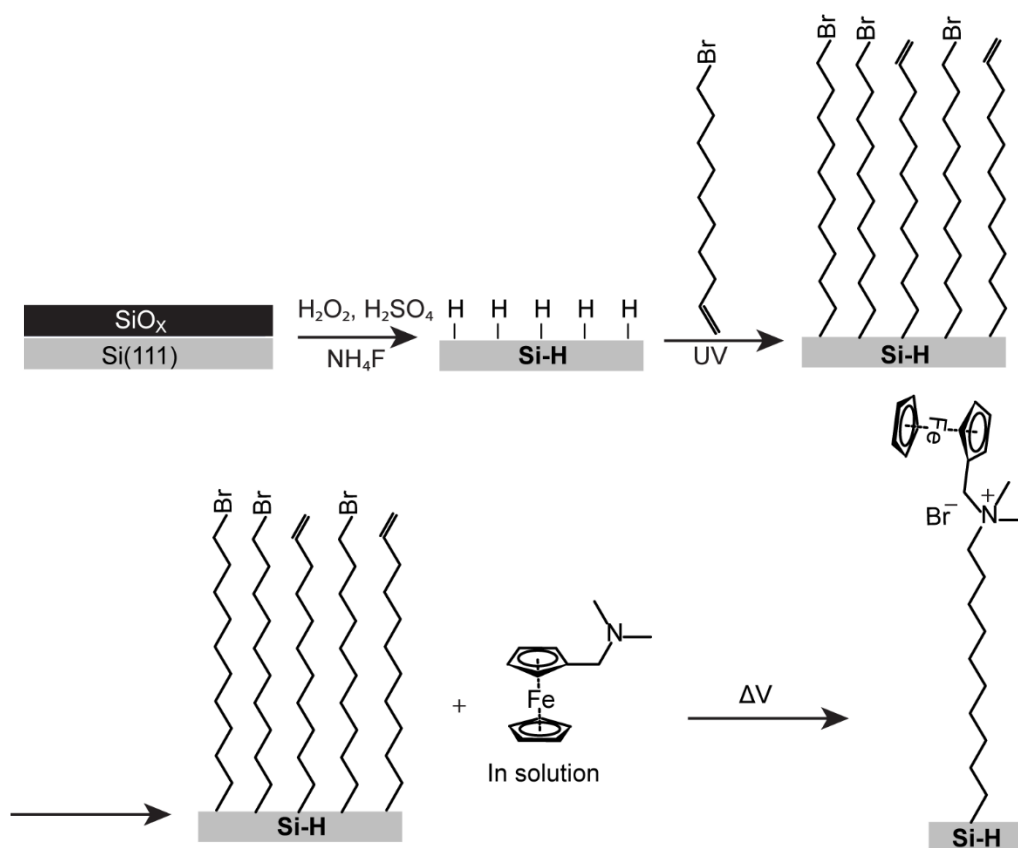


Figure 7.1. Schematic representation of semi-bulk electrostatic catalysis of Menshutkin reaction. A Br-ended SAMs (1,10-Dibromodecane) on a silicon wafer is prepared following the same procedure described in Chapter 3. Subsequently, the silicon wafer is used as working electrode in a solution containing a (dimethylaminomethyl)ferrocene, which under the effect of an EEF undergoes to electrostatic catalysis. The presence of ferrocene on the reactant molecules allows having an immediate control of the reaction success by CV.

However, this project will not be further discussed in this thesis, as the research is still ongoing, and any achievement will be presented in future peer-reviewed publications.

Finally, ECL and pro-fluorescence imaging have been shown to hold another great potential for example, in medical diagnosis and therapy. The Continuous development of these techniques is a fundamental aspect.³⁴⁶⁻³⁴⁹ ECL imaging has been a powerful tool, employed in assays, like enzyme assays and immunoassays or genotoxicity screening.³⁵⁰⁻³⁵² Additionally, ECL sensing has been utilized for metal ions, small molecules sensing, and antigens/antibodies identification for cells and microorganisms sensing,^{353, 354} as well as proteins,³⁵⁵ and DNA detection.³⁵⁴ These are just some of the many possible applications of ECL.³⁵⁴ Fluorescence is also an equally viable

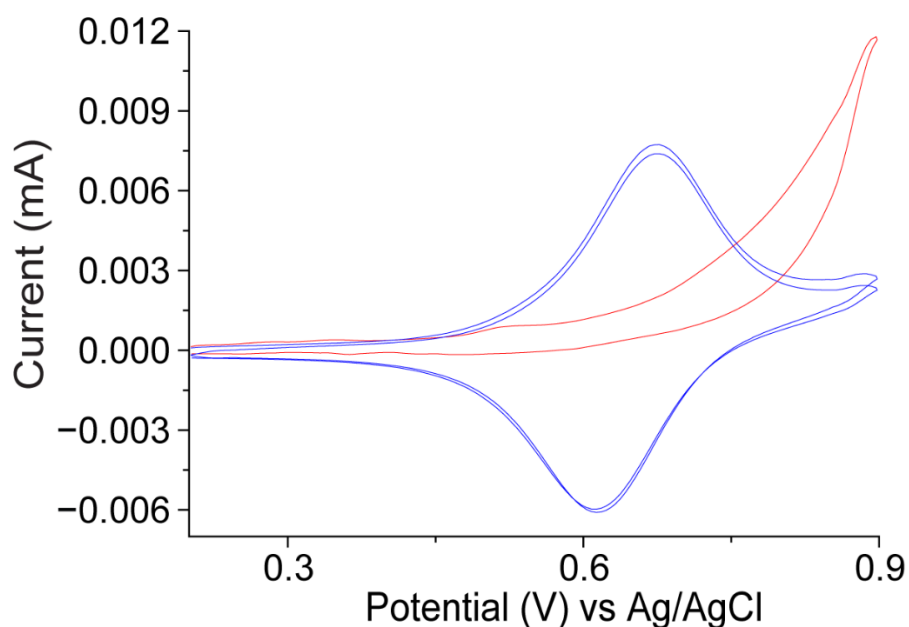


Figure 7.2. Representative cyclic voltammograms of 1,10-Dibromodecane functionalized silicon (111, highly doped, P-type) in 0.1 M $\text{Bu}_4\text{NClO}_4/\text{MeCN}$, before (red trace) and after (blue trace) the electrostatic catalysis of Menshutkin reaction. In brief, the functionalized silicon electrode was fitted in a custom cell, along with a platinum counter electrode and a leakless Ag/AgCl reference electrode, then the CV (red trace) was recorded in 0.1 M $\text{Bu}_4\text{NClO}_4/\text{MeCN}$. Subsequently, a second solution containing dimethylaminomethyl ferrocene, (1.0×10^{-3} M) in 0.1 M $\text{Bu}_4\text{NClO}_4/\text{MeCN}$, was added, and an EEF was applied. Finally, the cell and the electrode were washed thoroughly with acetone and fresh MeCN. A second CV (blue trace) was obtained, showing the presence of ferrocene on the silicon surface.

alternative.^{356, 357} However, several ongoing challenges remain,³⁴⁷ and the development of new ECL molecules is imperative to overcome these obstacles.

Appendix 1: Supporting Information Paper 1

A1.1 Experimental Procedures

A1.1.1 Materials. Unless noted otherwise, reagents were of analytical grade and used without further purification. Milli-QTM water (>18.2 M Ω cm resistivity) was used for surface cleaning procedures and to prepare electrolytic solutions. Luciferin sodium salt was purchased from Cayman Chemical Company (≥ 95 %, Ann Arbor, Michigan). Adenosine 5'-monophosphate monohydrate (≥ 97.0 %, AMP), N,N'-dicyclohexylcarbodiimide (DCC, ≥ 99.0 %), tetrabutylammonium perchlorate (Bu_4NClO_4 , ≥ 98.0 %), lithium perchlorate (LiClO_4 , ≥ 98.0 %), anhydrous dimethyl sulfoxide (DMSO, ≥ 99.9 %), tetrahydrofuran (THF, ≥ 99.0 %, anhydrous, with 250 ppm of butylated hydroxytoluene as inhibitor), potassium dioxide (KO_2 , ≥ 95 %), and D-luciferin ethyl ester (≥ 97.5 %) were purchased from Sigma. Pyridine (≥ 99.5 %, Honeywell, Charlotte, North Carolina), N,N-dimethylformamide (DMF, 99.9%) was purchased from VWR Chemicals (Pennsylvania), and tetrabutylammonium nitrate (Bu_4NNO_3 , 97%), tetrabutylammonium hexafluorophosphate (Bu_4NPF_6 , 98%), sodium tetrakis[3,5-bis(trifluoromethyl)phenyl]borate (NaBARF, 97%) were purchased from Alfa Aesar. Sodium perchlorate monohydrate ($\text{NaClO}_4 \cdot \text{H}_2\text{O}$, 90.0%) was purchased from Univar. Argon (Ar , >99.999 %) and oxygen gas (O_2 , ≥ 99.5 %) were supplied from Coregas. Deuterated DMSO (d_6 -DMSO, 99.5%) was purchased from Cambridge Isotope Laboratories, Inc.

A1.1.2 Synthetic procedures. Firefly luciferyl adenylate (**AMP-luc**) was prepared according to the procedure of White and co-workers (Figure S18).¹¹¹ In brief, luciferin sodium salt (0.33×10^{-3} mol) and AMP (0.37×10^{-3} mol) were dissolved in pyridine (~ 5.0 mL), then the solution was acidified with 0.5 M aqueous hydrochloric acid (0.5 mL). DCC (0.63×10^{-3} mol) in pyridine (~ 2.0 mL) was added in one portion, under nitrogen, to the stirred and ice-cold reaction mixture. The reaction mixture was stirred under nitrogen at 0 °C for a further 30 min. Cold acetone (~ 20 mL, -20 °C, containing) was then added to the crude reaction mixture in one portion. A pale yellow precipitate formed and was recovered by filtration on 0.45 μm nylon filters (BaseLine Chromtech). The solid was washed extensively with cold acetone (~ 100 mL, cold acetone containing ~ 5.0 % v/v of water). The **AMP-luc** yellow powder product was dried under vacuum,

then stored at $-20\text{ }^{\circ}\text{C}$ under argon prior to use. ^1H NMR (400 MHz, DMSO- d_6) δ 9.55 (1H, s), 8.39 (1H, s), 8.16 (1H, s), 7.96 (1H, d, 9 Hz), 7.46 (1H, d, 3 Hz), 7.28 (2H, s), 7.08 (1H, dd, 9 Hz, 3 Hz), 5.93 (1H, d, 6 Hz), 5.46 (1H, t, 9 Hz), 4.62 (1H, t, 5 Hz), 4.21 (1H, dd, 5 Hz, 3 Hz), 4.07 (1H, br. s), 4.05 (1H, br. s), 3.94 (3H, m), 3.75 (1H, dd, 11 Hz, 9 Hz), 3.66 (1H, dd, 11 Hz, 9 Hz). **AMP-luc** purity was estimated by titrating the reaction product with aqueous sodium hydroxide. The electrolyte/**AMP-luc** solution was placed in an optical glass rectangular cuvette (40 × 10 × 45 mm, part 3/G/40, Starna, Hainault) with the largest face facing a focusing lens (LA4647, Thorlabs) interfaced with an optical fiber (Model QP600-1-SR, Ocean Optics) connected to a compact silicon CCD array spectrometer (Flame-S-VIS-NIR-ES, Ocean Optics Inc., Orlando, Florida). The cuvette was fitted with a three electrodes system as described in the next section (spectroelectrochemical measurements). The titration was performed inside a light-proof metal box. The titration procedure was as follows: sodium hydroxide solution (2.0×10^{-3} M) was added dropwise to 9 mL of a vigorously stirred **AMP-luc** solution (0.2 g/L) in 0.2 M $\text{Bu}_4\text{NClO}_4/\text{DMSO}$. **AMP-luc** is progressively consumed in a stoichiometric reaction with sodium hydroxide.¹¹² The emission intensity in response to the electrochemically triggered light emission from the residual, unreacted **AMP-luc** (working electrode bias set to -2.0 V) was monitored continuously, allowing a short interval (1 min) between successive additions of the base. When all **AMP-luc** is consumed, light emission ceases and this is the titration endpoint. The amount of **AMP-luc** present in the crude reaction product ranged from 55% to 75% w/w (and the reaction yield ranged from 32% to 47%).

A1.1.3 Spectroelectrochemical measurements. All spectroelectrochemical measurements were acquired with freshly made solutions of **AMP-luc** (0.43×10^{-3} M) in DMSO, with either Bu_4NClO_4 (0.2 M), Bu_4NNO_3 (0.2 M), Bu_4NPF_6 (0.2 M), LiClO_4 (2.0 M, 0.2 M and 5.0×10^{-3} M) NaClO_4 (0.2 M), and NaBARF (0.2 M) as electrolytes, or in THF with LiClO_4 (0.2 M and 5.0×10^{-3} M) or NaBARF (0.05 M), or in DMF with Bu_4NClO_4 (0.2 M). Unless specified otherwise, oxygen gas ($\geq 99.95\%$, Coregas) was bubbled through the **AMP-luc** solution (~ 20 mL) for at least 20 min prior to the experiments. Spectroelectrochemical measurements were carried out under ambient air, at room temperature, using an Emstat3 Blue potentiostat (PalmSens BV, Houten, Netherlands) and a single-compartment, three-electrode setup. A platinum rectangular mesh (7 × 6 mm overall size) served as the working electrode (EF-1355 SEC-C Gauze, 80

mesh, wire diameter of 80 μm , BASi, Lafayette, Indiana), a platinum coil as counter electrode, and a leakless Ag|AgCl as the reference electrode (ET072-1, eDAQ, Colorado Springs, Colorado, 3.4 M aqueous potassium chloride as filling solution). The spectroelectrochemical cell was a quartz cuvette of 0.5 mm optical length (EF-1364 SEC-C, BASi), fitted with a perforated PTFE cap was holding up the electrodes (EF-1359 SEC-C). Light emission was recorded with a Cary Eclipse (Varian, Palo Alto, California) fluorescence spectrophotometer operated in Bio/Chemi-luminescence mode. The photomultiplier voltage was set to 800 V, and unless specified otherwise, the emission slit was set to 5 nm for experiments in DMSO, and to 20 nm for experiments in THF. Platinum electrodes were cleaned prior to the experiments by continuous potential cycling between -0.2 and 1.0 V (0.5 M HNO_3 , 0.01 V s^{-1}).

A1.1.4 Photon Counting. Photon counting experiments were performed with a single-photon counting module (SPCM-AQR-14, Excelitas Technologies) interfaced with an avalanche photodiode (APD) controller (Nanonics Imaging Ltd., Figure S19). The photon counts rate output of the APD controller was monitored with a data logger (DrDAQ, Pico Technology). The time constant of the APD counter was set to 1.0 ms. The electrochemical setup is the one described in the previous section, and light emission was measured from a 0.43×10^{-3} M solution of **AMP-luc** in DMSO, containing 0.2 M Bu_4NClO_4 as supporting electrolyte, and with the platinum mesh working electrode bias ramped from 0.0 V to -2.0 V. The photon counts rate was corrected for the nominal wavelength-dependent efficiency of the counting module (ca. 70% at 625 nm). The 99% confidence limit of the mean photon counts value is reported as $t_{n-1}s/n^{1/2}$, where t_{n-1} is 3.05, s is the standard deviation, and n the number of repeated measurements (13).³⁵⁸

A1.1.5 Luminescence imaging. Time-resolved chemiluminescence images were recorded on a Nikon Eclipse Ti2-U inverted microscope fitted with a custom-built optoelectrochemical cell (Figure S20a) and using either a Plan Apo λ 4 \times /0.45 objective (part 88-378, Nikon, CFI Plan Fluor) or a Plan Apo λ 10 \times /0.45 objective (part 88-379, Nikon, CFI Plan Fluor). As for the spectroelectrochemical measurements, the electrolytic solution (**AMP-luc**, 0.43×10^{-3} M in 0.2 M $\text{Bu}_4\text{NClO}_4/\text{DMSO}$) was oxygen saturated and loaded in a glass Petri dish mounted on the microscope holder. Light emission was triggered by applying -2.0 V vs Ag/AgCl to a platinum

mesh working electrode. The electrochemical set up is analogous to the one described above for the spectroelectrochemical measurements, with the difference that the single-compartment electrochemical cell is made up from the petri dish and a PTFE holder designed to hold the working electrode's main face normal to the microscope objective axis (Figure S20b–c). Prior to the experiments, platinum electrodes were cleaned by continuous potential cycling as described above. Cathodic electrolysis of the **AMP-luc** solution leads to a transient light emission whose front diffuses away from the electrode surface. Time-resolved imaging of the **AMP-luc** electrochemically generated emission was performed with a colour camera (DS-Fi3, Nikon, Tokyo, Japan) without any filtering nor any excitation light, and using either 1.0 s (Figure 1c) or 500 ms (Figure 4a–c) exposure time. The gain set to its maximum for the shorter exposures. All microscopy images were analyzed with the Fiji image processing package.³¹⁸ Diffusivities were estimated by analyzing the profile of the red electrochemiluminescence intensity along the surface normal direction, as function of time after the initial cathodic potential pulse. Time-stamped light-intensity line profiles were used to estimate the distance from the electrode (r) at which the intensity reaches half of its maximum value. This distance was arbitrarily defined as the diffusion front. Images were not background subtracted, and for this analysis no attempts were made to improve contrast and sharpness. Line profiles such as those of Figure 4a–c of the main text are measured along a direction normal to the electrode surface, with point A being generally within 1–3 μm from the electrode surface. The diffusion coefficient was calculated assuming an Einstein's random walk ($r^2 = 2Dt$).^{319, 320} This procedure was repeated for 2 different videos, with at least 10 different locations sampled in each video. The 99% confidence limit of the mean photon counts value is reported as $t_{n-1}s/n^{1/2}$, where t_{n-1} is 2.68, s is the standard deviation and n the number of measurements (48).³⁵⁸ Electrochemiluminescence images shown in Figure 2 (main text) were recorded using a CMOS camera (CS235CU, Thorlabs) fitted with a machine-vision lens (MVL50M23, Thorlabs, 50 mm, f/2.8). Selected video frames reproduced in Figure 4a–c of the main text have been background subtracted for clarity (Fiji).

A1.1.6 Fluorescence imaging. The electrochemical conversion of **AMP-luc** to **ox-luc** can be used to map optically diffusivities. Unlike the electrolysis' starting material (**AMP-luc**), the product of the electroluminescent reaction, **ox-luc**, is fluorescent.¹⁴⁰ The procedure for the in-

situ optical mapping of diffusivities was similar to that reported above for the electroluminescence imaging and consisted in the analysis of the distance (r) travelled over time by the fluorescence front, away from the electrode surface and along the A–B line marked in Figure S17. Time-lapsed fluorescence emission images for the excitation of the electrochemically generated **ox-luc** were recorded with a CMOS monochrome camera (DS-Qi2, Nikon) using a 20 ms exposure time. Excitation and emission light were defined by a FITC filter/dichroic mirror cube (LED-FITC-A-NTF-ZERO, excitation filter part number FF01-474/27-25, emission filter part number FF01- 525/45-25, dichroic mirror part number FF495-Di03-25x36, BrightLine® , Semrock, Illinois). The obtained “optical” D values are in line with what can be obtained by established electrochemical methods for molecules of similar molecular weight, such as methyl viologen.³⁵⁹

A1.1.7 Theoretical calculations. To determine a reaction the mechanism, density functional theory (DFT) and time-dependent DFT (TD-DFT) calculations were performed using Gaussian 16 revision C.01.³⁶⁰ Geometry optimizations and frequency calculations were performed at the M062X/6-31+G(d,p) level of theory in the presence of DMSO, which was modelled using the SMD continuum solvent model.³⁶¹ All structures were conformationally searched using the Energy Directed Tree Search (EDTS) algorithm,³⁶² and all transition states were confirmed using Intrinsic Reaction Coordinate (IRC) calculations. Improved single point energies in solution were calculated using the ω B97XD functional with the Def2TZVP basis set with the SMD solvent model.³⁶³ Gibbs free energies were calculated using the direct method,³⁶⁴ whereby ideal gas partition functions were evaluated using the solution-phase geometries and frequencies. The conversion ($RT\ln(RT/P)$) from the gas-phase standard state of $P = 1.0$ atm used in the partition function calculations to the solution-phase standard of 1.0 M was added to the final Gibbs free energies.²⁷² pKa values (298 K, DMSO) were computed via an isodesmic method using 4-hydroxydinaphtho[2,1-d:1',2'-f][1,3,2]dioxaphosphepine 4-oxide (experimental pKa = 3.37¹³¹) as a reference. To determine the spectral tuning, excited state computations were performed employing QM and QM/MM calculations for vacuum and explicit solvents (THF and DMSO), respectively. The initial geometries of the luciferin for Quantum Mechanics/Molecular Mechanics (QM/MM) calculations in the explicit solvents were selected from MD snapshots of Classical MM simulations of keto-form in both dimethyl sulfoxide (DMSO)

and tetrahydrofuran (THF) solvents. The MM simulations were performed via Amber-18 suite employing ff10 force field.^{365, 366} We used DFT-B3LYP/6-311++G (p,d)³⁶⁷⁻³⁶⁹ with the IEFPCM implicit solvent model,³⁷⁰ GAFF force field³⁷¹ and RESP charges to parameterize the nonstandard residues in DMSO and THF. The keto form is solvated with an octahedral solvent box of 18 Å solvent molecules via standard amber tools techniques. The force fields of DMSO and THF molecules were parameterized as reported by Fox and Kollman method,³⁷² while the RESP method reported by Dupradeau et al.³⁷³ is used to assign their atomic charges. The solvated systems were then pre-equilibrated at constant volume and temperature, heating from 0 to 300 K, and then a 20-ns molecular dynamic simulation run was performed at constant temperature (300 K) and pressure (1atm) using Berendsen barostat as implemented in Amber-18.³⁷⁴ A cluster analysis performed over the snapshots extracted every 100 fs from the equilibrated system trajectory; then the snapshots characterized by highest populations and the lowest potential energies were extracted to be used as starting structures for the subsequent QM/MM calculations. Only solvent molecules within a 15Å distance from the keto-form atoms were eventually considered in defining the solvation shells around the solutes in the following QM/MM computations. To carry out the QM/MM calculation in DMSO and THF, a three-layer HML scheme has been designed through COBRAMM package,¹³⁶ where the QM region (high layer, H) involves the keto or the enol forms (enol form was adapted from the keto form snapshot after shifting the H atom from C5' to O11'), the surrounding solvent molecules that are 5Å apart were left free to move (medium layer, M), and the remaining solvent molecules were kept frozen at their snapshot coordinates (low layer, L). The keto and enol forms were treated quantum mechanically using the complete active space self-consistent field (CASSCF) level of theory as follows, while solvent molecules were described by the AMBER force field. The QM calculations were carried out using Molcas 8 as implemented in the QM/MM COBRAMM package employing an electrostatic embedding scheme.^{136, 375} The S1 excited-state geometries of the luciferin fluorophores (keto- and enol-forms) were optimized using unconstrained optimizations employing the complete active space self-consistent field (CASSCF) level of theory³⁷⁶ with ANO-S-VDZP basis set³⁵⁹ and averaging over the first two roots. In all the calculations and in agreement with our studies in different environment,³⁷⁷⁻³⁷⁹ the ionization-potential-electron-affinity shift³⁸⁰ was fixed at 0.0 au while the value 0.2 au was chosen for the imaginary shift.³⁸¹ An active space (AS) including 16 electrons distributed in 14

orbitals CAS(16,14) was used for optimizations, while the extended multistate second order perturbation correction method (XMS-CASPT2) was employed on top of the excited state optimized geometries to account for correlation energy and get experimentally accurate estimates of the emission spectra. An extended AS comprising 18 electrons in 15 orbitals, CAS (18, 15), was used in this case (Figures S21 and S22) by averaging over the first two (SA-2) roots.³⁸² Computations in the presence of an external linear homogeneous electric field in the Z-direction were performed using the FFPT module as incorporated in Molcas. All the structures have been re-optimized using the CASSCF gradients under the effect of an external homogenous electric field in each environment, employing Molcas and the QM/MM COBRAMM code. Applying the electric field along the z-direction this direction is associated with both direction of the charge transfer and the direction of the dipole moment change upon S 1 → S₀ transition (see Figure S11) consequently a maximum effect on the emission spectra is shown with applying the electric field in this direction.

A1.2 Supporting Figures

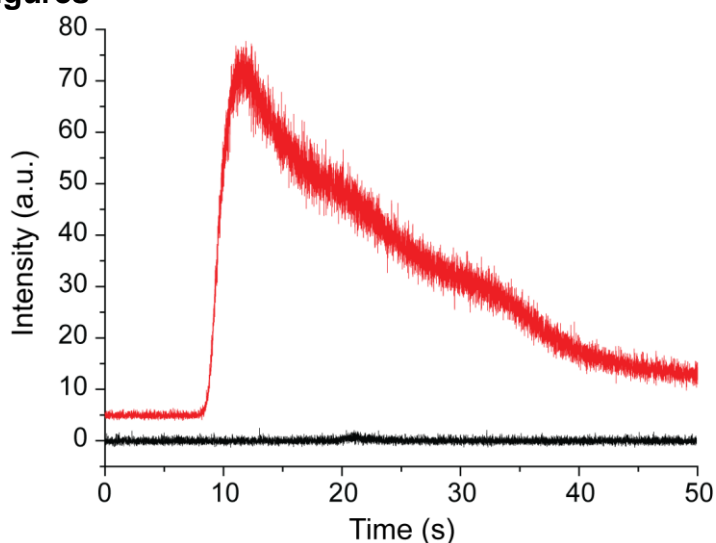


Figure S1. Time-evolution of the electrochemically generated light emission upon the electrolysis of **AMP-luc** (0.43×10^{-3} M in 0.2 M Bu₄NClO₄/DMSO) at a platinum mesh electrode. The electrolytic solution was either oxygen-saturated (red trace), or argon-saturated (black trace). The voltage of the working electrode was ramped from 0.0 V to -2.0 V (and back, one cycle) at a scan rate of 0.1 V/s. The electrochemiluminescence was monitored at 626 nm (emission slit set to 2.5 nm). The red trace is vertically offset by 5 a.u. for clarity purposes.

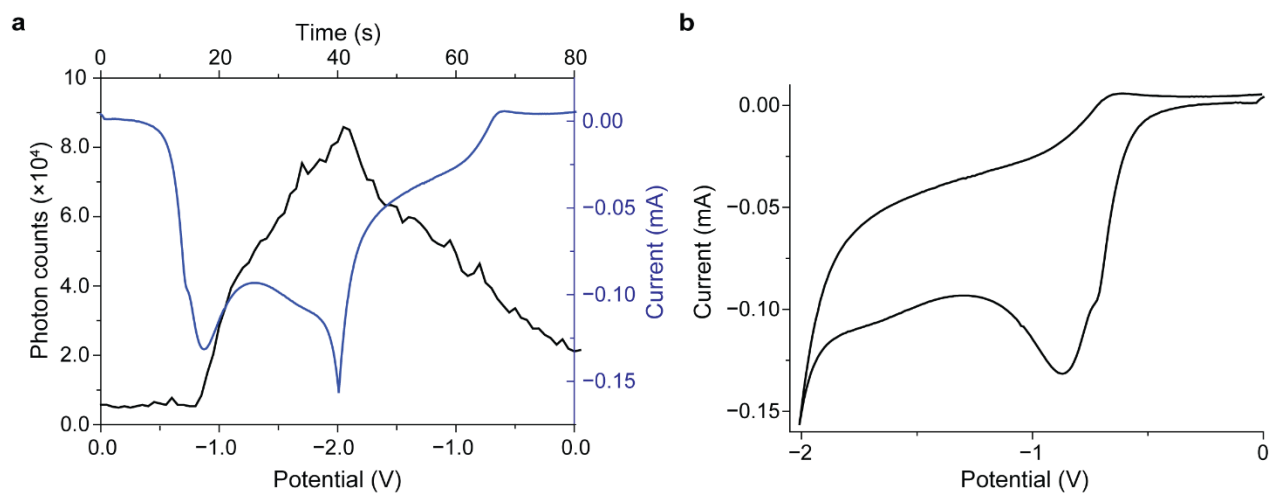


Figure S2. (a) Representative simultaneous photon counting and current recording for the electrochemically generated light emission from the electrolysis of an oxygen-saturated **AMP-luc** solution (0.43×10^{-3} M in in 0.2 M $\text{Bu}_4\text{NClO}_4/\text{DMSO}$) at a platinum mesh electrode. (b) The electrode potential was swept cyclically between 0.0 V (starting point) and -2.0 V at a voltage sweep rate of 0.05 V/s. The emission peak corresponds to $\sim 8.5 \times 10^4$ photon/s.

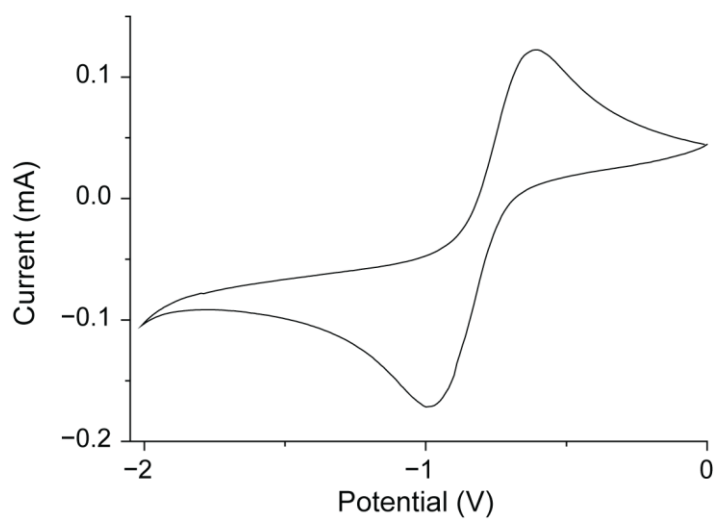


Figure S3. Representative cyclic voltammogram (CV) recorded at a platinum mesh electrode in oxygen-saturated 0.2 M $\text{Bu}_4\text{NClO}_4/\text{DMSO}$ (without **AMP-luc**). The voltage scan rate is 0.05 V/s.

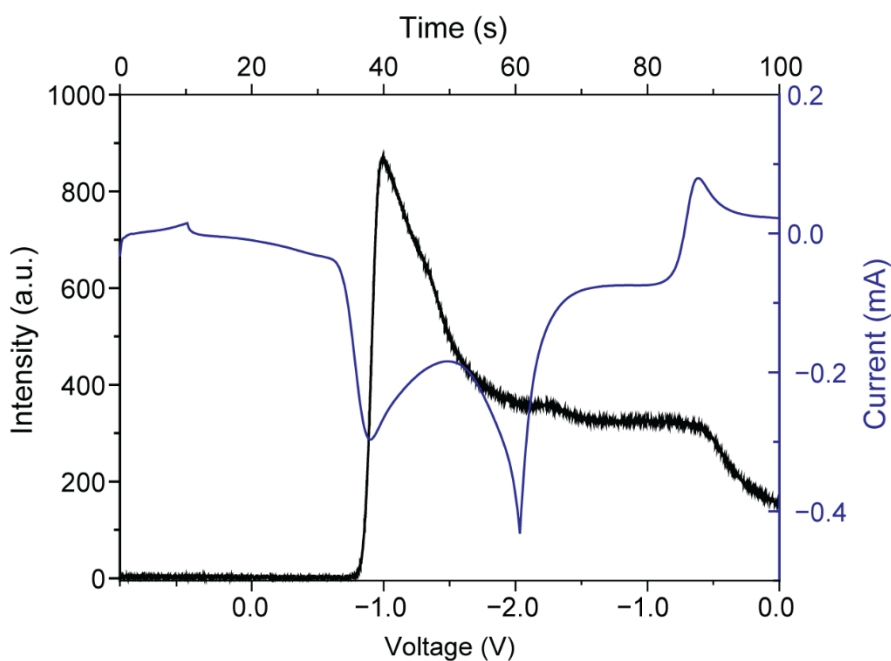


Figure S4. Time-evolution of the electro-generated emission of an oxygen-saturated **AMP-luc** solution (0.43×10^{-3} M in 0.2 M $\text{Bu}_4\text{NClO}_4/\text{DMSO}$) at a platinum mesh electrode. Light emission was recorded during a cyclic voltammetry (CV) experiment, with the working electrode bias ramped first from 0.0 V to +0.5 V, then from +0.5 V to -2.0 V (and back to 0.0 V). The electrochemiluminescence is monitored at 626 nm (black trace, Cary Eclipse). The potential scan rate was 0.05 V/s and the CV current (blue line) is plotted vs time.

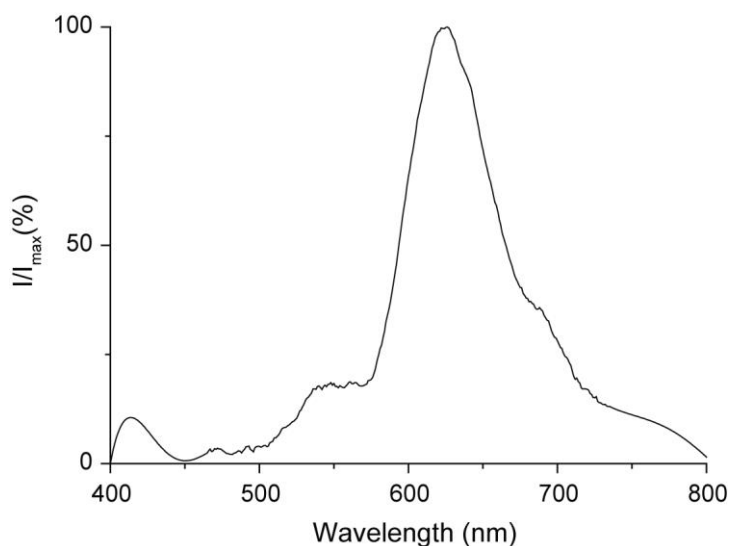


Figure S5. Representative emission spectrum for the cathodic electrolysis of an oxygen-saturated D-luciferin ethyl ester solution (0.5×10^{-3} M) at a platinum mesh electrode. The electrolyte was 0.2 M $\text{Bu}_4\text{NClO}_4/\text{DMSO}$. The working electrode bias is -3.0 V. At -2.5 V the emission was almost undetectable, and at -2.0 V no emission was detectable. The emission slit was set to 20 nm.

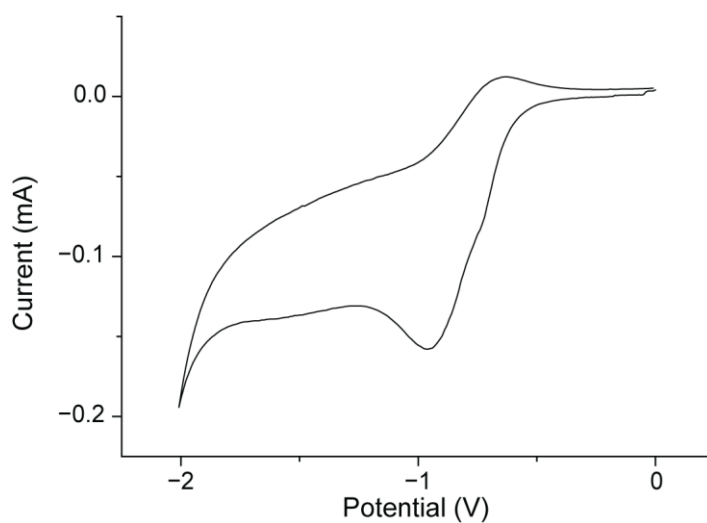


Figure S6. Representative cyclic voltammogram (CV) at a platinum mesh electrode of an **AMP-luc** solution ($\sim 0.43 \times 10^{-3}$ M in oxygen-saturated 0.2 M $\text{Bu}_4\text{NClO}_4/\text{DMSO}$) showing a clear reduction band for the one-electron reduction of oxygen to superoxide. The voltage scan rate is 0.05 V/s.

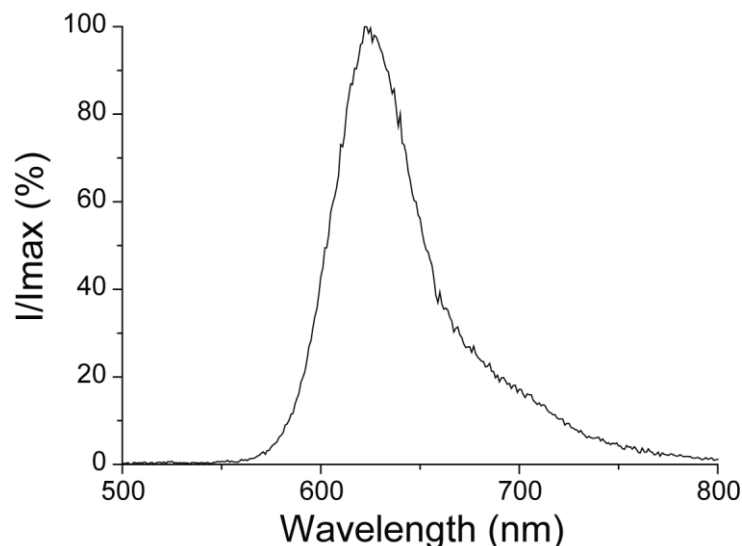


Figure S7. Emission spectrum from an **AMP-luc** solution (0.43×10^{-3} M, 0.2 M $\text{Bu}_4\text{NClO}_4/\text{DMSO}$) added to 0.02 g of KO_2 . The **AMP-luc** solution was bubbled with argon gas for ~ 20 min prior to the experiment. Full experimental details are in the experimental section, but in brief, a cuvette containing the KO_2 powder was placed in the spectrometer chamber (Cary Eclipse). To ensure no ambient light was reaching the detector, the **AMP-luc** solution (4 mL) was fed in one portion from a plastic syringe to the cuvette through a small tube silicone tubing (3.0 mm diameter). The emission spectra were recorded while the solution was being added to the cuvette (over a period of ~ 4.0 s), initiating the chemiluminescent reaction. A complete spectrum was recorded in approximately 1.5 s. The spectrometer sample compartment was kept under positive argon gas pressure. The solubility of KO_2 in DMSO is limited.³⁸³ The addition of the **AMP-luc** solution to the solid KO_2 sample results in a cloudy suspension, and unreacted solid KO_2 is still visible in the cuvette after the spectral measurement.

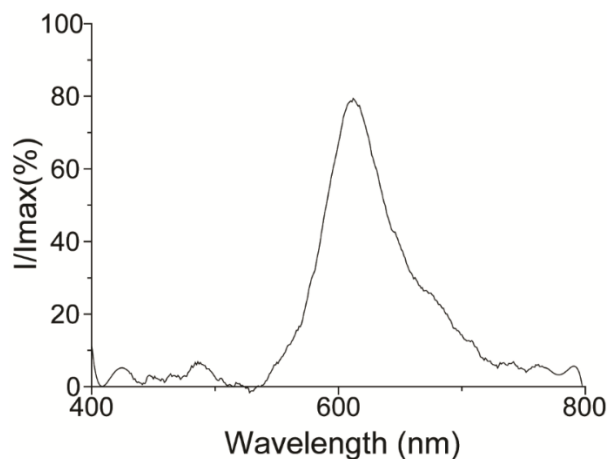


Figure S8. Representative emission spectrum for the cathodic electrolysis of an oxygen saturated **AMP-luc** solution (0.43×10^{-3} M) on a platinum mesh electrode. The electrolyte was 2.0 M LiClO₄ in DMSO. At such high concentrations of LiClO₄, the electrochemically triggered luciferin emission undergoes a blue shift. Data are collected applying a -2.5 V bias to the working electrode.

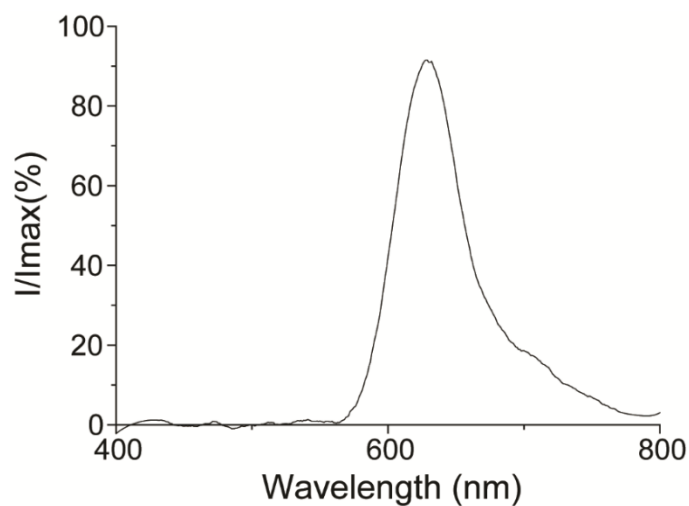


Figure S9. Representative emission spectrum obtained upon the cathodic electrolysis of an oxygen saturated **AMP-luc** solution (0.43×10^{-3} M) at a platinum mesh electrode. The electrolyte was 5.0×10^{-3} M LiClO₄/DMSO. Unlike for THF (Figure 3c, main text), with DMSO there is no shift at very low concentrations of LiClO₄. Data were collected applying -1.5 V to working electrode.

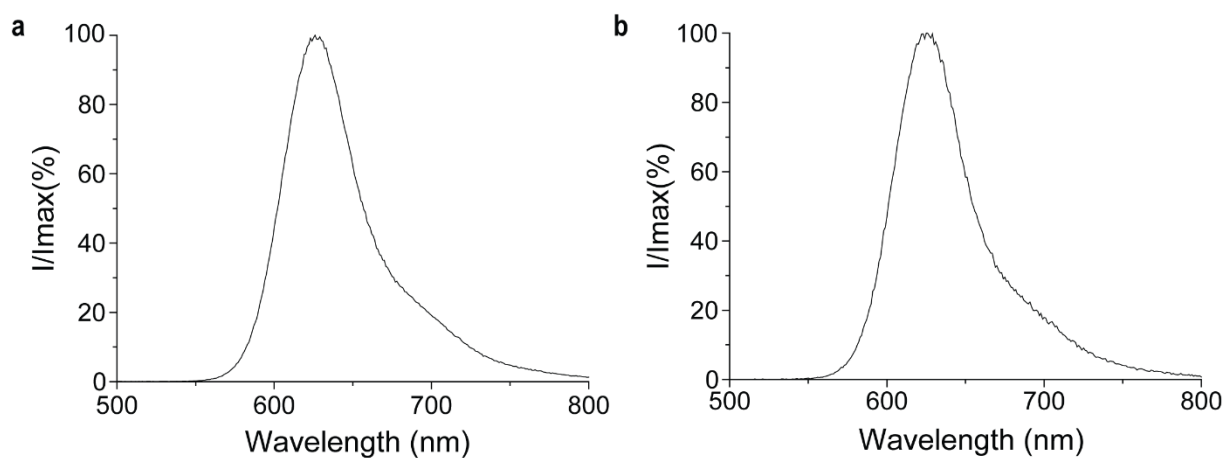


Figure S10. Representative emission spectra for the cathodic electrolysis of oxygen saturated **AMP-luc** solutions (0.43×10^{-3} M) at a platinum mesh electrode. The electrolytes were 0.2 M $\text{Bu}_4\text{NNO}_3/\text{DMSO}$ in (a), and 0.2 M $\text{Bu}_4\text{NPF}_6/\text{DMSO}$ in (b). Changes to the anion have no measurable effect on the energy of the **AMP-luc** electroluminescence. Data were collected applying -2.5 V to the working electrode.

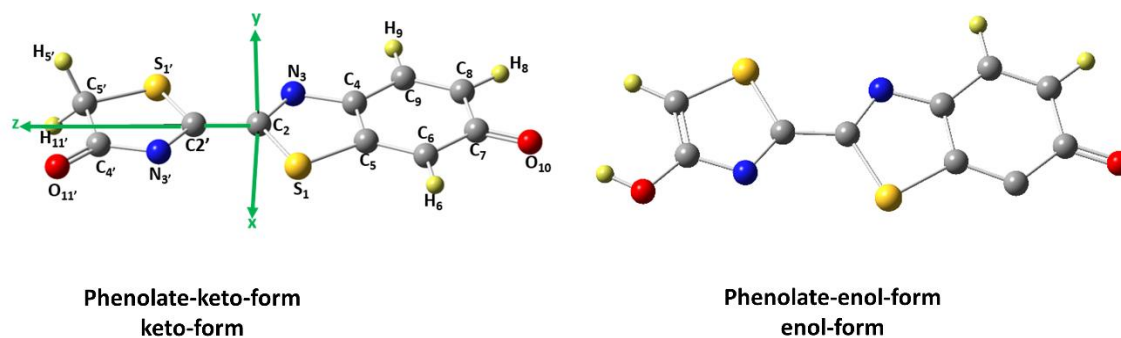


Figure S11. 3D model of the two luciferin isomers. The keto-form is shown on the right, and the enol-form on the left.

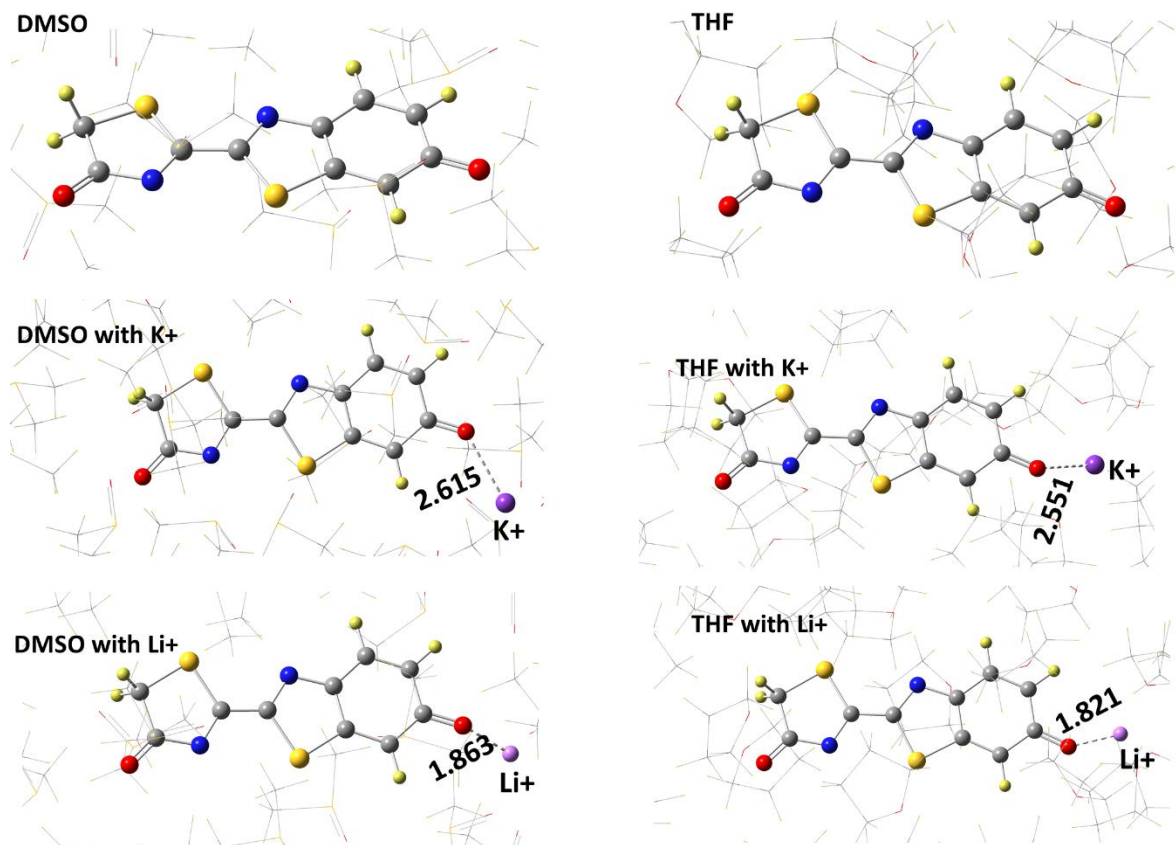


Figure S12. CASSCF optimized structure(s) of the Table 1 excited (emitter) species in molecular mechanics (MM) DMSO (left) and THF (right).

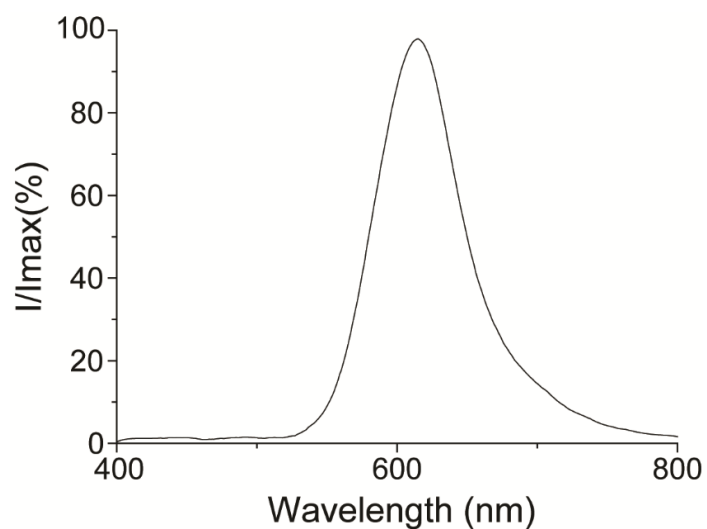


Figure S13. Representative emission spectra for the cathodic electrolysis of an oxygen saturated **AMP-luc** solution (0.43×10^{-3} M) at a platinum mesh electrode. The electrolyte was 0.2 M NaClO₄/THF. Unlike for LiClO₄, with NaClO₄ as electrolyte there is no shift in the **AMP-luc** electrochemiluminescent emission. Data were collected applying -2.0 V to the working electrode.

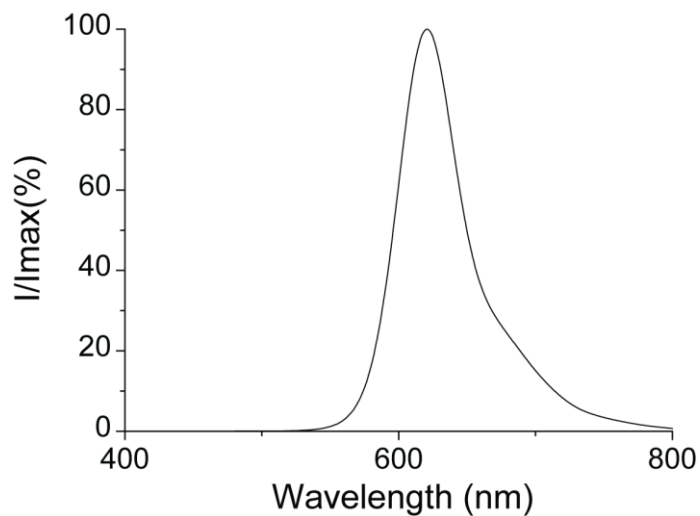


Figure S14. Representative emission spectrum for the cathodic electrolysis of an oxygen saturated **AMP-luc** solution (0.43×10^{-3} M) at a platinum mesh electrode. The electrolyte was 0.2 M $\text{Bu}_4\text{NClO}_4/\text{THF}$. Unlike for LiClO_4 , with B_4NClO_4 there is no shift in the **AMP-luc** emission. Data were collected applying -2.0 V to the working electrode.

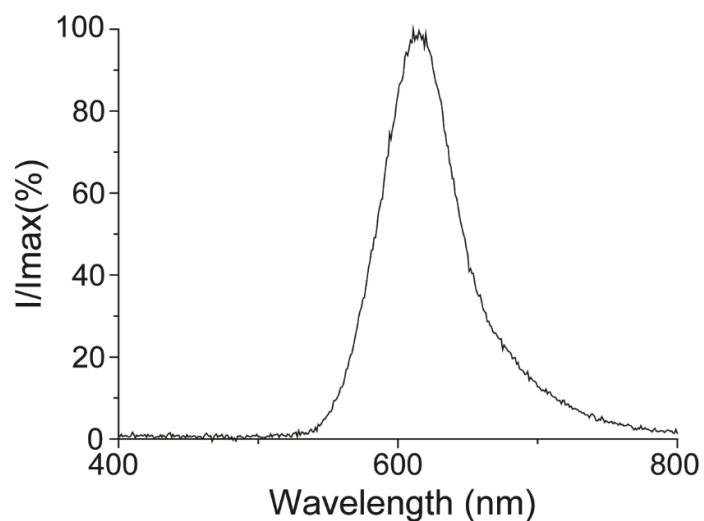


Figure S15. Representative emission spectrum for the cathodic electrolysis of an oxygen saturated **AMP-luc** solution (0.43×10^{-3} M) at a platinum mesh electrode. The electrolyte was 0.05 M NaBARF/THF. Experiments with a completely non-coordinating anion as BARF^- were used to exclude the anion influence on the spectral tuning of the **AMP-luc** electrochemiluminescent emission. Data were collected applying -2.0 V to the working electrode.

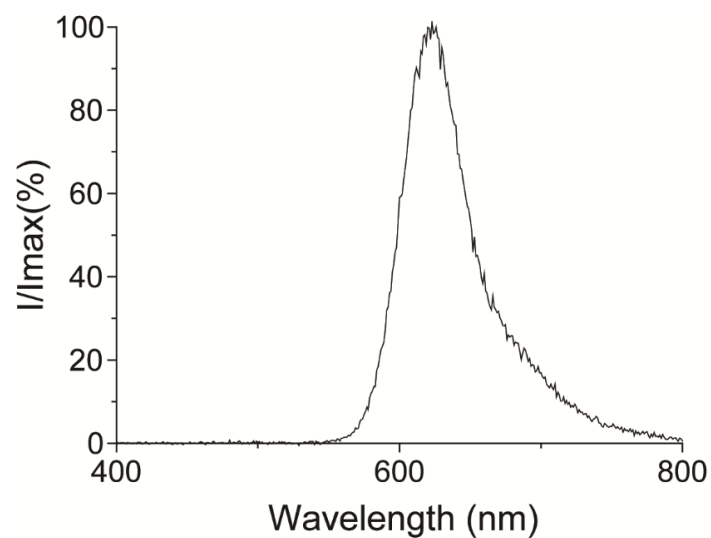


Figure S16. Representative emission spectrum for the cathodic electrolysis of an oxygen saturated **AMP-luc** solution (0.43×10^{-3} M) at a platinum mesh electrode. The electrolyte was 0.2 M $\text{Bu}_4\text{NClO}_4/\text{DMF}$. DMF is a solvent with a high dielectric constant (marginally lower than DMSO), consequently the emission remains in the red. Data was collected applying -2.5 V to the working electrode.

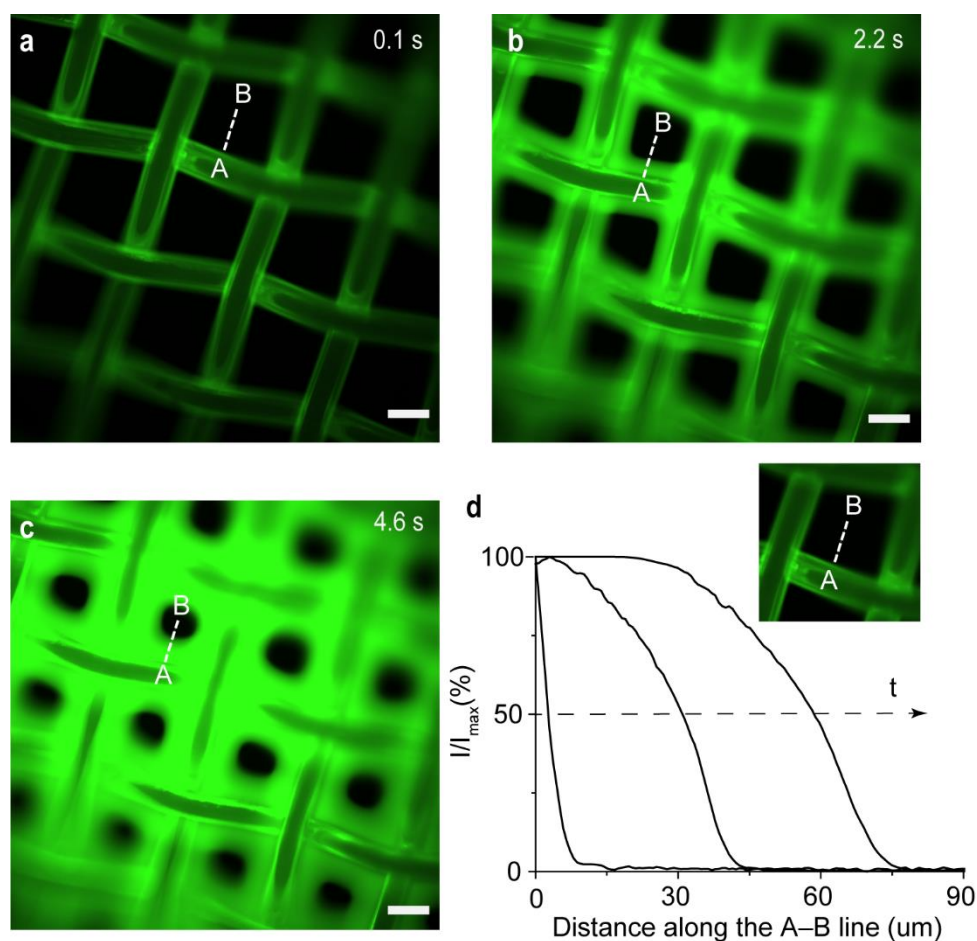


Figure S17. Selected time-stamped images (10 \times magnification) of in-situ generated **ox-luc** fluorescence (474 nm, excitation; 525 nm emission), recorded during the electrolysis of an oxygen-saturated **AMP-luc** solution (0.43×10^{-3} M in 2.0×10^{-1} M $\text{Bu}_4\text{NClO}_4/\text{DMSO}$). The fluorescence micrographs were captured under ambient air in a dark room at 0.1 s (a), 2.2 s (b) and 4.6 s (c) after the onset of the cathodic bias voltage (-2.0 V). Scale bars in (a–c) are 100 μm . (d) Selected fluorescence profiles sampled along the A–B line marked in (a–c) and in the panel inset, capturing the movement of the **ox-luc** diffusion front, away from the electrode’s surface, at electrolysis times (t) ranging between 0.1 and 4.6 s. The three thicker lines are the fluorescence intensity profiles for the time-stamped images in (a–c). By modelling diffusivity as an Einstein’s random walk ($r^2 = 2Dt$), we were able to estimate the **ox-luc** diffusivity (D) to 3.3×10^{-6} $\text{cm}^2 \text{s}^{-1}$.

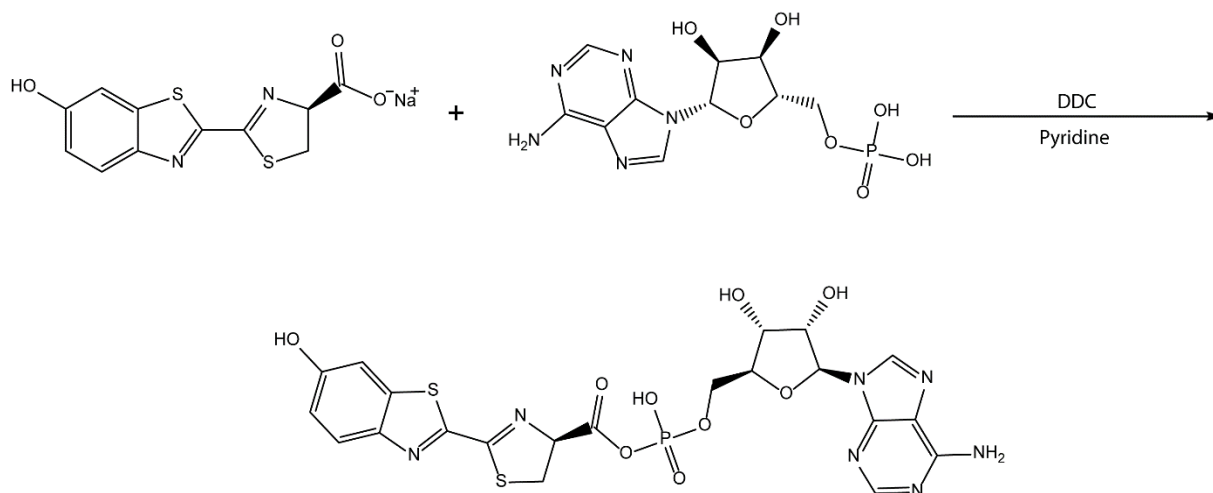


Figure S18. Synthetic scheme for the preparation of **AMP-luc** from luciferin sodium salt and adenosine monophosphate.

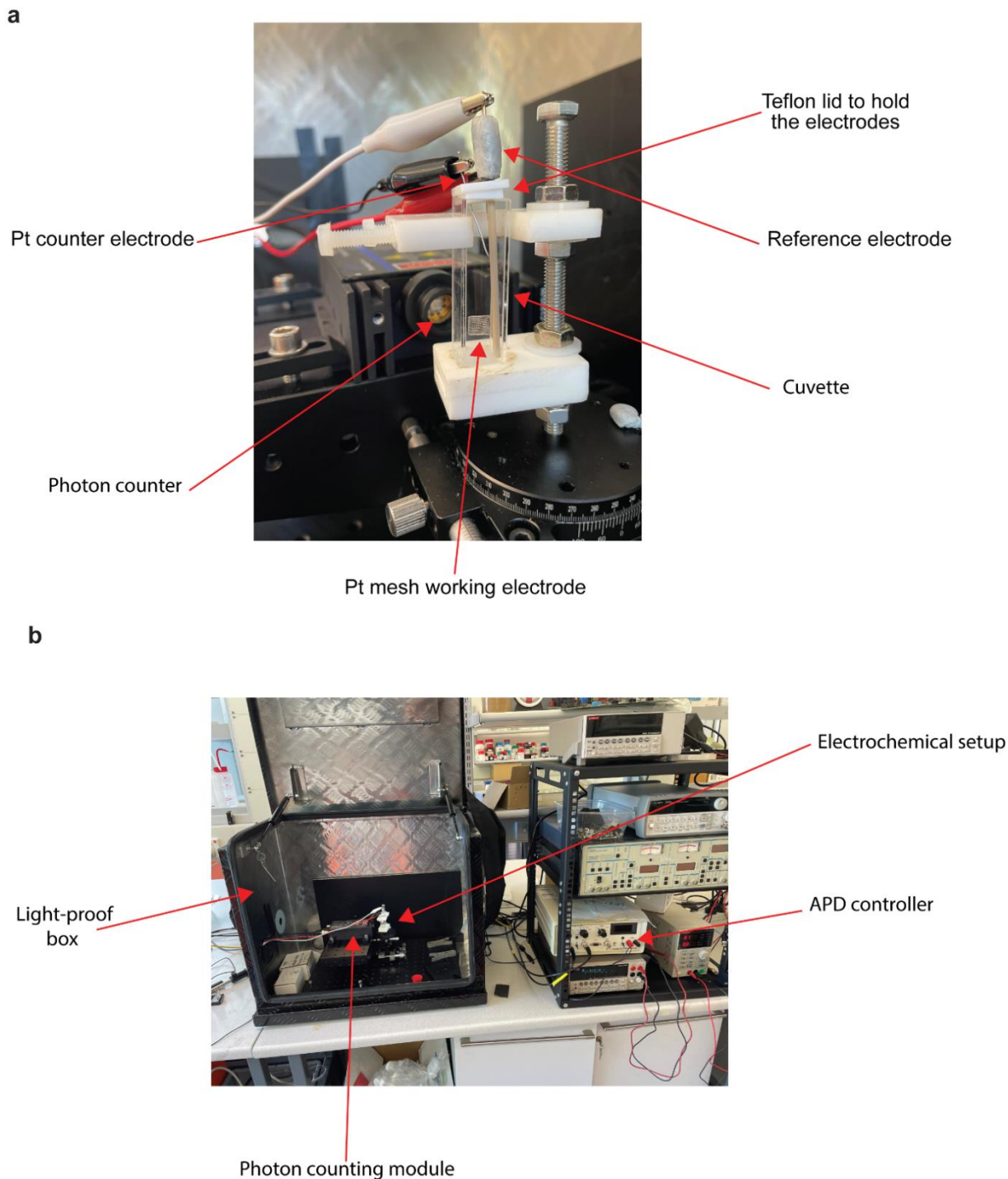


Figure S19. Experimental setup used for the photon-counting (quantitative) electrochemiluminescence experiments. (a) The cuvette containing the electrolytic solution and the three electrodes is placed in front of the counting module using a xyz stage for ensuring consistent positioning of the working electrode (a Pt mesh) relative

to the photon counter. Further details in the experimental. (b) Overall view of the experimental apparatus. When the light-proof box is sealed, the dark count approaches 500 photon/s.

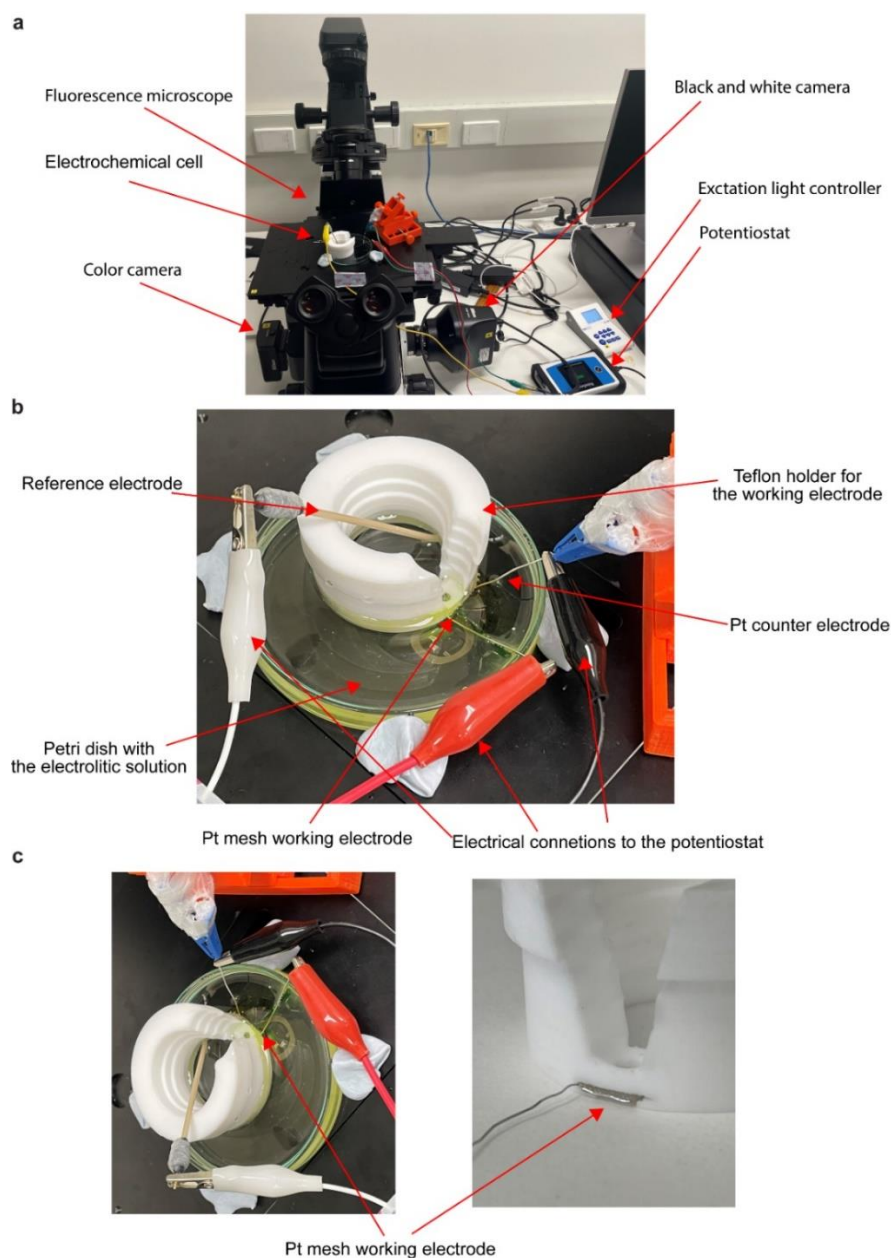


Figure S20. (a) Overview of the experimental setup for the collection of emission (electrochemiluminescence) and fluorescence time-resolved images. (b) A custom electrochemical cell was placed inside a Petri dish resting on the stage of an inverted microscope. The **AMP-luc** solution undergoing electrolysis was placed in the Petri dish. (c) A PTFE holder held the platinum mesh (working electrode) parallel to the Petri dish surface (~2 mm away from it). The electrolytic solution could reach the working electrode both from above (through a rounded hole) and below (opening clearly visible in figure). Further experimental details are in the experimental section.

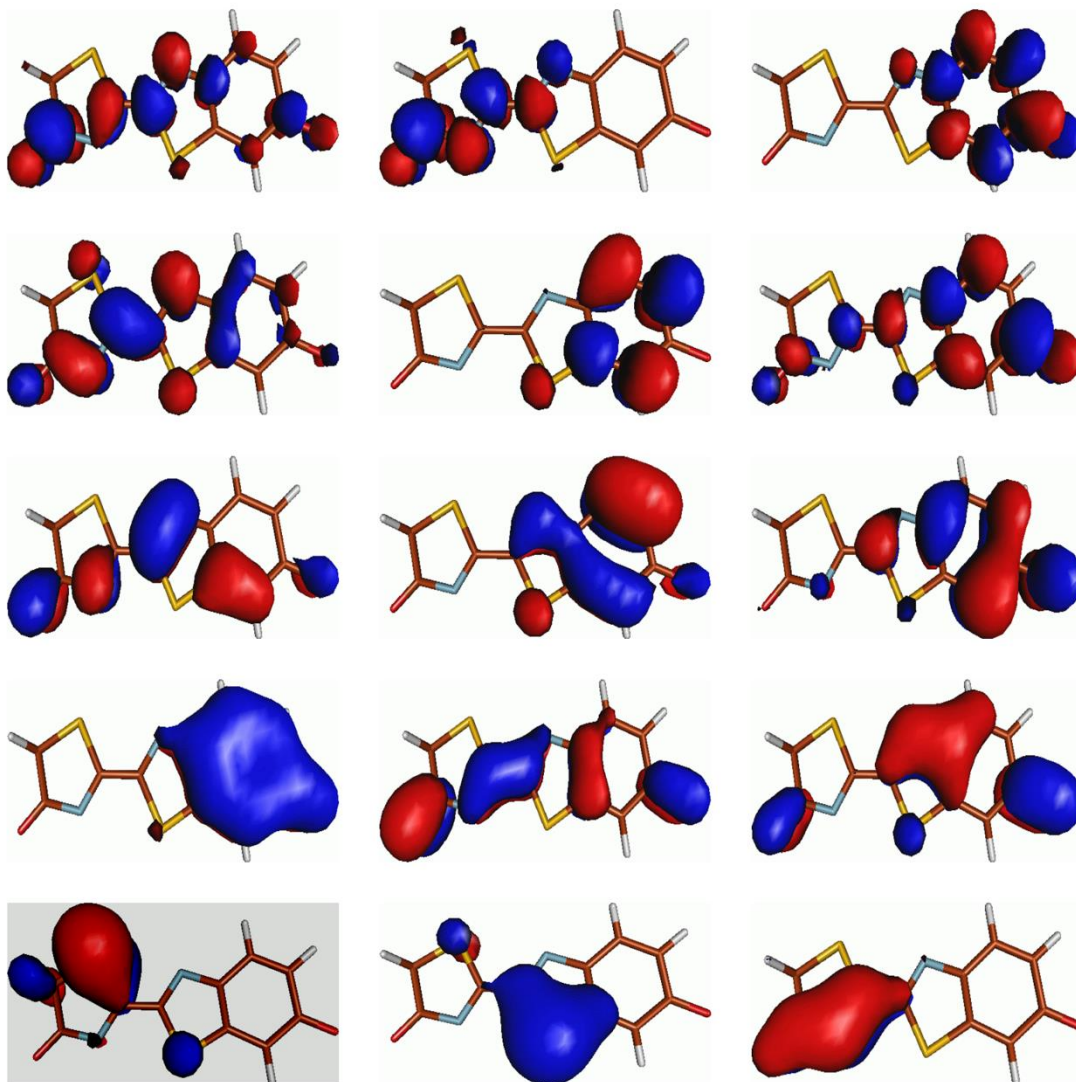


Figure S21. Active orbitals for the CAS(18,15) used in single point calculations for the keto form, the orbital shaded in gray is excluded to adapt CAS(16,14) for geometry optimization calculations. Orbital are arranged from left to right and bottom to top descending according to the occupation number.

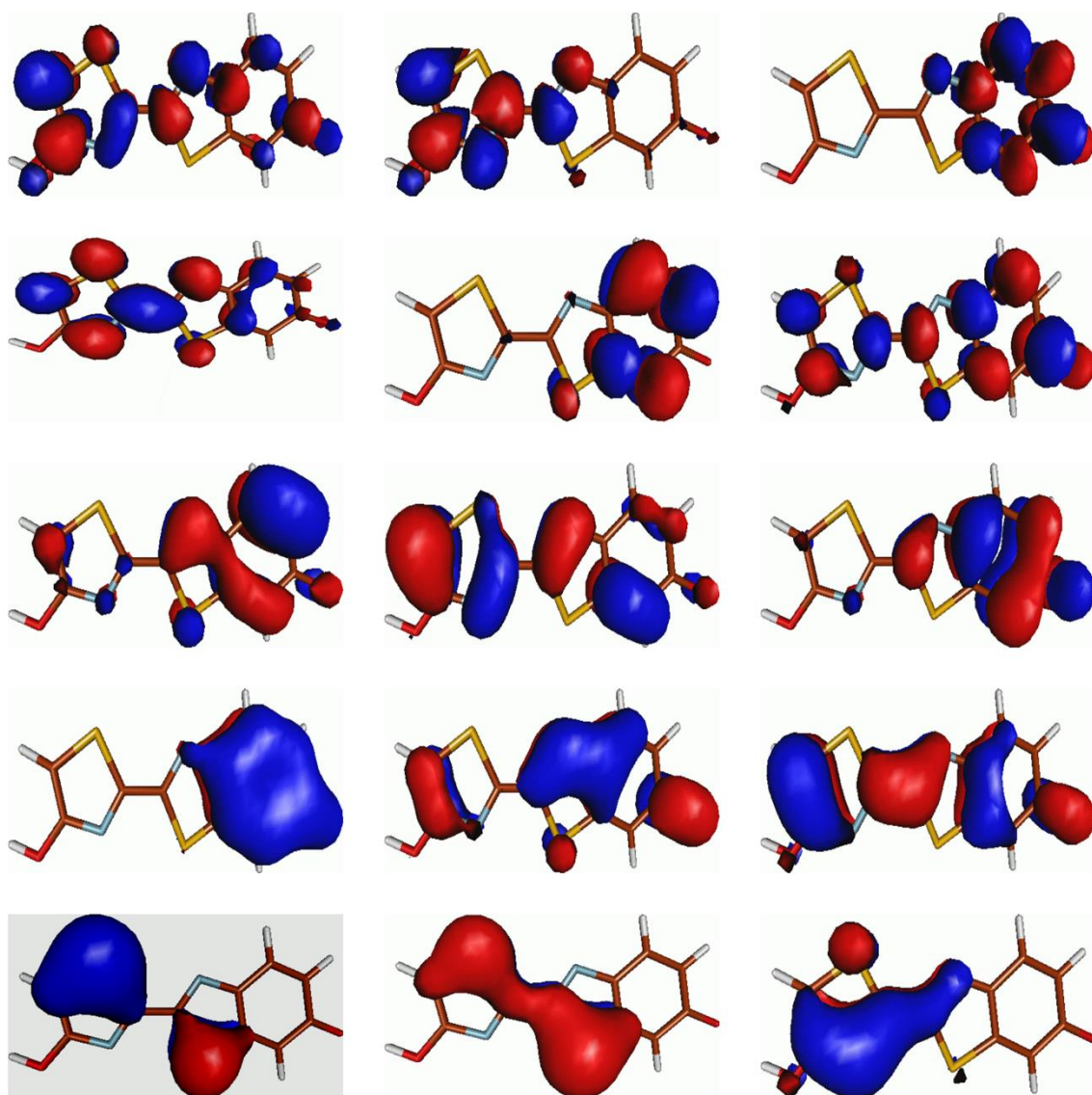


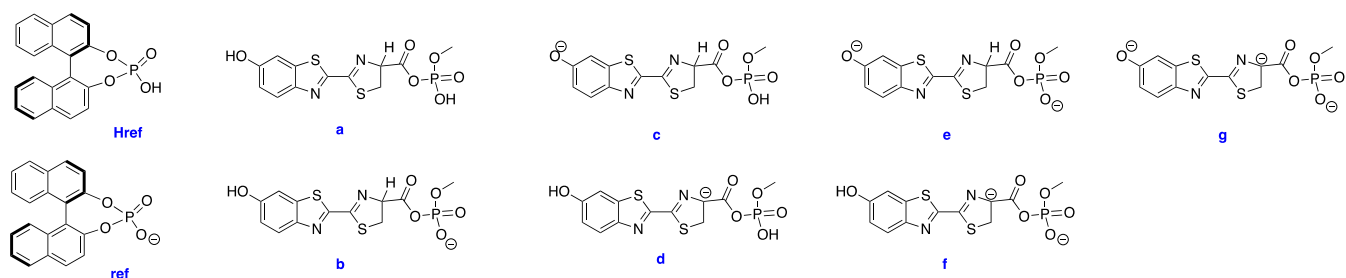
Figure S22. Active orbitals for the CAS(18,15) used in single point calculations for the enol form, the orbital shaded in gray is excluded to adapt CAS(16,14) for geometry optimization calculations. Orbital are arranged from left to right and bottom to top descending according to the occupation number.

A1.3 Supporting Tables

Table S1. The emission maxima (λ_{\max} in nm) of keto-form and enol-form computed at XMS-CASPT2 level of theory in different environments.

	Vacuum	DMSO	DMSO -K ⁺ ion- pair	DMSO-Li ⁺ ion-pair	THF	THF- K ⁺ ion- pair	THF-Li ⁺ ion-pair
Emission Maximums (λ_{\max})							
Enol	611	574	554	533	584	558	518
Keto	660	633	603	584	639	608	578
Exp		625					575
high conc.			610- 615				610
Relative Energy (kJ/mol)							
Enol	67.4	56.5	86.2	86.6	60.7	63.2	68.6
Keto	0	0	0	0	0	0	0
CT							
Enol	-0.27	-0.26	-0.28	-0.28	-0.27	-0.30	-0.27
Keto	-0.18	-0.20	-0.27	-0.25	-0.21	-0.26	-0.28

Table S2. Gaussian raw data (in a.u., otherwise indicated) and the value of imaginary frequencies (iFreq) for the species use to compute the pK_a values in Scheme 2. Nomenclature is below; note that **b** is the same as **AMP-luc⁻** in Scheme 3.

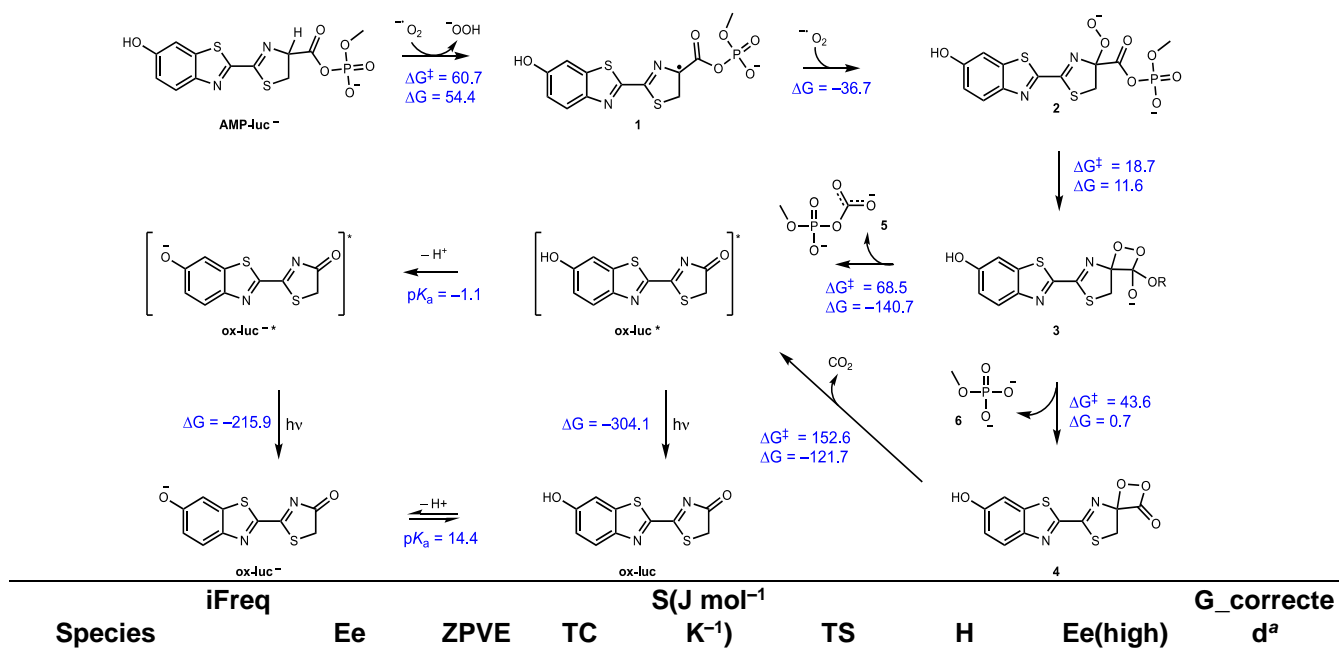


Specie	iFre				S(J mol ⁻¹ K ⁻¹)				G_corrected
s	q	Ee	ZPVE	TC	1)	TS	H	Ee(high)	a

Href	N/A	-	0.28573	0.01926	574.325373	0.06522	-	-	-
	1411.946770	9	6			0	1411.641765	1412.422039	1412.179245
ref	N/A	-	0.27445	0.01869	564.180896	0.06406	-	-	-
	1411.500551	9	4			8	1411.207398	1411.967450	1411.735357
a	N/A	-	0.23558	0.02291	684.611343	0.07774	-	-	-
	2162.163981	1	2			4	2161.905488	2162.744440	2162.560681
b	N/A	-	0.22402	0.02241	678.306269	0.07702	-	-	-
	2161.716635	6	6			8	2161.470193	2162.288971	2162.119557
c	N/A	-	0.22176	0.02282	683.854030	0.07765	-	-	-
	2161.685728	8	3			8	2161.441137	2162.258748	2162.088806
d	N/A	-	0.22132	0.02294	676.131194	0.07678	-	-	-
	2161.690944	3	7			1	2161.446673	2162.259660	2162.089162
e	N/A	-	0.21054	0.02216	673.559851	0.07648	-	-	-
	2161.236871	7	7			9	2161.004157	2161.801718	2161.642484
f	N/A	-	0.20939	0.02251	670.336866	0.07612	-	-	-
	2161.229334	6	5			3	2160.997423	2161.789833	2161.631035
g	N/A	-	0.19621	0.02216	664.480896	0.07545	-	-	-
	2160.739142	1	4			8	2160.520767	2161.291730	2161.145804

^aAfter adding phase change correction term to the Gibbs free energy

Table S3. Gaussian raw data (in a.u. unless otherwise indicated) and number of imaginary frequencies (NImag) for the species use to compute the Gibbs free energy barriers and reaction energies in Scheme 3. The nomenclature is defined in Scheme 3, which is reproduced here for convenience.



CO₂	N/A	-	0.01174	0.00357	0.02428	-	-	-
	188.518140	7	8	213.808955	0	188.502815	188.607090	188.616045
O₂⁻	N/A	-	0.00296	0.00331	0.02307	-	-	-
	150.388339	7	5	203.197761	5	150.382057	150.453385	150.470177
HOO-	N/A	-	0.01370	0.00383	0.02555	-	-	-
	150.992777	1	9	225.054179	7	150.975237	151.055559	151.063576
H₂O₂	N/A	-	0.02607	0.00382	0.02593	-	-	-
	151.502184	9	5	228.365224	3	151.472280	151.581668	151.577697
5	N/A	-	0.06877	0.01009	0.04562	-	-	-
	870.909434	2	8	401.728358	0	870.830564	871.209630	871.176380
6	N/A	-	0.05381	0.00744	0.03907	-	-	-
	682.354516	2	8	344.128507	9	682.293256	682.573549	682.551368
AMP-luc⁻	N/A	-	0.22402	0.02241	0.07702	-	-	-
	2161.71663	5	6	678.306269	8	2161.47019	2162.28897	2162.11955
AMP-luc⁻ to 1 TS	328.0	-	0.22384	0.02510	0.08269	-	-	-
	2312.08299	9	3	728.200896	4	2311.83405	2312.72985	2312.56360
1	N/A	-	0.21011	0.02235	0.07653	-	-	-
	2161.09067	1	1	674.000149	9	2160.85821	2161.66135	2161.50543
2	N/A	-	0.21876	0.02420	0.08055	-	-	-
	2311.52454	2	2	709.382537	7	2311.28157	2312.14900	2311.98659
2 to 3 TS	207.1	-	0.21807	0.02330	0.07740	-	-	-
	2311.51732	0	6	681.617313	4	2311.27594	2312.14343	2311.97946
3	N/A	-	0.21866	0.02346	0.07812	-	-	-
	2311.52137	7	7	687.931194	1	2311.27924	2312.14616	2311.98216
3 to ox-luc⁺ TS	594.4	-	0.21658	0.02350	0.07736	-	-	-
	2311.49488	4	8	681.309104	9	2311.25479	2312.11879	2311.95607
ox-luc	N/A	-	0.14805	0.01383	0.05452	-	-	-
	1440.75102	7	9	480.163134	7	1440.58913	1441.08560	1440.97823
ox-luc⁺	N/A	-	0.25057	0.01424	0.05557	-	-	-
	1440.73819	1	7	489.374179	3	1440.47337	1441.07163	1440.86239

		-					-	-	-
		1440.27717	0.13436	0.01369		0.05441	1440.12912	1440.60410	1440.51045
ox-luc⁻	N/A	9	1	6	479.185672	6	2	0	9
		-					-	-	-
		2311.49629	0.21785	0.02321		0.07673	2311.25522	2312.12538	2311.96105
3 to 4 TS	118.4	2	8	1	675.726119	5	3	5	2
		-					-	-	-
		1629.13177	0.16267	0.01626		0.06064	1628.95284	1629.54734	1629.42906
4	N/A	9	1	0	534.064478	8	8	6	3
		-					-	-	-
		1578.1629.06219	0.15896	0.01651		0.06148	1628.88671	1629.48492	1629.37093
4 to ox-luc⁺ TS	2	5	1	7	541.399851	1	7	9	2

^aAfter adding phase change correction term to the Gibbs free energy

Table S4. Cartesian coordinates all species used to compute the optimized geometries used to produce the data in Tables S2 and S3

a.xyz				C	4.279309	0.626142	0.043297
O	7.742842	-1.526816	0.254083	N	3.053800	1.231545	-0.022528
C	6.560653	-0.865680	0.174441	C	5.525403	1.282852	0.165340
C	5.347881	-1.533638	0.046778	H	5.549544	2.369193	0.212562
H	5.309087	-2.618582	0.005210	C	6.679592	0.542871	0.221940
C	4.192224	-0.752943	-0.024227	H	7.642583	1.038597	0.315613
S	2.539557	-1.275135	-0.181695	C	2.096043	0.359860	-0.128671
C	4.239295	0.655322	0.028873	C	0.693799	0.723227	-0.241017
N	3.010457	1.282690	-0.047420	N	-0.249960	-0.131053	-0.335475
C	5.478499	1.303520	0.156493	S	0.271228	2.456298	-0.294947
H	5.518966	2.387441	0.198131	C	-1.482691	1.986910	-0.111990
C	6.627752	0.543319	0.228114	C	-1.529178	0.510691	-0.572883
H	7.601243	1.012001	0.328050	H	-2.108259	2.627829	-0.732231
C	2.060632	0.413311	-0.155712	H	-1.769684	2.094123	0.937788
C	0.645510	0.781673	-0.263850	C	-2.647634	-0.216377	0.138963
N	-0.275155	-0.087774	-0.379416	H	-1.745524	0.466348	-1.650185
S	0.207131	2.503097	-0.264867	O	-2.553963	-1.112469	0.927077
C	-1.541841	2.002556	-0.090980	O	-3.852144	0.327474	-0.233877
C	-1.570516	0.537467	-0.584464	P	-5.271367	-0.144039	0.451652
H	-2.175874	2.649339	-0.696075	O	-5.424629	0.161431	1.878310
H	-1.825315	2.083621	0.961645	O	-6.278163	0.670827	-0.472715
C	-2.663431	-0.241045	0.114071	O	-5.411032	-1.678596	0.105120
H	-1.791551	0.510658	-1.661617	C	-5.287469	-2.165930	-1.247984
O	-2.540382	-1.211053	0.804280	H	-4.337416	-1.850224	-1.687033
O	-3.875208	0.344466	-0.147195	H	-5.314832	-3.251748	-1.179509
P	-5.274633	-0.220693	0.512024	H	-6.127190	-1.815729	-1.853609
O	-5.383235	-0.115304	1.970846	H	-6.116553	0.623398	-1.431485
O	-6.306713	0.710820	-0.260293				
O	-5.421387	-1.692508	-0.040878	d.xyz			
C	-5.340726	-1.988001	-1.451976	O	7.779380	-1.446203	-0.078294
H	-4.399339	-1.621130	-1.869792	C	6.583816	-0.792850	-0.071498
H	-5.378327	-3.072713	-1.533826	C	5.373726	-1.468812	0.063819
H	-6.192628	-1.551445	-1.979761	H	5.349928	-2.550265	0.170306
H	7.596372	-2.483898	0.210626	C	4.204386	-0.708021	0.057572
H	-6.180220	0.791302	-1.222189	S	2.552688	-1.254972	0.202240
				C	4.224686	0.694854	-0.078726
c.xyz				N	2.983853	1.310615	-0.068179
O	7.785052	-1.559981	0.218687	C	5.457508	1.348508	-0.212754
C	6.699005	-0.914329	0.164051	H	5.485586	2.428752	-0.319188
C	5.418158	-1.559259	0.041638	C	6.626879	0.605664	-0.209075
H	5.386026	-2.644005	-0.004364	H	7.592939	1.089316	-0.312340
C	4.265765	-0.794399	-0.014559	C	2.029415	0.435425	0.067613
S	2.603982	-1.329029	-0.162921	C	0.632174	0.754852	0.109561
				N	-0.304784	-0.132411	0.228947

S	0.080849	2.458569	-0.020309	O	-5.408914	-1.685727	0.208078
C	-1.666828	1.898015	0.122061	C	-5.381026	-2.221933	-1.111800
C	-1.556054	0.381858	0.238698	H	-4.422787	-2.006900	-1.599730
H	-2.223624	2.219570	-0.763090	H	-5.497091	-3.303265	-1.020472
H	-2.126260	2.362514	0.999673	H	-6.195777	-1.815120	-1.718021
C	-2.665655	-0.474243	0.341158				
O	-2.750519	-1.693314	0.429125	f.xyz			
O	-3.868387	0.300989	0.325442	O	7.761045	-1.515246	-0.010595
P	-5.323930	-0.387622	0.325110	C	6.575943	-0.836067	-0.023897
O	-5.792607	-1.078146	1.537775	C	5.348607	-1.491433	0.067938
O	-6.223396	0.903669	0.011451	H	5.304338	-2.574135	0.156222
O	-5.382709	-1.313852	-0.967039	C	4.192209	-0.713981	0.043126
C	-4.768410	-0.896294	-2.197230	S	2.526941	-1.243057	0.133507
H	-3.680917	-0.870842	-2.088472	C	4.233067	0.692321	-0.069246
H	-5.043488	-1.639871	-2.944071	N	3.005592	1.330624	-0.082705
H	-5.140300	0.083870	-2.511583	C	5.481890	1.322475	-0.157844
H	-5.830449	1.526356	-0.622205	H	5.532848	2.403877	-0.244681
H	7.637506	-2.398914	0.023169	C	6.642690	0.560310	-0.135752
				H	7.617538	1.032829	-0.204652
e.xyz				C	2.020586	0.467350	0.013500
O	7.752545	-1.583505	0.228328	C	0.646636	0.792066	0.027564
C	6.669257	-0.931368	0.172297	N	-0.322168	-0.094936	0.122977
C	5.386454	-1.568001	0.033558	S	0.085181	2.501598	-0.079685
H	5.348948	-2.652073	-0.024324	C	-1.662407	1.927827	-0.007574
C	4.237284	-0.796899	-0.022511	C	-1.546059	0.413669	0.118471
S	2.574015	-1.322517	-0.188220	H	-2.193045	2.235778	-0.913931
C	4.256851	0.621701	0.050586	H	-2.168221	2.385180	0.847973
N	3.032414	1.234173	-0.017075	C	-2.705427	-0.444327	0.211746
C	5.504391	1.270656	0.188163	O	-2.709532	-1.662704	0.316078
H	5.533702	2.356363	0.246929	O	-3.848441	0.303457	0.149162
C	6.655603	0.524430	0.245198	P	-5.408839	-0.267840	0.413739
H	7.619877	1.015372	0.350801	O	-5.500688	-0.922635	1.753792
C	2.072674	0.368570	-0.139120	O	-6.265913	0.903757	0.035648
C	0.668767	0.734799	-0.254759	O	-5.531017	-1.433021	-0.721449
N	-0.273056	-0.116685	-0.366116	C	-5.322614	-1.062381	-2.077534
S	0.245211	2.469897	-0.285961	H	-4.272789	-0.796470	-2.252045
C	-1.509175	1.991916	-0.123682	H	-5.574703	-1.928172	-2.693531
C	-1.557948	0.521456	-0.597691	H	-5.960621	-0.218044	-2.359273
H	-2.131815	2.639966	-0.739319	H	7.594958	-2.465547	0.070701
H	-1.804507	2.087773	0.925024	O	7.789825	-1.571719	0.026527
C	-2.696256	-0.202896	0.108121	C	6.704206	-0.902080	-0.001677
H	-1.761654	0.489057	-1.676985	C	5.410682	-1.520708	0.088042
O	-2.551980	-1.077370	0.926062	H	5.360444	-2.602556	0.182973
O	-3.864192	0.301092	-0.303617	C	4.258513	-0.744677	0.053724
P	-5.390452	-0.071310	0.380668	S	2.583909	-1.274358	0.142993
O	-5.351180	0.248048	1.836209	C	4.282078	0.662386	-0.069515
O	-6.338341	0.572889	-0.579417	N	3.043327	1.289829	-0.093489

C	5.534599	1.292773	-0.159715	H	-3.756901	-3.770127	-0.157455
H	5.578265	2.376032	-0.256061	H	0.716534	-3.513970	-1.765309
C	6.695470	0.539971	-0.127791	H	-1.621137	-4.213387	-1.237131
H	7.662388	1.033311	-0.198712	C	-3.412476	-2.794947	0.176723
C	2.069396	0.429789	0.006222	C	-2.480618	-0.298362	1.041933
C	0.677471	0.755127	0.010797	C	-3.737670	-0.732527	1.387585
N	-0.286470	-0.112511	0.123331	C	-4.218093	-1.988246	0.940729
S	0.137827	2.471874	-0.117933	H	-2.125536	0.660894	1.404158
C	-1.618073	1.917446	-0.102284	H	-4.367960	-0.109132	2.014576
C	-1.526764	0.408691	0.103211	H	-5.216585	-2.312990	1.216505
H	-2.097952	2.191958	-1.048220	O	2.124448	-0.396542	1.204761
H	-2.154201	2.429607	0.702016	O	1.790388	-1.237261	-1.151270
C	-2.677906	-0.427597	0.201963	P	2.881116	-1.210133	0.037474
O	-2.713586	-1.646482	0.361948	O	3.405006	-2.492705	0.520722
O	-3.826859	0.325494	0.062471	O	3.995717	-0.262168	-0.577762
P	-5.381962	-0.183085	0.401587	H	3.664729	0.541841	-1.017424
O	-5.488518	-0.660404	1.816036				
O	-6.232931	0.940770	-0.117955	ref.xyz			
O	-5.543865	-1.486689	-0.570651	C	3.132565	-3.415710	-0.954541
C	-5.267285	-1.316186	-1.952292	C	2.083985	-3.857219	-0.186012
H	-4.196108	-1.146577	-2.116006	C	1.029457	-2.978157	0.184370
H	-5.561185	-2.237290	-2.460800	C	1.075248	-1.612383	-0.223522
H	-5.834829	-0.477077	-2.369975	C	2.163126	-1.193396	-1.041720
				C	3.161073	-2.069681	-1.396391
Href.xyz				H	-0.105735	-4.491601	1.241457
-1.630201	4.320959	-0.965516		H	3.931575	-4.094532	-1.236484
C	-0.502523	4.340127	-0.183728	H	2.034333	-4.891437	0.145409
C	0.141381	3.129832	0.194013	C	-0.083845	-3.449668	0.933325
C	-0.410810	1.882122	-0.220211	C	0.017480	-0.723892	0.168667
C	-1.565422	1.897342	-1.052132	H	2.196254	-0.169622	-1.400435
C	-2.155860	3.084065	-1.414224	H	3.976996	-1.728716	-2.026865
H	1.748980	4.112441	1.264443	C	-1.070870	-1.253615	0.838951
H	-2.114034	5.249079	-1.253630	C	-1.122875	-2.611330	1.237020
H	-0.073324	5.280270	0.152438	H	-1.995173	-2.956571	1.782997
C	1.342607	3.154203	0.953543	C	-1.122993	2.611280	-1.237017
C	0.232947	0.662064	0.180133	C	-0.084001	3.449665	-0.933321
H	-1.975349	0.960915	-1.416159	C	1.029323	2.978203	-0.184368
H	-3.031827	3.074639	-2.055786	C	1.075176	1.612431	0.223521
C	1.427511	0.762811	0.861499	C	0.017448	0.723892	-0.168668
C	1.993034	1.990157	1.266685	C	-1.070926	1.253567	-0.838951
H	2.924815	1.982467	1.823150	H	2.034113	4.891529	-0.145405
C	0.035148	-2.864724	-1.225346	H	-1.995308	2.956483	-1.782992
C	-1.247480	-3.241392	-0.927838	H	-0.105939	4.491598	-1.241451
C	-2.101148	-2.380699	-0.184997	C	2.083812	3.857312	0.186014
C	-1.631086	-1.099811	0.228822	C	2.163074	1.193491	1.041717
C	-0.312295	-0.679818	-0.155391	C	3.160983	2.069819	1.396387
C	0.480785	-1.590076	-0.819963	C	3.132413	3.415848	0.954540

H	2.196249	0.169717	1.400429
H	3.976922	1.728890	2.026860
H	3.931393	4.094706	1.236484
O	-2.118531	-0.440866	1.183981
O	-2.118550	0.440771	-1.183981
P	-3.210022	-0.000071	-0.000000
O	-3.915439	1.201184	0.534366
O	-3.915389	-1.201354	-0.534366

CO2.xyz

O	0.000000	-0.000000	1.162759
C	0.000000	0.000000	0.000000
O	0.000000	-0.000000	-1.162759

5xyz

C	-1.820464	0.083596	-0.067256
O	-2.835202	-0.427842	-0.574858
O	-0.613867	-0.348635	-0.692897
P	0.827581	-0.573398	0.062799
O	0.670095	-1.427282	1.289153
O	1.772356	-0.977062	-1.040668
O	1.244480	0.926311	0.587047
C	1.152446	1.987779	-0.345850
H	0.102754	2.202076	-0.576680
H	1.605853	2.870866	0.112683
H	1.691849	1.753543	-1.272123
O	-1.713620	0.922790	0.841319

H2O2.xyz

O	0.703698	0.109897	-0.063895
O	-0.703877	-0.110093	-0.063568
H	-1.017402	0.609069	0.509351
H	1.018832	-0.607500	0.510356

HOO-.xyz

O	0.055511	0.790000	-0.000000
O	0.055511	-0.680438	0.000000
H	-0.888183	-0.876497	0.000000

6.xyz

P	-0.478739	0.207147	0.000000
O	-0.836952	-0.551152	1.288633
O	-0.836952	1.696545	0.000000
O	-0.836952	-0.551152	-1.288633
O	1.232398	0.257960	0.000000
C	1.872123	-0.989371	0.000000
H	1.609411	-1.580145	0.890322

H	1.609411	-1.580145	-0.890322
H	2.957181	-0.828296	0.000000

O2-*.xyz

O	0.000000	0.000000	0.661719
O	0.000000	-0.000000	-0.661719

3 to 4TS.xyz

O	-8.190274	-0.949107	-0.049395
C	-6.934744	-0.434992	-0.038249
C	-5.803979	-1.243838	-0.050563
H	-5.890525	-2.326914	-0.070077
C	-4.561502	-0.605580	-0.035532
S	-2.975353	-1.320214	-0.042212
C	-4.445588	0.799874	-0.008301
N	-3.150060	1.277374	0.004885
C	-5.605494	1.592071	0.002038
H	-5.519551	2.673948	0.021728
C	-6.838284	0.973486	-0.012789
H	-7.754568	1.554510	-0.004928
C	-2.303749	0.300688	-0.010848
C	-0.850021	0.495015	0.019035
N	-0.043117	-0.495434	-0.011817
S	-0.207706	2.130027	0.136464
C	1.472306	1.432066	-0.054396
C	1.336039	-0.072265	0.134976
H	2.164157	1.855892	0.669334
H	1.843337	1.640416	-1.057229
C	2.273512	-1.079815	-0.543289
O	1.851518	-0.582908	1.385833
O	2.349972	-1.630923	-1.598274
O	3.868921	0.444385	-0.507587
P	5.410565	0.258202	-0.488772
O	5.997309	-0.361388	-1.753053
O	6.133309	1.498806	0.048973
O	5.664759	-0.947822	0.670166
C	5.249739	-0.627997	1.974641
H	4.234178	-0.211906	1.980782
H	5.252762	-1.546130	2.574663
H	5.930894	0.095811	2.446073
O	2.585634	-1.632781	0.692768
H	-8.156576	-1.917643	-0.064054

3 to ox-luc* TS.xyz

O	-7.998218	-1.091473	-0.241893
C	-6.754010	-0.535730	-0.245640
C	-5.641571	-1.212542	0.248274

H	-5.736378	-2.216061	0.654828	N	0.178398	-0.342133	0.754159
C	-4.411308	-0.556708	0.198560	S	-0.050030	2.270438	0.449518
S	-2.851078	-1.133901	0.728845	C	1.642700	1.622995	0.674445
C	-4.276720	0.744243	-0.327871	C	1.515924	0.143985	1.057459
N	-2.992729	1.262731	-0.309099	H	2.159841	2.183167	1.454009
C	-5.414182	1.401351	-0.817420	H	2.183255	1.710388	-0.272147
H	-5.323332	2.403796	-1.224746	C	2.658618	-0.850216	0.603491
C	-6.642695	0.761947	-0.774692	O	1.811564	-0.113373	2.422073
H	-7.536975	1.250485	-1.148234	O	2.491758	-1.791107	-0.198104
C	-2.152757	0.413104	0.209534	O	3.880521	-0.074529	0.494396
C	-0.750621	0.653322	0.384512	P	4.563810	0.391524	-0.921984
N	0.074187	-0.203430	0.903242	O	3.556080	1.046220	-1.830129
S	0.000409	2.180333	-0.194195	O	5.816365	1.126639	-0.518179
C	1.565952	1.677944	0.619717	O	4.985449	-1.019499	-1.642804
C	1.373512	0.184746	0.813019	C	5.710511	-1.957255	-0.866831
H	1.691438	2.224540	1.566098	H	5.069594	-2.376386	-0.083492
H	2.407212	1.894739	-0.040192	H	6.032524	-2.759342	-1.536552
C	2.494634	-1.067261	-0.458632	H	6.596818	-1.497642	-0.411961
O	2.284995	-0.442908	1.660883	O	2.681957	-1.239799	2.109615
O	1.945478	-1.774846	-1.277848	H	-7.746459	-2.145322	-0.590123
O	3.392876	-0.098657	-0.808256				
P	5.059614	-0.336778	-0.771637				
O	5.364392	-1.756155	-1.129414	4 to ox-luc*TS.xyz			
O	5.598224	0.837998	-1.531483	O	6.236927	0.074940	0.189461
O	5.390255	-0.162654	0.815909	C	4.921984	-0.238662	0.088630
C	5.217717	1.123337	1.395505	C	4.016982	0.816132	0.110356
H	4.189348	1.476458	1.268100	H	4.368624	1.837935	0.203460
H	5.425998	1.025756	2.463378	C	2.664235	0.495975	0.007078
H	5.909468	1.847865	0.953656	S	1.297870	1.568461	-0.011845
O	2.701353	-1.581292	0.856913	C	2.213628	-0.837059	-0.115240
H	-7.963027	-1.980550	0.140611	N	0.846970	-0.988447	-0.210040
				C	3.150805	-1.882563	-0.132989
3.xyz				H	2.812794	-2.909643	-0.226909
O	-7.807037	-1.186409	-0.716160	C	4.493722	-1.579817	-0.032682
C	-6.588002	-0.612490	-0.546382	H	5.234892	-2.374805	-0.046902
C	-5.457286	-1.358042	-0.232309	C	0.255481	0.160412	-0.167782
H	-5.513185	-2.436322	-0.111551	C	-1.202553	0.316895	-0.262477
C	-4.254473	-0.664481	-0.079143	N	-1.962817	-0.604193	-0.715438
S	-2.680109	-1.296525	0.308800	S	-1.949107	1.838195	0.282553
C	-4.175679	0.734368	-0.234358	C	-3.509805	1.319202	-0.488698
N	-2.914102	1.271179	-0.053021	C	-3.336518	-0.207606	-0.612571
C	-5.333461	1.462169	-0.552191	H	-3.602167	1.762108	-1.482974
H	-5.277508	2.539454	-0.673746	H	-4.361117	1.601785	0.130987
C	-6.528545	0.788307	-0.706027	C	-3.953397	-0.978685	0.776073
H	-7.441571	1.320756	-0.951830	O	-4.229354	-0.890937	-1.277908
C	-2.058847	0.344516	0.228436	O	-3.623823	-0.741135	1.880601
C	-0.635055	0.599031	0.486817	O	-4.794517	-1.799238	0.256284
				H	6.776442	-0.729776	0.163661

4.xyz

O	6.207980	-0.989340	-0.017401
C	4.954611	-0.474435	0.001100
C	3.822636	-1.280823	-0.030959
H	3.906629	-2.363443	-0.071791
C	2.582281	-0.639347	-0.009384
S	0.995877	-1.350392	-0.042372
C	2.469661	0.766750	0.043930
N	1.177681	1.245729	0.060858
C	3.632164	1.556480	0.076909
H	3.548317	2.637797	0.118581
C	4.861835	0.934707	0.055159
H	5.780213	1.511956	0.078783
C	0.329780	0.269320	0.020789
C	-1.117794	0.478978	0.012256
N	-1.939866	-0.506087	-0.017064
S	-1.737729	2.124522	0.015169
C	-3.417883	1.440338	0.198156
C	-3.290587	-0.048234	-0.123401
H	-4.121730	1.936197	-0.471195
H	-3.738830	1.572437	1.234379
C	-4.329080	-0.987143	0.482110
O	-3.866341	-0.435403	-1.409564
O	-4.683485	-1.388091	1.540169
O	-4.824391	-1.312231	-0.746623
H	6.174485	-1.957544	-0.052698

Ox-luc-.xyz

O	0.607877	-5.542321	0.000000
C	0.222913	-4.345030	0.000000
C	1.142543	-3.233271	0.000000
H	2.207873	-3.443338	0.000000
C	0.653769	-1.944332	0.000000
S	1.539390	-0.437411	-0.000000
C	-0.746966	-1.646742	0.000000
N	-1.067510	-0.334402	0.000000
C	-1.669743	-2.727488	0.000000
H	-2.735168	-2.510638	0.000000
C	-1.203408	-4.011114	0.000000
H	-1.895900	-4.848826	0.000000
C	0.000000	0.426983	-0.000000
C	-0.054378	1.856716	-0.000000
N	1.012186	2.605069	-0.000000
S	-1.637747	2.643640	-0.000000
C	-0.804923	4.248976	-0.000000
C	0.698690	3.960658	-0.000000

H	-1.066807	4.824347	0.890612
H	-1.066807	4.824347	-0.890612
O	1.527974	4.848276	-0.000000

1.xyz

O	-7.739970	-1.500723	0.029784
C	-6.555552	-0.837085	0.036210
C	-5.336305	-1.500392	-0.059095
H	-5.295385	-2.582764	-0.145400
C	-4.178873	-0.721214	-0.039409
S	-2.521198	-1.245403	-0.132964
C	-4.225606	0.686001	0.070238
N	-3.000478	1.316269	0.077983
C	-5.472292	1.327820	0.162713
H	-5.515975	2.409169	0.247190
C	-6.624523	0.567582	0.145990
H	-7.601508	1.034440	0.216877
C	-2.033610	0.447609	-0.019356
C	-0.646881	0.803674	-0.035036
N	0.320293	-0.111206	-0.129528
S	-0.124591	2.471658	0.070541
C	1.612854	1.919481	-0.016051
C	1.519591	0.423200	-0.123979
H	2.154617	2.233785	0.881902
H	2.108349	2.362617	-0.885996
C	2.725927	-0.438059	-0.223942
O	2.682207	-1.643171	-0.333254
O	3.831440	0.311283	-0.164662
P	5.424494	-0.275983	-0.412209
O	5.478738	-0.946328	-1.741613
O	6.259642	0.908150	-0.047097
O	5.502419	-1.413187	0.742830
C	5.412675	-0.999065	2.103871
H	4.417950	-0.592776	2.322685
H	5.576671	-1.885464	2.718981
H	6.170990	-0.245561	2.335352
H	-7.589424	-2.454747	-0.049689

ox-luc.xyz

O	0.237113	-5.551744	0.000000
C	-0.057633	-4.229098	0.000000
C	0.930597	-3.252117	0.000000
H	1.982836	-3.520599	0.000000
C	0.510914	-1.920020	0.000000
S	1.482573	-0.479360	0.000000
C	-0.857187	-1.568678	0.000000
N	-1.108202	-0.215708	0.000000

C	-1.834789	-2.580051	0.000000	N	-1.148450	-0.274301	0.000000
H	-2.886717	-2.312852	0.000000	C	-1.877083	-2.635000	0.000000
C	-1.432007	-3.897447	0.000000	H	-2.925653	-2.349767	0.000000
H	-2.157997	-4.703773	0.000000	C	-1.496883	-3.947746	0.000000
C	0.000000	0.454237	0.000000	H	-2.236419	-4.743501	0.000000
C	0.042180	1.913787	0.000000	C	0.000000	0.429475	0.000000
N	1.158447	2.559242	0.000000	C	0.065877	1.837769	0.000000
S	-1.476011	2.794229	0.000000	N	1.211813	2.519219	0.000000
C	-0.532990	4.339277	0.000000	S	-1.439487	2.773514	0.000000
C	0.944822	3.950089	0.000000	C	-0.457713	4.296832	0.000000
H	-0.758068	4.929739	0.891181	C	1.020118	3.869615	0.000000
H	-0.758068	4.929739	-0.891181	H	-0.669108	4.896970	0.888891
O	1.842924	4.759093	0.000000	H	-0.669108	4.896970	-0.888891
H	1.197556	-5.683558	0.000000	O	1.914512	4.714411	0.000000

Ox-luc*.xyz

O	0.271430	-5.508280	0.000000
C	-0.051566	-4.225043	0.000000
C	0.951893	-3.212899	0.000000
H	2.001829	-3.491862	0.000000
C	0.532565	-1.911193	0.000000
S	1.503847	-0.450616	0.000000
C	-0.869759	-1.558985	0.000000
N	-1.149710	-0.258887	0.000000
C	-1.849539	-2.612513	0.000000
H	-2.901534	-2.346633	0.000000
C	-1.440633	-3.915458	0.000000
H	-2.149913	-4.736382	0.000000
C	0.000000	0.471485	0.000000
C	0.031834	1.872757	0.000000
N	1.167653	2.570885	0.000000
S	-1.492890	2.775342	0.000000
C	-0.539398	4.315535	0.000000
C	0.947106	3.919037	0.000000
H	-0.764082	4.910292	0.889173
H	-0.764082	4.910292	-0.889173
O	1.824102	4.777856	0.000000
H	1.237595	-5.638259	0.000000

Ox-luc-.xyz

O	0.253075	-5.552797	0.000000
C	-0.092863	-4.352362	0.000000
C	0.905287	-3.281591	0.000000
H	1.953957	-3.563587	0.000000
C	0.492261	-1.974801	0.000000
S	1.486083	-0.522893	0.000000
C	-0.889573	-1.601247	0.000000

AMP-luc- to 1 TS.xyz

O	-7.894154	-1.258433	-0.483944
C	-6.673114	-0.662431	-0.411793
C	-5.496861	-1.397975	-0.302846
H	-5.518217	-2.484144	-0.272033
C	-4.297144	-0.687172	-0.235826
S	-2.674503	-1.308172	-0.094219
C	-4.259829	0.721057	-0.277181
N	-2.993799	1.278769	-0.206462
C	-5.460964	1.436673	-0.387236
H	-5.441321	2.521745	-0.419889
C	-6.657220	0.745018	-0.453534
H	-7.601580	1.272692	-0.539400
C	-2.087481	0.356068	-0.112026
C	-0.665606	0.618827	-0.023964
N	0.217248	-0.315676	0.056973
S	-0.060815	2.298191	-0.037691
C	1.655521	1.650020	-0.100021
C	1.495118	0.167847	0.239562
H	2.272285	2.190322	0.620427
H	2.069613	1.808715	-1.102535
C	2.617236	-0.747466	0.043145
H	1.363572	0.205026	1.782966
O	2.550501	-1.962300	-0.033052
O	3.783755	-0.061735	0.010841
P	5.278053	-0.798675	-0.306808
O	5.705274	-1.596471	0.881287
O	5.238716	-1.341058	-1.702091
O	6.129620	0.595043	-0.273083
C	5.913394	1.533992	-1.320884
H	6.595014	2.369968	-1.150402
H	6.122142	1.086413	-2.297312

H 4.881768 1.904307 -1.305194
O 1.077102 0.282033 2.835751
O -0.267609 0.135177 2.882611
H -7.797084 -2.221678 -0.448446

AMP-luc-xyz

O 7.717587 -1.544258 0.237811
C 6.536492 -0.879015 0.169256
C 5.322073 -1.542320 0.033192
H 5.280966 -2.626502 -0.023739
C 4.167890 -0.758394 -0.027036
S 2.513947 -1.274331 -0.194056
C 4.218108 0.648652 0.044847
N 2.990437 1.280395 -0.026519
C 5.458442 1.292123 0.181895
H 5.501202 2.375306 0.238437
C 6.606535 0.528605 0.242956
H 7.581002 0.993957 0.349079
C 2.038382 0.415528 -0.148126
C 0.623427 0.785836 -0.262658
N -0.297503 -0.080261 -0.388443
S 0.187879 2.510026 -0.265726
C -1.564031 2.008842 -0.121507
C -1.594200 0.541790 -0.607846
H -2.187427 2.655403 -0.737639
H -1.866446 2.095442 0.925698
C -2.717199 -0.212983 0.091542
H -1.794273 0.512817 -1.687758
O -2.553087 -1.115437 0.874442
O -3.891523 0.298574 -0.285300
P -5.407234 -0.108605 0.407479
O -5.342633 0.153570 1.873039
O -6.370891 0.569203 -0.512308
O -5.418980 -1.714343 0.171215
C -5.417942 -2.197879 -1.169508
H -4.472967 -1.955530 -1.670359
H -5.523717 -3.282840 -1.118230
H -6.249608 -1.774097 -1.739900
H 7.568377 -2.500116 0.180249

2 to 3 TS.xyz

O -7.831332 -1.208142 -0.655364
C -6.611779 -0.628101 -0.509770
C -5.475967 -1.364929 -0.193433
H -5.528098 -2.440746 -0.050803
C -4.273045 -0.666191 -0.067081
S -2.693518 -1.287466 0.318044

C -4.198538 0.729171 -0.251492
N -2.935563 1.271866 -0.094236
C -5.361296 1.448176 -0.570227
H -5.309265 2.523033 -0.713189
C -6.556991 0.769209 -0.697100
H -7.473749 1.295407 -0.942483
C -2.075946 0.352937 0.198112
C -0.648892 0.612806 0.435850
N 0.164780 -0.317321 0.725120
S -0.068345 2.287684 0.339407
C 1.623011 1.665170 0.609919
C 1.511466 0.181606 1.029783
H 2.111307 2.239396 1.398028
H 2.194303 1.754688 -0.318565
C 2.587565 -0.729860 0.381378
O 1.794117 -0.006838 2.371657
O 2.360641 -1.600251 -0.437547
O 3.832442 -0.128211 0.481611
P 4.721239 0.353250 -0.839371
O 3.850645 1.144301 -1.772260
O 5.975749 0.930633 -0.249613
O 5.061904 -1.056625 -1.590685
C 5.669999 -2.081739 -0.819392
H 4.974466 -2.451162 -0.057535
H 5.921105 -2.897394 -1.501486
H 6.585812 -1.722723 -0.335986
O 2.445833 -1.306096 2.278382
H -7.766684 -2.164258 -0.511542

2.xyz

O -7.704595 -1.703433 -0.085711
C -6.529583 -1.028256 -0.178548
C -5.343498 -1.533771 0.341744
H -5.319286 -2.495204 0.846691
C -4.192750 -0.757312 0.187084
S -2.570211 -1.104901 0.713188
C -4.218920 0.491218 -0.466140
N -2.997213 1.136696 -0.540208
C -5.430802 0.978556 -0.979977
H -5.455762 1.939989 -1.483373
C -6.575286 0.219631 -0.834819
H -7.527830 0.567298 -1.221038
C -2.072210 0.432498 0.022428
C -0.664536 0.849189 0.105539
N 0.218427 0.122309 0.647260
S -0.210912 2.417505 -0.592764
C 1.502575 2.127688 -0.062108

C	1.550100	0.742809	0.667487
H	1.788539	2.880076	0.672375
H	2.155060	2.157431	-0.936610
C	2.512110	-0.180979	-0.109701
O	2.024988	0.858297	1.952755
O	2.137430	-1.086748	-0.815537
O	3.777798	0.195836	0.061564
P	5.110099	-0.470760	-0.775368
O	4.886005	-0.315207	-2.241520
O	6.278817	0.125909	-0.057678
O	4.948147	-2.042138	-0.394100
C	5.063075	-2.415341	0.976163
H	4.240665	-1.993101	1.566031
H	5.006314	-3.504620	1.017299
H	6.017139	-2.081454	1.394757
O	1.196905	1.813009	2.668276
H	-7.572469	-2.543477	0.378938

Appendix 2: Supporting Information Paper 2

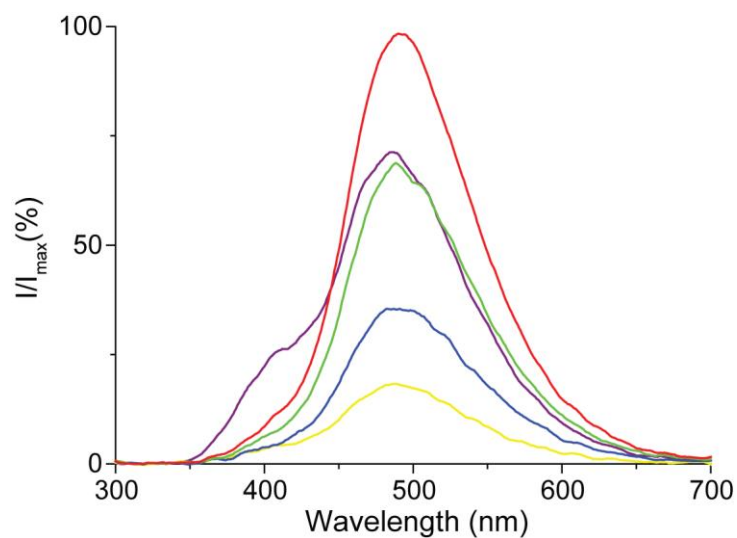


Figure S1. ECL of luminol (1.0×10^{-3} M) in [BMIM][NTf₂], recorded at a platinum mesh electrode biased at -1.0 V (violet line), -1.5 V (yellow line), -2.0 V (blue line), -2.5 V (green line) and -3.0 V (red line). Spectra are normalized to the maximum intensity of the -3.0 V data set.

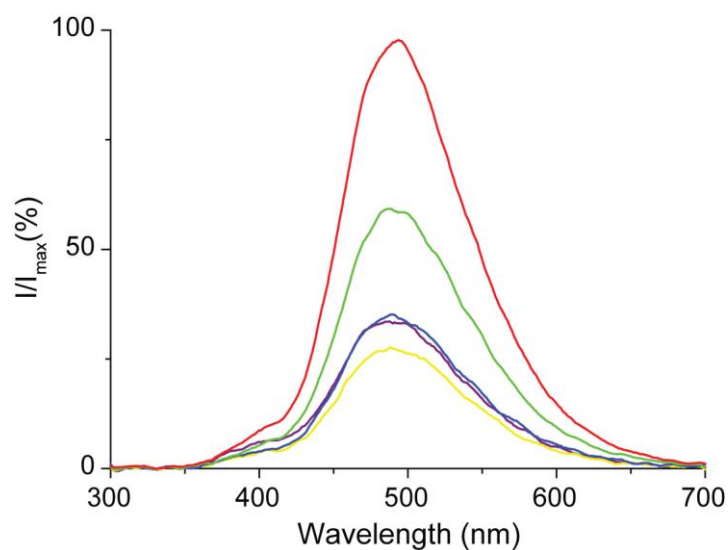


Figure S2. ECL of luminol (1.0×10^{-3} M) in [BMIM][PF₆], recorded at a platinum mesh electrode biased at -1.0 V (violet line), -1.5 V (yellow line), -2.0 V (blue line), -2.5 V (green line) and -3.0 V (red line). Spectra are normalized to the maximum intensity of the -3.0 V data set.

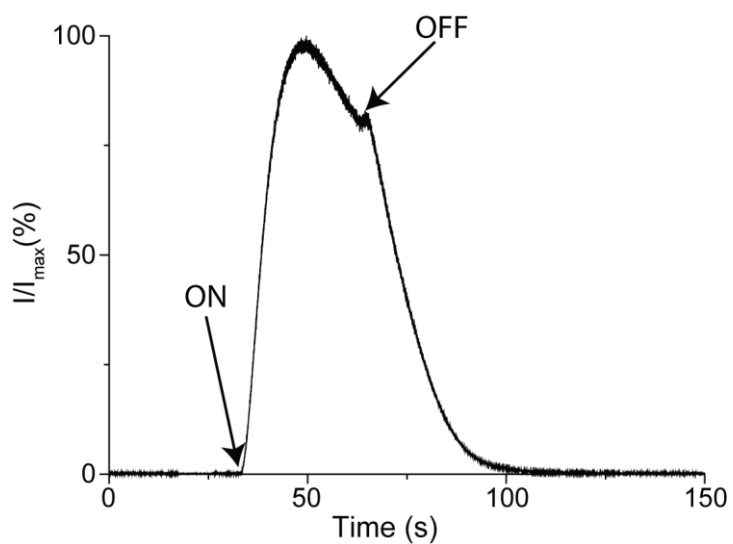


Figure S3. Time-resolved emission spectra (490 nm) of a luminol (1.0×10^{-3} M) solution in 0.1 M $\text{Bu}_4\text{NClO}_4/\text{DMSO}$ (-2.5 V). The ON label indicates when the working electrode voltage bias is switched from open-circuit to -2.5 V. The OFF label indicates the end of the 30 s voltage pulse

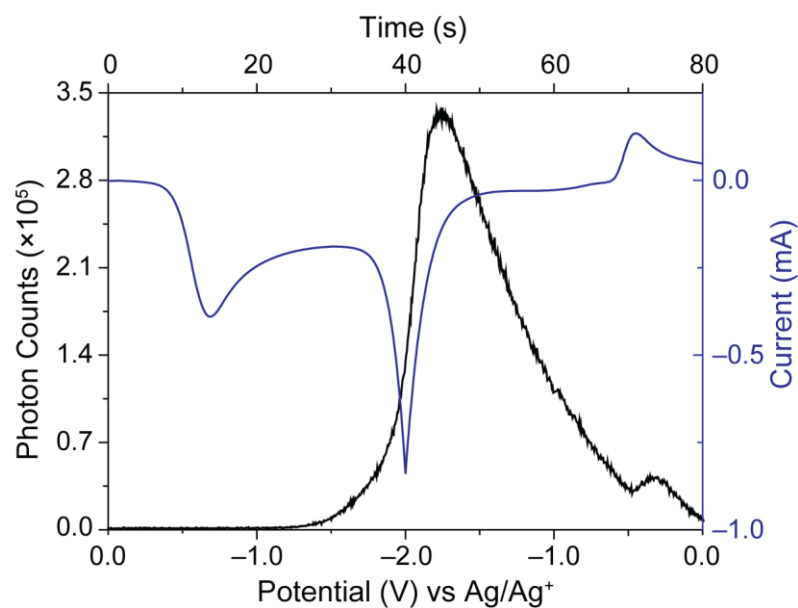


Figure S4. Photon counting experiments of luminol ECL during a cyclic voltammogram (the voltage was swept from 0.0 V towards -2.0 V, and back, at a scan rate of 0.05 V/s). Luminol (1.0×10^{-3} M) solution in 0.1 M $\text{Bu}_4\text{NClO}_4/\text{DMSO}$. Overlay plot of simultaneously acquired photon counts and current trace.

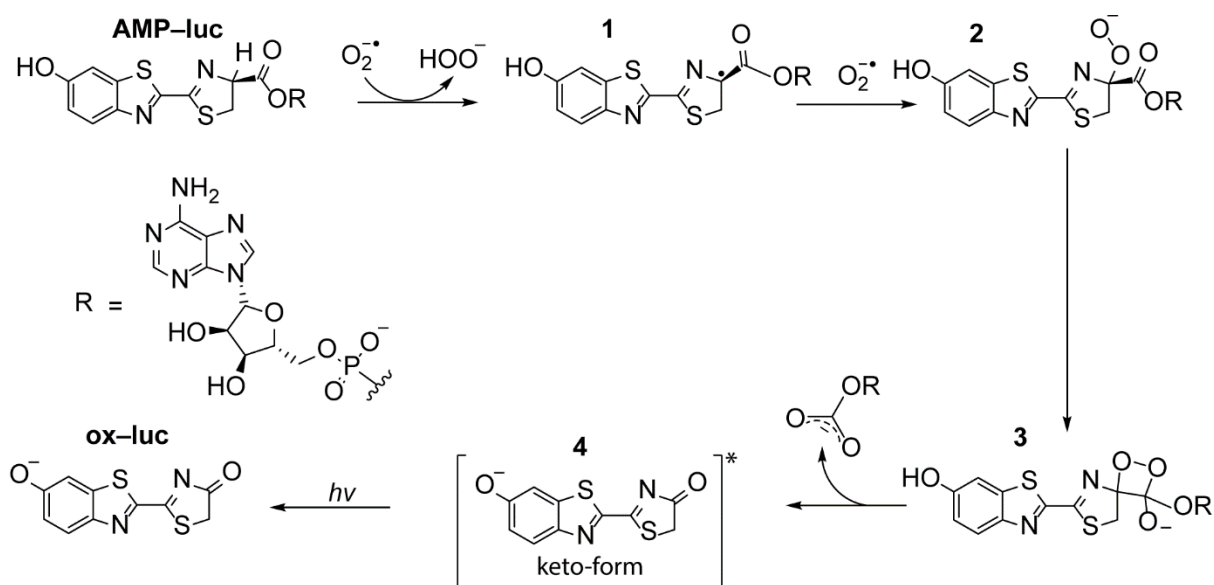


Figure S5. Proposed mechanism of the **AMP-luc** electrochemically generated light path.²⁰¹

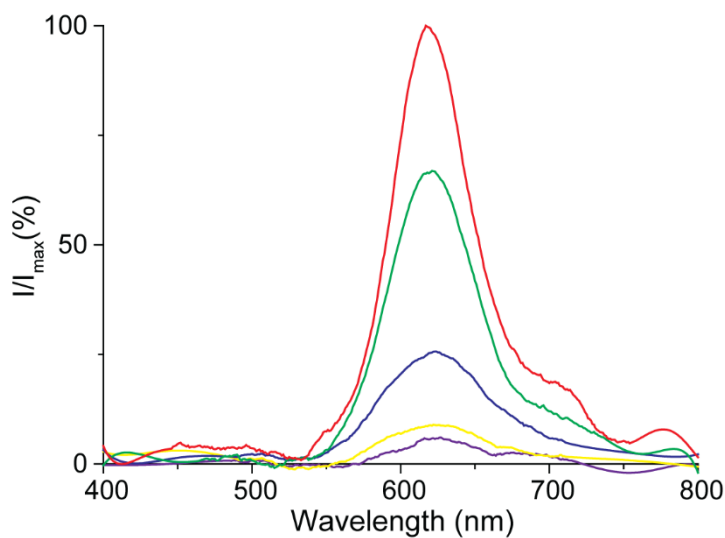


Figure S6. ECL of **AMP-luc** ($4.3 \times 10^{-4}M$) in $[BMIM][NTf_2]$, recorded at a platinum mesh electrode biased at -1.0 V (violet line), -1.5 V (yellow line), -2.0 V (blue line), -2.5 V (green line), and -3.0 V (red line). Spectra are normalized to the maximum intensity of the -3.0 V data set.

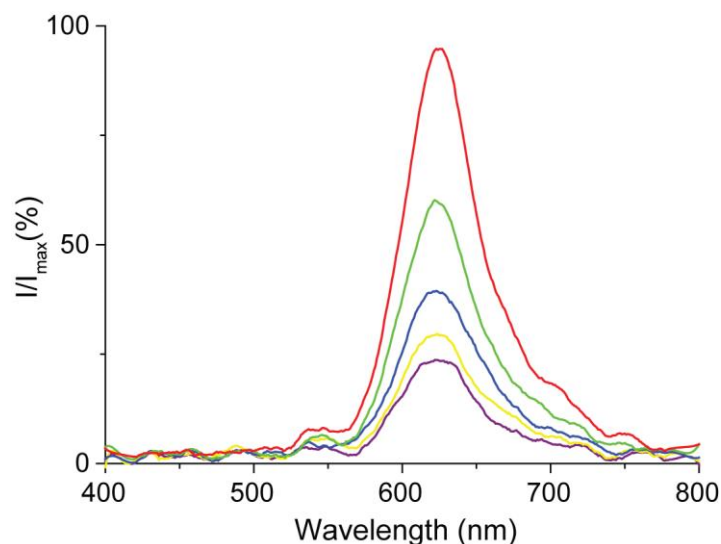


Figure S7. ECL of **AMP-luc** (4.3×10^{-4} M) in [BMIM][PF₆], recorded at a platinum mesh electrode biased at -1.0 V (violet line), -1.5 V (yellow line), -2.0 V (blue line), -2.5 V (green line) and -3.0 V (red line). Spectra are normalized to the maximum intensity of the -3.0 V data set.

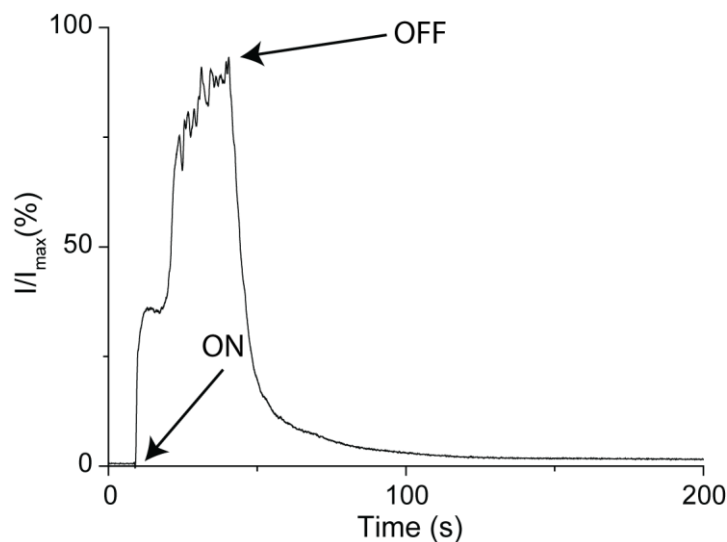


Figure S8. Time-resolved emission spectra (625 nm) of an **AMP-luc** (0.43×10^{-3} M) solution in 0.1 M Bu₄NClO₄/DMSO (-2.5 V). The ON label indicates when the working electrode voltage bias is switched from open-circuit to -2.5 V. The OFF label indicates the end of the 30 s voltage pulse.

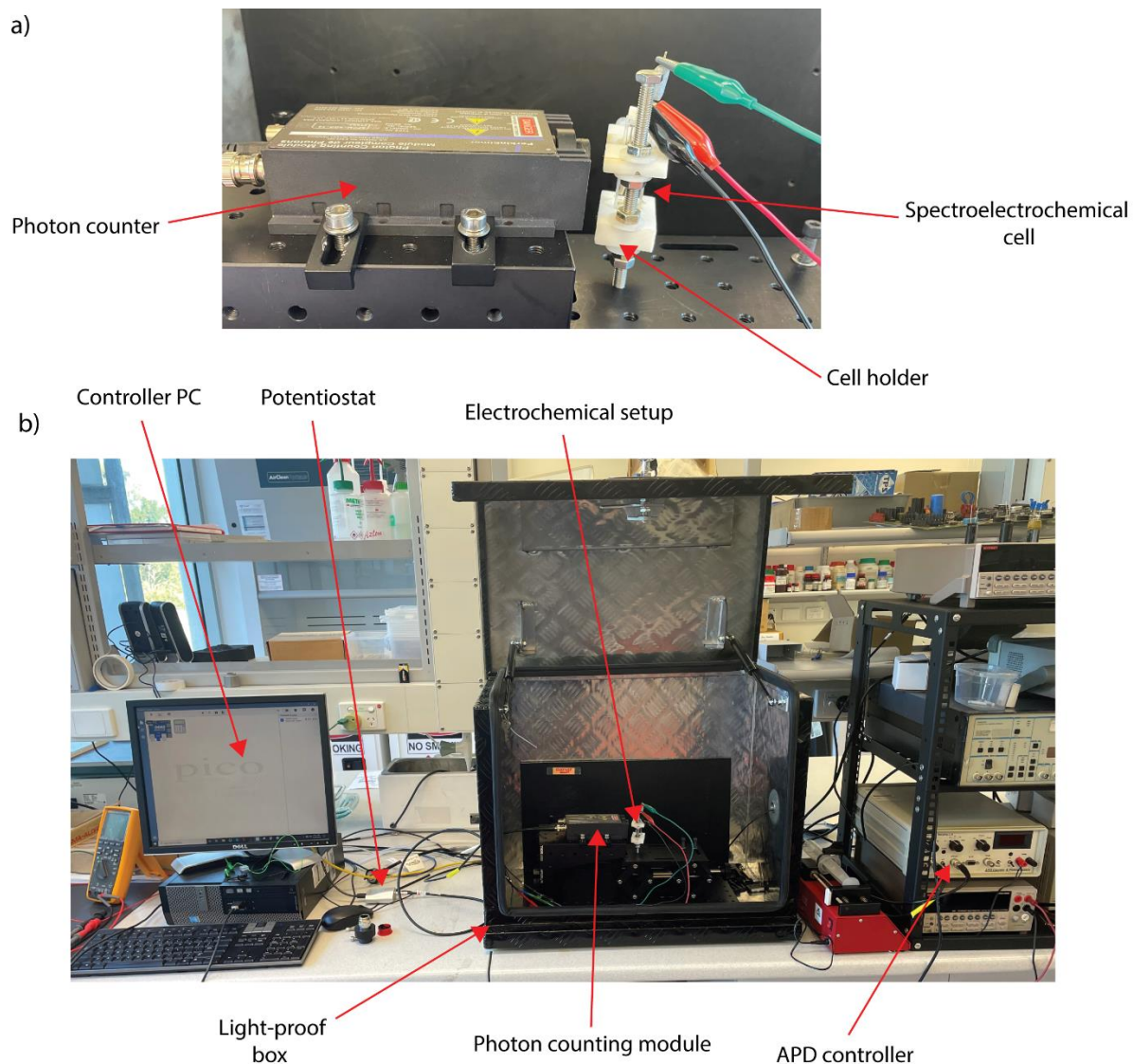


Figure S9. Experimental setup used for the photon-counting (quantitative) electrochemiluminescence experiments. (a) The spectroelectrochemical cell containing the RTIL solution and the three electrodes is placed in front of the counting module using a custom holder secured on a xyz stage allowing for consistent positioning of the working electrode relative to the photon counter. Further details are in the main text experimental section. (b) Overall view of the experimental apparatus. When the light-proof box is sealed, the dark count approaches 500 photon/sec.

Appendix 3: Supporting Information Paper 3

A3.1 Supplementary Experimental and Computational Results

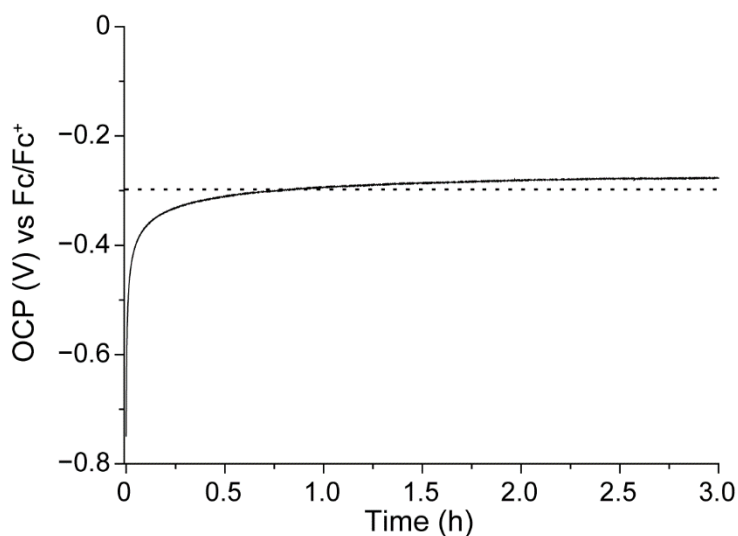


Figure S1. Representative OCP–time measurement acquired with a platinum electrode immersed in [EMIM][EtSO₄]. The OCP measurement began immediately after a 60 s negative pulse (–1.0 V relative to the system’s initial OCP). The dotted horizontal line indicates the OCP prior to the pulse. The electrode’s OCP relaxes asymptotically.

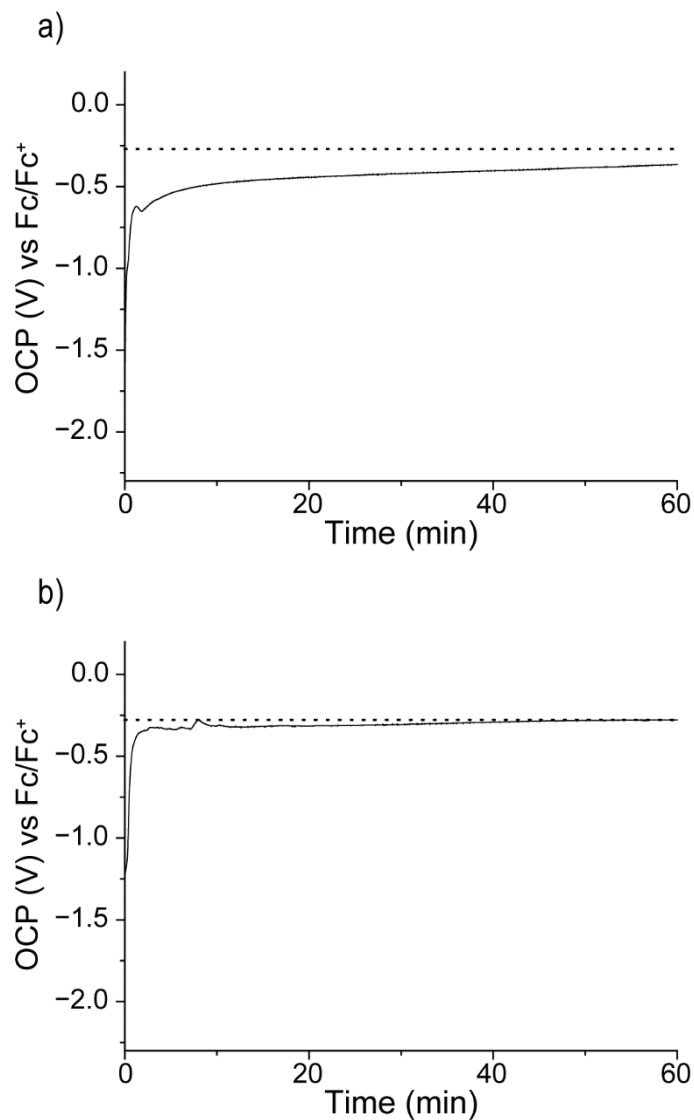


Figure S2. Representative OCP–time measurements acquired with platinum electrodes immersed in acetonitrile containing either (a) 0.1 M (a), or (b) 0.5 M Bu₄NClO₄. The recording of OCP versus time started after a 60 s negative pulse (–2.0 V from the initial OCP). The dotted horizontal line indicates the initial OCP (recorded prior to the pulse). In contrast to the OCP relaxation experiments performed with RTILs, molecular solvent/electrolyte systems did not result in discrete OCP plateaus.

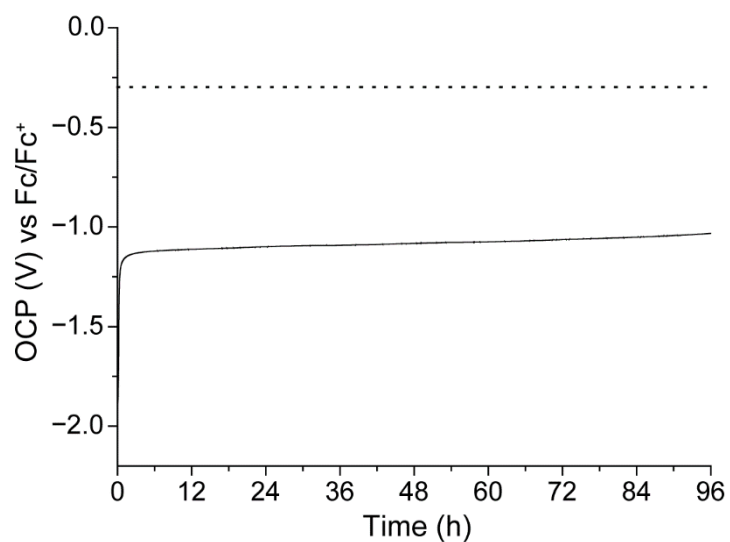


Figure S3. OCP–time measurement acquired with a platinum electrode immersed in [EMIM][EtSO₄]. The OCP measurement began immediately after a 60 s negative pulse (–2.0 V relative to the system’s initial OCP). The dotted horizontal line indicates the OCP prior to the pulse. The negative bias excursion led to an exceedingly stable OCP plateau, located around –1.10 V, which lasted at least 96 hours.

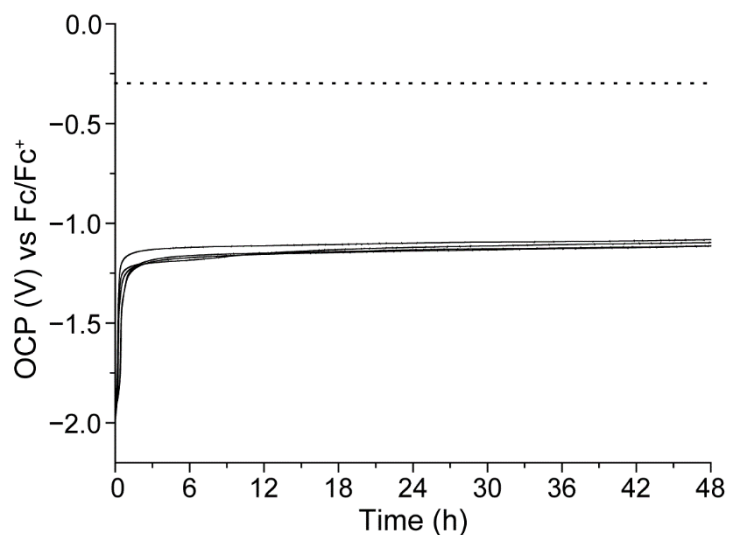


Figure S4. OCP–time measurements acquired with a platinum electrode immersed in [EMIM][EtSO₄]. The OCP measurement began immediately after a 60 s negative pulse (–2.0 V relative to the system’s initial OCP). The dotted horizontal line indicates the average OCP prior to the pulse. The negative bias excursion led to OCP plateaus located around between –1.13 V and –1.25 V that lasted at least 48 hours.

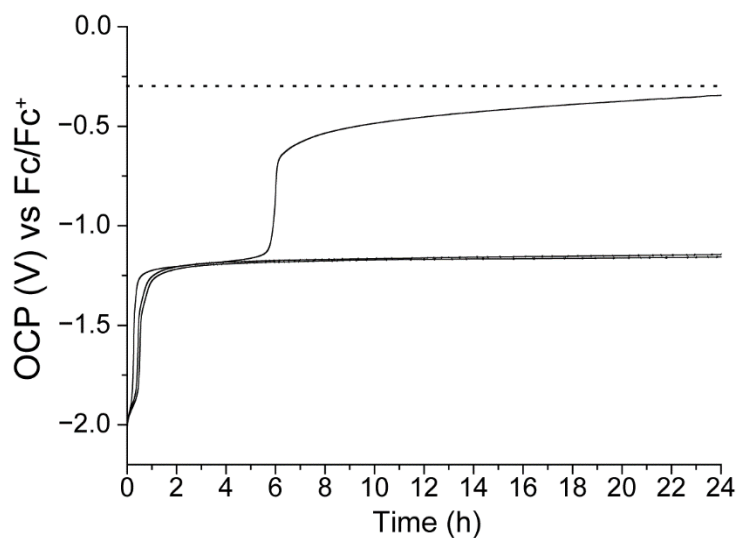


Figure S5. OCP–time measurements acquired with a platinum electrode immersed in [EMIM][EtSO₄]. The OCP measurement began immediately after a 60 s negative pulse (–2.0 V relative to the system’s initial OCP). The dotted horizontal line indicates the average OCP prior to the pulse. The negative bias excursion led to OCP plateaus located around –1.25 V that lasted between 6 and 24 hours.

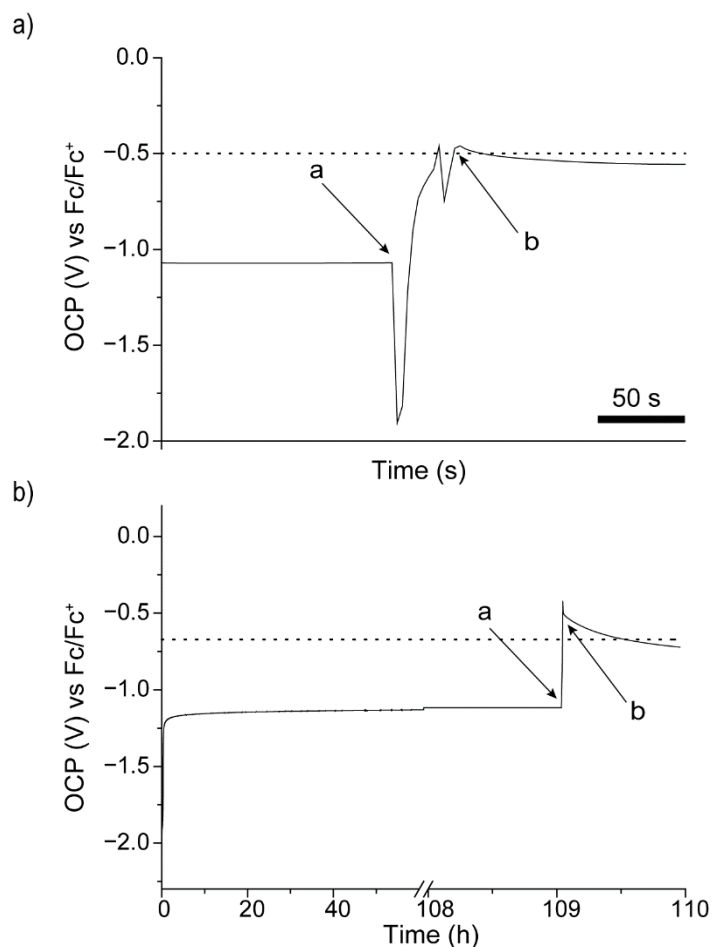


Figure S6. Representative OCP–time data showing how the stable OCP plateau, indicative of the overscreened dipolar layer formed on a platinum electrode in [EMIM][EtSO₄] after a cathodic pulse, is being lost after mechanical shaking. The leftmost portion of the OCP traces shown here are data recorded approximately either 24 h (a) or 109 h (b) after the end of the 60 s cathodic pulse (–2.0 V relative to the system’s initial OCP). The dotted horizontal lines represent the initial OCP prior to the pulse. Mechanical shaking of the electrode, while this was held under nitrogen over the liquid sample (point marked as “a”), disrupted the ordered RTIL structure, as indicated by a sharp positive shift of the electrode’s OCP back towards its initial rest value once this is re-immersed in the RTIL sample (point marked as “b”).

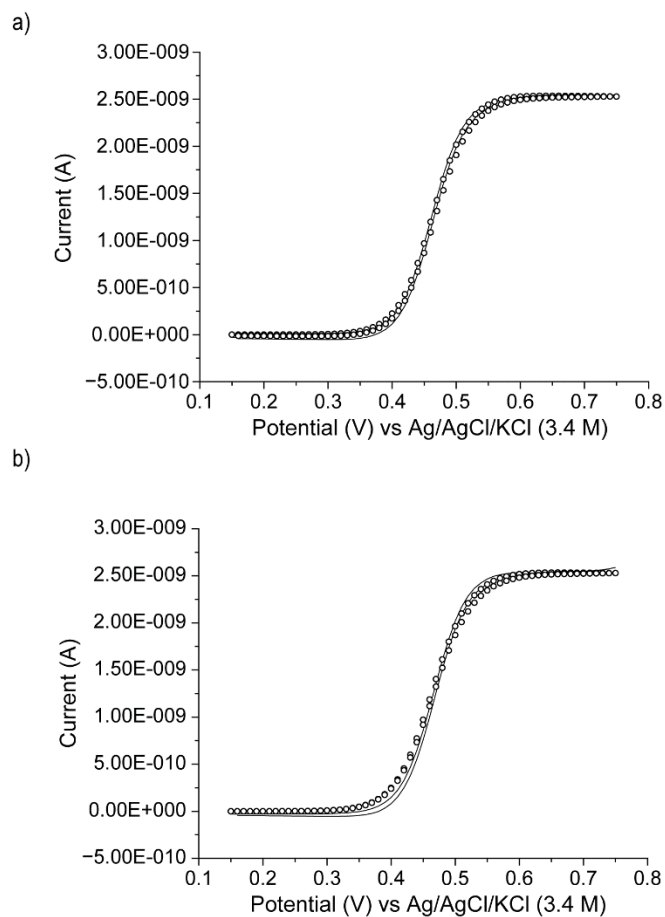


Figure S7. Voltammograms (50 mV s^{-1}) for the oxidation of ferrocene ($5.5 \times 10^{-4} \text{ M}$ ferrocene in acetonitrile with $2.5 \times 10^{-2} \text{ M}$ of Bu_4NPF_6) obtained on a platinum microdisk electrode (nominal radius of $5 \text{ }\mu\text{m}$) after its immersion and removal from a $[\text{EMIM}][\text{EtSO}_4]$ sample while holding it at either open circuit (a) or applying to it a voltage pulse of -2.0 V relative to the system's initial OCP. The experimental and simulated curves are plotted as solid lines and empty symbols, respectively. The standard deviation between experiments and simulations was less than 0.01, and indicated no changes to the electrode active area ($9.85 \times 10^{-7} \text{ cm}^2$ prior and after the pulse).

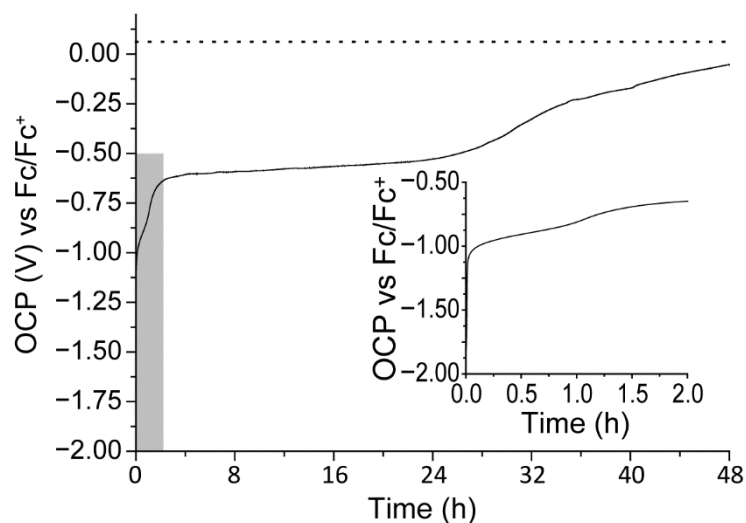


Figure S8. Representative OCP–time measurement acquired with a platinum electrode immersed in [EMIM][BF₄], after the application of a -2.0 V potential pulse away (cathodically) from the system’s initial OCP. The pulse lasted 60 seconds. The grey shaded area in indicates the data plotted as figure inset, which highlight the onset of crowding in [EMIM][BF₄], as an OCP horizontal step located around -1 V. The overscreening OCP signature of the platinum/[EMIM][BF₄] system is found around -0.62 V. The dotted horizontal line represents the initial OCP prior to the pulse.

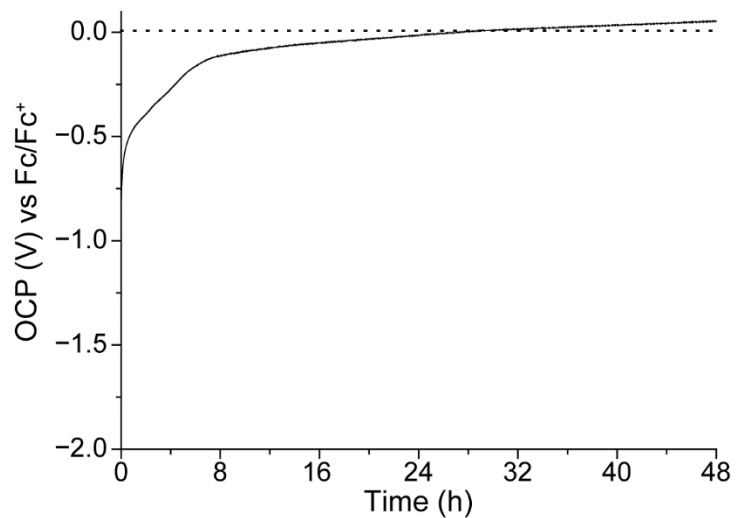


Figure S9. Representative OCP–time measurement acquired with a platinum electrode immersed in [HMIM][PF₆]. The electrode OCP recording started immediately after a 360 s cathodic pulse (–2.0 V relative to the system’s initial OCP). The dotted horizontal line represents the initial OCP prior to the pulse.

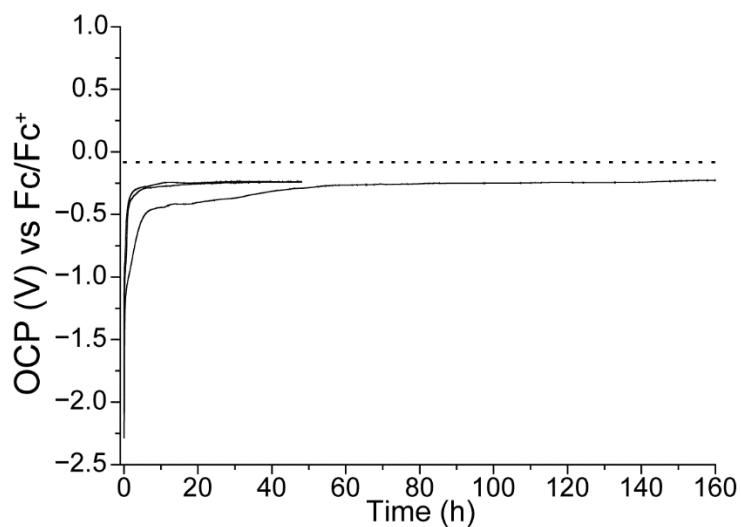


Figure S10. Representative OCP–time measurements acquired with platinum electrodes immersed in [BMPyrr][NTf₂]. The OCP measurement began immediately after the end of a 60 s cathodic potential step (–2.0 V relative to the system’s initial OCP). The dotted horizontal line marks the average initial OCP prior to the pulse.

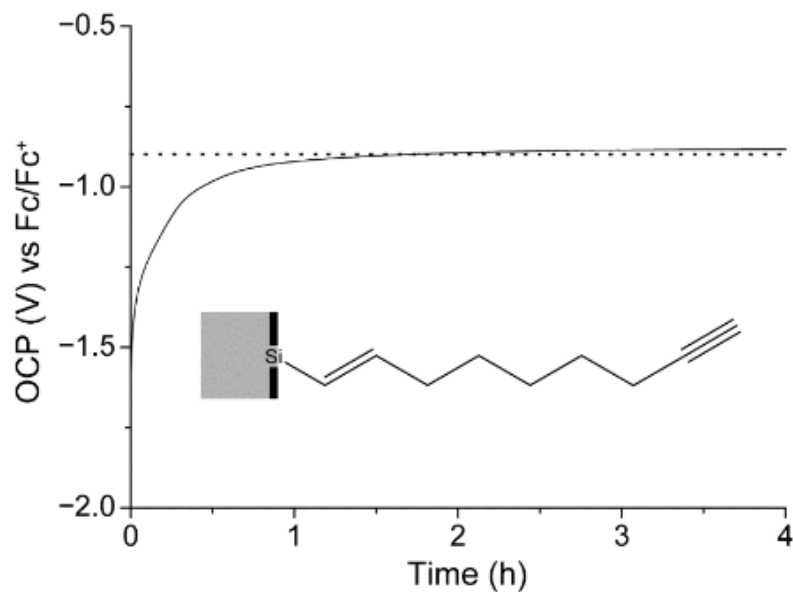


Figure S11. Representative OCP–time measurement acquired on a monolayer-modified silicon electrode immersed in [EMIM][EtSO₄]. The electrode was coated with a Si–C-bound monolayer prepared by grafting 1,8-nonadiyne on hydrogen-terminated Si(111). The electrode OCP recording started immediately after a 60 s cathodic pulse (–2.0 V relative to the system’s initial OCP). The dotted horizontal line marks the OCP prior to the cathodic pulse.

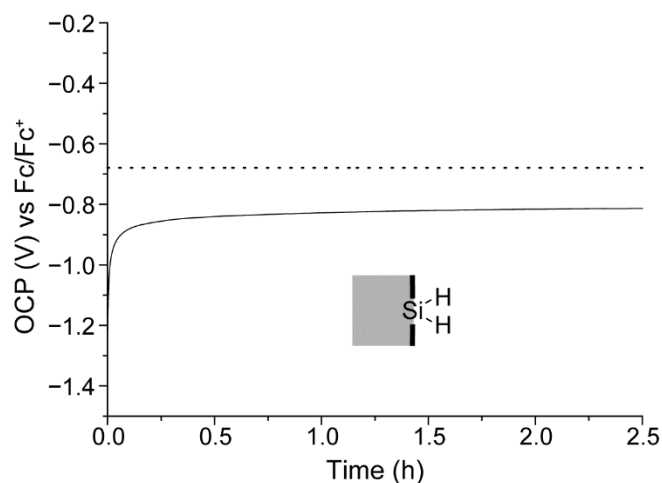


Figure S12. Representative OCP–time measurement acquired on a hydrogen-terminated Si(111) electrode in [EMIM][EtSO₄]. The recording of the electrode’s OCP started immediately after a 60 s cathodic pulse (–2.0 V relative to the system’s initial OCP). The dotted horizontal line marks the OCP prior to the cathodic pulse. The OCP after the pulse asymptotically relaxed back towards its initial value, but never reached it. The cathodic shift of the final OCP is indicative of a degree of surface corrosion, which is expected given the lack of chemical passivation of the hydride surface (see Figure S11 for a comparison with a chemically passivated Si surface).

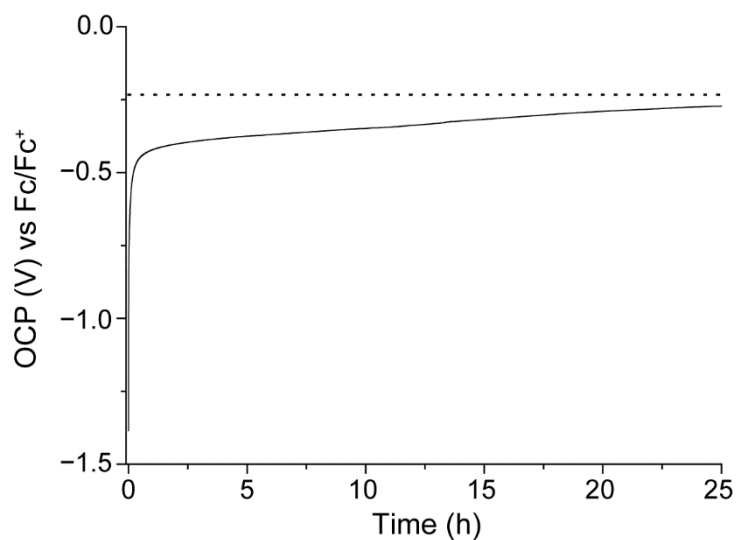


Figure S13. Representative OCP–time measurement acquired with a carbon plate working electrode and a platinum counter immersed in [EMIM][EtSO₄]. The electrode OCP recording started after a 60 s cathodic pulse (–2.0 V relative to the system’s initial OCP). The dotted horizontal line represents the initial OCP prior to the pulse.

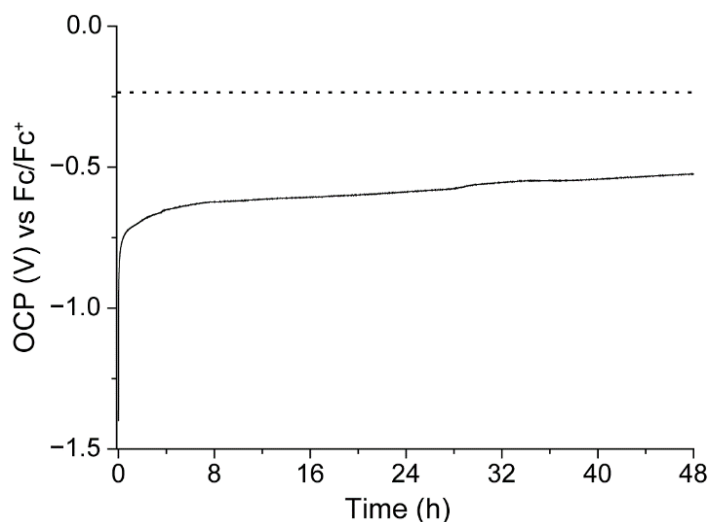


Figure S14. Representative OCP–time measurements acquired with a gold wire working electrode and a platinum counter immersed in [EMIM][EtSO₄]. The electrode OCP recording started immediately after a 60 s cathodic pulse (−2.0 V relative to the system’s initial OCP). Dotted horizontal lines represent the average initial OCP. Negative bias excursions lead to very stable OCP plateaus located between −0.6 V and −0.8 V.

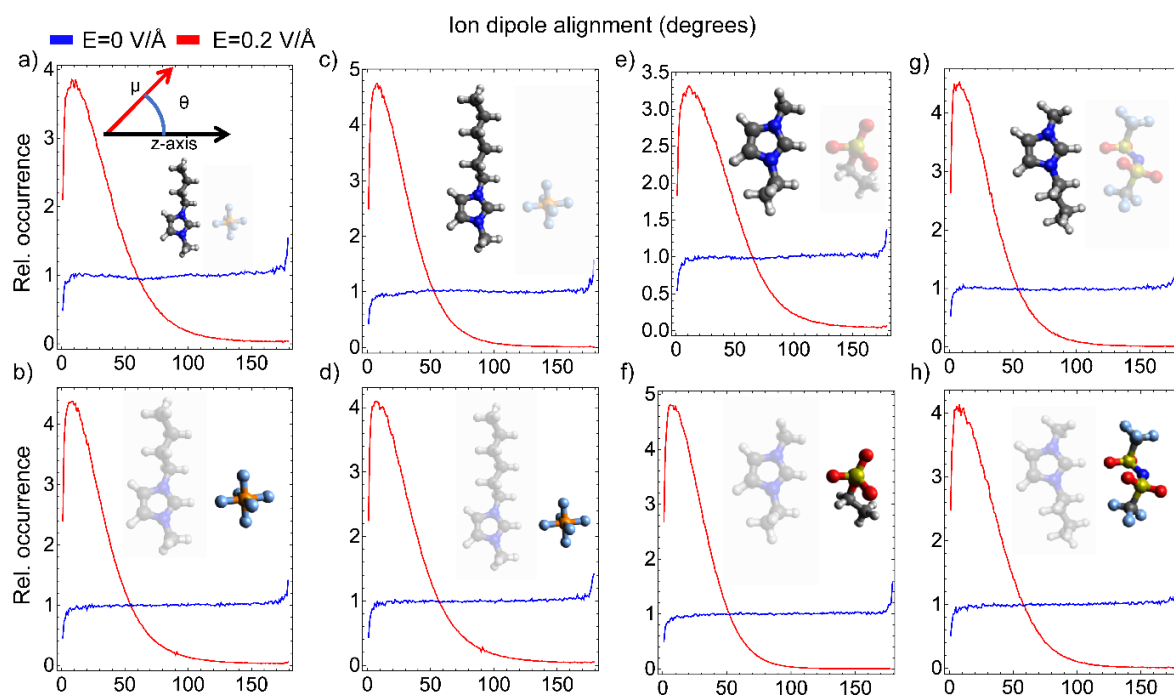


Figure S15. Cone-corrected angular distributions ion dipoles relative to the z-axis of (a) BMIM⁺ and (b) PF₆⁻ in [BMIM][PF₆], (c) HMIM⁺ and (d) PF₆⁻ in [HMIM][PF₆], (e) EMIM⁺ and (f) EtSO₄⁻ in [EMIM][EtSO₄] and (g) BMIM⁺ and (h) NTf₂⁻ in [BMIM][NTf₂].

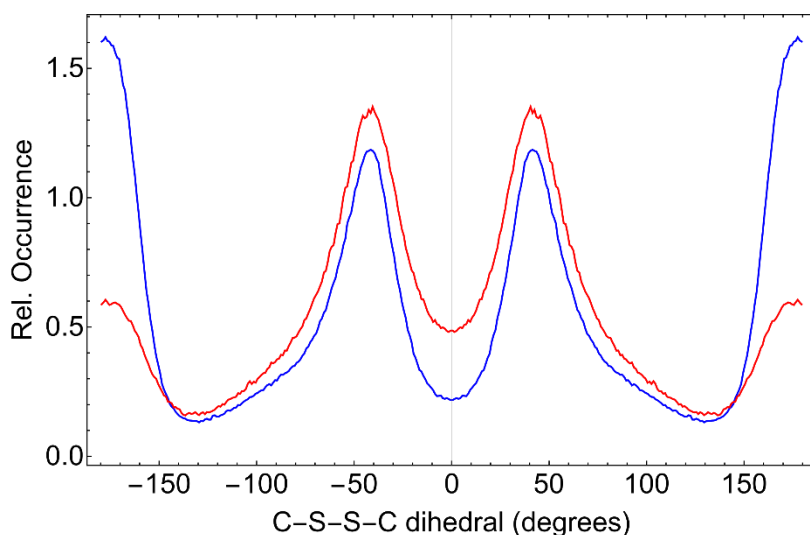


Figure S16. Dihedral distribution function of the C-S-S-C dihedral in NTf_2^- across simulations in the absence of an electric field (blue) and in a 0.2 V/\AA external electric field (red).

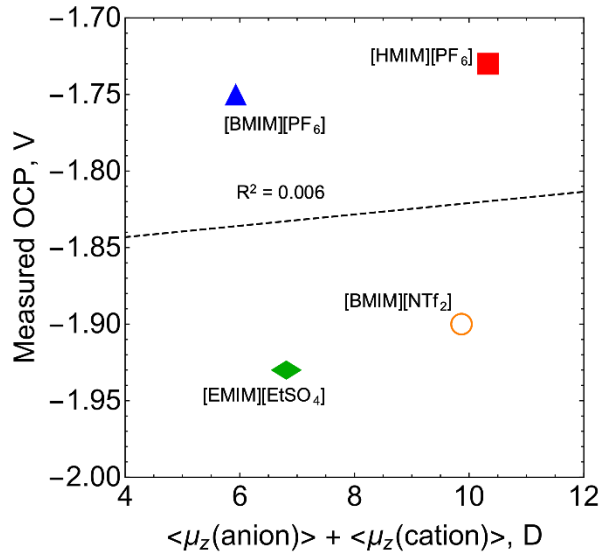


Figure S17. Plot of the sum of the mean dipole projection of constituent ions against the measured OCP (crowding) values of [BMIM][PF₆], [HMIM][PF₆], [EMIM][EtSO₄] and [BMIM][NTf₂].

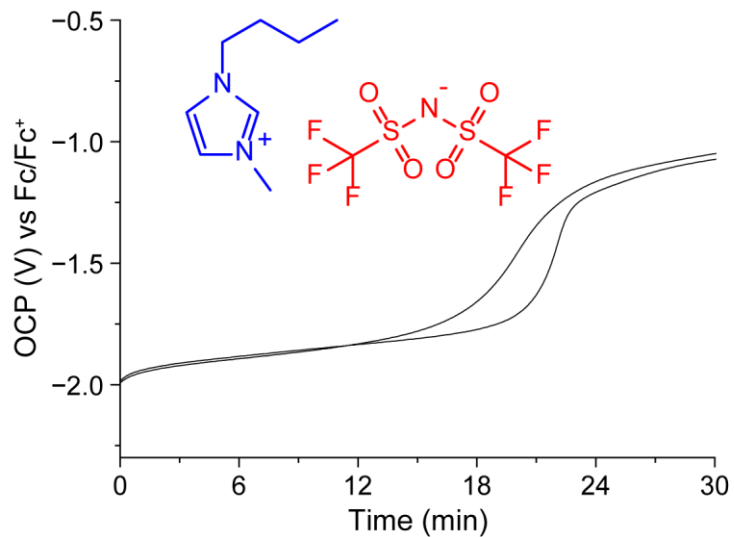


Figure S18. Representative OCP–time measurements acquired with platinum electrodes immersed in [BMIM][NTf₂] immediately after a negative potential step (60 s). The potential step was of -2.0 V relative to the electrode initial rest OCP. The crowding plateau in [BMIM][NTf₂] is found at -1.9 V.

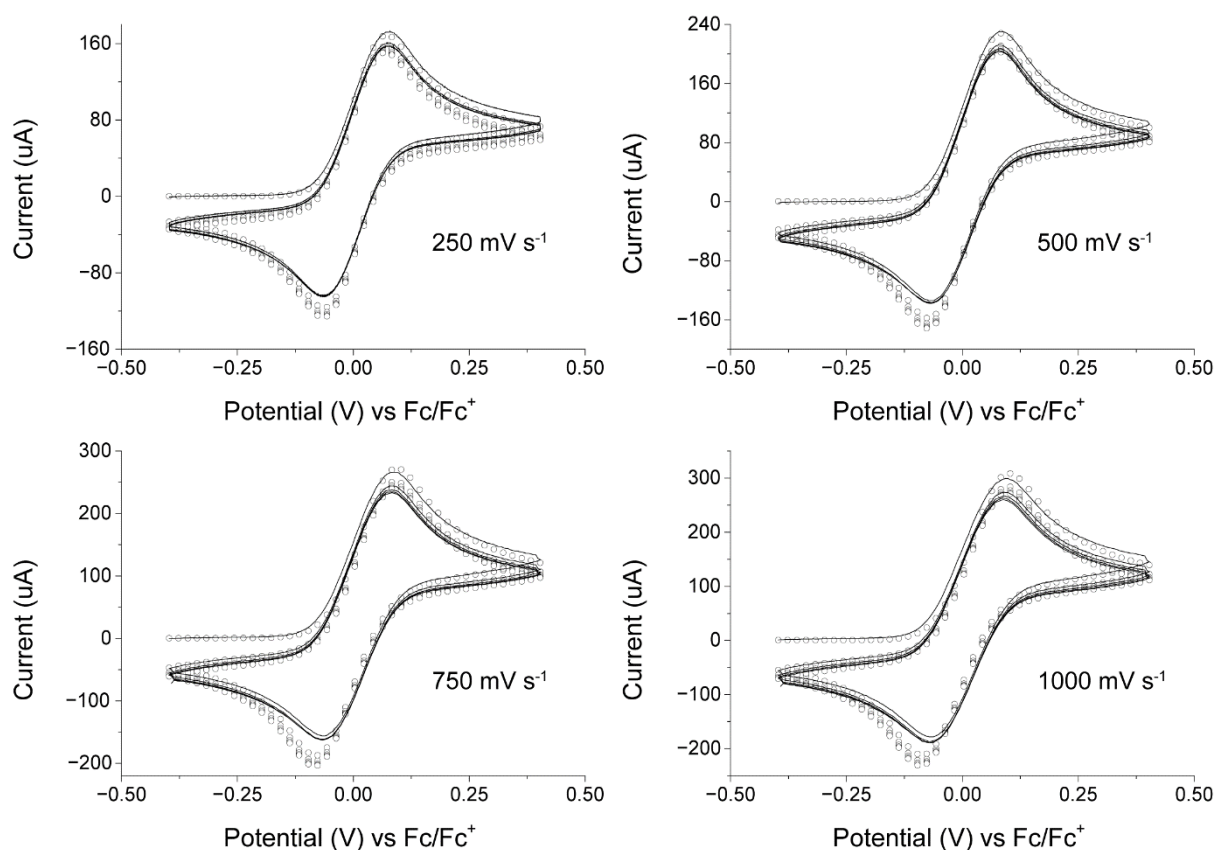


Figure S19. Experimental (solid line) and simulated (empty symbols) cyclic voltammograms at a platinum wire in an acetonitrile solution containing 1.0×10^{-3} M ferrocene and 1.0×10^{-1} Bu_4NClO_4 . The voltage sweep rate is indicated as labels to the figures. The diffusivity of ferrocene (Fc in shorthand) was set to $2.3 \times 10^{-5} \text{ cm}^2 \text{ s}^{-1}$. The refined parameters (E mechanism) are: $E^0(\text{Fc}/\text{Fc}^+) = 0.597 \text{ V vs. Ag}/\text{AgCl}$ (“leakless”, see experimental section), $k^0(\text{Fc}/\text{Fc}^+) = 0.01 \text{ cm s}^{-1}$, $\alpha = 0.5$. The cell iR drop was not compensated during measurement. Values of cell resistance used in the fittings were measured by electrochemical impedance spectroscopy prior to the experiment and used in the simulations. Butler–Volmer kinetics was used to estimate charge transfer parameters, and the diffusion was considered as semi-infinite 1D. The electrochemically-determined effective area of the platinum wire electrode is 0.28 cm^2 .

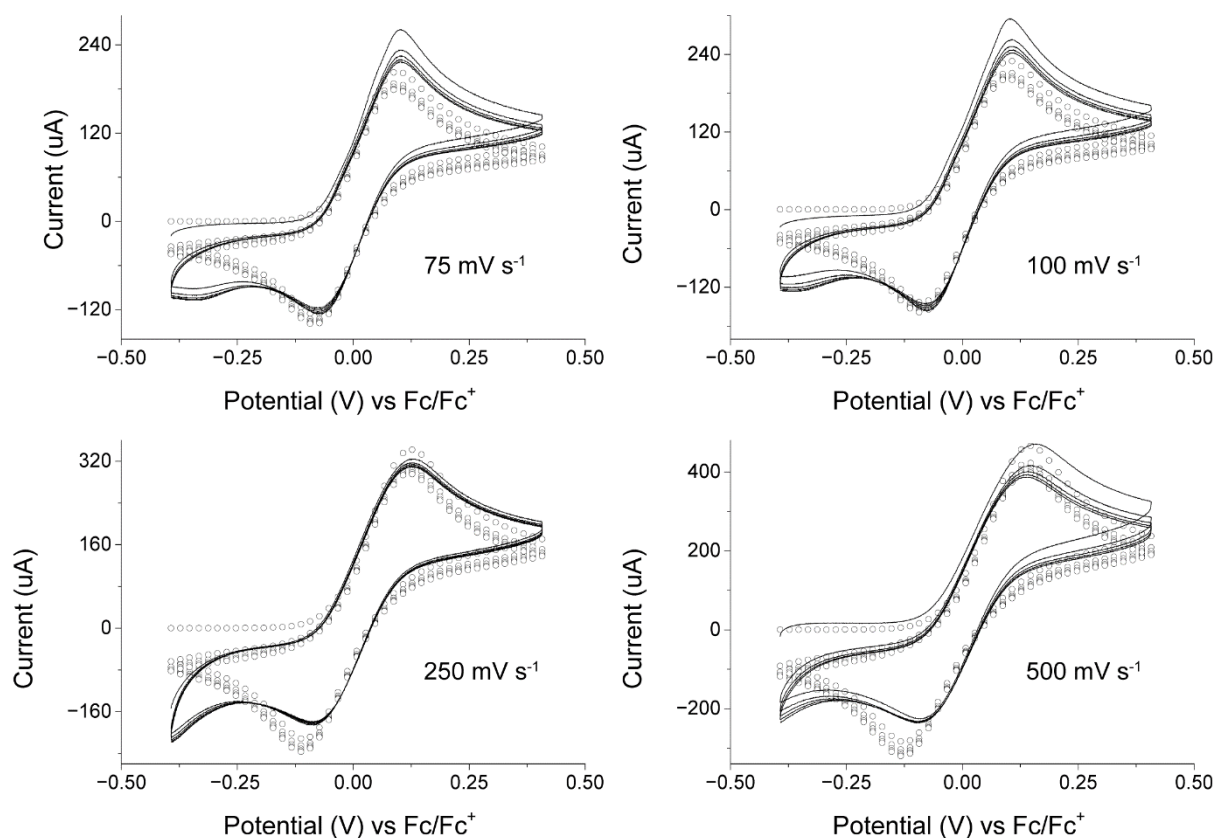


Figure S20. Experimental (solid line) and simulated (empty symbols) cyclic voltammograms at a platinum wire in an acetonitrile solution containing 1.0×10^{-3} M ferrocene and 1.0×10^{-1} Bu_4NClO_4 . The voltage sweep rate is indicated as labels to the figures. The diffusivity of ferrocene (Fc in shorthand) was set to 2.3×10^{-5} $\text{cm}^2 \text{s}^{-1}$. The refined parameters (E mechanism) are: $E^0(\text{Fc}/\text{Fc}^+) = 0.592$ V vs. Ag/AgCl (“leakless”, see experimental section), $k^0(\text{Fc}/\text{Fc}^+) = 0.01$ cm s^{-1} , $\alpha = 0.5$. The cell iR drop was not compensated during measurement. Values of cell resistance used in the fittings were measured by electrochemical impedance spectroscopy prior to the experiment and used in the simulations. Butler–Volmer kinetics was used to estimate charge transfer parameters, and the diffusion was considered as semi-infinite 1D. The electrochemically-determined effective area of the platinum wire electrode is 0.63 cm^2 .

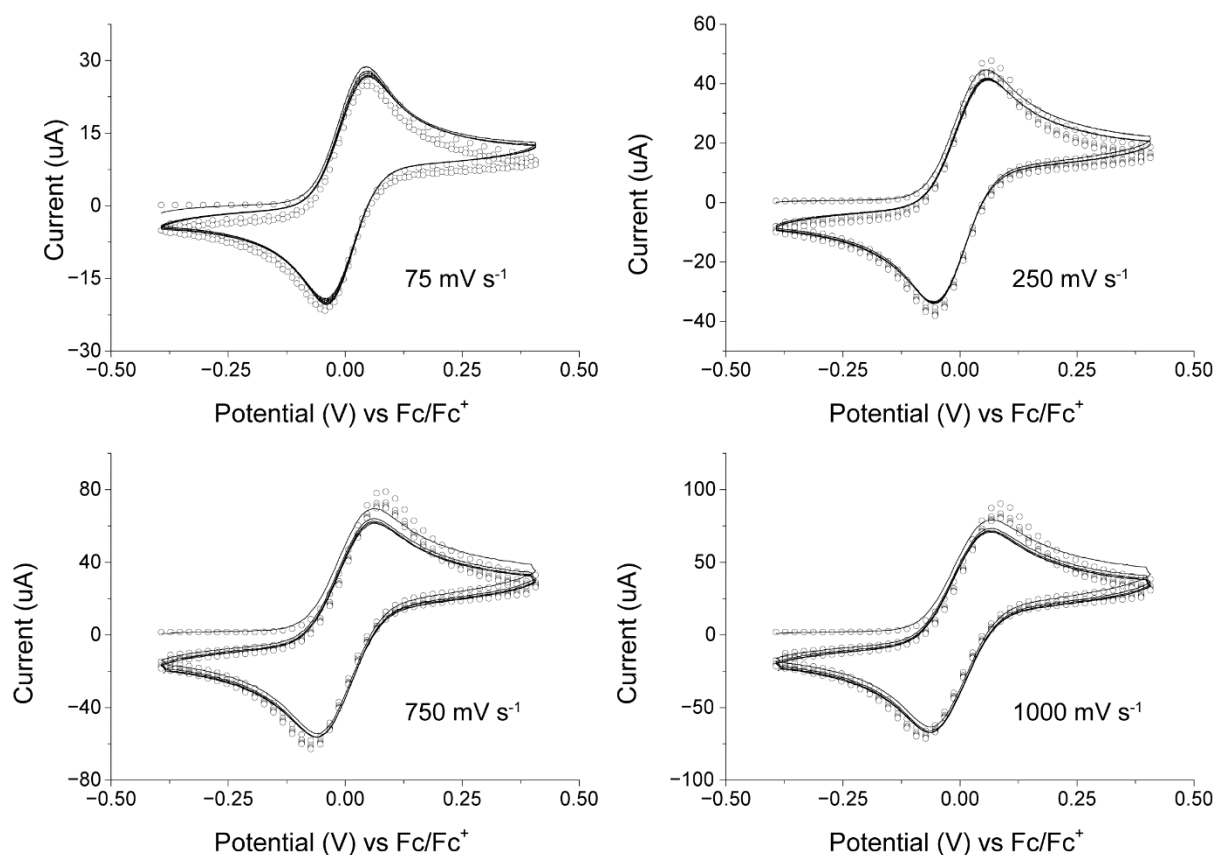


Figure S21. Experimental (solid line) and simulated (empty symbols) cyclic voltammograms at a platinum disk in an acetonitrile solution containing 1.0×10^{-3} M ferrocene and 1.0×10^{-1} Bu₄NClO₄. The voltage sweep rate is indicated as labels to the figures. The diffusivity of ferrocene (Fc in shorthand) was set to 2.3×10^{-5} cm²s⁻¹. The refined parameters (E mechanism) are: $E^0(\text{Fc}/\text{Fc}^+) = 0.593$ V vs. Ag/AgCl (“leakless”, see experimental section), $k^0(\text{Fc}/\text{Fc}^+) = 0.01$ cm s⁻¹, $\alpha = 0.5$. The cell iR drop was not compensated during measurement. Values of cell resistance used in the fittings were measured by electrochemical impedance spectroscopy prior to the experiment and used in the simulations. Butler–Volmer kinetics was used to estimate charge transfer parameters, and the diffusion was considered as semi-infinite 2D. The electrochemically-determined effective area of the platinum disk electrode is 0.08 cm².

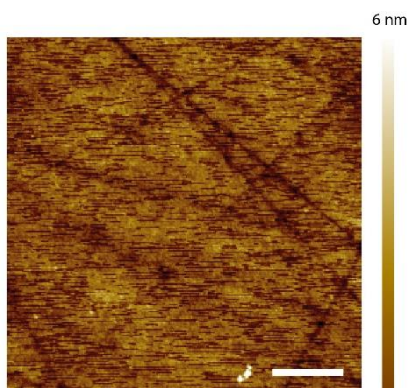


Figure S22. Representative AFM topography (height) image (5×5 μm) of a glassy carbon electrode. The scale bar at bottom right represents 1 μm. Using the region analysis function in the image processing software XEI (Park System Corporation), the root-mean-square (RMS) roughness of the sample surface was estimated to 1.365 nm.

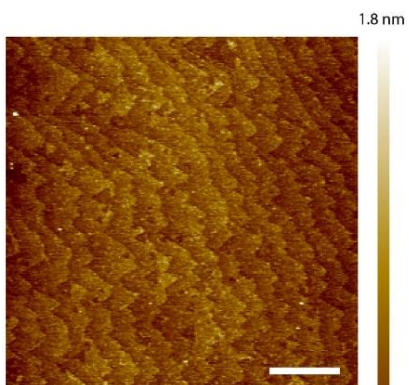


Figure S23. Representative AFM topography (height) image (5×5 μm) of a monolayer-coated silicon electrode. The scale bar at bottom right represents 1 μm. The silicon was highly doped (phosphorous, 0.007–0.013 ohm cm), n-type hydrogen-terminated Si(111) coated with a Si–C-bound monolayer of 1,8-nonadiyne. The clear terraced structure and the negligible amount of rounded features indicates an exceedingly low level of substrate oxidation. The root-mean-square (RMS) roughness of the sample is 0.301 nm (XEI software, Park System Corporation).

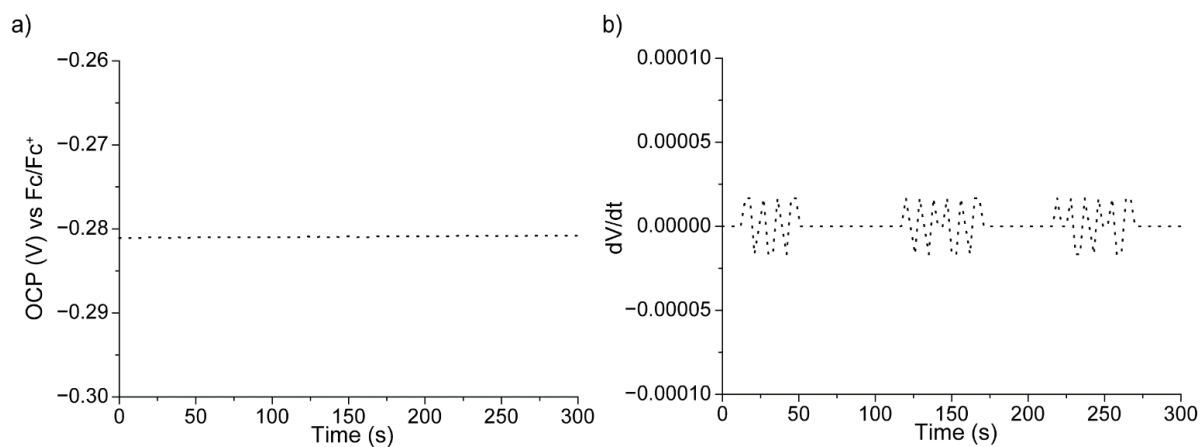


Figure S24. Prior to any external biasing, electrodes were left to equilibrate in contact with the ionic liquid sample until the first derivative of the OCP versus time trace (dV/dt) felt below $|0.0001|$. (a) Example of initial equilibration of the OCP for a platinum electrode immersed in [EMIM][EtSO₄], and its first derivative shown in (b).

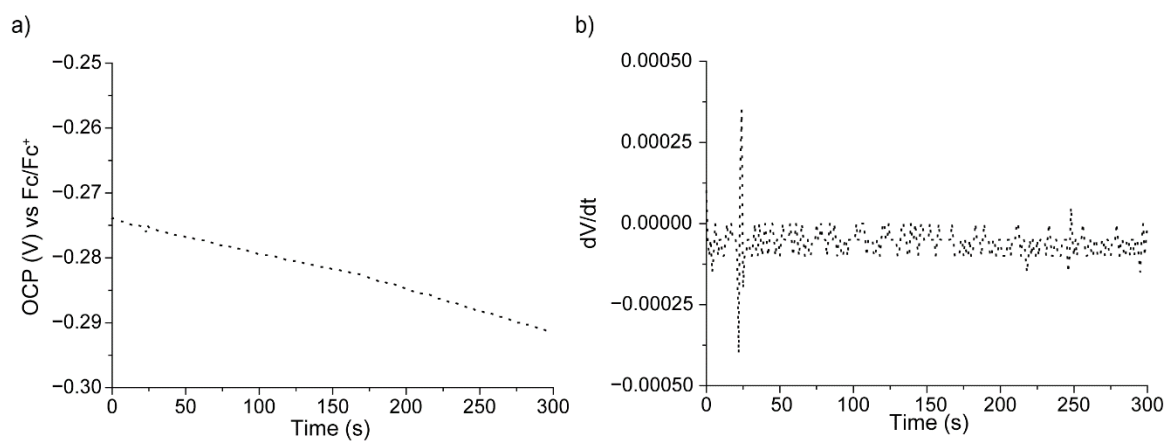


Figure S25. (a) Representative initial OCP–time measurement acquired with a platinum electrode immersed in [BMIM][PF₆], and its first derivative (b). Prior to any external bias being applied to the interface, electrodes were left to equilibrate in contact with the ionic liquid sample until the first derivative of the OCP versus time trace (dV/dt) dropped below $|0.0001|$.

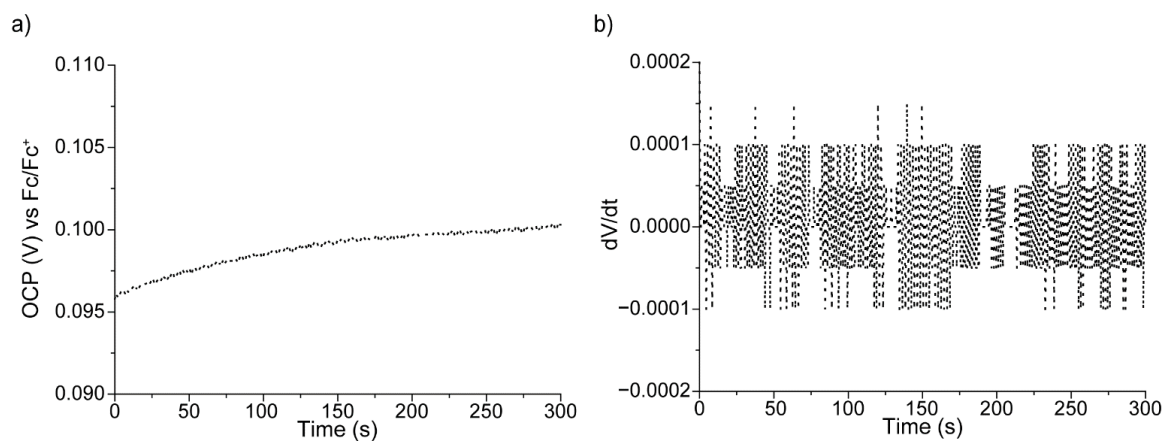


Figure S27. Example of initial OCP–time measurement acquired with a platinum electrode immersed in $[P_{1466}][NTf_2]$ (a) and its first derivative (b). Electrodes were left to equilibrate in contact with the ionic liquid sample until the first derivative of the OCP versus time traces (dV/dt) dropped below $|0.0001|$.

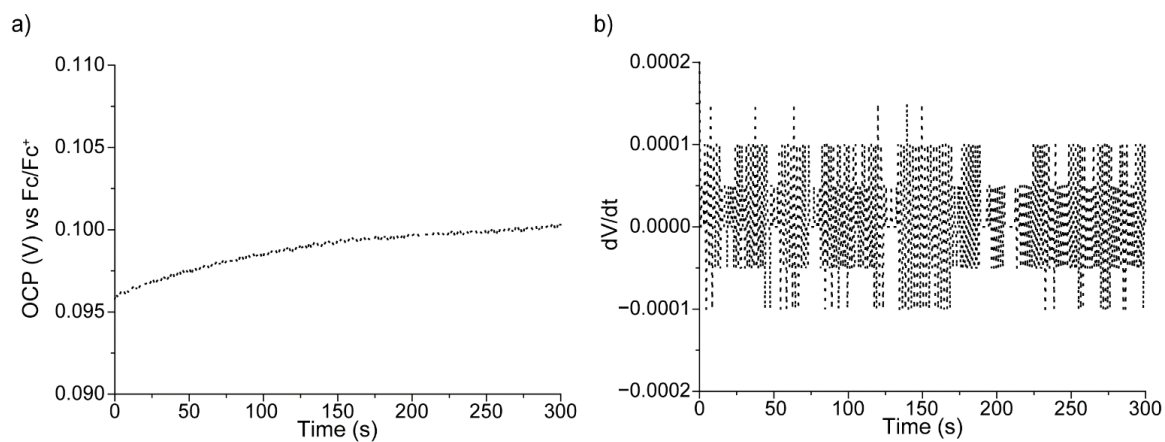


Figure S27. Example of initial OCP–time measurement acquired with a platinum electrode immersed in $[P_{1466}][NTf_2]$ (a) and its first derivative (b). Electrodes were left to equilibrate in contact with the ionic liquid sample until the first derivative of the OCP versus time traces (dV/dt) dropped below $|0.0001|$.

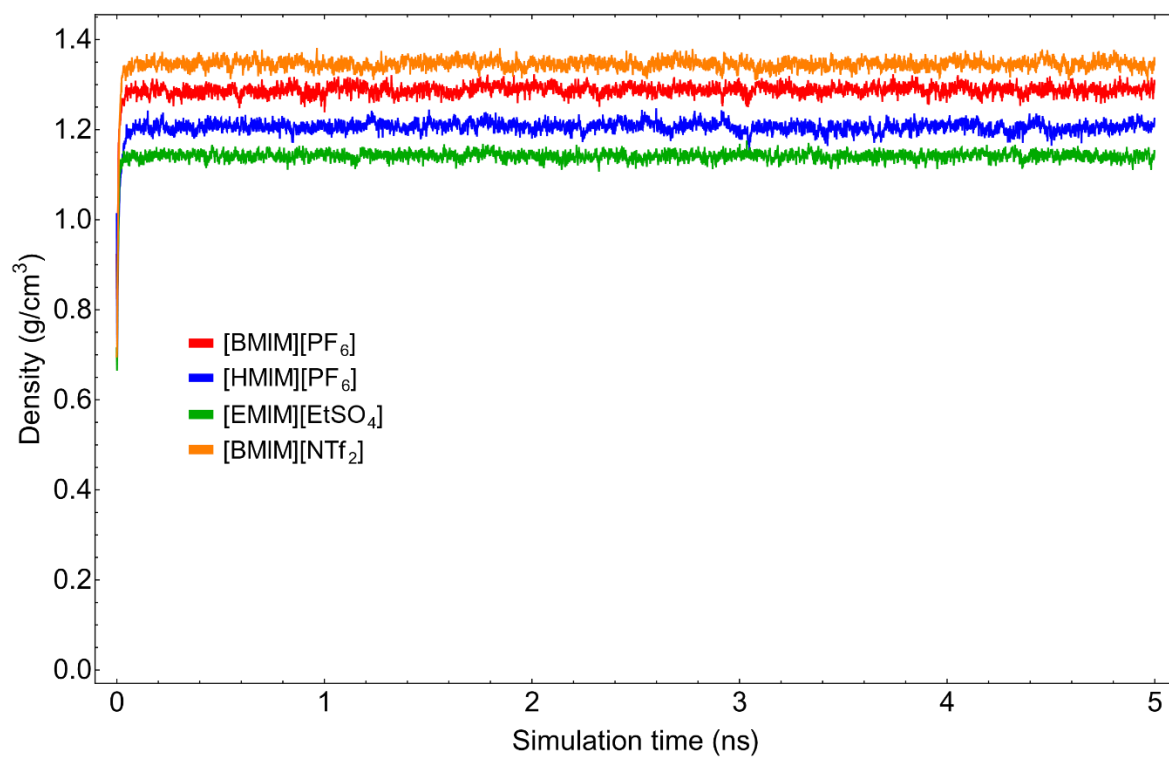


Figure S28. Evolution of density over time in equilibration molecular simulation runs of [BMIM][PF₆] (red), [HMIM][PF₆] (blue), [EMIM][EtSO₄] (green) and [BMIM][NTf₂] (orange).

Table S1. k_{ij} parameters calculated for this work. Minimum energy configurations were obtained from a thorough geometry search of possible starting configurations subject to M06-2X/cc-pVTZ calculations, with implicit ethanol solvation represented with the CPCM model.³⁸⁴ Frequency analysis confirmed local minima of minimum energy structures, determined by SRS-MP2^{385, 386} single point energy calculations. Minimum energy structures were subject to SAPT2+/aug-cc-pVDZ³⁸⁷ calculations to determine k_{ij} parameters. All frequency and geometry optimisations were performed with GAUSSIAN16a03,³⁸⁸ with SAPT2+ and single point calculations performed with PSI4.³⁸⁹

Interacting pair	k_{ij} value
EMIM⁺-PF₆⁻	0.55
EMIM⁺-EtSO₄⁻	0.52
PF₆⁻-C₄H₁₀	0.57
PF₆⁻-C₆H₁₄	0.58

Table S2. Comparison of equilibrated densities from molecular dynamics simulations to literature.

Ionic liquid	ρ^{exp} g/cm³	ρ^{sim} g/cm³	% dev.
[BMIM][PF₆]	1.323 ³⁹⁰	1.288	-2.6
[HMIM][PF₆]	1.251 ³⁹¹	1.204	-3.8
[EMIM][EtSO₄]	1.201 ³⁹²	1.142	-4.9
[BMIM][NTf₂]	1.386 ³⁹³	1.346	-2.9

Table S3. Observed diffusion coefficients of ions in production simulations, in the absence of an external electric field

Ionic liquid	D(cation) × 10¹¹ m²/s	D(anion) × 10¹¹ m²/s
[BMIM][PF₆]	12.2	9.6
[HMIM][PF₆]	3.7	4.7
[EMIM][EtSO₄]	14.9	10.2
[BMIM][NTf₂]	17.6	16.6

Table S4. Observed diffusion coefficients of ions in production simulations, in an external electric field of 0.2 V/Å

Ionic liquid	D(cation) × 10⁷ m²/s	D(anion) × 10⁷ m²/s
[BMIM][PF₆]	24.5	22.6
[HMIM][PF₆]	22.2	29.6
[EMIM][EtSO₄]	16.6	17.2
[BMIM][NTf₂]	15.0	3.7

Table S5. Calculated molar volumes of cations using HF/aug-cc-pVTZ electron densities³⁹⁴

Cation	V_m (Å³)
BMIM⁺	185.5
HMIM⁺	246.7

Appendix 4: Supporting Information Paper 4

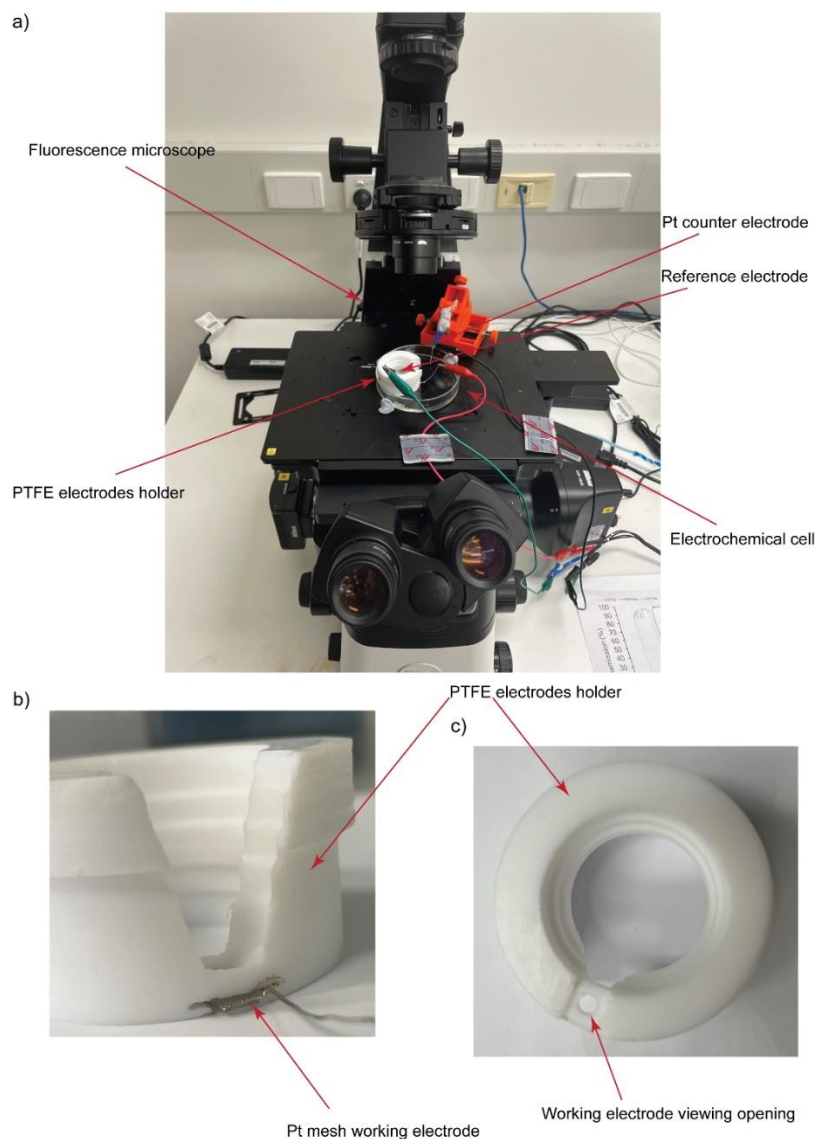


Figure S1. Experimental setup for the collection of ECL and fluorescence time-resolved micrographs. (a) A Petri dish, resting on the sample stage of an inverted fluorescence microscope, is loaded with the electrolytic solution and fitted with a custom PTFE electrodes holder. (b) Side view of the PTFE electrode holder showing the horizontal slot for the Pt mesh working electrode. The platinum mesh position is sitting parallel and ~ 2 mm away from the bottom glass surface of the Petri dish. (c) Bottom view of the PTFE holder.

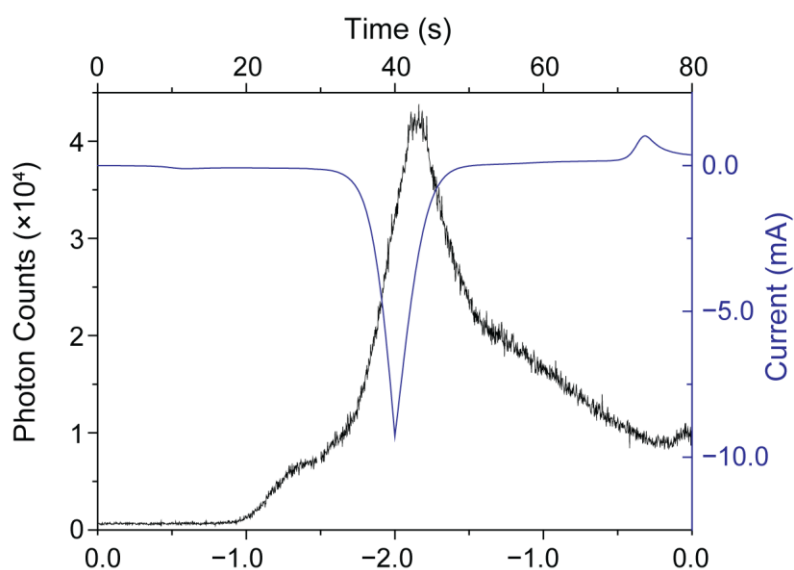


Figure S2. Overlaid plots of simultaneously acquired photon counts (black trace) and current (blue trace) during the cathodic electrolysis at a platinum mesh electrode of an 0.4×10^{-3} M **AMP-luc** oxygen-saturated solution in [EMIM][EtSO₄]. The potential was swept cyclically from 0.0 V to -2.0 V, and back, at a scan rate of 0.05 V/s. The emission peak corresponds to $\sim 4.20 \times 10^4$ photon/s.

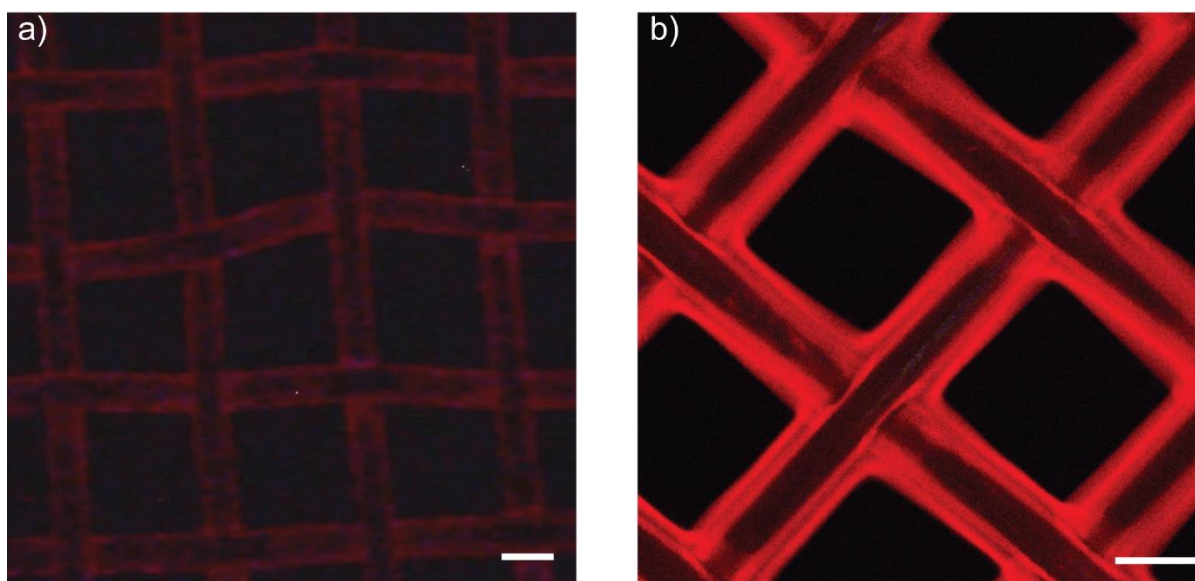


Figure S3. Full field of view for the ECL micrographs shown partially cropped in Figure 1b of the main text. (a) The ECL image was captured in a dark room, ~ 2.0 s after a -2.0 V cathodic pulse (30 s long) is applied to a Pt mesh immersed in a 0.4×10^{-3} M **AMP-luc** oxygen-saturated solution in [EMIM][EtSO₄]. (b) A similar experiment as in (a) but carried out in a molecular solvent-based electrolyte (0.4×10^{-3} M **AMP-luc** in oxygen-saturated 0.2 Bu₄NClO₄/DMSO). The micrograph shown in (a) is edited to maximise contrast. Scale bars are 100 μ m.

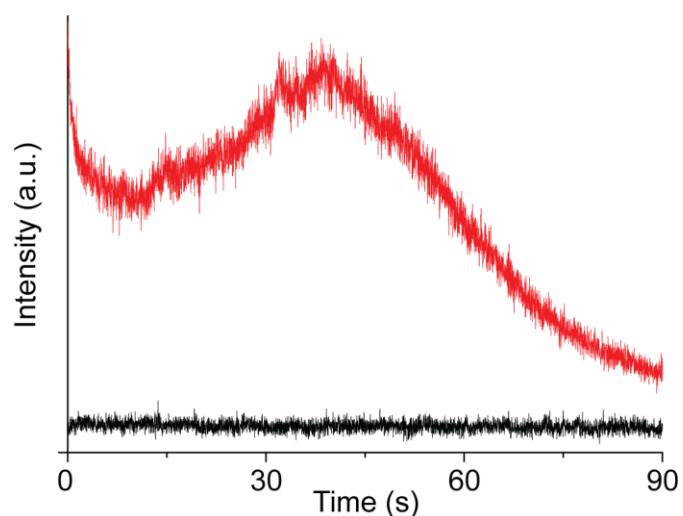


Figure S4. Time evolution of the electrochemically generated light emission (ECL) upon the electrolysis at a platinum mesh electrode of an **AMP-luc** solution (0.4×10^{-3} M in [EMIM][EtSO₄]). The room temperature ionic liquid solution was either oxygen-saturated (red trace) or argon-saturated (black trace). Electrolytic solutions were bubbled with either oxygen (red trace) or argon (black trace) for at least 20 min prior to the ECL experiments. To trigger the ECL the voltage of the working electrode was stepped from open circuit to -2.5 V vs Ag/AgCl for 30 s. The ECL is monitored at 626 nm (emission slit set to 20 nm). The experiment with the argon-saturated **AMP-luc** solution was performed under positive argon pressure and with a small amount of oxygen scavenger (ammonium sulfite 0.5 % w/v) added to the solution.

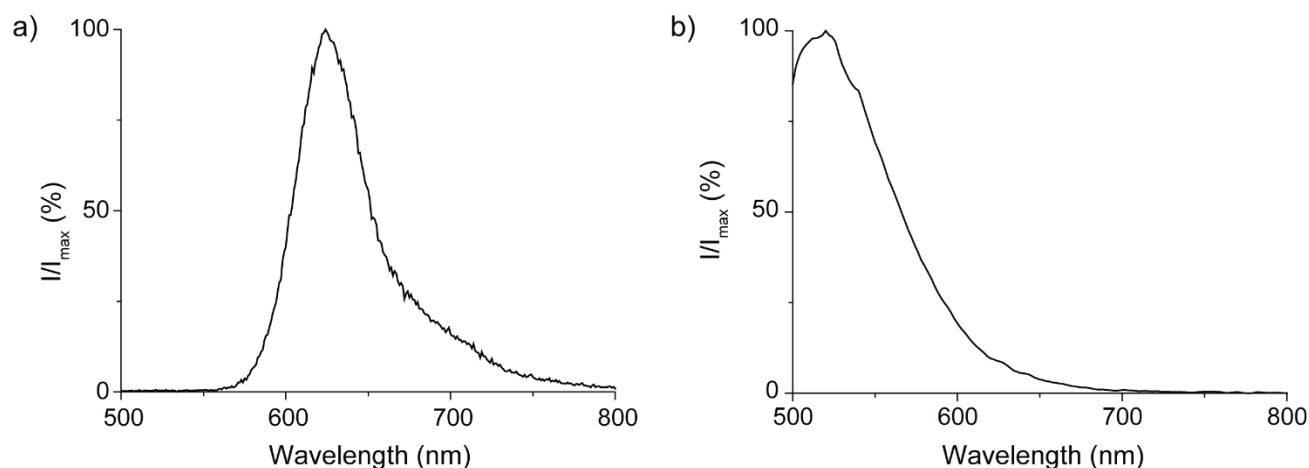


Figure S5. (a) Spectrum of the chemically induced **AMP-luc** luminescence. Argon gas was bubbled through an **AMP-luc** solution (0.4×10^{-3} M, 0.2 M $\text{Bu}_4\text{NClO}_4/\text{DMSO}$) for at least 20 min prior to the experiment. A quartz cuvette ($10 \times 10 \times 40$ mm) was loaded with KO_2 (0.02 g) and placed inside the spectrometer sample compartment (Varian, Palo Alto, California). Using silicone tubing (diameter 3.0 mm) **AMP-luc** solution (4 mL) was transferred in one portion from a syringe to the cuvette containing the KO_2 powder, avoiding ambient light to interfere with the ECL recording. Spectral acquisition started once the injection was completed, and recording a full spectrum took ~ 1.5 s. Throughout all the procedure a gentle flow of argon gas was maintained inside the sample compartment. (b) Fluorescence spectrum recorded ~ 30 s after the **AMP-luc** sample injection to the cuvette containing KO_2 . The excitation wavelength was set to 474 nm and the emission slit to 20 nm.

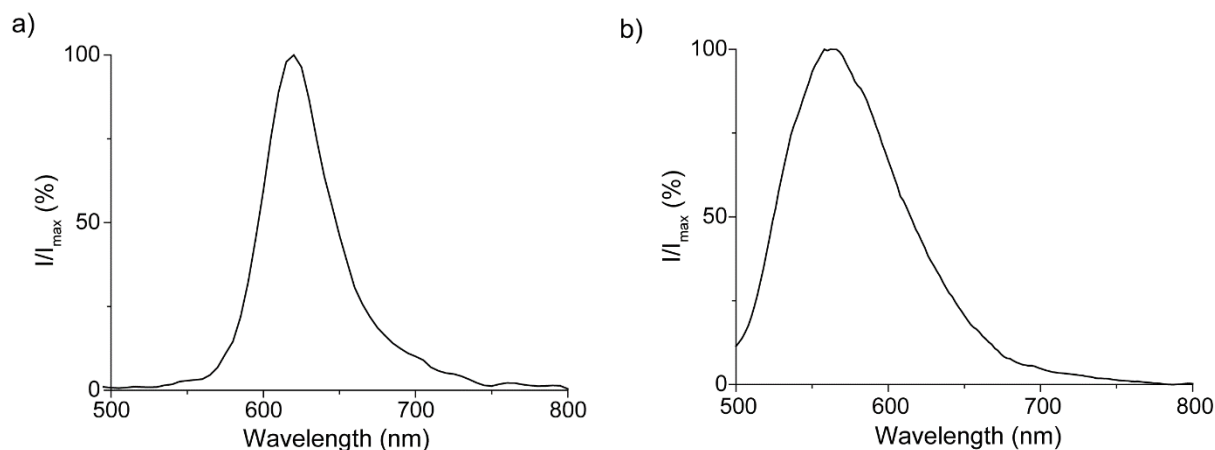


Figure S6. (a) Spectrum of the chemically induced **AMP-luc** luminescence. Argon gas was bubbled through an **AMP-luc** solution (0.4×10^{-3} M in [EMIM][EtSO₄]) for at least 20 min prior to the experiment. A quartz cuvette (10×10×40 mm) was loaded with KO₂ (0.02 g) and placed inside the spectrometer sample compartment (Varian, Palo Alto, California). Using silicone tubing (diameter 3.0 mm) **AMP-luc** solution (4 mL) was transferred in one portion from a syringe to the cuvette containing the KO₂ powder, avoiding ambient light to interfere with the ECL recording. Spectral acquisition started once the injection was completed, and recording a full spectrum took ~1.5 s. Throughout all the procedure a gentle flow of argon gas was maintained inside the sample compartment. (b) Fluorescence spectrum recorded ~30 s after the **AMP-luc** sample injection to the cuvette containing KO₂. The excitation wavelength was set to 474 nm and the emission slit to 20 nm.

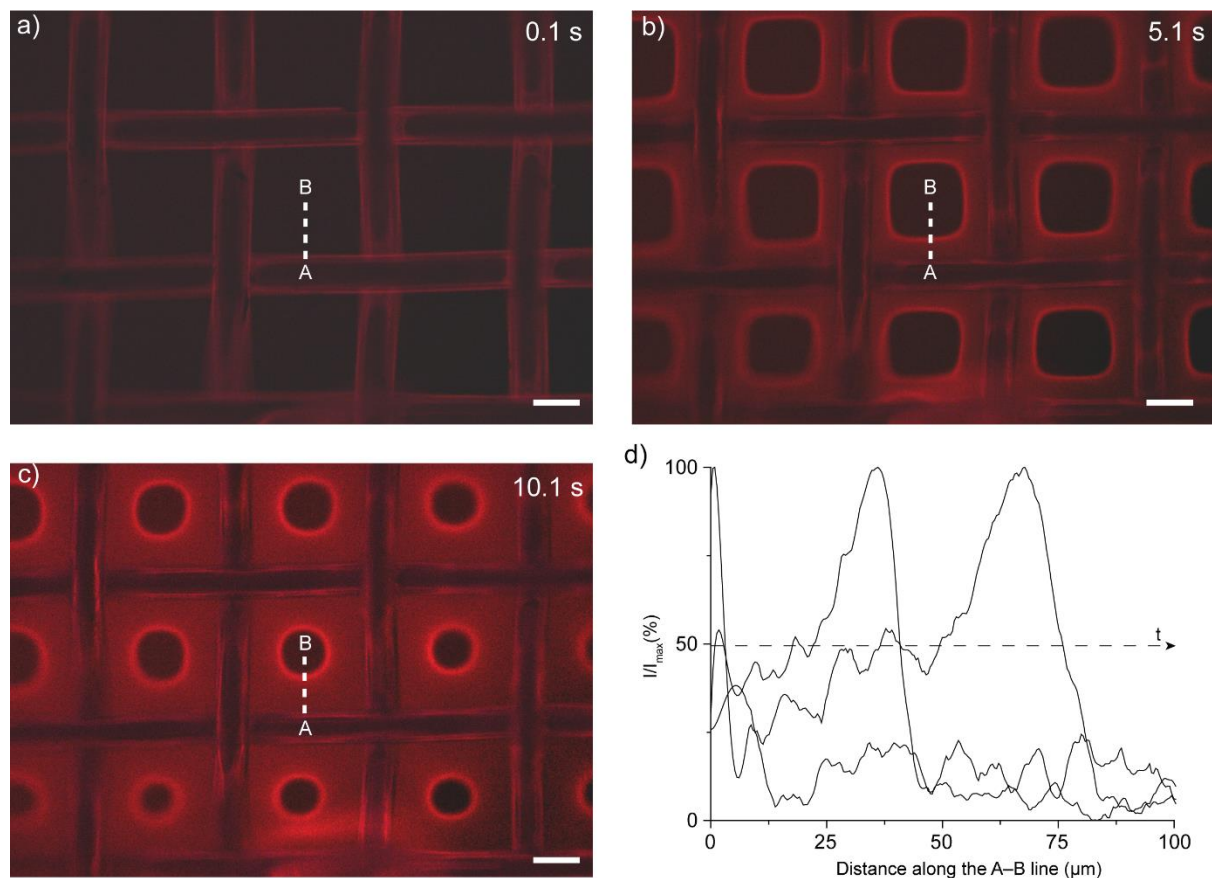


Figure S7. (a–c) Selected time-stamped micrographs (10 \times magnification, micrographs edited to maximise contrast) showing the movement of the **AMP-luc** electrochemiluminescent front (diffusion of superoxide away from the Pt mesh electrode where it forms). The electrochemiluminescent reaction is triggered upon the cathodic electrolysis (-2.0 V) of an oxygen-saturated **AMP-luc** solution (0.4×10^{-3} M) in 2.0×10^{-1} M $\text{Bu}_4\text{NClO}_4/\text{DMSO}$. The video was recorded in a dark room and the time stamps (0.1 s (a), 5.1 s (b) and 10.1 s (c)) refer to the time that has elapsed after the working electrode potential is stepped from open circuit to -2.0 V (vs. reference). Scale bars in (a–c) are $100 \mu\text{m}$. (d) Electrochemiluminescence profile sampled along the A–B line marked in (a–c), capturing the position of the diffusion front, from electrode’s surface, (t) of 0.1, 5.1, and 10.1 s. The optically determined superoxide diffusion coefficient is $2.62 \times 10^{-6} \text{ cm}^2\text{s}^{-1}$. Point A is placed approximately on the platinum wire edge (top view).

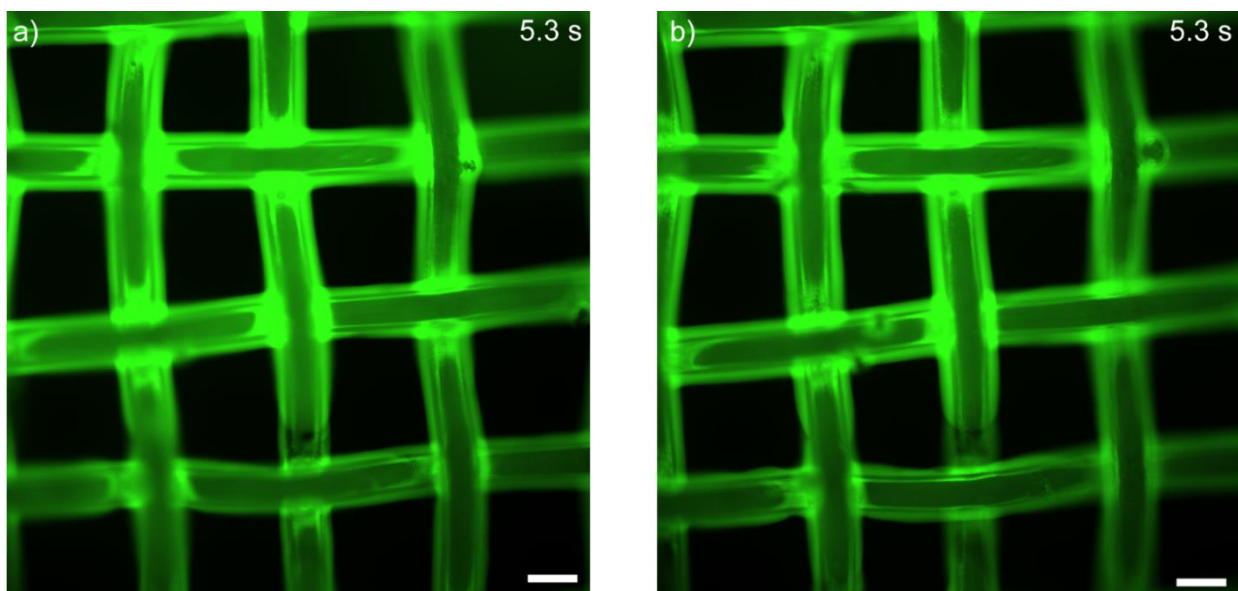


Figure S8. Fluorescence micrographs (10 \times magnification) recorded during the cathodic electrolysis (-2.0 V vs Ag/AgCl) of an oxygen-saturated **AMP-luc** solution (0.4×10^{-3} M in [EMIM][EtSO₄]) at a platinum mesh working electrode. The counter electrode (Pt coil) was placed either on the left (a) or on the right side (b) of the working electrode.

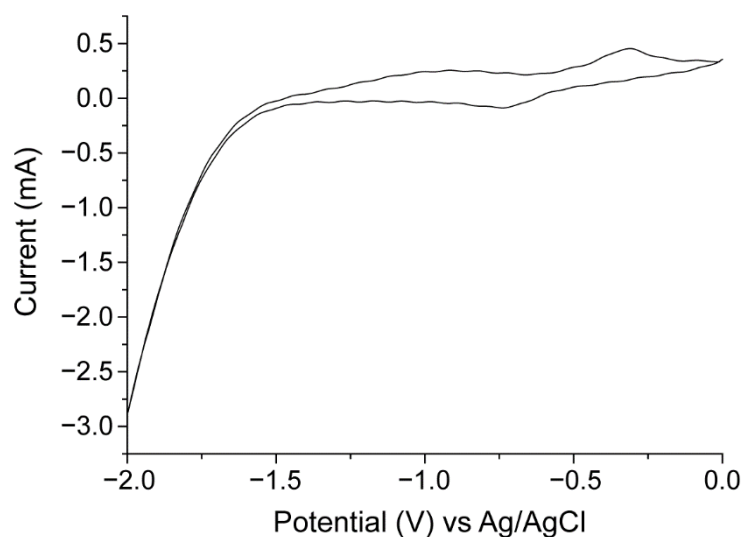


Figure S9. Representative cyclic voltammogram (CV) recorded at a platinum mesh electrode in oxygen-saturated [EMIM][EtSO₄], without **AMP-luc**. The voltage scan rate is 0.05 V/s. In the dynamic CV measurement the oxygen reduction peak is appearing at about -0.7 V vs Ag/AgCl (-1.15 vs Fc/Fc⁺), a potential where overscreening should already be occurring (Figure 2f, main text, onset of overscreening is at approximately -0.75 V vs Fc/Fc⁺). These data suggest that the cation rich-structure effectively slows down inner-sphere reactions (such as hydrogen evolution) only at large negative potentials, where crowding sets in.

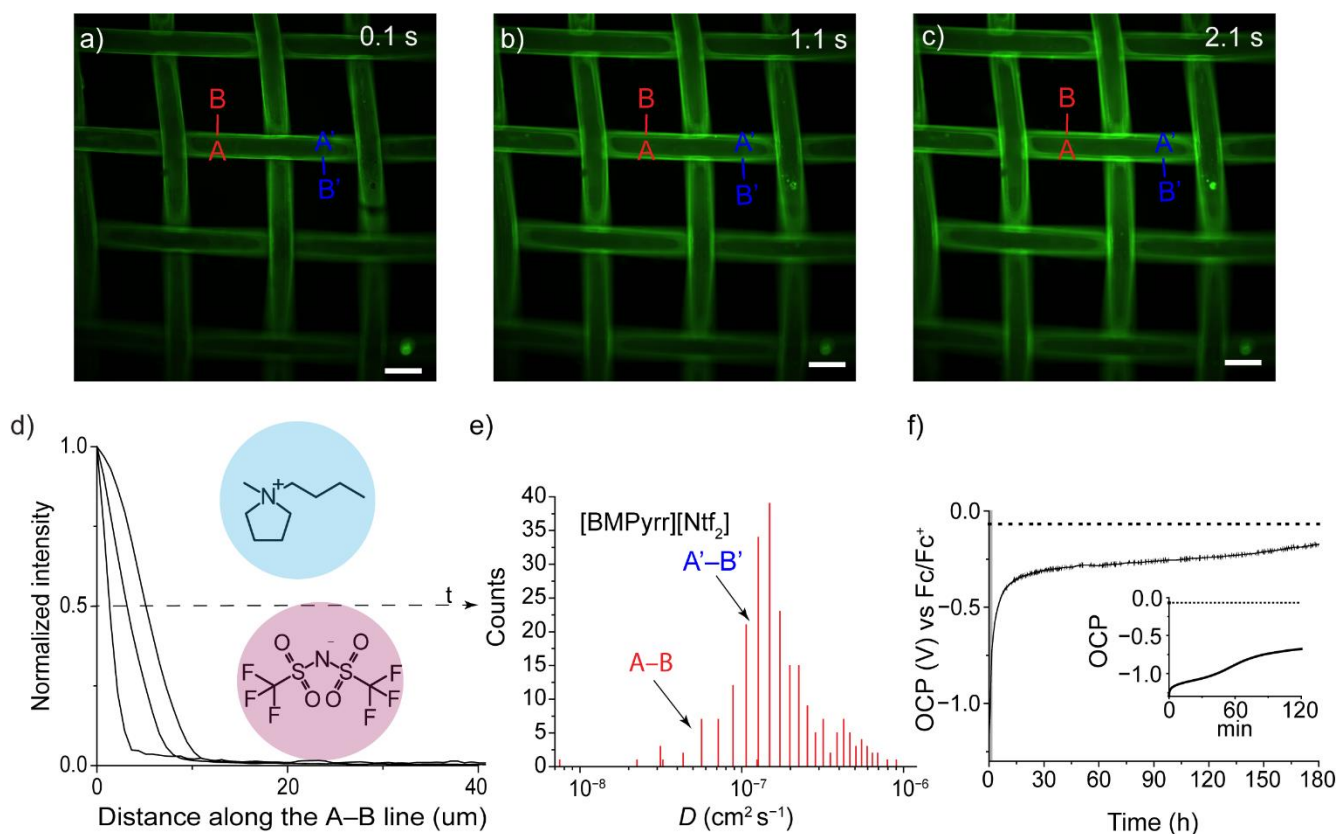


Figure S10. (a–c) Selected time-stamped fluorescence micrographs (10× magnification, 461.0–487.5 nm excitation, 502.5–547.5 nm emission) capturing the movement of the electrochemically generated **ox-luc**. **ox-luc** is the product of the cathodic electrolysis of an oxygen-saturated **AMP-luc** solution (0.4×10^{-3} M in [BMPyrr][NTf₂]) at a platinum mesh electrode. The time stamps shown in panels (a–c) refer to the time that has elapsed after the working electrode potential is stepped from open circuit to -2.0 V (0.1 s (a), 1.1 s (b) and 2.1 s (c)). Representative fluorescence profiles, sampled along the A–B line, at electrolysis times of 0.1, 1.1 and 2.1 s. The procedure (tracking the movement of the diffusion front) was repeated in at least 20 different locations per experiment, and at least 10 independent experiments were performed. Approximately 200 values of diffusivity were calculated for each system, and the distribution of these values is shown by the histogram in (e). For example, by tracking superoxide diffusion along the A–B line, we obtained a diffusion coefficient (D) for superoxide of 0.40×10^{-7} cm² s⁻¹, while the same approach along the A'–B' line led to a D of 1.10×10^{-7} cm² s⁻¹. Scale bars in (a–c) are 100 μm. The mode of the optically determined superoxide D is 1.30×10^{-7} cm² s⁻¹. (f) Representative OCP–time measurement for a platinum mesh electrode immersed in [BMPyrr][NTf₂] (125 ppm water content). The OCP logging started after the end of a 60 s negative bias pulse (-2.0 V vs the initial OCP). The dotted line represents the initial OCP. The gray shaded area in (f) indicates the data plotted in the figure inset. This inset reveals the onset of crowding between -1.0 V and -1.2 V. The overscreening OCP signature (plateau in OCP) lays between -0.25 V and -0.35 V.

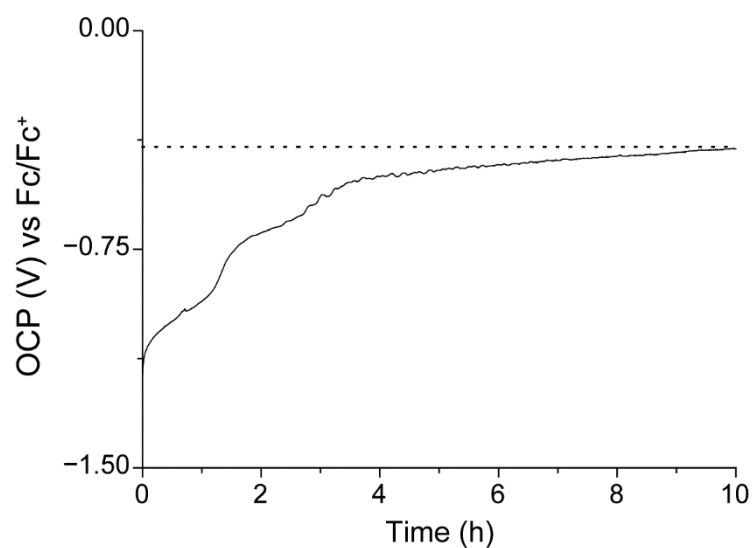


Figure S11. Representative OCP–time measurement of a platinum mesh electrode immersed in [EMIM][BF₄]. The OCP measurement was started after the end of a 60 s cathodic pulse (–2.0 V away from the system’s initial OCP). The dotted horizontal line represents the initial OCP before the cathodic pulse.

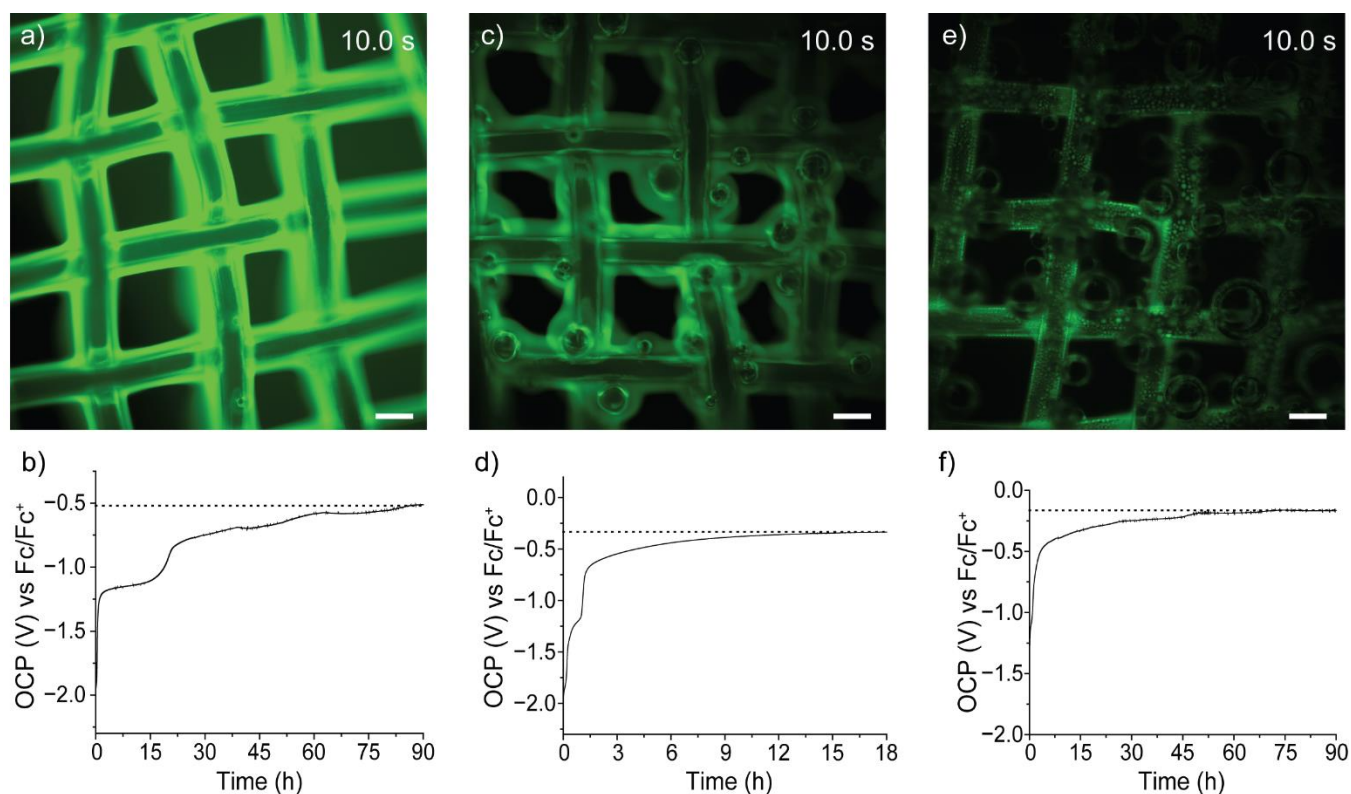


Figure S12. (a,c,e) Selected time-stamped fluorescence micrographs recorded 10 s after the working electrode potential is stepped cathodically (-2.0 V) away from open circuit ($10\times$ magnification $461.0\text{--}487.5$ nm excitation, $502.5\text{--}547.5$ nm emission). The fluorescence images capture the evolution of gases upon the electrolysis of oxygen-saturated **AMP-luc** solutions (0.4×10^{-3} M) in various RTILs. The RTIL in (a) and in (c) is [EMIM][EtSO₄], spiked respectively with either 2.0% (a) or 5% (c) of water. The RTIL in (e) is [BMPyrr][NTf₂], spiked with 2.0% of water. (b,d,f) OCP–time measurement for the mesh platinum electrode immersed in the RTIL systems of (a), (c) and (e). The OCP was recorded after the application of -2.0 V relative to the system’s initial OCP.

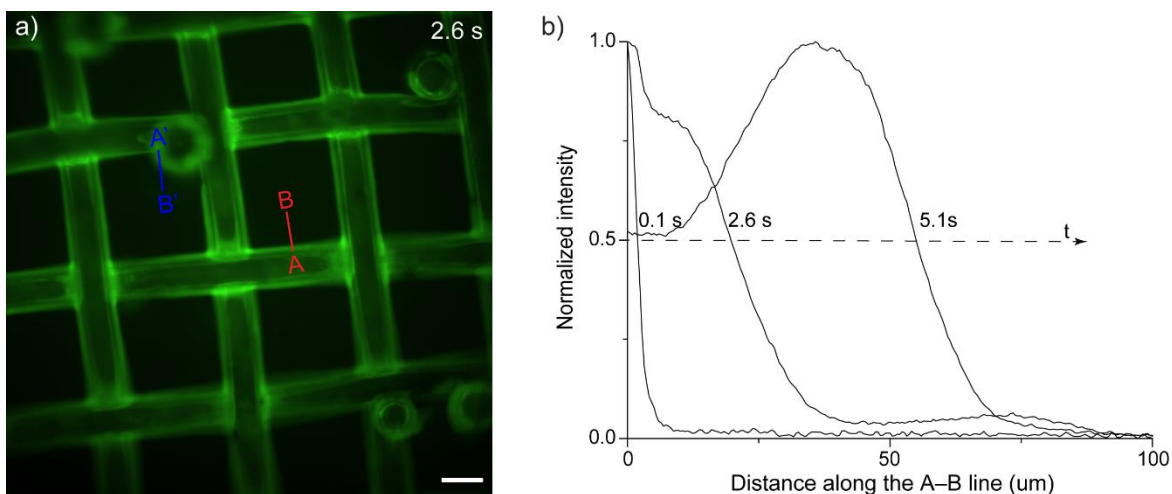


Figure S13. Selected time-stamped fluorescence micrograph (10 \times magnification) recorded during the cathodic electrolysis (-2.0 V vs Ag/AgCl) of an oxygen-saturated **AMP-luc** solution (0.4×10^{-3} M in [EMIM][BF₄]). (b) Representative fluorescence intensity plot profiles sampled along the A'–B' line marked in (a) and in Figure 3a–b, recorded 0.1, 2.6 and 5.1 s after the working electrode bias is stepped from open circuit to -2.0 V, used for the analysis of the movement over time of the superoxide diffusion front (triggering the **ox-luc** formation). The D values reported in the main text are calculated from the front distance travelled after 5.1 s, and are therefore an average apparent diffusivity during this time, but as data in (b) show, the apparent diffusion is not uniform over time, with the front progressing faster as the bubbles become larger.

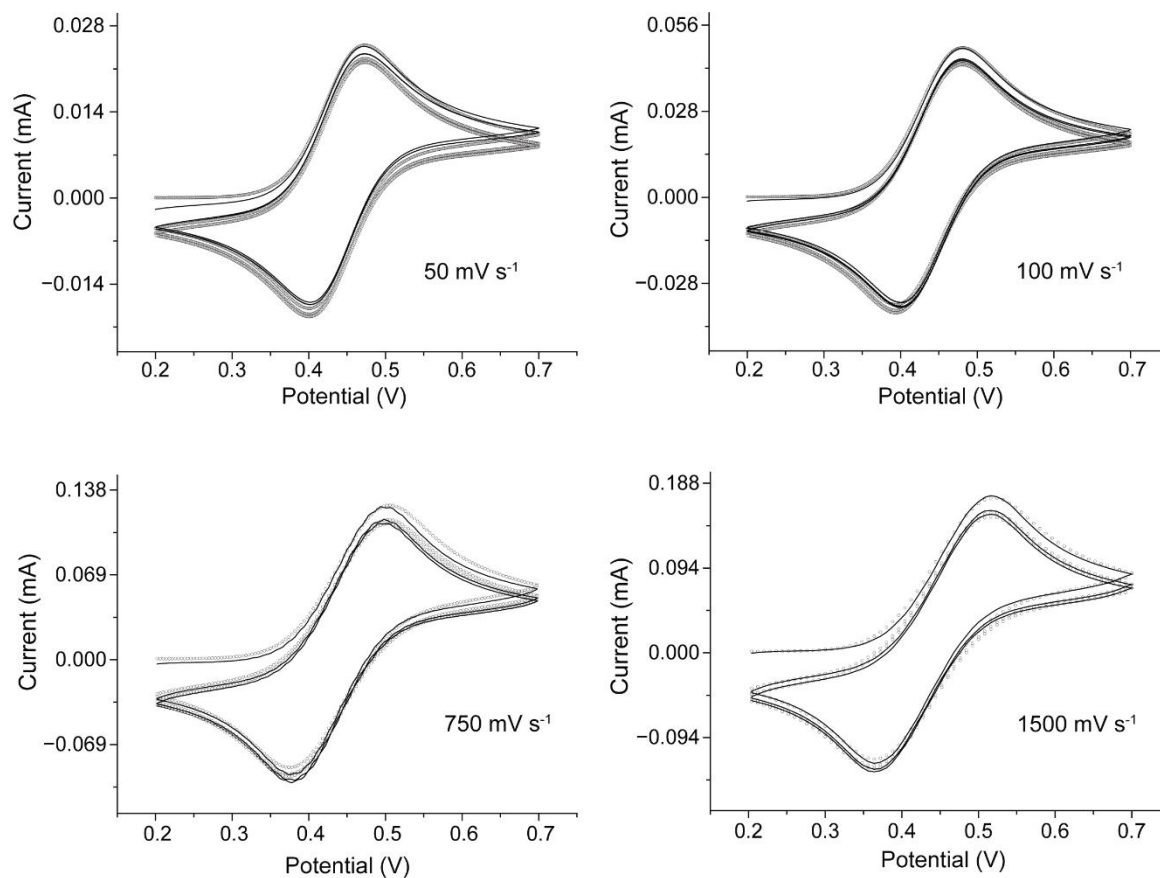


Figure S14. Representative experimental (solid line) and simulated (empty symbols) cyclic voltammograms recorded at a platinum disk electrode in an acetonitrile solution containing 1.0×10^{-3} M ferrocene and 1.0×10^{-1} Bu₄NPF₆. The voltage sweep rate is indicated as a label to the figures. The diffusivity (D) of ferrocene and ferricenium (Fc and Fc⁺ hereafter) was set to 2.60×10^{-5} cm² s⁻¹.³⁹⁵ The best-fit parameters (E mechanism) are E^0 (Fc/Fc⁺) = 0.4371 V (vs. Ag/AgCl “leakless”, upper limit 0.4374, lower limit 0.4368, 95.4% confidence level), and k_{et} = 0.040 cm s⁻¹ (upper limit 0.043, lower limit 0.037, 95.4% confidence level). The electrochemically-determined effective area of the platinum disk is 0.08 cm².

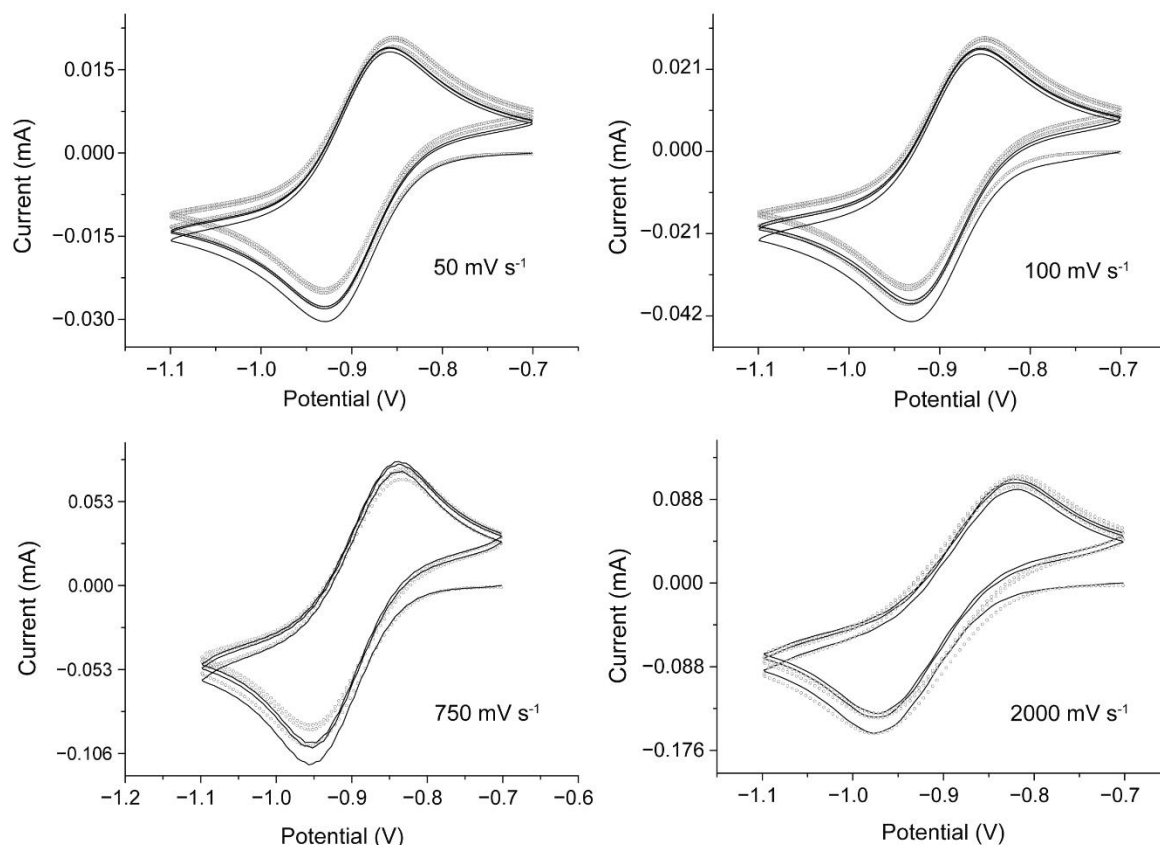


Figure S15. Representative experimental (solid line) and simulated (empty symbols) cyclic voltammograms recorded at a platinum disk electrode in an acetonitrile solution containing 1.0×10^{-3} M cobaltocenium hexafluorophosphate and 1.0×10^{-1} Bu₄NPF₆. The voltage sweep rate is indicated by labels to the figures. The D of cobaltocene and cobaltocenium (Cc and Cc⁺ hereafter) was set to 3.25×10^{-5} cm² s⁻¹.³⁹⁶ The best-fit parameters (E mechanism) are E^0 (Cc/Cc⁺) -0.8824 V (vs. Ag/AgCl “leakless”, upper limit -0.8919 , lower limit -0.8929 , 95.4% confidence level), and $k_{et} = 0.044$ cm s⁻¹ (upper limit 0.049, lower limit 0.039, 95.4% confidence level). The electrochemically-determined effective area of the platinum disk is 0.08 cm².

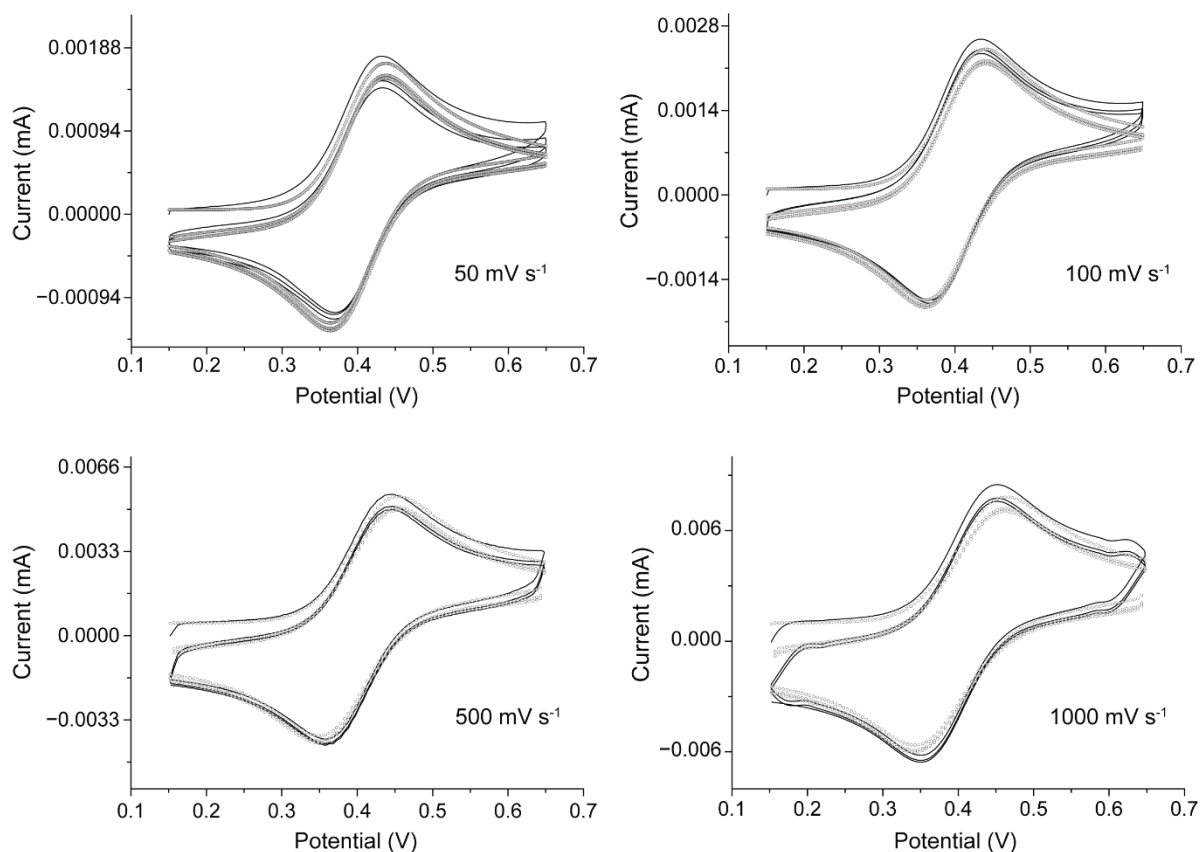


Figure S16. Representative experimental (solid line) and simulated (empty symbols) cyclic voltammograms at a platinum disk electrode in [EMIM][EtSO₄] containing 1.0×10^{-3} M ferrocene. The voltage sweep rate is indicated by the labels to the figures. The best-fit parameters (E mechanism) are E^0 (Fc/Fc⁺) = 0.4001 V (vs. Ag/AgCl “leakless”, upper limit 0.4000, lower limit 0.3998, 95.4% confidence level), k_{et} = 0.0011 cm s⁻¹ (upper limit 0.0012, lower limit 0.0010, 95.4% confidence level), and D = 0.608×10^{-7} cm² s⁻¹ (upper limit 0.611, lower limit 0.605, 95.4% confidence level). The electrochemically-determined effective area of the platinum disk is 0.08 cm².

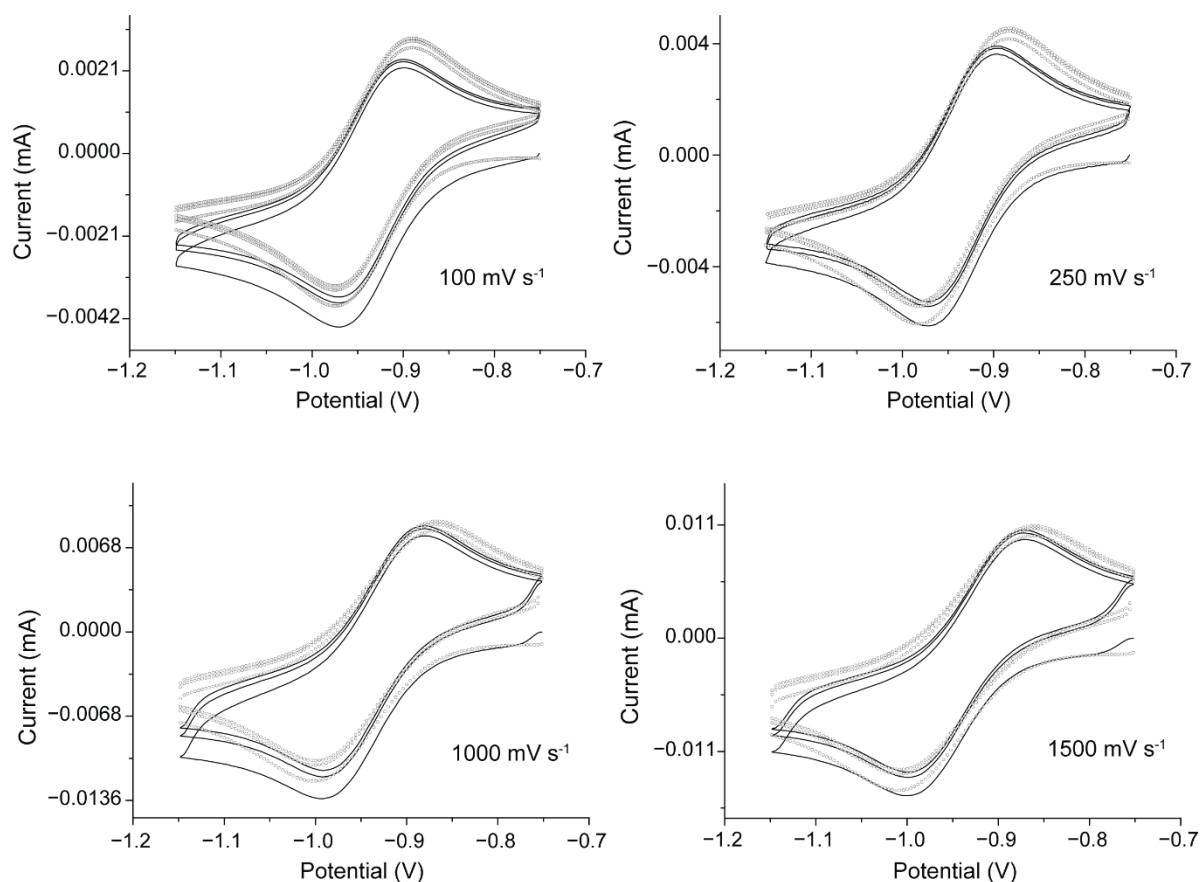


Figure S17. Representative experimental (solid line) and simulated (empty symbols) cyclic voltammograms at a platinum disk electrode in [EMIM][EtSO₄] containing 1.0×10^{-3} M cobaltocenium hexafluorophosphate. The voltage sweep rate is indicated by the labels to the figures. The best-fit parameters (E mechanism) are E^0 (Cc /Cc⁺) = -0.9317 V (vs. Ag/AgCl “leakless”, upper limit -0.9307 , lower limit -0.9327 , 95.4% confidence level), $k_{\text{et}} = 0.0019$ cm s⁻¹ (upper limit 0.0021, lower limit 0.0018, 95.4% confidence level), and $D = 2.90 \times 10^{-7}$ cm² s (upper limit 2.93, lower limit 2.86, 95.4% confidence level). The electrochemically-determined effective area of the platinum disk is 0.08 cm².

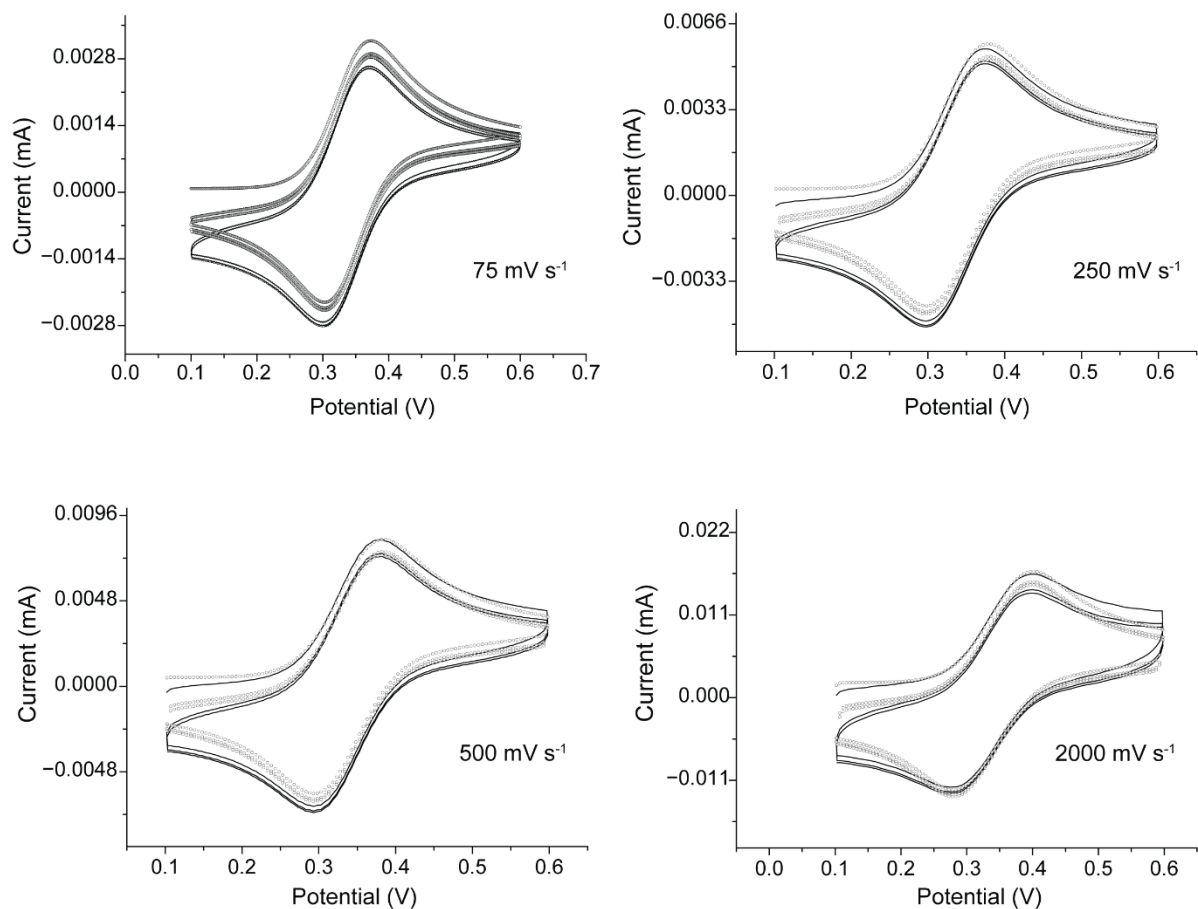


Figure S18. Representative experimental (solid line) and simulated (empty symbols) cyclic voltammograms at a platinum disk electrode in [BMPyrr][NTf₂] containing 1.0×10^{-3} M ferrocene. The voltage sweep rate is indicated by labels to the figures. The best-fit parameters are (E mechanism) E^0 (Fc/Fc⁺) was 0.3377 V (vs. Ag/AgCl “leakless”, upper limit 0.3382, lower limit 0.3373, 95.4% confidence level), $k_{\text{et}} = 0.0046 \text{ cm s}^{-1}$ (upper limit 0.0052, lower limit 0.0042, 95.4% confidence level), and $D = 2.37 \times 10^{-7} \text{ cm}^2 \text{ s}^{-1}$ (upper limit 2.41, lower limit 2.33, 95.4% confidence level). The electrochemically-determined effective area of the platinum disk is 0.08 cm^2

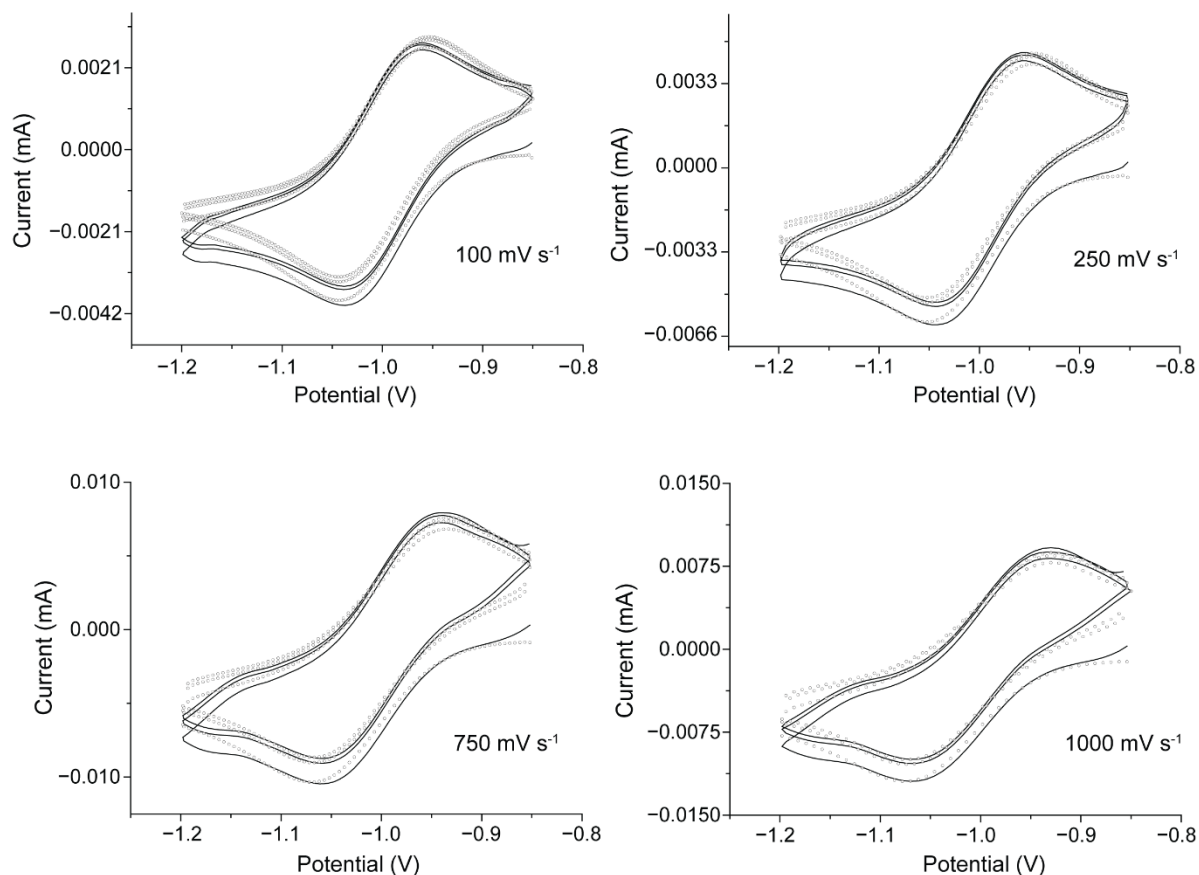


Figure S19. Representative experimental (solid line) and simulated (empty symbols) cyclic voltammograms at a platinum disk electrode in [BMPyrr][NTf₂] containing 1.0×10^{-3} M cobaltocenium hexafluorophosphate. The voltage sweep rate is indicated by labels to the figures. The voltage sweep rate is indicated as labels to the figures. The best-fit parameters (E mechanism) are E^0 (Cc/Cc⁺) = -0.9978 V (vs. Ag/AgCl “leakless”, upper limit -0.9973 , lower limit -0.9983 , 95.4% confidence level), $k_{\text{et}} = 0.0131$ cm s⁻¹ (upper limit 0.0136, lower limit 0.0126, 95.4% confidence level), and $D = 1.92 \times 10^{-7}$ cm² s⁻¹ (upper limit 1.94, lower limit 1.90, 95.4% confidence level). The electrochemically-determined effective area of the platinum disk is 0.08 cm².

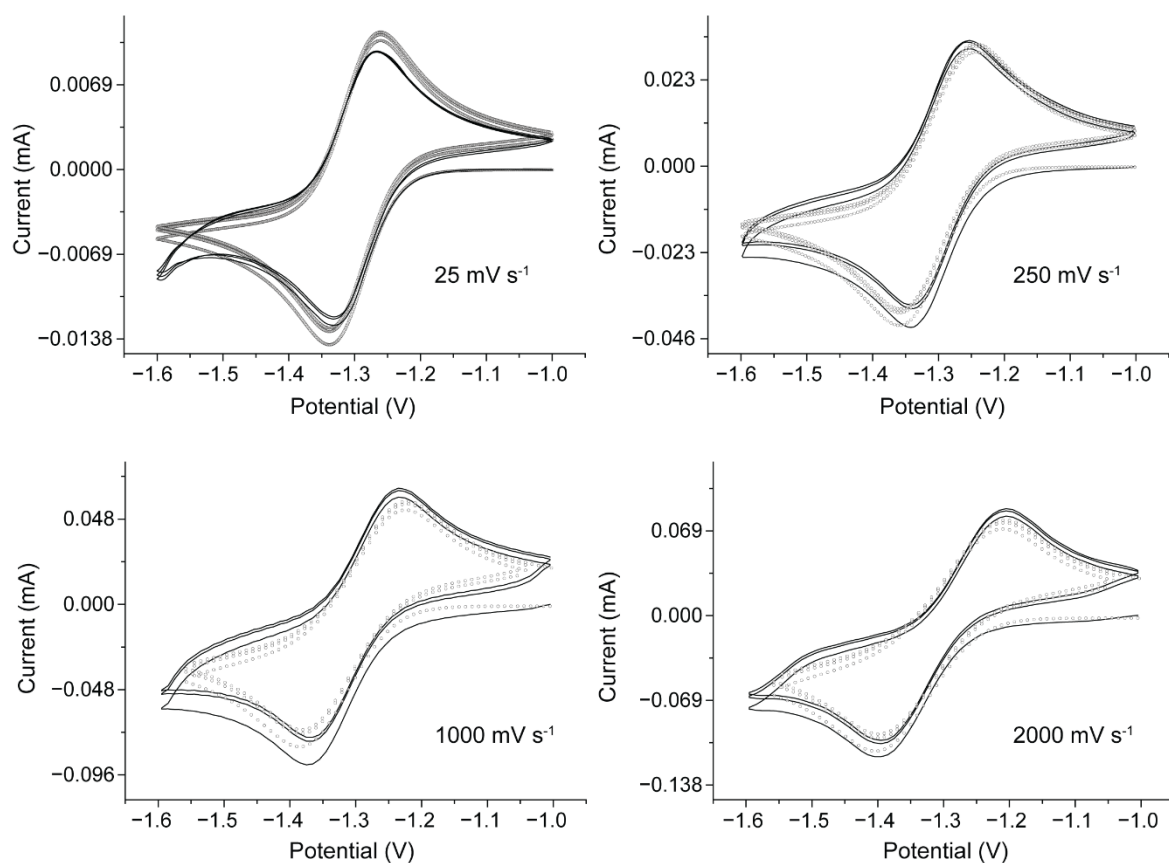


Figure S20. Representative experimental (solid line) and simulated (empty symbols) cyclic voltammograms at a platinum disk electrode in an acetonitrile solution containing 1.0×10^{-3} M decamethyl cobaltocenium hexafluorophosphate ($\text{Me}_{10}(\text{Cc})^+$ hereafter) and 1.0×10^{-1} Bu_4NPF_6 . The voltage sweep rate is indicated by labels to the figures. The best-fit parameters (E mechanism) are E^0 ($\text{Me}_{10}(\text{Cc})/\text{Me}_{10}(\text{Cc})^+$) = -1.300 V (vs. Ag/AgCl “leakless”, upper limit -1.299 , lower limit -1.301 , 95.4% confidence level), $k_{\text{et}} = 0.016$ cm s^{-1} (upper limit 0.017 , lower limit 0.014 , 95.4% confidence level), and $D = 1.65 \times 10^{-5}$ $\text{cm}^2 \text{s}^{-1}$ (upper limit 1.67 , lower limit 1.63 , 95.4% confidence level). The electrochemically-determined effective area of the platinum disk is 0.08 cm^2 .

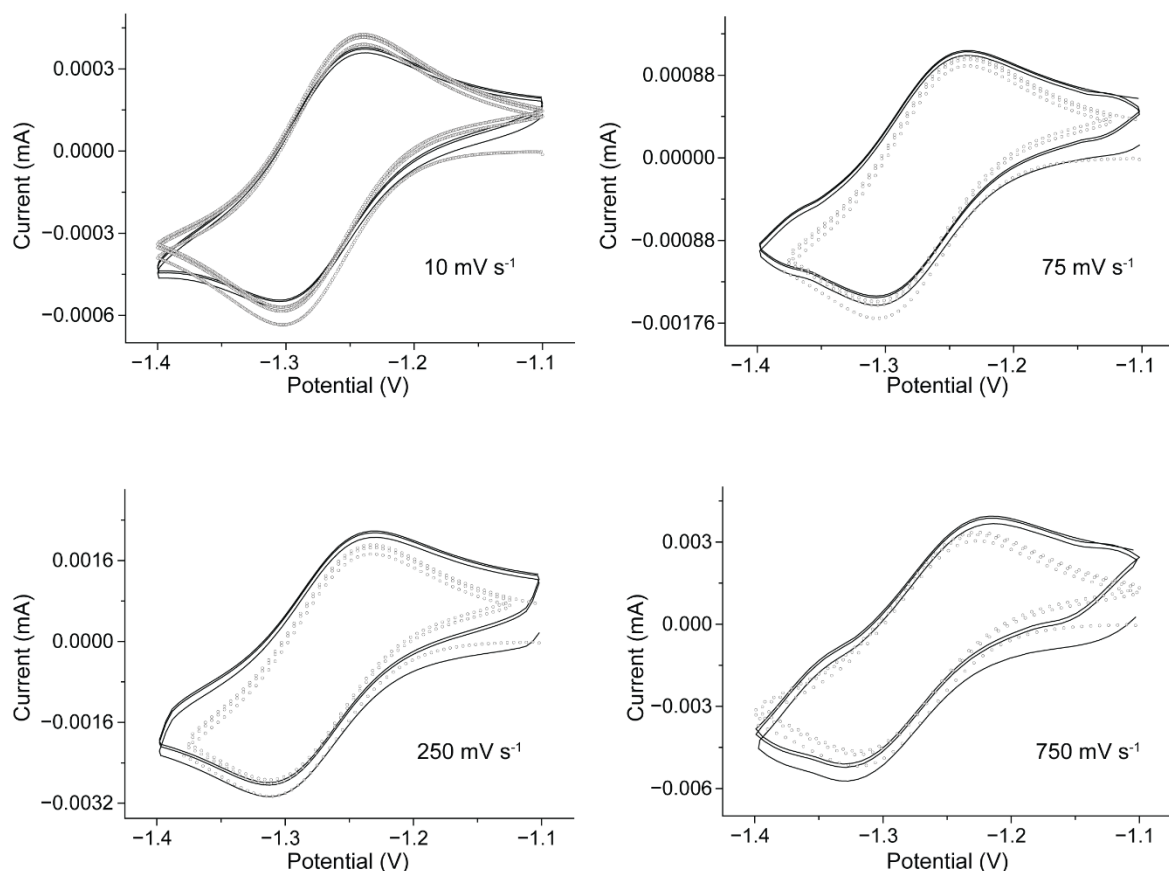



Figure S21. Representative experimental (solid line) and simulated (empty symbols) cyclic voltammograms at a platinum disk electrode in [EMIM][EtSO₄] containing 1.0×10^{-3} M Me₁₀(Cc)⁺. The voltage sweep rate is indicated by labels to the figures. The best-fit parameters (E mechanism) are E^0 (Me₁₀(Cc)/Me₁₀(Cc)⁺) = -1.2729 V (vs. Ag/AgCl “leakless”, upper limit -1.214, lower limit -1.2724, 95.4% confidence level), $k_{\text{et}} = 0.0023$ cm s⁻¹ (upper limit 0.0027, lower limit 0.0019, 95.4% confidence level), and $D = 0.805 \times 10^{-7}$ cm² s⁻¹ (upper limit 0.816, lower limit 0.794, 95.4% confidence level). The electrochemically-determined effective area of the platinum disk is 0.08 cm².

Appendix 5: Copyright forms and declaration

Copyright information related to Figure 1.3

Home Help Email Support Sign In Create Account

The Electrostatic Screening Length in Concentrated Electrolytes Increases with Concentration

Author: Alexander M. Smith, Alpha A. Lee, Susan Perkin
Publication: Journal of Physical Chemistry Letters
Publisher: American Chemical Society
Date: Jun 1, 2016
Copyright © 2016, American Chemical Society

PERMISSION/LICENSE IS GRANTED FOR YOUR ORDER AT NO CHARGE

This type of permission/license, instead of the standard Terms and Conditions, is sent to you because no fee is being charged for your order. Please note the following:


- Permission is granted for your request in both print and electronic formats, and translations.
- If figures and/or tables were requested, they may be adapted or used in part.
- Please print this page for your records and send a copy of it to your publisher/graduate school.
- Appropriate credit for the requested material should be given as follows: "Reprinted (adapted) with permission from (COMPLETE REFERENCE CITATION). Copyright (YEAR) American Chemical Society." Insert appropriate information in place of the capitalized words.
- One-time permission is granted only for the use specified in your RightsLink request. No additional uses are granted (such as derivative works or other editions). For any uses, please submit a new request.

If credit is given to another source for the material you requested from RightsLink, permission must be obtained from that source.

[BACK](#) [CLOSE WINDOW](#)

© 2022 Copyright - All Rights Reserved | [Copyright Clearance Center, Inc.](#) | [Privacy statement](#) | [Terms and Conditions](#)
Comments? We would like to hear from you. E-mail us at customer@copyright.com

Copyright information related to Figure 1.5



Reproducible flaws unveil electrostatic aspects of semiconductor electrochemistry

Author: Yan B. Vogel et al
Publication: Nature Communications
Publisher: Springer Nature
Date: Dec 12, 2017
Copyright © 2017, The Author(s)

Creative Commons

This is an open access article distributed under the terms of the [Creative Commons CC BY](#) license, which permits unrestricted use, distribution, and reproduction in any medium, provided the original work is properly cited.

You are not required to obtain permission to reuse this article.
To request permission for a type of use not listed, please contact [Springer Nature](#)

Copyright information related to Figure 1.6

Order Date	18-Jan-2023	Type of Use	Republish in a thesis/dissertation
Order License ID	1312464-1	Publisher	FARADAY DIVISION OF THE CHEMICAL SOCIETY,
ISSN	0300-9599	Portion	Chart/graph/table/figure

LICENSED CONTENT

Publication Title	Journal of the Chemical Society, Faraday transactions I	Rightholder	Royal Society of Chemistry
Article Title	Measurement of forces between two mica surfaces in aqueous electrolyte solutions in the range 0–100 nm	Publication Type	Journal
Author/Editor	CHEMICAL SOCIETY (GREAT BRITAIN), ROYAL SOCIETY OF CHEMISTRY (GREAT BRITAIN).	Start Page	975
Date	01/01/1972	Issue	0
Language	English	Volume	74
Country	United Kingdom of Great Britain and Northern Ireland		

REQUEST DETAILS

Portion Type	Chart/graph/table/figure	Distribution	Worldwide
Number of Charts / Graphs / Tables / Figures Requested	1	Translation	Original language of publication
Format (select all that apply)	Print, Electronic	Copies for the Disabled?	No
Who Will Republish the Content?	Academic institution	Minor Editing Privileges?	No
Duration of Use	Life of current edition	Incidental Promotional Use?	No
Lifetime Unit Quantity	Up to 499	Currency	AUD
Rights Requested	Main product		

NEW WORK DETAILS

Title	Towards optical and potentiometric measurements of double layer structures and dynamics	Institution Name	Curtin University
Instructor Name	Mattia belotti	Expected Presentation Date	2023-05-08

ADDITIONAL DETAILS

Order Reference Number	N/A	The Requesting Person/Organization to Appear on the License	Mattia Belotti, Curtin University
------------------------	-----	---	-----------------------------------

REUSE CONTENT DETAILS

Title, Description or Numeric Reference of the Portion(s)	Figure 3	Title of the Article/Chapter the Portion Is From	Measurement of forces between two mica surfaces in aqueous electrolyte solutions in the range 0–100 nm
Editor of Portion(s)	Israelachvili, Jacob N.; Adams, Gayle E.	Author of Portion(s)	Israelachvili, Jacob N.; Adams, Gayle E.
Volume of Serial or Monograph	74	Issue, if Republishing an Article From a Serial	0
Page or Page Range of Portion	975	Publication Date of Portion	1978-01-01

Copyright information related to Figure 1.8

Real-Space Investigation of Electrical Double Layers. Potential Gradient Measurement with a Nanometer Potential Probe



Author: Young-Hwan Yoon, Dae-Ha Woo, Taeho Shin, et al
Publication: The Journal of Physical Chemistry C
Publisher: American Chemical Society
Date: Sep 1, 2011

Copyright © 2011, American Chemical Society

PERMISSION/LICENSE IS GRANTED FOR YOUR ORDER AT NO CHARGE

This type of permission/license, instead of the standard Terms and Conditions, is sent to you because no fee is being charged for your order. Please note the following:

- Permission is granted for your request in both print and electronic formats, and translations.
- If figures and/or tables were requested, they may be adapted or used in part.
- Please print this page for your records and send a copy of it to your publisher/graduate school.
- Appropriate credit for the requested material should be given as follows: "Reprinted (adapted) with permission from {COMPLETE REFERENCE CITATION}. Copyright (YEAR) American Chemical Society." Insert appropriate information in place of the capitalized words.
- One-time permission is granted only for the use specified in your RightsLink request. No additional uses are granted (such as derivative works or other editions). For any uses, please submit a new request.

If credit is given to another source for the material you requested from RightsLink, permission must be obtained from that source.

BACK

CLOSE WINDOW

Copyright information related to Figure 1.10

Strong Electric Field Observed at the Interface of Aqueous Microdroplets



Author: Hanqing Xiong, Jae Kyoo Lee, Richard N. Zare, et al
Publication: Journal of Physical Chemistry Letters
Publisher: American Chemical Society
Date: Sep 1, 2020

Copyright © 2020, American Chemical Society

PERMISSION/LICENSE IS GRANTED FOR YOUR ORDER AT NO CHARGE

This type of permission/license, instead of the standard Terms and Conditions, is sent to you because no fee is being charged for your order. Please note the following:

- Permission is granted for your request in both print and electronic formats, and translations.
- If figures and/or tables were requested, they may be adapted or used in part.
- Please print this page for your records and send a copy of it to your publisher/graduate school.
- Appropriate credit for the requested material should be given as follows: "Reprinted (adapted) with permission from {COMPLETE REFERENCE CITATION}. Copyright (YEAR) American Chemical Society." Insert appropriate information in place of the capitalized words.
- One-time permission is granted only for the use specified in your RightsLink request. No additional uses are granted (such as derivative works or other editions). For any uses, please submit a new request.

If credit is given to another source for the material you requested from RightsLink, permission must be obtained from that source.

BACK

CLOSE WINDOW

Copyright information related to Figure 1.11

Order Date	11-Jan-2022	Type of Use	Republish in a thesis/dissertation
Order License ID	1176273-1	Publisher	AMERICAN ASSOCIATION FOR THE ADVANCEMENT OF SCIENCE
ISSN	1095-9203	Portion	Chart/graph/table/figure

LICENSED CONTENT

Publication Title	Science	Publication Type	e-Journal
Article Title	Tuning the electronic absorption of protein-embedded all-trans-retinal.	Start Page	1340
Author/Editor	American Association for the Advancement of Science.	End Page	1343
Date	01/01/1880	Issue	6112
Language	English	Volume	338
Country	United States of America	URL	http://www.sciencemag.org/archive
Rights holder	American Association for the Advancement of Science		

REQUEST DETAILS

Portion Type	Chart/graph/table/figure	Distribution	Worldwide
Number of charts / graphs / tables / figures requested	1	Translation	Original language of publication
Format (select all that apply)	Print, Electronic	Copies for the disabled?	No
Who will republish the content?	Academic institution	Minor editing privileges?	No
Duration of Use	Life of current edition	Incidental promotional use?	No
Lifetime Unit Quantity	Up to 19,999	Currency	AUD
Rights Requested	Main product		

NEW WORK DETAILS

Title	Mattia Belotti PhD thesis	Institution name	Curtin University
Instructor name	Mattia Belotti	Expected presentation date	2023-04-05

ADDITIONAL DETAILS


Order reference number	N/A	The requesting person / organization to appear on the license	Mattua Belotti, Curtin Univeristy
------------------------	-----	---	-----------------------------------


REUSE CONTENT DETAILS

Title, description or numeric reference of the portion(s)	Figure 3	Title of the article/chapter the portion is from	Tuning the electronic absorption of protein-embedded all-trans-retinal.
Editor of portion(s)	Wang, Wenjing; Nossoni, Zahra; Berbasova, Tetyana; Watson, Camille T; Yapici, Ipek; Lee, Kin Sing Stephen; Vasileiou, Chrysoula; Geiger, James H; Borhan, Babak	Author of portion(s)	Wang, Wenjing; Nossoni, Zahra; Berbasova, Tetyana; Watson, Camille T; Yapici, Ipek; Lee, Kin Sing Stephen; Vasileiou, Chrysoula; Geiger, James H; Borhan, Babak
Volume of serial or monograph	338	Issue, if republishing an article from a serial	6112
Page or page range of portion	1340-1343	Publication date of portion	2012-12-07

RIGHTS HOLDER TERMS AND CONDITIONS

Copyright information related to Figure 1.12

Home Help Live Chat Mattia Belotti

 **Red Light in Chemiluminescence and Yellow-Green Light in Bioluminescence: Color-Tuning Mechanism of Firefly, Photinus pyralis, Studied by the Symmetry-Adapted Cluster–Configuration Interaction Method**

Author: Naoki Nakatani, Jun-ya Hasegawa, Hiroshi Nakatsuji
Publication: Journal of the American Chemical Society
Publisher: American Chemical Society
Date: Jul 1, 2007
Copyright © 2007, American Chemical Society

PERMISSION/LICENSE IS GRANTED FOR YOUR ORDER AT NO CHARGE

This type of permission/license, instead of the standard Terms and Conditions, is sent to you because no fee is being charged for your order. Please note the following:

- Permission is granted for your request in both print and electronic formats, and translations.
- If figures and/or tables were requested, they may be adapted or used in part.
- Please print this page for your records and send a copy of it to your publisher/graduate school.
- Appropriate credit for the requested material should be given as follows: "Reprinted (adapted) with permission from (COMPLETE REFERENCE CITATION), Copyright (YEAR) American Chemical Society." Insert appropriate information in place of the capitalized words.
- One-time permission is granted only for the use specified in your RightsLink request. No additional uses are granted (such as derivative works or other editions). For any uses, please submit a new request.

If credit is given to another source for the material you requested from RightsLink, permission must be obtained from that source.

[BACK](#) [CLOSE WINDOW](#)

© 2022 Copyright - All Rights Reserved | Copyright Clearance Center, Inc. | Privacy statement | Terms and Conditions
Comments? We would like to hear from you. E-mail us at customer-care@copyright.com

Copyright information related to Figure 1.15

Order Date	16-Feb-2022	Type of Use	Republish in a thesis/dissertation
Order License ID	1189531-1	Publisher	ROYAL SOCIETY OF CHEMISTRY
ISSN	1364-548X	Portion	Image/photo/illustration

LICENSED CONTENT

Publication Title	Chemical communications	Rightsholder	Royal Society of Chemistry
Article Title	Probing double layer structures of Au (111)-BMIPF6 ionic liquid interfaces from potential-dependent AFM force curves.	Publication Type	e-Journal
Author/Editor	Royal Society of Chemistry (Great Britain)	Start Page	582
Date	01/01/1996	End Page	584
Language	English	Issue	4
Country	United Kingdom of Great Britain and Northern Ireland	Volume	48

REQUEST DETAILS

Portion Type	Image/photo/illustration	Distribution	Worldwide
Number of images / photos / illustrations	1	Translation	Original language of publication
Format (select all that apply)	Print, Electronic	Copies for the disabled?	No
Who will republish the content?	Academic institution	Minor editing privileges?	No
Duration of Use	Life of current edition	Incidental promotional use?	No
Lifetime Unit Quantity	Up to 499	Currency	AUD
Rights Requested	Main product		

NEW WORK DETAILS

Title	Mattia Belotti's thesis	Institution name	Curtin university
Instructor name	Mattia Belotti	Expected presentation date	2023-02-15

ADDITIONAL DETAILS

Order reference number	N/A	The requesting person / organization to appear on the license	Mattia Belotti
------------------------	-----	---	----------------

REUSE CONTENT DETAILS

Title, description or numeric reference of the portion(s)	Figure 1	Title of the article/chapter the portion is from	Probing double layer structures of Au (111)-BMIPF6 ionic liquid interfaces from potential-dependent AFM force curves.
Editor of portion(s)	Zhang, Xiao; Zhong, Yun-Xin; Yan, Jia-Wei; Su, Yu-Zhuan; Zhang, Meng; Mao, Bing-Wei	Author of portion(s)	Zhang, Xiao; Zhong, Yun-Xin; Yan, Jia-Wei; Su, Yu-Zhuan; Zhang, Meng; Mao, Bing-Wei
Volume of serial or monograph	48	Issue, if republishing an article from a serial	4
Page or page range of portion	582-584	Publication date of portion	2012-01-14

Copyright information related to paper 1: Mattia Belotti, Mohsen M. T. El-Tahawy, Li-Juan Yu, Isabella C. Russell, Nadim Darwish, Michelle L. Coote, Marco Garavelli, and Simone Ciampi. Luciferase-free Luciferin Electrochemiluminescence Angew. Chem. Int. Ed. 2022.

License Number 5471780669330

[Printable Details](#)

License date Jan 18, 2023

Licensed Content

Licensed Content Publisher John Wiley and Sons
Licensed Content Publication Angewandte Chemie International Edition
Licensed Content Title Luciferase-free Luciferin Electrochemiluminescence
Licensed Content Author Mattia Belotti, Mohsen M. T. El-Tahawy, Li-Juan Yu, et al
Licensed Content Date Oct 25, 2022
Licensed Content Volume 61
Licensed Content Issue 46
Licensed Content Pages 9

Order Details

Type of use Dissertation/Thesis
Requestor type Author of this Wiley article
Format Print and electronic
Portion Full article
Will you be translating? No

About Your Work

Title Towards optical and potentiometric measurements of double layer structures and dynamics
Institution name Curtin University
Expected presentation date May 2023

Additional Data

Order reference number 3939

Requestor Location

Curtin University
kent street

Tax Details

Publisher Tax ID EU826007151

Requestor Location

Bentley, WA 6102
Australia
Attn: Curtin University

Copyright information related to paper 2: Mattia Belotti, Mohsen M. T. El-Tahawy, Nadim Darwish, Marco Garavelli, and Simone Ciampi. Electrochemically Generated Luminescence of Luminol and Luciferin in Ionic Liquids, ChemElectroChem 2022



Electrochemically Generated Luminescence of Luminol and Luciferin in Ionic Liquids

Author: Mattia Belotti, Mohsen M. T. El-Tahawy, Nadim Darwish, et al
Publication: ChemElectroChem
Publisher: John Wiley and Sons
Date: Dec 22, 2022

© 2022 The Authors. ChemElectroChem published by Wiley-VCH GmbH

Open Access Article

This is an open access article distributed under the terms of the [Creative Commons CC BY](#) license, which permits unrestricted use, distribution, and reproduction in any medium, provided the original work is properly cited.

You are not required to obtain permission to reuse this article.

For an understanding of what is meant by the terms of the Creative Commons License, please refer to [Wiley's Open Access Terms and Conditions](#).

Permission is not required for this type of reuse.

Wiley offers a professional reprint service for high quality reproduction of articles from over 1400 scientific and medical journals. Wiley's reprint service offers:

- Peer reviewed research or reviews
- Tailored collections of articles
- A professional high quality finish
- Glossy journal style color covers
- Company or brand customisation
- Language translations
- Prompt turnaround times and delivery directly to your office, warehouse or congress.

Please contact our Reprints department for a quotation. Email corporatesales@wiley.com or corporatesalesusa@wiley.com or corporatesalesDE@wiley.com.

Copyright information related to paper 3: Mattia Belotti, Xin Lyu, Longkun Xu, Peter Halat, Nadim Darwish, Debbie S. Silvester, Ching Goh, Ekaterina I. Izgorodina, Michelle L. Coote and Simone Ciampi. Experimental Evidence of Long-Lived Electric Fields of Ionic Liquid Bilayers. J. Am. Chem. Soc. 2021

Experimental Evidence of Long-Lived Electric Fields of Ionic Liquid Bilayers



Author: Mattia Belotti, Xin Lyu, Longkun Xu, et al
Publication: Journal of the American Chemical Society
Publisher: American Chemical Society
Date: Oct 1, 2021

Copyright © 2021, American Chemical Society

PERMISSION/LICENSE IS GRANTED FOR YOUR ORDER AT NO CHARGE

This type of permission/license, instead of the standard Terms and Conditions, is sent to you because no fee is being charged for your order. Please note the following:

- Permission is granted for your request in both print and electronic formats, and translations.
- If figures and/or tables were requested, they may be adapted or used in part.
- Please print this page for your records and send a copy of it to your publisher/graduate school.
- Appropriate credit for the requested material should be given as follows: "Reprinted (adapted) with permission from (COMPLETE REFERENCE CITATION). Copyright (YEAR) American Chemical Society." Insert appropriate information in place of the capitalized words.
- One-time permission is granted only for the use specified in your RightsLink request. No additional uses are granted (such as derivative works or other editions). For any uses, please submit a new request.

If credit is given to another source for the material you requested from RightsLink, permission must be obtained from that source.

BACK

CLOSE WINDOW

Copyright information related to paper 4: Mattia Belotti, Mohsen M. T. El-Tahawy, Marco Garavelli, Michelle L. Coote, K. Swaminathan Iyer, and Simone Ciampi. Separating Convective from Diffusive Mass Transport Mechanisms in Ionic Liquids by Redox Pro-fluorescence Microscopy. Anal Chem. 2023

Separating Convective from Diffusive Mass Transport Mechanisms in Ionic Liquids by Redox Pro-fluorescence Microscopy



Author: Mattia Belotti, Mohsen M. T. El-Tahawy, Marco Garavelli, et al
Publication: Analytical Chemistry
Publisher: American Chemical Society
Date: Jul 1, 2023

Copyright © 2023, American Chemical Society

PERMISSION/LICENSE IS GRANTED FOR YOUR ORDER AT NO CHARGE

This type of permission/license, instead of the standard Terms and Conditions, is sent to you because no fee is being charged for your order. Please note the following:

- Permission is granted for your request in both print and electronic formats, and translations.
- If figures and/or tables were requested, they may be adapted or used in part.
- Please print this page for your records and send a copy of it to your publisher/graduate school.
- Appropriate credit for the requested material should be given as follows: "Reprinted (adapted) with permission from (COMPLETE REFERENCE CITATION). Copyright (YEAR) American Chemical Society." Insert appropriate information in place of the capitalized words.
- One-time permission is granted only for the use specified in your RightsLink request. No additional uses are granted (such as derivative works or other editions). For any uses, please submit a new request.

If credit is given to another source for the material you requested from RightsLink, permission must be obtained from that source.

BACK

CLOSE WINDOW

A fair-minded effort has been made to acknowledge the owners of copyright figures and papers. I would be pleased to hear from any copyright owner who has been missed or inexactly acknowledged.

Appendix 6: Statement of contributions of others

Statement of contribution of others for paper 1

Mattia Belotti, Mohsen M. T. El-Tahawy, Li-Juan Yu, Isabella C. Russell, Nadim Darwish, Michelle L. Coote, Marco Garavelli, and Simone Ciampi. Luciferase-free Luciferin Electrochemiluminescence. *Angew. Chem. Int. Ed.* **2022**, 61, 46 e202209670. Paper included in Chapter 2.

I, Mattia Belotti, as the first author, performed all the electrochemiluminescence experiments, chemical synthesis and significant part of the data analysis. I drafted the first version of the manuscript, prepared most of the figures related to the experimental part of the manuscript, except for the contributions of co-authors as specified below.

Mohsen M. T. El-Tahawy and Marco Garavelli performed the computational work related to the spectra tuning of the electrochemiluminescence experiments. They also contributed significantly with the experimental data analysis and manuscript writing as well as drafting figures and table. Marco Garavelli co-supervised the project.

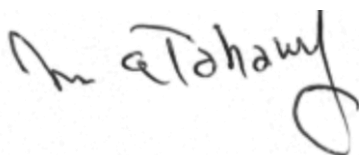
Li-Juan Yu, Isabella C. Russell and Michelle Coote developed the proposed reaction mechanism and performed all the related computations and modelling and co-wrote the manuscript. Michelle Coote also contributed with manuscript editing and preparation of figures, tables and schemes. Michelle Coote co-supervised the project.

Nadim Darwish co-supervised the project.

Simone Ciampi planned the research, supervised the project, assisted in the data analysis and interpretation, and co-wrote the manuscript.

Co-author's signatures:

Mohsen M. T. El-Tahawy



Li-Juan Yu



Isabella C. Russell



Nadim Darwish



Michelle L. Coote 

Marco Garavelli 


Simone Ciampi

Statement of contribution of others for paper 2

Mattia Belotti, Mohsen M. T. El-Tahawy, Nadim Darwish, Marco Garavelli, and Simone Ciampi. Electrochemically Generated Luminescence of Luminol and Luciferin in Ionic Liquids, ChemElectroChem 2022, 10, 1, e202201033. Paper included in Chapter 4.

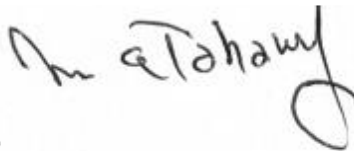
I, Mattia Belotti, as the first author, performed all the electrochemiluminescence experiments, chemical synthesis, and data analysis, I drafted the first version of the manuscript, prepared figures and schemes related to the experimental part of the manuscript, except for the contributions of co-authors as specified below.

Mohsen M. T. El-Tahawy and Marco Garavelli contributed with manuscript editing and drafting figures. Marco Garavelli co-supervised the project.

Nadim Darwish and Simone Ciampi planned the research, supervised the project, assisted in the data analysis and interpretation, and co-wrote the manuscript.

Co-author's signatures:

Mohsen M. T. El-Tahawy



Nadim Darwish



Marco Garavelli



Simone Ciampi



Statement of contribution of others for paper 3

Mattia Belotti, Xin Lyu, Longkun Xu, Peter Halat, Nadim Darwish, Debbie S. Silvester, Ching Goh, Ekaterina I. Izgorodina, Michelle L. Coote and Simone Ciampi. Experimental Evidence of Long-Lived Electric Fields of Ionic Liquid Bilayers. J. Am. Chem. Soc. 2021, 143, 42, 17431–17440. Paper included in Chapter 5.

I, Mattia Belotti, as the first author, performed the open circuit potentiometry and impedance experiments, and data analysis, I drafted the first version of the manuscript, and prepared figures and schemes related to the experimental part of the manuscript, except for the contributions of co-authors as specified below.

Xin Lyu acquired the AFM data.

provided computational work for interfacial dynamics and polarizable molecular dynamics.

Longkun Xu, Michelle Coote, Peter Halat and Ekaterina I. Izgorodina performed the computational work for the interfacial dynamics and polarizable molecular dynamics, prepared the relevant figures, data analysis and data interpretation and co-wrote the manuscript.

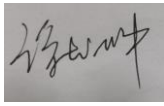
Ching Goh acquired Karl-Fisher data.

Debbie S. Silvester edited the manuscript.

Nadim Darwish and Simone Ciampi designed the project, supervised the project, interpreted the data and co-wrote the manuscript.

Co-author's signatures:


Xin Lyu 

Longkun Xu 


Peter Halat 

Ching Goh 

Debbie S. Silvester 

Ekaterina I. Izgorodina 

Michelle Coote 

Nadim Darwish 

Simone Ciampi



Statement of contribution of others for paper 4

Mattia Belotti, Mohsen M. T. El-Tahawy, Nadim Darwish, Marco Garavelli, Michelle L. Coote and Simone Ciampi. Paper 4 included in Chapter 6

I, Mattia Belotti, as the first author, performed all the experiments and most of the data analysis with inputs from all co-authors', I drafted the first version of the manuscript, and prepared figures and schemes related to the experimental part of the manuscript, except for the contributions of co-authors as specified below.

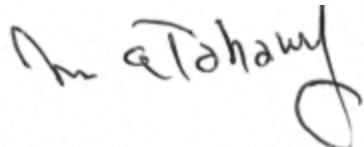
Mohsen M. T. El-Tahawy and Marco Garavelli contributed with manuscript editing and drafting figures. Marco Garavelli co-supervised the project.

Michelle L. Coote contributed with manuscript editing, drafting figures, and co-supervised the project.

Nadim Darwish co-supervised the project.

Simone Ciampi supervised the project and edited the manuscript.

Co-author's signatures:

Mohsen M. T. El-Tahawy 

Marco Garavelli 

Michelle Coote 

Nadim Darwish 

Simone Ciampi



References

1. E. Gileadi, *Electrode kinetics for chemists, chemical engineers, and materials scientists*, Capstone, 1993.
2. S. Trasatti and E. Lust, in *Mod. Aspects Electrochem.*, Springer, 2002, pp. 1-215.
3. M. A. V. Devanathan and B. V. K. S. R. A. Tilak, *Chem. Rev.*, 1965, **65**, 635-684.
4. P. Delahay, *J. Electrochem. Soc.*, 1966, **113**, 967.
5. D. C. Grahame, *Chem. Rev.*, 1947, **41**, 441-501.
6. S. Ciampi, I. Díez-Pérez, M. L. Coote and N. Darwish, in *Effects of Electric Fields on Structure and Reactivity: New Horizons in Chemistry*, The Royal Society of Chemistry, 2021, pp. 71-118.
7. R. Parsons, *Chem. Rev.*, 1990, **90**, 813-826.
8. S. Ciampi, N. Darwish, H. M. Aitken, I. Díez-Pérez and M. L. Coote, *Chem. Soc. Rev.*, 2018, **47**, 5146–5164.
9. A. M. Smith, A. A. Lee and S. Perkin, *J. Phys. Chem. Lett.*, 2016, **7**, 2157-2163.
10. A. Aragonès, N. Haworth, N. Darwish, S. Ciampi, N. Bloomfield, G. Wallace, I. Díez-Pérez and M. Coote, *Nature*, 2016, **531**, 88–91.
11. M. Belotti, X. Lyu, L. Xu, P. Halat, N. Darwish, D. S. Silvester, C. Goh, E. I. Izgorodina, M. L. Coote and S. Ciampi, *J. Am. Chem. Soc.*, 2021.
12. A. J. Bard and L. R. Faulkner, *Surface Technology*, 1983, **20**, 91-92.
13. H. Helmholtz, *Ann. Phys.*, 1853, **165**, 211-233.
14. P. Attard, *Phys. Rev. E*, 1993, **48**, 3604.
15. W. Schmickler, *Electrochemical theory: double layer*, 2014.
16. A. J. Bard, L. R. Faulkner and H. S. White, *Electrochemical methods: fundamentals and applications*, John Wiley & Sons, 2022.
17. R. Leote de Carvalho and R. Evans, *Mol. Phys.*, 1994, **83**, 619-654.
18. M. V. Fedorov and A. A. Kornyshev, *Chem. Rev.*, 2014, **114**, 2978–3036.
19. R. Ramanan, D. Danovich, D. Mandal and S. Shaik, *J. Am. Chem. Soc.*, 2018, **140**, 4354-4362.
20. K. Dutta Dubey, T. Stuyver, S. Kalita and S. Shaik, *J. Am. Chem. Soc.*, 2020, **142**, 9955-9965.
21. S. J. Benkovic and S. Hammes-Schiffer, *Science*, 2003, **301**, 1196-1202.
22. S. Shaik, S. P. de Visser and D. Kumar, *J. Am. Chem. Soc.*, 2004, **126**, 11746-11749.
23. S. Shaik, D. Mandal and R. Ramanan, *Nat. Chem.*, 2016, **8**, 1091-1098.
24. R. Meir, H. Chen, W. Lai and S. Shaik, *Chem. Phys. Chem.*, 2010, **11**, 301-310.
25. L. Zhang, E. Laborda, N. Darwish, B. B. Noble, J. H. Tyrell, S. Pluczyk, A. P. Le Brun, G. G. Wallace, J. Gonzalez, M. L. Coote and S. Ciampi, *J. Am. Chem. Soc.*, 2018, **140**, 766-774.
26. N. Darwish, A. C. Aragonès, T. Darwish, S. Ciampi and I. Díez-Pérez, *Nano Lett.*, 2014, **14**, 7064-7070.
27. A. C. Aragonès, N. Darwish, S. Ciampi, F. Sanz, J. J. Gooding and I. Díez-Pérez, *Nature Comm.*, 2017, **8**, 15056.
28. J. N. Israelachvili and G. E. Adams, *J. Chem. Soc. , Faraday Trans. 1*, 1978, **74**, 975-1001.
29. W. A. Ducker, T. J. Senden and R. M. Pashley, *Nature*, 1991, **353**, 239-241.
30. M. Favaro, B. Jeong, P. N. Ross, J. Yano, Z. Hussain, Z. Liu and E. J. Crumlin, *Nature Comm.*, 2016, **7**, 12695.
31. C. Corbella, E. Pascual, G. Oncins, C. Canal, J. L. Andújar and E. Bertran, *Thin Solid Films*, 2005, **482**, 293-298.
32. Y.-H. Yoon, D.-H. Woo, T. Shin, T. D. Chung and H. Kang, *J. Phys. Chem. C*, 2011, **115**, 17384-17391.
33. P. K. Eggers, N. Darwish, M. N. Paddon-Row and J. J. Gooding, *J. Am. Chem. Soc.*, 2012, **134**, 7539-7544.
34. N. Darwish, P. K. Eggers, S. Ciampi, Y. Tong, S. Ye, M. N. Paddon-Row and J. J. Gooding, *J. Am. Chem. Soc.*, 2012, **134**, 18401-18409.
35. S. K. Haram, in *Handbook of Electrochemistry*, ed. C. G. Zoski, Elsevier, Amsterdam, 2007, pp. 329-389.

36. L. Zhang, Y. B. Vogel, B. B. Noble, V. R. Gonçales, N. Darwish, A. L. Brun, J. J. Gooding, G. G. Wallace, M. L. Coote and S. Ciampi, *J. Am. Chem. Soc.*, 2016, **138**, 9611–9619.
37. Y. B. Vogel, L. Zhang, N. Darwish, V. R. Gonçales, A. Le Brun, J. J. Gooding, A. Molina, G. G. Wallace, M. L. Coote, J. Gonzalez and S. Ciampi, *Nat. Commun.*, 2017, **8**, 2066.
38. Y. B. Vogel, A. Molina, J. Gonzalez and S. Ciampi, *Anal. Chem.*, 2019, **91**, 5929-5937.
39. S. Ciampi, T. Böcking, K. A. Kilian, M. James, J. B. Harper and J. J. Gooding, *Langmuir*, 2007, **23**, 9320–9329.
40. J. N. Israelachvili and R. M. Pashley, *Nature*, 1983, **306**, 249-250.
41. H. K. Christenson, R. G. Horn and J. N. Israelachvili, *J. Colloid Interface Sci.*, 1982, **88**, 79-88.
42. R. M. Pashley and J. N. Israelachvili, *J. Colloid Interface Sci.*, 1984, **97**, 446-455.
43. E. J. W. Verwey, J. T. G. Overbeek and K. Van Nes, *Theory of the stability of lyophobic colloids: the interaction of sol particles having an electric double layer*, Elsevier Publishing Company, 1948.
44. B. V. Derjaguin, *Acta Phys. Chim.*, 1941, **14**, 633–662.
45. H. K. Christenson, *J. Chem. Soc., Faraday Trans. 1*, 1984, **80**, 1933-1946.
46. R. M. Pashley, *J. Colloid Interface Sci.*, 1981, **83**, 531-546.
47. P. Van der Heide, *X-ray photoelectron spectroscopy: an introduction to principles and practices*, John Wiley & Sons, 2011.
48. P. Wang, Y. Li, L. Wang, J. Klos, Z. Peng, N. Kim, H. Bluhm, K. Gaskell, P. Liu, S. B. Lee, B. W. Eichhorn and Y. Wang, *EcoMat*, 2020, **2**, e12023.
49. H. Ali, R. Golnak, R. Seidel, B. Winter and J. Xiao, *ACS Appl. Nano Mater.*, 2020, **3**, 264-273.
50. M. F. Lichterman, M. H. Richter, B. S. Brunschwig, N. S. Lewis and H.-J. Lewerenz, *J. Electron Spectrosc. Relat. Phenom.*, 2017, **221**, 99-105.
51. G. Binnig, H. Rohrer, C. Gerber and E. Weibel, *Phys. Rev. Lett.*, 1982, **49**, 57-61.
52. C. Hurth, C. Li and A. J. Bard, *J. Phys. Chem. C*, 2007, **111**, 4620-4627.
53. A. C. Hillier, S. Kim and A. J. Bard, *J. Phys. Chem.*, 1996, **100**, 18808-18817.
54. K. Hu, Z. Chai, J. K. Whitesell and A. J. Bard, *Langmuir*, 1999, **15**, 3343-3347.
55. M. Nonnenmacher, M. o'Boyle and H. K. Wickramasinghe, *Appl. Phys. Lett.*, 1991, **58**, 2921-2923.
56. R. Viswanathan and M. B. Heaney, *Phys. Rev. Lett.*, 1995, **75**, 4433.
57. C. K. Li, K., presented in part at the the 201st meeting of the electrochemical society philadelphia, 2002, 2002.
58. Y. Liang, J. H. K. Pfisterer, D. McLaughlin, C. Csoklich, L. Seidl, A. S. Bandarenka and O. Schneider, *Small Methods*, 2019, **3**, 1800387.
59. D.-H. Woo, J.-S. Yoo, S.-M. Park, I. C. Jeon and H. Kang, *Bull. Korean Chem. Soc.*, 2004, **25**, 577-580.
60. Y.-H. Yoon, T. Shin, E.-Y. Shin, H. Kang, J.-S. Yoo and S.-M. Park, *Electrochim. Acta*, 2007, **52**, 4614-4621.
61. R. F. Hamou, P. U. Biedermann, A. Erbe and M. Rohwerder, *Electrochem. Commun.*, 2010, **12**, 1391-1394.
62. R. F. Hamou, P. U. Biedermann, A. Erbe and M. Rohwerder, *Electrochim. Acta*, 2010, **55**, 5210-5222.
63. N. Darwish, M. N. Paddon-Row and J. J. Gooding, *Acc. Chem. Res.*, 2014, **47**, 385-395.
64. T. J. Duffin, N. Nerngchamnong, D. Thompson and C. A. Nijhuis, *Electrochim. Acta*, 2019, **311**, 92-102.
65. J. K. Lee, S. Banerjee, H. G. Nam and R. N. Zare, *Q. Rev. Biophys.*, 2015, **48**, 437-444.
66. R. M. Bain, C. J. Pulliam, F. Thery and R. G. Cooks, *Angew. Chem. Int. Ed.*, 2016, **55**, 10478-10482.
67. R. M. Bain, C. J. Pulliam and R. G. Cooks, *Chem. Sci.*, 2015, **6**, 397-401.
68. Y.-H. Lai, S. Sathyamoorthi, R. M. Bain and R. N. Zare, *J. Am. Soc. Mass Spectrom.*, 2018, **29**, 1036-1043.
69. F. A. Houle, A. A. Wiegel and K. R. Wilson, *J. Phys. Chem. Lett.*, 2018, **9**, 1053-1057.
70. Z. Zhou, X. Yan, Y.-H. Lai and R. N. Zare, *J. Phys. Chem. Lett.*, 2018, **9**, 2928-2932.
71. H. Xiong, J. K. Lee, R. N. Zare and W. Min, *J. Phys. Chem. Lett.*, 2020, **11**, 7423-7428.
72. L. Xu, E. I. Izgorodina and M. L. Coote, *J. Am. Chem. Soc.*, 2020, **142**, 12826-12833.

73. P. Sharma and T. S. Bhatti, *Energy Convers. Manage.*, 2010, **51**, 2901–2912.
74. W. Wang, Z. Nossoni, T. Berbasova, C. T. Watson, I. Yapici, K. S. S. Lee, C. Vasileiou, J. H. Geiger and B. Borhan, *Science*, 2012, **338**, 1340-1343.
75. K. Fujimoto, S. Hayashi, J.-y. Hasegawa and H. Nakatsuji, *J. Chem. Theory Comput.*, 2007, **3**, 605-618.
76. V. R. Viviani, *Cell. Mol. Life Sci.*, 2002, **59**, 1833-1850.
77. N. Nakatani, J. Y. Hasegawa and H. Nakatsuji, *J. Am. Chem. Soc.*, 2007, **129**, 8756–8765.
78. G. J. Wendel, D. H. Stedman, C. A. Cantrell and L. Damrauer, *Anal. Chem.*, 1983, **55**, 937-940.
79. D. Marino and J. Ingle, *Anal. Chem.*, 1981, **53**, 455-458.
80. C. A. Marquette and L. J. Blum, *Anal. Bioanal. Chem.*, 2006, **385**, 546-554.
81. P. Khan, D. Idrees, M. A. Moxley, J. A. Corbett, F. Ahmad, G. von Figura, W. S. Sly, A. Waheed and M. I. Hassan, *Appl. Biochem. Biotechnol.*, 2014, **173**, 333-355.
82. Y. B. Vogel, N. Darwish and S. Ciampi, *Cell Rep. Phys. Sci.*, 2020, **1**, 100107.
83. F. H. Stillinger, in *The Physical Chemistry of Aqueous System*, Springer, 1973, pp. 43-60.
84. A. Poynor, L. Hong, I. K. Robinson, S. Granick, Z. Zhang and P. A. Fenter, *Phys. Rev. Lett.*, 2006, **97**, 266101.
85. S. Chattopadhyay, A. Uysal, B. Stripe, Y.-g. Ha, T. J. Marks, E. A. Karapetrova and P. Dutta, *Phys. rev. lett.*, 2010, **105**, 037803.
86. M. Mezger, H. Reichert, S. Schöder, J. Okasinski, H. Schröder, H. Dosch, D. Palms, J. Ralston and V. Honkimäki, *Proc. Natl. Acad. Sci.*, 2006, **103**, 18401-18404.
87. A. Giussani, P. Farahani, D. Martínez-Muñoz, M. Lundberg, R. Lindh and D. Roca-Sanjuan, *Chem. Eu. J.*, 2019, **25**, 5202-5213.
88. L. E. Barrosse-Antle, A. M. Bond, R. G. Compton, A. M. O'Mahony, E. I. Rogers and D. S. Silvester, *Chem. Asian J.*, 2010, **5**, 202–230.
89. Z. S. Qureshi, K. M. Deshmukh and B. M. Bhanage, *Clean Technol. Environ. Policy*, 2014, **16**, 1487-1513.
90. M. Z. Bazant, B. D. Storey and A. A. Kornyshev, *Phys. Rev. Lett.*, 2011, **106**, 046102.
91. A. A. Kornyshev, *J. Phys. Chem. B*, 2007, **111**, 5545–5557.
92. R. Atkin and G. G. Warr, *J. Phys. Chem. C*, 2007, **111**, 5162–5168.
93. S. Toda, R. Clark, T. Welton and S. Shigeto, *Langmuir*, 2021, **37**, 5193–5201.
94. X. Zhang, Y.-X. Zhong, J.-W. Yan, Y.-Z. Su, M. Zhang and B.-W. Mao, *Chem. Comm.*, 2012, **48**, 582–584.
95. S. Perkin, L. Crowhurst, H. Niedermeyer, T. Welton, A. M. Smith and N. N. Gosvami, *Chem. Comm.*, 2011, **47**, 6572–6574.
96. B. R. Branchini, T. L. Southworth, N. F. Khattak, E. Michelini and A. Roda, *Anal. Biochem.*, 2005, **345**, 140–148.
97. B. R. Branchini, D. M. Ablamsky, J. M. Rosenman, L. Uzasci, T. L. Southworth and M. Zimmer, *Biochemistry*, 2007, **46**, 13847–13855.
98. V. R. Bevilaqua, T. Matsuhashi, G. Oliveira, P. S. L. Oliveira, T. Hirano and V. R. Viviani, *Sci. Rep.*, 2019, **9**, 8998.
99. J. Ihssen, N. Jovanovic, T. Sirec and U. Spitz, *PLoS One*, 2021, **16**, e0244200.
100. W. Miao, *Chem. Rev.*, 2008, **108**, 2506–2553.
101. A. K. Campbell, *Chemiluminescence. Principles and applications in biology and medicine*, 1988, (Ellis Horwood).
102. I. Durrant, *Nature*, 1990, **346**, 297–298.
103. H. Seliger, J. Buck, W. Fastie and W. McElroy, *J. Gen. Physiol.*, 1964, **48**, 95–104.
104. W. H. Biggley, J. E. Lloyd and H. H. Seliger, *J. Gen. Physiol.*, 1967, **50**, 1681–1692.
105. J. H. Kim, J. H. Ahn, P. W. Barone, H. Jin, J. Zhang, D. A. Heller and M. S. Strano, *Angew. Chem.*, 2010, **122**, 1498–1501.
106. P. Watthaisong, P. Kamutira, C. Kesornpun, V. Pongsupasa, J. Phonbuppha, R. Tinikul, S. Maenpuen, T. Wongnate, R. Nishihara, Y. Ohmiya and P. Chaiyen, *Angew. Chem. Int. Ed.*, 2022, **61**, e202116908.

107. D. C. New, D. M. Miller-Martini and Y. H. Wong, *Phytother. Res.*, 2003, **17**, 439–448.
108. I. Bronstein, J. Fortin, P. E. Stanley, G. S. A. B. Stewart and L. J. Kricka, *Anal. Biochem.*, 1994, **219**, 169–181.
109. W. D. McElroy, *Proc. Natl. Acad. Sci.*, 1947, **33**, 342–345.
110. B. Bitler and E. W. Mc, *Arch. Biochem. Biophys.*, 1957, **72**, 358–368.
111. E. H. White, E. Rapaport, H. H. Seliger and T. A. Hopkins, *Bioorg. Chem.*, 1971, **1**, 92–122.
112. E. H. White, M. G. Steinmetz, J. D. Miano, P. D. Wildes and R. Morland, *J. Am. Chem. Soc.*, 1980, **102**, 3199–3208.
113. T. A. Hopkins, H. H. Seliger, E. H. White and M. W. Cass, *J. Am. Chem. Soc.*, 1967, **89**, 7148–7150.
114. E. H. White, J. D. Miano and M. Umbreit, *J. Am. Chem. Soc.*, 1975, **97**, 198–200.
115. I. Navizet, Y.-J. Liu, N. Ferré, H.-Y. Xiao, W.-H. Fang and R. Lindh, *J. Am. Chem. Soc.*, 2010, **132**, 706–712.
116. N. Nakatani, J.-y. Hasegawa and H. Nakatsuji, *Chem. Phys. Lett.*, 2009, **469**, 191–194.
117. S. Hosseinkhani, *Cell. Mol. Life Sci.*, 2011, **68**, 1167–1182.
118. R. S. Chittock, A. Glidle, C. W. Wharton, N. Berovic, T. D. Beynon and J. M. Cooper, *Anal. Chem.*, 1998, **70**, 4170–4176.
119. R. S. Chittock, C. W. Wharton, B. Jackson, N. Berovic, D. Beynon and J. M. Cooper, *Chem. Comm.*, 1996, DOI: 10.1039/CC9960002493, 2493–2494.
120. A. Tagami, N. Ishibashi, D.-i. Kato, N. Taguchi, Y. Mochizuki, H. Watanabe, M. Ito and S. Tanaka, *Chem. Phys. Lett.*, 2009, **472**, 118–123.
121. H. Fraga, *Photochem. Photobiol. Sci.*, 2008, **7**, 146–158.
122. B. R. Branchini, C. E. Behney, T. L. Southworth, D. M. Fontaine, A. M. Gulick, D. J. Vinyard and G. W. Brudvig, *J. Am. Chem. Soc.*, 2015, **137**, 7592–7595.
123. L. Pinto da Silva and J. C. G. Esteves da Silva, *Photochem. Photobiol. Sci.*, 2013, **12**, 1615–1621.
124. H. H. Seliger and E. W. Mc, *Science*, 1962, **138**, 683–685.
125. J. W. Hastings, W. D. McElroy and J. Coulombre, *J. Cell. Comp. Physiol.*, 1953, **42**, 137–150.
126. W. McElroy, *Mechanism of action of firefly luciferase*, 1962.
127. J. Wang, Z. Jiang, L. Xie, M. Liu and Y. Yuan, *Microchim. Acta*, 2017, **184**, 289–296.
128. Z. Chen, J. Wang, Z. Lin and G. Chen, *Electrochim. Acta*, 2006, **51**, 5864–5869.
129. E. H. White, E. Rapaport, T. A. Hopkins and H. H. Seliger, *J. Am. Chem. Soc.*, 1969, **91**, 2178–2180.
130. F. Si, Y. Zhang, L. Yan, J. Zhu, M. Xiao, C. Liu, W. Xing and J. Zhang, in *Rotating Electrode Methods and Oxygen Reduction Electrocatalysts*, eds. W. Xing, G. Yin and J. Zhang, Elsevier, Amsterdam, 2014, DOI: <https://doi.org/10.1016/B978-0-444-63278-4.00004-5>, pp. 133–170.
131. P. Christ, A. G. Lindsay, S. S. Vormittag, J. M. Neudörfl, A. Berkessel and A. C. O'Donoghue, *Chem. – Eur. J.*, 2011, **17**, 8524–8528.
132. J.-G. Zhou, Q. L. Williams, W. Walters Jr and Z.-Y. Deng, *J. Phys. Chem. B*, 2015, **119**, 10399–10405.
133. J. H. Jumppanen and M. L. Riekkola, *Electrophoresis*, 1995, **16**, 1441–1444.
134. V. A. Safonov, L. Y. Komissarov and O. A. Petrii, *Electrochim. Acta*, 1997, **42**, 675–687.
135. Q. Cao, C. Zuo, L. Li and G. Yan, *Biomicrofluidics*, 2011, **5**, 44119.
136. P. Altoè, M. Stenta, A. Bottoni and M. Garavelli, **2007**.
137. L. P. da Silva and J. C. G. Esteves da Silva, *J. Chem. Th. Com.*, 2011, **7**, 809–817.
138. S.-F. Chen, Y.-J. Liu, I. Navizet, N. Ferré, W.-H. Fang and R. Lindh, *J. Chem. Theory Comput.*, 2011, **7**, 798–803.
139. T. Hirano, Y. Hasumi, K. Ohtsuka, S. Maki, H. Niwa, M. Yamaji and D. Hashizume, *J. Am. Chem. Soc.*, 2009, **131**, 2385–2396.
140. N. Suzuki, M. Sato, K. Okada and T. Goto, *Tetrahedron*, 1972, **28**, 4065–4074.
141. N. Suzuki and T. Goto, *Agric. Biol. Chem.*, 1972, **36**, 2213–2221.
142. R. A. Morton, T. A. Hopkins and H. H. Seliger, *Biochemistry*, 1969, **8**, 1598–1607.
143. C.-H. Li and S.-C. Tu, *Biochemistry*, 2005, **44**, 12970–12977.

144. B. R. Branchini, R. A. Magyar, M. H. Murtiashaw and N. C. Portier, *Biochemistry*, 2001, **40**, 2410–2418.
145. M.-J. Shi and H. Cui, *Electrochim. Acta*, 2006, **52**, 1390–1397.
146. R. C. Engstrom, K. W. Johnson and S. DesJarlais, *Anal. Chem.*, 1987, **59**, 670–673.
147. R. C. Engstrom, C. M. Pharr and M. D. Koppang, *J. Electroanal. Chem. Interfacial Electrochem.*, 1987, **221**, 251–255.
148. R. C. Engstrom, S. Ghaffari and H. Qu, *Anal. Chem.*, 1992, **64**, 2525–2529.
149. J. E. Vitt and R. C. Engstrom, *Anal. Chem.*, 1997, **69**, 1070–1076.
150. C. Amatore, A. Chovin, P. Garrigue, L. Servant, N. Sojic, S. Szunerits and L. Thouin, *Anal. Chem.*, 2004, **76**, 7202–7210.
151. A. D. Goolsby and D. T. Sawyer, *Anal. Chem.*, 1968, **40**, 83–86.
152. M. Belotti, X. Lyu, L. Xu, P. Halat, N. Darwish, D. S. Silvester, C. Goh, E. I. Izgorodina, M. L. Coote and S. Ciampi, *J. Am. Chem. Soc.*, 2021, **143**, 17431–17440.
153. A. Angulo, P. van der Linde, H. Gardeniers, M. Modestino and D. Fernández Rivas, *Joule*, 2020, **4**, 555–579.
154. S. Ciampi and K. S. Iyer, *Curr. Opin. Electrochem.*, 2022, 100992.
155. Y. B. Vogel, C. W. Evans, M. Belotti, L. Xu, I. C. Russell, L.-J. Yu, A. K. K. Fung, N. S. Hill, N. Darwish, V. R. Gonçalves, M. L. Coote, K. Swaminathan Iyer and S. Ciampi, *Nat. Commun.*, 2020, **11**, 6323.
156. S.-y. Tan, J. P. Hallett and G. H. Kelsall, *Electrochim. Acta*, 2020, **353**, 136460.
157. R. Chen and R. Hempelmann, *Electrochem. Commun.*, 2016, **70**, 56–59.
158. Y. S. Seo and S. Satija, *Langmuir*, 2006, **22**, 7113–7116.
159. L. R. Pratt and D. Chandler, *J. Chem. Phys.*, 1977, **67**, 3683–3704.
160. Y. Zhao, J. Yu, G. Xu, N. Sojic and G. Loget, *J. Am. Chem. Soc.*, 2019, **141**, 13013–13016.
161. K. Lum, D. Chandler and J. D. Weeks, *Journal*, 1999, **103**, 4570-4577.
162. R. Helmy, Y. Kazakevich, C. Ni and A. Y. Fadeev, *J. Am. Chem. Soc.*, 2005, **127**, 12446-12447.
163. R. A. Pierotti, *J. Phys. Chem.*, 1965, **69**, 281-288.
164. S. Mitra, R. Das and S. Mukherjee, *J. Photochem. Photobiol. , A* 1995, **87**, 225-230.
165. A. Cembran, R. González-Luque, P. Altoè, M. Merchán, F. Bernardi, M. Olivucci and M. Garavelli, *J. Phys. Chem. A*, 2005, **109**, 6597-6605.
166. A. Fontijn and J. Lee, *JOSA*, 1972, **62**, 1095-1098.
167. W. Wang, H. Cui, Z.-X. Deng, Y.-P. Dong and J.-Z. Guo, *J. Electroanal. Chem.*, 2008, **612**, 277–287.
168. W. Guo, J. Yan and Y. Tu, *Sci. China Chem.*, 2011, **54**, 1640–1644.
169. C. Tanford, *Science*, 1978, **200**, 1012-1018.
170. J. Sagiv, *J. Am. Chem. Soc.*, 1980, **102**, 92-98.
171. D. Chandler, *Nature*, 2005, **437**, 640-647.
172. D. Richard, C. Clanet and D. Quéré, *Nature*, 2002, **417**, 811-811.
173. P.-G. de Gennes, *Langmuir*, 2002, **18**, 3413-3414.
174. Y.-S. Seo and S. Satija, *Langmuir*, 2006, **22**, 7113-7116.
175. M. James, T. A. Darwish, S. Ciampi, S. O. Sylvester, Z. Zhang, A. Ng, J. J. Gooding and T. L. Hanley, *Soft Matter*, 2011, **7**, 5309-5318.
176. M. Mezger, H. Reichert, B. M. Ocko, J. Daillant and H. Dosch, *Phys. Rev. Lett.*, 2011, **107**, 249801.
177. R. Steitz, T. Gutberlet, T. Hauss, B. Klösgen, R. Krastev, S. Schemmel, A. C. Simonsen and G. H. Findenegg, *Langmuir*, 2003, **19**, 2409-2418.
178. Y. Wang, Y. Jiang and W. Wang, *Anal. Chem.*, 2019, **91**, 11696-11702.
179. W. Wang, Z. Nossoni, T. Berbasova, C. T. Watson, I. Yapici, K. S. S. Lee, C. Vasileiou, J. H. Geiger and B. Borhan, *Science*, 2012, **338**, 1340–1343.
180. A. Giussani, P. Farahani, D. Martínez-Muñoz, M. Lundberg, R. Lindh and D. Roca-Sanjuán, *Chem. – Eur. J.*, 2019, **25**, 5202-5213.
181. M.-J. Shi and H. Cui, *Electrochim. Acta*, 2006, **52**, 1390–1397.

182. E. H. White and M. M. Bursley, *J. Am. Chem. Soc.*, 1964, **86**, 941–942.
183. L. Chen, Y. Chi, X. Zheng, Y. Zhang and G. Chen, *Anal. Chem.*, 2009, **81**, 2394–2398.
184. Y. Yue, W. Xiang, Y. Yuan, Y. Dong and C. Yue, *J. Electrochem. Soc.*, 2021, **168**, 116509.
185. L. Zheng, Y. Chi, Y. Dong, L. Zhang and G. Chen, *J. Phys. Chem. C*, 2008, **112**, 15570–15575.
186. K. Ghandi, *Green and Sustainable Chem.*, 2013, **04**, 44–53.
187. N. Sojic, *Analytical electrogenerated chemiluminescence: from fundamentals to bioassays*, Royal Society of Chemistry, 2019.
188. R. Dufford, D. Nightingale and L. Gaddum, *J. Am. Chem. Soc.*, 1927, **49**, 1858–1864.
189. N. Harvey, *J. Phys. Chem.*, 2002, **33**, 1456–1459.
190. D. M. Hercules, *Science*, 1964, **145**, 808–809.
191. R. E. Visco and E. A. Chandross, *J. Am. Chem. Soc.*, 1964, **86**, 5350–5351.
192. K. S. V. Santhanam and A. J. Bard, *J. Am. Chem. Soc.*, 1965, **87**, 139–140.
193. N. Leventis, *J. Am. Chem. Soc.*, 2005, **127**, 2015–2016.
194. Y. B. Vogel, J. J. Gooding and S. Ciampi, *Chem. Soc. Rev.*, 2019, **48**, 3723–3739.
195. Y. B. Vogel, V. R. Gonçalves, J. J. Gooding and S. Ciampi, *J. Electrochem. Soc.*, 2017, **165**, H3085–H3092.
196. M. H. Choudhury, S. Ciampi, Y. Yang, R. Tavallaie, Y. Zhu, L. Zarei, V. R. Gonçalves and J. J. Gooding, *Chem. Sci.*, 2015, **6**, 6769–6776.
197. L. Li, Y. Chen and J.-J. Zhu, *Anal. Chem.*, 2017, **89**, 358–371.
198. Y. Zhao, J. Yu, J.-F. Bergamini, Y. Léger, N. Sojic and G. Loget, *Cell Rep. Phys. Sci.*, 2021, **2**, 100670.
199. Y. Chi, L. Chen, L. Zheng, L. Zhang and G. Chen, *Electrochem. Commun.*, 2008, **10**, 1665–1668.
200. M. Freemantle, *An introduction to ionic liquids*, Royal Society of chemistry, 2010.
201. M. Belotti, El-Tahawy, M..M.T., Yu, L., Russell, I..C., Darwish, N., Coote, M..L., Garavelli, M. and Ciampi, S., *Angew. Chem. Int. Ed.*, 2022, **61**, e202209670.
202. K. Anandhan, M. Cerón, V. Perumal, P. Ceballos, P. Gordillo-Guerra, E. Pérez-Gutiérrez, A. E. Castillo, S. Thamotharan and M. J. Percino, *RSC Adv.*, 2019, **9**, 12085–12096.
203. P. Suppan, *J. Photochem. Photobiol. , A*, 1990, **50**, 293–330.
204. P. Khan, D. Idrees, M. A. Moxley, J. A. Corbett, F. Ahmad, G. von Figura, W. S. Sly, A. Waheed and M. I. Hassan, *Appl. Biochem. Biotechnol.*, 2014, **173**, 333–355.
205. Irkham, R. R. Rais, T. A. Ivandini, A. Fiorani and Y. Einaga, *Anal. Chem.*, 2021, **93**, 2336–2341.
206. I. M. AlNashef, M. L. Leonard, M. A. Matthews and J. W. Weidner, *Ind. Eng. Chem. Res.*, 2002, **41**, 4475–4478.
207. M. Han and R. M. Espinosa-Marzal, *ACS Appl. Mater. Interfaces*, 2019, **11**, 33465–33477.
208. I. M. AlNashef, M. L. Leonard, M. C. Kittle, M. A. Matthews and J. W. Weidner, *Electrochem. Solid-State Lett.*, 2001, **4**, D16.
209. M. Hayyan, M. A. Hashim and I. M. AlNashef, *Chem. Rev.*, 2016, **116**, 3029–3085.
210. A. René, D. Hauchard, C. Lagrost and P. Hapiot, *J. Phys. Chem. B*, 2009, **113**, 2826–2831.
211. Y. Nosaka, Y. Yamashita and H. Fukuyama, *J. Phys. Chem. B*, 1997, **101**, 5822–5827.
212. K. E. Haapakka and J. J. Kankare, *Anal. Chim. Acta*, 1982, **138**, 263–275.
213. W. D. McCulloch, N. Xiao, G. Gourdin and Y. Wu, *Chem. – Eur. J.*, 2018, **24**, 17627–17637.
214. M. V. Fedorov and A. A. Kornyshev, *Electrochim. Acta*, 2008, **53**, 6835–6840.
215. R. Hayes, N. Borisenko, M. K. Tam, P. C. Howlett, F. Endres and R. Atkin, *J. Phys. Chem. C*, 2011, **115**, 6855–6863.
216. H. Li, F. Endres and R. Atkin, *Phys. Chem. Chem. Phys.*, 2013, **15**, 14624–14633.
217. S. Gabriel and J. Weiner, *Berichte der deutschen chemischen Gesellschaft*, 1888, **21**, 2669–2679.
218. P. Bonhôte, A.-P. Dias, N. Papageorgiou, K. Kalyanasundaram and M. Grätzel, *Inorg. Chem.*, 1996, **35**, 1168–1178.
219. N. De Vos, C. Maton and C. V. Stevens, *Chem. Electro. Chem.*, 2014, **1**, 1258–1270.
220. C. Zhong, Y. Deng, W. Hu, J. Qiao, L. Zhang and J. Zhang, *Chem. Soc. Rev.*, 2015, **44**, 7484–7539.

221. J. Wu, Z. Lan, J. Lin, M. Huang, Y. Huang, L. Fan and G. Luo, *Chem. Rev.*, 2015, **115**, 2136–2173.
222. I. Osada, H. de Vries, B. Scrosati and S. Passerini, *Angew. Chem. Int. Ed.*, 2016, **55**, 500–513.
223. M. Watanabe, M. L. Thomas, S. Zhang, K. Ueno, T. Yasuda and K. Dokko, *Chem. Rev.*, 2017, **117**, 7190–7239.
224. H. Li and M. N. Kozbrak, *J. Chem. Phys.*, 2009, **131**, 194507.
225. M. A. Gebbie, M. Valtiner, X. Banquy, E. T. Fox, W. A. Henderson and J. N. Israelachvili, *Proc. Natl. Acad. Sci.*, 2013, **110**, 9674–9679.
226. S. Perkin, M. Salanne, P. Madden and R. Lynden-Bell, *Proc. Natl. Acad. Sci.*, 2013, **110**, E4121–E4121.
227. T. Welton, *Chem. Rev.*, 1999, **99**, 2071–2084.
228. J. P. Hallett and T. Welton, *Chem. Rev.*, 2011, **111**, 3508–3576.
229. I. Krossing, J. M. Slattey, C. Dagueuet, P. J. Dyson, A. Oleinikova and H. Weingärtner, *J. Am. Chem. Soc.*, 2006, **128**, 13427–13434.
230. X. Gong, A. Kozbial and L. Li, *Chem. Sci.*, 2015, **6**, 3478–3482.
231. M. Mezger, H. Schröder, H. Reichert, S. Schramm, J. S. Okasinski, S. Schöder, V. Honkimäki, M. Deutsch, B. M. Ocko, J. Ralston, M. Rohwerder, M. Stratmann and H. Dosch, *Science*, 2008, **322**, 424–428.
232. R. Yamamoto, H. Morisaki, O. Sakata, H. Shimotani, H. Yuan, Y. Iwasa, T. Kimura and Y. Wakabayashi, *Appl. Phys. Lett.*, 2012, **101**, 053122.
233. H. Li, M. W. Rutland and R. Atkin, *Phys. Chem. Chem. Phys.*, 2013, **15**, 14616–14623.
234. M. Sha, G. Wu, Q. Dou, Z. Tang and H. Fang, *Langmuir*, 2010, **26**, 12667–12672.
235. N. Nishi, J. Uchiyashiki, Y. Ikeda, S. Katakura, T. Oda, M. Hino and N. L. Yamada, *J. Phys. Chem. C*, 2019, **123**, 9223–9230.
236. M. A. Gebbie, H. A. Dobbs, M. Valtiner and J. N. Israelachvili, *Proc. Natl. Acad. Sci.*, 2015, **112**, 7432–7437.
237. B. Bozzini, B. Busson, C. Humbert, C. Mele, P. Raffa and A. Tadjeddine, *J. Electroanal. Chem.*, 2011, **661**, 20–24.
238. S. Arzhantsev, H. Jin, N. Ito and M. Maroncelli, *Chem. Phys. Lett.*, 2006, **417**, 524–529.
239. N. Nishi, Y. Hirano, T. Motokawa and T. Kakiuchi, *Phys. Chem. Chem. Phys.*, 2013, **15**, 11615–11619.
240. B. Roling, M. Drüscher and B. Huber, *Faraday Discuss.*, 2012, **154**, 303–311.
241. W. Zhou, Y. Xu and Y. Ouchi, *ECS Trans.*, 2013, **50**, 339–348.
242. S. Makino, Y. Kitazumi, N. Nishi and T. Kakiuchi, *Electrochem. Commun.*, 2011, **13**, 1365–1368.
243. M. V. Fedorov and A. A. Kornyshev, *J. Phys. Chem. B*, 2008, **112**, 11868–11872.
244. S. Baldelli, *J. Phys. Chem. B*, 2005, **109**, 13049–13051.
245. S. Baldelli, *Acc. Chem. Res.*, 2008, **41**, 421–431.
246. M. T. Alam, M. M. Islam, T. Okajima and T. Ohsaka, *J. Phys. Chem. C*, 2007, **111**, 18326–18333.
247. A. Uysal, H. Zhou, G. Feng, S. S. Lee, S. Li, P. Fenter, P. T. Cummings, P. F. Fulvio, S. Dai, J. K. McDonough and Y. Gogotsi, *J. Phys. Chem. C*, 2014, **118**, 569–574.
248. S. Rivera-Rubero and S. Baldelli, *J. Phys. Chem. B*, 2004, **108**, 15133–15140.
249. V. Lockett, R. Sedev, J. Ralston, M. Horne and T. Rodopoulos, *J. Phys. Chem. C*, 2008, **112**, 7486–7495.
250. C. Aliaga and S. Baldelli, *J. Phys. Chem. B*, 2006, **110**, 18481–18491.
251. L. A. Jurado and R. M. Espinosa-Marzal, *Sci. Rep.*, 2017, **7**, 4225.
252. A. Brandt, S. Pohlmann, A. Varzi, A. Balducci and S. Passerini, *MRS Bulletin*, 2013, **38**, 554–559.
253. M. Salanne, in *Ionic Liquids II*, eds. B. Kirchner and E. Perlt, Springer International Publishing, Cham, 2018, DOI: 10.1007/978-3-319-89794-3_2, pp. 29–53.
254. N. Ramaswamy and S. Mukerjee, *J. Phys. Chem. C*, 2011, **115**, 18015–18026.
255. M. A. Bhat, P. P. Ingole, V. R. Chaudhari and S. K. Haram, *J. Phys. Chem. B*, 2009, **113**, 2848–2853.
256. S. Shaik, D. Mandal and R. Ramanan, *Nat. Chem.*, 2016, **8**, 1091–1098.
257. R. Meir, H. Chen, W. Lai and S. Shaik, *Chem. phys. chem.*, 2010, **11**, 301–310.
258. S. Shaik, R. Ramanan, D. Danovich and D. Mandal, *Chem. Soc. Rev.*, 2018, **47**, 5125–5145.

259. J. J. Gooding and S. Ciampi, *Chem. Soc. Rev.*, 2011, **40**, 2704–2718.
260. M. V. Fedorov, N. Georgi and A. A. Kornyshev, *Electrochem. Commun.*, 2010, **12**, 296–299.
261. R. F. Peart, *Physica Status Solidi (b)*, 1966, **15**, K119–K122.
262. C. Gomes, R. Costa, C. M. Pereira and A. F. Silva, *RSC Adv.*, 2014, **4**, 28914–28921.
263. C. Alonso, R. C. Salvarezza, J. M. Vara, A. J. Arvia, L. Vazquez, A. Bartolome and A. M. Baro, *J. Electrochem. Soc.*, 1990, **137**, 2161–2166.
264. K. Low, L. Wylie, D. L. A. Scarborough and E. I. Izgorodina, *Chem. Commun.*, 2018, **54**, 11226–11243.
265. M. N. Kobrak and N. Sandalow, *ECS Proceedings Volumes*, 2004, **24**, 417.
266. R. Clark, M. von Domaros, A. J. S. McIntosh, A. Luzar, B. Kirchner and T. Welton, *J. Chem. Phys.*, 2019, **151**, 164503.
267. J. Rigby and E. I. Izgorodina, *J. Chem. Theory Comput.*, 2014, **10**, 3111–3122.
268. E. I. Izgorodina, M. Forsyth and D. R. MacFarlane, *Phys. Chem. Chem. Phys.*, 2009, **11**, 2452–2458.
269. B. Evanko, S. W. Boettcher, S. J. Yoo and G. D. Stucky, *ACS Energy Lett.*, 2017, **2**, 2581–2590.
270. E. Mourad, L. Coustan, P. Lannelongue, D. Zigah, A. Mehdi, A. Vioux, S. A. Freunberger, F. Favier and O. Fontaine, *Nat. Mater.*, 2017, **16**, 446–453.
271. R. J. Gale and R. A. Osteryoung, *Electrochim. Acta*, 1980, **25**, 1527–1529.
272. V. Lockett, M. Horne, R. Sedev, T. Rodopoulos and J. Ralston, *Phys. Chem. Chem. Phys.*, 2010, **12**, 12499–12512.
273. A. D. Graves and D. Inman, *Nature*, 1965, **208**, 481–482.
274. S. Ferrie, N. Darwish, J. J. Gooding and S. Ciampi, *Nano Energy*, 2020, **78**, 105210.
275. J. N. Canongia Lopes, J. Deschamps and A. A. H. Pádua, *J. Phys. Chem. B*, 2004, **108**, 2038–2047.
276. J. N. Canongia Lopes, A. A. H. Pádua and K. Shimizu, *J. Phys. Chem. B*, 2008, **112**, 5039–5046.
277. K. Goloviznina, J. N. Canongia Lopes, M. Costa Gomes and A. A. H. Pádua, *J. Chem. Theory Comput.*, 2019, **15**, 5858–5871.
278. L. Martínez, R. Andrade, E. G. Birgin and J. M. Martínez, *J. Comput. Chem.*, 2009, **30**, 2157–2164.
279. S. Plimpton, *J. Comput. Phys.*, 1995, **117**, 1–19.
280. M. Brehm and B. Kirchner, *J. Chem. Inf. Model.*, 2011, **51**, 2007–2023.
281. M. Brehm, M. Thomas, S. Gehrke and B. Kirchner, *J. Chem. Phys.*, 2020, **152**, 164105.
282. M. C. Buzzeo, R. G. Evans and R. G. Compton, *ChemPhysChem*, 2004, **5**, 1106–1120.
283. G. Yang, Y. Song, Q. Wang, L. Zhang and L. Deng, *Mater. Des.*, 2020, **190**, 108563.
284. F. Zhou, A. Izgorodin, R. K. Hocking, L. Spiccia and D. R. MacFarlane, *Adv. Energy Mater.*, 2012, **2**, 1013–1021.
285. R. Rama, S. Meenakshi, K. Pandian and S. C. B. Gopinath, *Crit. Rev. Anal. Chem.*, 2022, **52**, 1422–1431.
286. M. C. Buzzeo, C. Hardacre and R. G. Compton, *Anal. Chem.*, 2004, **76**, 4583–4588.
287. J. R. Sangoro, A. Sergej, S. Naumov, P. Galvosas, J. Kärger, C. Wespe, F. Bordusa and F. Kremer, *Phys. Rev. E*, 2008, **77**, 051202.
288. S. Monaco, F. Soavi and M. Mastragostino, *J. Phys. Chem. Lett.*, 2013, **4**, 1379–1382.
289. J.-W. Park, K. Yoshida, N. Tachikawa, K. Dokko and M. Watanabe, *J. Power Sources*, 2011, **196**, 2264–2268.
290. H. Li, J. Wang, G. G. Warr and R. Atkin, *J. Colloid Interface Sci.*, 2023, **630**, 658–665.
291. A. J. Bard, *J. Am. Chem. Soc.*, 2010, **132**, 7559–7567.
292. H. Ahmad, S. K. Kamarudin, L. J. Minggu and M. Kassim, *Renewable Sustainable Energy Rev.*, 2015, **43**, 599–610.
293. X. Xiao, S. Pan, J. S. Jang, F.-R. F. Fan and A. J. Bard, *J. Phys. Chem. C*, 2009, **113**, 14978–14982.
294. Y. Ren, C. Yu, X. Tan, H. Huang, Q. Wei and J. Qiu, *Energy Environ. Sci.*, 2021, **14**, 1176–1193.
295. Y. Kiros and M. Bursell, *Int. J. Electrochem. Sci.*, 2008, **3**, 444–451.
296. R. J. Thorne, C. Sommerseth, A. P. Ratvik, S. Rørvik, E. Sandnes, L. P. Lossius, H. Linga and A. M. Svensson, *J. Electrochem. Soc.*, 2015, **162**, E104.

297. H. Vogt, *Electrochim. Acta*, 2017, **235**, 495–499.
298. T. Sato, G. Masuda and K. Takagi, *Electrochim. Acta*, 2004, **49**, 3603–3611.
299. X. Zhao, H. Ren and L. Luo, *Langmuir*, 2019, **35**, 5392–5408.
300. R. F. de Souza, J. C. Padilha, R. S. Gonçalves, M. O. de Souza and J. Rault-Berthelot, *J. Power Sources*, 2007, **164**, 792–798.
301. R. F. de Souza, G. Loget, J. C. Padilha, E. M. A. Martini and M. O. de Souza, *Electrochem. Commun.*, 2008, **10**, 1673–1675.
302. M. Filla, J. F. Davidson, J. F. Bates and M. A. Eccles, *Chem. Eng. Sci.*, 1976, **31**, 359–367.
303. T. Burdyny, P. J. Graham, Y. Pang, C.-T. Dinh, M. Liu, E. H. Sargent and D. Sinton, *ACS Sustainable Chem. Eng.*, 2017, **5**, 4031–4040.
304. Y. B. Vogel, A. Molina, J. Gonzalez and S. Ciampi, *Electrochim. Acta*, 2020, **356**, 136849.
305. C. Amatore, J. M. Savéant and D. Tessier, *J. Electroanal. Chem. Interfacial Electrochem.*, 1983, **147**, 39–51.
306. F. C. Hendriks, F. Meirer, A. V. Kubarev, Z. Ristanović, M. B. J. Roeflaers, E. T. C. Vogt, P. C. A. Bruijninx and B. M. Weckhuysen, *J. Am. Chem. Soc.*, 2017, **139**, 13632–13635.
307. J. R. Elliott and R. G. Compton, *J. Electroanal. Chem.*, 2022, **908**, 116114.
308. W. J. Bowyer, J. Xie and R. C. Engstrom, *Anal. Chem.*, 1996, **68**, 2005–2009.
309. C. M. Pharr, R. C. Engstrom, R. A. Tople, T. K. Bee and P. L. Unzelman, *J. Electroanal. Chem. Interfacial Electrochem.*, 1990, **278**, 119–128.
310. Y. B. Vogel, V. R. Gonçalves, J. J. Gooding and S. Ciampi, *J. Electrochem. Soc.*, 2018, **165**, H3085.
311. T. Doneux, L. Bouffier, B. Goudeau and S. Arbault, *Anal. Chem.*, 2016, **88**, 6292–6300.
312. N. C. Rudd, S. Cannan, E. Bitziou, I. Ciani, A. L. Whitworth and P. R. Unwin, *Anal. Chem.*, 2005, **77**, 6205–6217.
313. S. Cannan, I. Douglas Macklam and P. R. Unwin, *Electrochem. Commun.*, 2002, **4**, 886–892.
314. H. J. Kragt, C. P. Smith and H. S. White, *J. Electroanal. Chem. Interfacial Electrochem.*, 1990, **278**, 403–407.
315. B. D. Bath, R. D. Lee, H. S. White and E. R. Scott, *Anal. Chem.*, 1998, **70**, 1047–1058.
316. Y. Takahashi, A. I. Shevchuk, P. Novak, B. Babakinejad, J. Macpherson, P. R. Unwin, H. Shiku, J. Gorelik, D. Klenerman, Y. E. Korchev and T. Matsue, *Proc. Natl. Acad. Sci.*, 2012, **109**, 11540–11545.
317. M. B. Al-Handawi, S. Polavaram, A. Kurlevskaya, P. Commins, S. Schramm, C. Carrasco-López, N. M. Lui, K. M. Solntsev, S. P. Laptinok, I. Navizet and P. Naumov, *Chem. Rev.*, 2022, **122**, 13207–13234.
318. J. Schindelin, I. Arganda-Carreras, E. Frise, V. Kaynig, M. Longair, T. Pietzsch, S. Preibisch, C. Rueden, S. Saalfeld, B. Schmid, J.-Y. Tinevez, D. J. White, V. Hartenstein, K. Eliceiri, P. Tomancak and A. Cardona, *Nat. Methods*, 2012, **9**, 676–682.
319. H. C. Berg, in *Random Walks in Biology*, Princeton University Press, 2018.
320. R. G. Compton and C. E. Banks, *Understanding voltammetry*, World Scientific, 2018.
321. M. Belotti, M. M. T. El-Tahawy, N. Darwish, M. Garavelli and S. Ciampi, *ChemElectroChem*, 2022, DOI: <https://doi.org/10.1002/celec.202201033>, e202201033.
322. W. Sheng, H. A. Gasteiger and Y. Shao-Horn, *J. Electrochem. Soc.*, 2010, **157**, B1529.
323. C. Amatore, C. c. Pebay, L. Thouin, A. Wang and J. Warkocz, *Anal. Chem.*, 2010, **82**, 6933–6939.
324. C. Amatore, S. Szunerits, L. Thouin and J.-S. Warkocz, *J. Electroanal. Chem.*, 2001, **500**, 62–70.
325. N. Baltes, L. Thouin, C. Amatore and J. Heinze, *Angew. Chem., Int. Ed.*, 2004, **43**, 1431–1435.
326. T. Moazzenzade, X. Yang, L. Walterbos, J. Huskens, C. Renault and S. G. Lemay, *J. Am. Chem. Soc.*, 2020, **142**, 17908–17912.
327. I. Williams, S. Lee, A. Apriceno, R. P. Sear and G. Battaglia, *Proc. Natl. Acad. Sci.*, 2020, **117**, 25263–25271.
328. T. Prem Kumar, P. V. S. S. Prabhu, A. K. Srivastava, U. Bejoy Kumar, R. Ranganathan and R. Gangadharan, *J. Power Sources*, 1994, **50**, 283–294.

329. R. Hayes, G. G. Warr and R. Atkin, *Chem. Rev.*, 2015, **115**, 6357–6426.
330. J. Hui, X. Zhou, R. Bhargava, A. Chinderle, J. Zhang and J. Rodríguez-López, *Electrochim. Acta*, 2016, **211**, 1016–1023.
331. J. B. Cooper and A. M. Bond, *Anal. Chem.*, 1993, **65**, 2724–2730.
332. B. Hwang, M. S. Park and K. Kim, *Chem. Sus. Chem.*, 2015, **8**, 310–314.
333. X. Zhang, J. Leddy and A. J. Bard, *J. Am. Chem. Soc.*, 1985, **107**, 3719–3721.
334. Q.-W. Sun, K. Murase, T. Ichii and H. Sugimura, *J. Electroanal. Chem.*, 2010, **643**, 58–66.
335. D. Zigah, A. Wang, C. Lagrost and P. Hapiot, *J. Phys. Chem. B*, 2009, **113**, 2019–2023.
336. U. Schröder, J. D. Wadhawan, R. G. Compton, F. Marken, P. A. Suarez, C. S. Consorti, R. F. de Souza and J. Dupont, *New J. Chem.*, 2000, **24**, 1009–1015.
337. S. T. Mayer, R. W. Pekala and J. L. Kaschmitter, *J. Electrochem. Soc.*, 1993, **140**, 446.
338. E. Z. Faraggi, D. Davidov, G. Cohen, R. Neumann and Y. Avny, *Adv. Mater.*, 1996, **8**, 234–237.
339. H. Li, L. Bouffier, S. Arbault, A. Kuhn, C. F. Hogan and N. Sojic, *Electrochem. Commun.*, 2017, **77**, 10–13.
340. M. Li, J. Lu, Z. Chen and K. Amine, *Adv. Mater.*, 2018, **30**, 1800561.
341. A. Karabchevsky, A. Mosayyebi and A. V. Kavokin, *Light: Sci. Appl.*, 2016, **5**, e16164–e16164.
342. C. J. Barrelet, D. B. Robinson, J. Cheng, T. P. Hunt, C. F. Quate and C. E. D. Chidsey, *Langmuir*, 2001, **17**, 3460–3465.
343. W. Wang, N. C. Lai, Z. Liang, Y. Wang and Y. C. Lu, *Angew. Chem.*, 2018, **130**, 5136–5140.
344. V. S. Dilimon, C. Hwang, Y.-G. Cho, J. Yang, H.-D. Lim, K. Kang, S. J. Kang and H.-K. Song, *Sci. Rep.*, 2017, **7**, 17635.
345. M. Armand, F. Endres, D. R. MacFarlane, H. Ohno and B. Scrosati, *Nat. Mater.*, 2009, **8**, 621–629.
346. G. Zhao, Y. Du, N. Zhang, C. Li, H. Ma, D. Wu, W. Cao, Y. Wang and Q. Wei, *Anal. Chim. Acta*, 2023, **1253**, 341076.
347. J. Dong and J. Feng, *Anal. Chem.*, 2023, **95**, 374–387.
348. D. Zhu, X. Zhang, Y. Han, X. Luan and G. Wei, *Sens. Diagn.*, 2023.
349. A. Konno, K. Ino, Y. Utagawa and H. Shiku, *Curr. Opin. Electrochem.*, 2023, DOI: <https://doi.org/10.1016/j.coelec.2023.101270>, 101270.
350. J. Zhang, S. Arbault, N. Sojic and D. Jiang, *Annu. Rev. Anal. Chem.*, 2019, **12**, 275–295.
351. H. Qi and C. Zhang, *Anal. Chem.*, 2020, **92**, 524–534.
352. F. Du, Z. Dong, Y. Guan, A. M. Zeid, D. Ma, J. Feng, D. Yang and G. Xu, *Anal. Chem.*, 2022, **94**, 2189–2194.
353. C. Ma, Y. Cao, X. Gou and J.-J. Zhu, *Anal. Chem.*, 2020, **92**, 431–454.
354. Z. Zhang, P. Du, G. Pu, L. Wei, Y. Wu, J. Guo and X. Lu, *Mater. Chem. Front.*, 2019, **3**, 2246–2257.
355. D. Ege, W. G. Becker and A. J. Bard, *Anal. Chem.*, 1984, **56**, 2413–2417.
356. E. Betzig, G. H. Patterson, R. Sougrat, O. W. Lindwasser, S. Olenych, J. S. Bonifacino, M. W. Davidson, J. Lippincott-Schwartz and H. F. Hess, *Science*, 2006, **313**, 1642–1645.
357. C. Belthangady and L. A. Royer, *Nat. Methods*, 2019, **16**, 1215–1225.
358. J. Miller and J. C. Miller, *Statistics and chemometrics for analytical chemistry*, Pearson education, 2018.
359. K. Pierloot, B. Dumez, P.-O. Widmark and B. O. Roos, *Theor. Chim. Acc.*, 1995, **90**, 87–114.
360. M. J. Frisch, G. W. Trucks, H. B. Schlegel, G. E. Scuseria, M. A. Robb, J. R. Cheeseman, G. Scalmani, V. Barone, G. A. Petersson, H. Nakatsuji, X. Li, M. Caricato, A. V. Marenich, J. Bloino, B. G. Janesko, R. Gomperts, B. Mennucci, H. P. Hratchian, J. V. Ortiz, A. F. Izmaylov, J. L. Sonnenberg, Williams, F. Ding, F. Lipparini, F. Egidi, J. Goings, B. Peng, A. Petrone, T. Henderson, D. Ranasinghe, V. G. Zakrzewski, J. Gao, N. Rega, G. Zheng, W. Liang, M. Hada, M. Ehara, K. Toyota, R. Fukuda, J. Hasegawa, M. Ishida, T. Nakajima, Y. Honda, O. Kitao, H. Nakai, T. Vreven, K. Throssell, J. A. Montgomery Jr., J. E. Peralta, F. Ogliaro, M. J. Bearpark, J. J. Heyd, E. N. Brothers, K. N. Kudin, V. N. Staroverov, T. A. Keith, R. Kobayashi, J. Normand, K. Raghavachari, A. P. Rendell, J. C. Burant, S. S. Iyengar, J. Tomasi, M. Cossi, J. M. Millam,

- M. Klene, C. Adamo, R. Cammi, J. W. Ochterski, R. L. Martin, K. Morokuma, O. Farkas, J. B. Foresman and D. J. Fox, *Journal*, 2016, **Gaussian 16 Rev. C.01**.
361. A. V. Marenich, C. J. Cramer and D. G. Truhlar, *J. Phys. Chem. B*, 2009, **113**, 6378–6396.
362. E. I. Izgorodina, C. Y. Lin and M. L. Coote, *Phys. Chem. Chem. Phys.*, 2007, **9**, 2507–2516.
363. F. Weigend and R. Ahlrichs, *Phys. Chem. Chem. Phys.*, 2005, **7**, 3297–3305.
364. R. F. Ribeiro, A. V. Marenich, C. J. Cramer and D. G. Truhlar, *J. Phys. Chem. B*, 2011, **115**, 14556–14562.
365. D. Case, I. Ben-Shalom, S. Brozell, D. Cerutti, T. Cheatham III, V. Cruzeiro, T. Darden, R. Duke, D. Ghoreishi and M. Gilson, *University of California, San Francisco*, 2018.
366. N. Homeyer, A. H. Horn, H. Lanig and H. Sticht, *J. Mol. Model.*, 2006, **12**, 281–289.
367. L. Hedin and B. I. Lundqvist, *J. Phys. C: Solid State Phys.*, 1971, **4**, 2064.
368. C. Lee, W. Yang and R. G. Parr, *Phys. Rev. B*, 1988, **37**, 785–789.
369. E. Cancès, B. Mennucci and J. Tomasi, *J. Chem. Phys.*, 1997, **107**, 3032–3041.
370. R. Krishnan, J. S. Binkley, R. Seeger and J. A. Pople, *J. Chem. Phys.*, 1980, **72**, 650–654.
371. J. Wang, W. Wang, P. A. Kollman and D. A. Case, *J. Mol. Graphics Modell.*, 2006, **25**, 247–260.
372. T. Fox and P. A. Kollman, *J. Phys. Chem. B*, 1998, **102**, 8070–8079.
373. F.-Y. Dupradeau, A. Pigache, T. Zaffran, C. Savineau, R. Lelong, N. Grivel, D. Lelong, W. Rosanski and P. Cieplak, *Phys. Chem. Chem. Phys.*, 2010, **12**, 7821–7839.
374. H. J. Berendsen, J. v. Postma, W. F. Van Gunsteren, A. DiNola and J. R. Haak, *J. Chem. Phys.*, 1984, **81**, 3684–3690.
375. F. Aquilante, J. Autschbach, R. K. Carlson, L. F. Chibotaru, M. G. Delcey, L. De Vico, I. Fdez. Galván, N. Ferré, L. M. Frutos, L. Gagliardi, M. Garavelli, A. Giussani, C. E. Hoyer, G. Li Manni, H. Lischka, D. Ma, P. Å. Malmqvist, T. Müller, A. Nenov, M. Olivucci, T. B. Pedersen, D. Peng, F. Plasser, B. Pritchard, M. Reiher, I. Rivalta, I. Schapiro, J. Segarra-Martí, M. Stenrup, D. G. Truhlar, L. Ungur, A. Valentini, S. Vancoillie, V. Veryazov, V. P. Vysotskiy, O. Weingart, F. Zapata and R. Lindh, *J. Comput. Chem.*, 2016, **37**, 506–541.
376. B. O. Roos, P. R. Taylor and P. E. M. Sigbahn, *Chem. Phys.*, 1980, **48**, 157–173.
377. M. M. El-Tahawy, A. Nenov and M. Garavelli, *J. Chem. Theory Comput.*, 2016, **12**, 4460–4475.
378. M. M. El-Tahawy, A. Nenov, O. Weingart, M. Olivucci and M. Garavelli, *J. Phys. Chem. Lett.*, 2018, **9**, 3315–3322.
379. A. Bonvicini, B. Demoulin, S. F. Altavilla, A. Nenov, M. M. El-Tahawy, J. Segarra-Martí, A. Giussani, V. S. Batista, M. Garavelli and I. Rivalta, *Theor. Chem. Acc.*, 2016, **135**, 1–10.
380. G. Ghigo, B. O. Roos and P.-Å. Malmqvist, *Chem. Phys. Lett.*, 2004, **396**, 142–149.
381. N. Forsberg and P.-Å. Malmqvist, *Chem. Phys. Lett.*, 1997, **274**, 196–204.
382. T. Shiozaki, W. Györfy, P. Celani and H.-J. Werner, *J. Chem. Phys.*, 2011, **135**, 081106.
383. E. Johnson, K. H. Pool and R. Hamm, *Anal. Chem.*, 1966, **38**, 183–185.
384. K. Low, S. Y. S. Tan and E. I. Izgorodina, *Frontiers in Chemistry*, 2019, **7**.
385. S. Tan, S. Barrera Acevedo and E. I. Izgorodina, *J. Chem. Phys.*, 2017, **146**, 064108.
386. S. Y. S. Tan, L. Wylie, I. Begic, D. Tran and E. I. Izgorodina, *Phys. Chem. Chem. Phys.*, 2017, **19**, 28936–28942.
387. K. Goloviznina, J. N. Canongia Lopes, M. Costa Gomes and A. A. H. Pádua, *J. Chem. Theory Comput.*, 2019, **15**, 5858–5871.
388. M. J. Frisch, G. W. Trucks, H. B. Schlegel, G. E. Scuseria, M. A. Robb, J. R. Cheeseman, G. Scalmani, V. Barone, G. A. Petersson, H. Nakatsuji, X. Li, M. Caricato, A. V. Marenich, J. Bloino, B. G. Janesko, R. Gomperts, B. Mennucci, H. P. Hratchian, J. V. Ortiz, A. F. Izmaylov, J. L. Sonnenberg, Williams, F. Ding, F. Lipparini, F. Egidi, J. Goings, B. Peng, A. Petrone, T. Henderson, D. Ranasinghe, V. G. Zakrzewski, J. Gao, N. Rega, G. Zheng, W. Liang, M. Hada, M. Ehara, K. Toyota, R. Fukuda, J. Hasegawa, M. Ishida, T. Nakajima, Y. Honda, O. Kitao, H. Nakai, T. Vreven, K. Throssell, J. A. Montgomery Jr., J. E. Peralta, F. Ogliaro, M. J. Bearpark, J. J. Heyd, E. N. Brothers, K. N. Kudin, V. N. Staroverov, T. A. Keith, R. Kobayashi,

- J. Normand, K. Raghavachari, A. P. Rendell, J. C. Burant, S. S. Iyengar, J. Tomasi, M. Cossi, J. M. Millam, M. Klene, C. Adamo, R. Cammi, J. W. Ochterski, R. L. Martin, K. Morokuma, O. Farkas, J. B. Foresman and D. J. Fox, *Journal*, 2016, **Gaussian 16 Rev. A.03**.
389. D. G. A. Smith, L. A. Burns, A. C. Simmonett, R. M. Parrish, M. C. Schieber, R. Galvelis, P. Kraus, H. Kruse, R. Di Remigio, A. Alenaizan, A. M. James, S. Lehtola, J. P. Misiewicz, M. Scheurer, R. A. Shaw, J. B. Schriber, Y. Xie, Z. L. Glick, D. A. Sirianni, J. S. O'Brien, J. M. Waldrop, A. Kumar, E. G. Hohenstein, B. P. Pritchard, B. R. Brooks, H. F. Schaefer, A. Y. Sokolov, K. Patkowski, A. E. DePrince, U. Bozkaya, R. A. King, F. A. Evangelista, J. M. Turney, T. D. Crawford and C. D. Sherrill, *J. Chem. Phys.*, 2020, **152**, 184108.
390. M. A. A. Rocha, F. M. S. Ribeiro, A. I. M. C. L. Ferreira, J. A. P. Coutinho and L. M. N. B. F. Santos, *Journal of Molecular Liquids*, 2013, **188**, 196-202.
391. J.-G. Li, Y.-F. Hu, S. Ling and J.-Z. Zhang, *Journal of Chemical & Engineering Data*, 2011, **56**, 3068-3072.
392. A. Fernández, J. S. Torrecilla, J. García and F. Rodríguez, *Journal of Chemical & Engineering Data*, 2007, **52**, 1979-1983.
393. D. Tomida, S. Kanno, K. Qiao and C. Yokoyama, *High Temp.-High Pressures*, 2017, **46**.
394. E. I. Izgorodina, M. Forsyth and D. R. MacFarlane, *Phys. Chem. Chem. Phys.*, 2009, **11**, 2452-2458.
395. A. M. Bond, K. B. Oldham and G. A. Snook, *Anal. Chem.*, 2000, **72**, 3492-3496.
396. N. G. Tsierkezos, *Journal of Molecular Liquids*, 2008, **138**, 1-8.